THE UNIVERSITY OF ADELAIDE

Integrated Motor System Estimation Using Efficiency Maps

Author:
Gabriel HAINES

Supervisors:
Assoc. Prof. Nesimi ERTUGRUL
Assoc. Prof. Wen L. SOONG

A thesis submitted for the degree of Doctor of Philosophy

School of Electrical and Electronic Engineering
The University of Adelaide

February 2020

Contents

Abstract **xiii**

Declaration of Authorship **xv**

Acknowledgements **xvii**

List of Publications **xix**

1 Introduction **1**
1.1 Improving Efficiency in Motor Systems 1
1.2 Sensorless Estimation 4
1.2.1 Speed Estimation 5
1.2.2 Torque Estimation 6
1.2.3 Pump Application Estimation 9
1.3 Research Gaps 12
1.4 Original Contributions 14
1.5 Thesis Outline 16

2 Background Theory **19**
2.1 Permanent Magnet Motor Operation 19
2.1.1 Rotating Field and Back-EMF 20
2.1.2 Torque Production 22
2.1.3 Motor Control 24
2.1.4 Brushless DC Motor Control 27
2.2 Pump System Theory 30
2.2.1 Flow of Liquids 30
2.2.2 Pipe Losses 32
2.2.3 Rotodynamic Pumps 33
2.2.4 Hydraulic Systems 35
2.3 Power Conversion Operating Areas 37

3 Wide Speed Range Sensorless Operation of Brushless Permanent Magnet Motor Using Flux Linkage Increment **41**
3.1 Introduction . . . 42
3.2 Back-EMF Sensing Methods . . . 43
3.2.1 Zero Crossing Detection of Back-EMF Voltage . . . 43
3.2.2 Back-EMF Integration/Flux Linkage Increment . . . 45
3.3 Proposed Sensorless Method . . . 46
3.3.1 Terminal Voltage Measurement . . . 47
3.3.2 Pulse Width Modulation and Commutation Strategy . . . 47
3.3.3 Back-EMF Integration/Flux Linkage Increment . . . 50
3.4 Implementation . . . 52
3.5 Experimental Results . . . 54
3.5.1 Back-EMF Constant and Algorithm Tuning . . . 54
3.5.2 Flux Linkage Increment Operation . . . 55
3.5.3 Low Speed operation . . . 55
3.5.4 Position Error . . . 59
3.5.5 Dynamic Performance . . . 61
3.6 Conclusion . . . 62

4 Autonomously Obtaining System Efficiency Maps from Motor Drive Systems **65**
4.1 Introduction . . . 66
4.2 Efficiency Maps . . . 68
4.3 Autonomous Test System . . . 69
4.3.1 Autonomous Test Sequencer . . . 71
4.3.2 Power System and Devices . . . 73
4.3.3 Measurement and Data logging Modules . . . 73
4.4 Test Results . . . 73
4.5 Conclusion . . . 78

5 Motor System Sensorless State Estimation **79**
5.1 Introduction . . . 79
5.2 Overview of Proposed Method . . . 80
5.2.1 Efficiency Map Testing . . . 81
5.2.2 Inverter Measurements . . . 82
5.2.3 Modelling and Estimation . . . 83
5.3 Test Considerations . . . 85
5.3.1 Power Measurements . . . 85
5.3.2 Torque Measurements . . . 87

5.3.3 Steady State Temperature Detection . . . 88
5.4 Estimator Modelling . . . 93
5.5 Verification of Estimator Models . . . 96
5.5.1 Speed Estimator . . . 97
5.5.2 Torque Estimator . . . 99
5.5.3 Power and Efficiency Estimates . . . 101
5.6 Conclusion . . . 104

6 Pump System Sensorless State Estimation 107
6.1 Introduction . . . 107
6.2 Proposed Method for Pump State Estimation . . . 107
6.3 Test Considerations . . . 110
6.3.1 Flow Rate Measurements . . . 111
6.3.2 Pressure Measurements . . . 112
6.3.3 Flow Control Valve . . . 113
6.3.4 ISO 9906 Calculations . . . 114
6.4 Estimator Model Development and Verification . . . 118
6.4.1 Extrapolation of General Motor Estimators to a Pump Application . . . 118
6.4.2 Initial Modelling of the Pump System . . . 122
6.4.3 Verification of Initial Pump Model . . . 125
6.4.4 Second Pump Model . . . 127
6.4.5 Verification of Second Pump Model . . . 131
6.4.6 Third Pump Model . . . 133
6.4.7 Verification of Third Pump Model . . . 135
6.5 Temperature Effects . . . 140
6.6 Dynamic Performance . . . 146
6.7 Volume Estimate . . . 151
6.8 Conclusion . . . 155

7 Conclusion 157
7.1 Key Findings . . . 159
7.2 Recommendations and Future Work . . . 163

Bibliography 167

List of Figures

1.1 Breakdown of global motor usage by size and application. 2
1.2 Components of a typical motor system. 3
1.3 Proposed concept of an integrated motor system with sensorless state estimation. 16

2.1 Simplified operation of a PM motor 20
2.2 Space vectors in the stator and rotor reference frame. 23
2.3 Equivalent circuit models for an inverter and a PM motor 24
2.4 Field oriented control system diagram 25
2.5 Inverter space vectors 28
2.6 Brushless DC control system diagram 29
2.7 Illustration of Bernoulli's principle for liquids. 31
2.8 An example of a rotodynamic pump. 34
2.9 Example hydraulic systems and curves. 36
2.10 Power flow and losses in a motor system 37
2.11 Operating areas for a variety of power conversion devices 38

3.1 Inverter, brushless PM machine, and analogue to digital converter voltage divider. 47
3.2 Ideal shapes of six-step commutation sequence, machine back-EMF, machine flux linkage, resulting sectored back-EMF and resulting sectored flux linkage waveforms referenced to one electrical cycle . 49
3.3 Instantaneous floating single phase terminal voltage waveform during (a) rising and (b) falling back-EMF sectors. 50
3.4 Back-EMF integration and change in flux linkage $\Delta\psi$ for (a) sinusoidal and (b) trapezoidal back-EMF waveforms. 51
3.5 Enlarged view of the floating single phase terminal voltage waveform during: (a) rising and (b) falling back-EMF sectors. 54
3.6 Measured waveforms for operation at 2500 rpm 56
3.7 Measured waveforms for operation at 1765 rpm 57
3.8 Low speed operation at 42.1 rpm (1.404 Hz), $V_{DC} = 23.96$ V 58
3.9 Low speed operation at 19.0 rpm (0.6329 Hz), $V_{DC} = 5.614$ V 58

3.10 Position error versus speed for operation at 20 kHz PWM frequency. 60
3.11 Position error versus speed for operation at 10 kHz PWM frequency. 60
3.12 Position error versus load at when operated at rated speed. 61
3.13 Speed step response, showing the transition from open loop ramp to closed loop sensorless operation. 61
3.14 Speed step response, showing mechanical position and estimated position. 62

4.1 Summary of test procedures for (a) IEEE 1812, (b) IEC 60034-2-1 for PMSM, (c) IEEE 112, and (d) IEC 60034-2-1 for IM. 67
4.2 Summary of efficiency map measurement test procedures 68
4.3 Software and hardware for motor system testing. 70
4.4 Software and hardware for testing an integrated pump application. 71
4.5 Simplified flowchart describing the autonomous navigation. 72
4.6 Motor efficiency maps in terms of torque and speed 74
4.7 Actual sequencer measurement points and trajectory. 75
4.8 Steady state standard deviation for (a) the speed controlled device under test and (b) torque controlled load 75
4.9 Temperature of the device under test 76
4.10 Combined motor and pump test 77

5.1 Control system block diagram with proposed estimation method . 81
5.2 Inverter measurements with and without mechanical synchronisation 84
5.3 Dynamometer test system hardware 86
5.4 Autonomous test software graphical user interface (GUI) 86
5.5 Torque meter dynamic offset 87
5.6 Machine temperature during the steady state temperature detection test 89
5.7 Steady state temperature slope and predicted temperature vs. time 90
5.8 Steady state temperature detection error vs. slope 90
5.9 Steady state temperature detection error vs. time saved 91
5.10 Steady state temperature slope and predicted temperature vs. time when machine preheated 92
5.11 Motor modelling plots 95
5.12 Motor modelling test temperature 96
5.13 Motor verification test temperatures 97
5.14 Motor verification test points 97
5.15 Motor speed estimator errors 98

5.16 Motor torque estimator errors 99
5.17 Comparison torque estimation error from [23] 100
5.18 Measurement points used by [23] 101
5.19 Motor power estimator errors 102
5.20 Motor efficiency estimator errors 103
5.21 Motor efficiency for a cold and hot test 104

6.1 Control system block diagram with proposed estimation method . 109
6.2 Pump test system 110
6.3 Pump test system motor base frame 111
6.4 Autonomous test software graphical user interface (GUI) for pump testing 111
6.5 Water density and dynamic viscosity versus temperature 115
6.6 Autonomous test software pump configuration dialogue window . 117
6.7 Pump system test points and temperature for the first modelling test 119
6.8 Pump system d-axis current for the first modelling test 119
6.9 Motor system speed and torque estimators used for a pump load . 120
6.10 Motor system power and efficiency estimators used for a pump load 121
6.11 Modelling plots from the pump system's first modelling test 123
6.12 Verification of first pump model 125
6.13 Measured points compared to the head pressure model's surface . 126
6.14 Relationship between pump and motor quantities, fluctuations in measured signals 128
6.15 Verification of second pump model 131
6.16 Modelling plots from the pump system's third modelling test . . . 134
6.17 Flow estimator performance for all three pump models 136
6.18 Head estimator performance for all three pump models 137
6.19 Motor stator winding temperatures and pump water temperatures. 140
6.20 Torque and speed estimator errors for a pump application. 142
6.21 Power estimator errors for a pump application. 143
6.22 Efficiency estimator errors for a pump application. 145
6.23 Dynamic step responses of the pump estimator model with valve open 147
6.24 Dynamic step responses of the pump estimator model with valve closed 148
6.25 Dynamic responses of the pump estimator model to valve step changes. 149
6.26 Pump volume estimator performance during the third pump model verification test 153

6.27 Pump volume estimator performance corresponding to the dynamic tests in Fig. 6.23–6.25. 154

List of Tables

3.1 Specifications for test motor, Bodine 34B3FEBL. 52
3.2 Comparison of the speed range reported in the literature. 59

5.1 Steady state temperature test results from four tests over two days 91
5.2 Estimator model coefficients for general motor system operation . . 94
5.3 Motor system model's goodness of fit 94

6.1 Low pass filter specifications used for each pump model 109
6.2 Model coefficients from the pump system's first estimator model . 124
6.3 Goodness of fit for the pump system's first estimator model 124
6.4 Model coefficients from the pump system's second estimator model 129
6.5 Goodness of fit for the pump system's second estimator model . . . 129
6.6 Model coefficients from the pump system's third estimator model . 133
6.7 Goodness of fit for the pump system's third estimator model 133
6.8 Pump volume measurements at the end of Fig. 6.26 152
6.9 Pump volume measurements at the end of Fig. 6.27 152

Abstract

A motor combined with an inverter based variable speed drive and an end load device forms a motor system that can operate over a wide area of different speed and load combinations. The majority of the motor systems used in the world are low power systems that have poor motor and system efficiency, resulting in higher energy consumption. Because of cost considerations, such systems rarely include the sensors required for more efficient feedback control schemes. In cases where physical sensors are used, those motor systems experience higher cost and reduced reliability.

Using models of the motor and/or load, it is possible for a variable speed drive to estimate some motor system quantities. Position sensorless control is the most common form of sensorless operation, but it is also possible to estimate motor torque, pump pressure and pump flow. Sensorless estimates can replace physical sensors, increasing reliability and reducing both the size and cost of the motor system. For efficient and effective sensorless motor operation, accurate knowledge of a motor system's operation over a wide area must be understood in terms of the real time system state and the efficiency of the system components.

This research considers sensorless state estimation of a low-cost motor system integrated with an end application/load. A focus is given to expanding the operating area of sensorless techniques, and to better understand a motor system's performance over a wide operating area. Motor systems using permanent magnet (PM) machines were studied because of their high efficiency, high power density, and ability to operate using a range of position sensorless control schemes.

An improved method of position sensorless control for brushless DC motors was developed, enabling wider speed operation compared to methods of similar complexity. The method was implemented on a low-cost motor drive, and the performance was verified experimentally.

To better understand the performance of an integrated motor system over a large operating area, a method of autonomous testing was developed. The flexible hardware and software-based test system was adaptable to different motor system applications and collected large volumes of temperature-controlled efficiency data, allowing for a motor system to be characterised in greater detail over its operating area.

Using large sets of experimental data, a new method for general motor state sensorless estimation was developed. Estimator models were developed for speed, torque, DC power, AC power, mechanical power, inverter efficiency, motor efficiency and system efficiency. The estimators were implemented in the firmware of a low-cost inverter, and the performance over the operating area of the motor system was experimentally verified.

The method of sensorless state estimation was then extended to a pump system, demonstrating the method's ability to model the nonlinear relationship between motor and pump quantities. Estimator models were developed for pump head pressure, flow, hydraulic power, efficiency and total volume pumped. Estimator performance over the system's operating area was experimentally verified, with temperature changes and dynamic performance also being considered. The methods discussed are not limited to pump systems, but are applicable to fans, compressors, vehicles and other motor systems with multiple components, sensors, and room for efficiency improvements.

Declaration of Authorship

I certify that this work contains no material which has been accepted for the award of any other degree or diploma in my name, in any university or other tertiary institution and, to the best of my knowledge and belief, contains no material previously published or written by another person, except where due reference has been made in the text. In addition, I certify that no part of this work will, in the future, be used in a submission in my name, for any other degree or diploma in any university or other tertiary institution without the prior approval of the University of Adelaide and where applicable, any partner institution responsible for the joint-award of this degree.

I acknowledge that copyright of published works contained within this thesis resides with the copyright holder(s) of those works.

I also give permission for the digital version of my thesis to be made available on the web, via the University's digital research repository, the Library Search and also through web search engines, unless permission has been granted by the University to restrict access for a period of time.

I acknowledge the support I have received for my research through the provision of an Australian Government Research Training Program Scholarship.

Signed: _____

Date: 14/02/2020

Acknowledgements

I would like thank my supervisor Assoc. Prof. Nesimi Ertugrul for his support, time and guidance through this journey. I'm grateful for the opportunities he has provided me and have appreciated my time working with him. I'd also like to thank my co-supervisor Assoc. Prof. Wen Soong for his kind advice and guidance.

I would like to thank the Engineering Computer and Mathematical Science (ECMS) faculty's workshop staff for their support with the experimental parts of this research. I'd would like to especially thank Mr. Brad Pullen for his hard work and outstanding effort machining and assembling the motor and pump test system hardware.

I'd like to thank my wife Alyona and daughter Esther for their love and support during my time studying. I am grateful for their patience and encouragement, without which I would not have made it this far.

List of Publications

[1] G. Haines and N. Ertugrul, "Wide Speed Range Sensorless Operation of Brushless Permanent-Magnet Motor Using Flux Linkage Increment", *IEEE Trans. Ind. Electron.*, vol. 63, no. 7, pp. 4052–4060, Jul. 2016, ISSN: 0278-0046. DOI: 10.1109/TIE.2016.2544250,

[2] G. Haines, N. Ertugrul, and W. L. Soong, "Autonomously Obtaining System Efficiency Maps from Motor Drive Systems", in *2019 IEEE Int. Conf. on Ind. Technol. (ICIT)*, Melbourne, Australia, Feb. 2019, pp. 231–236. DOI: 10.1109/ICIT.2019.8755199,

[3] G. Haines and N. Ertugrul, "Application Sensorless State and Efficiency Estimation for Integrated Motor Systems", in *13th IEEE Int. Conf. on Power Electronics and Drive Systems (PEDS 2019)*, Toulouse, France, Jul. 2019, pp. 1–6.

List of Abbreviations

AC	**A**lternating **C**urrent
ADC	**A**nalogue to **D**igital **C**onverter
BEP	(pump) **B**est **E**fficiency **P**oint
BLDC	**B**rush**l**ess **DC** Motor
`cftool`	MATLAB's **C**urve **F**itting **Tool**
COAG	**C**ouncil **o**f **A**ustralian **G**overnments
DAQ	**D**ata **Acq**uisition
DC	**D**irect **C**urrent
DOL	**D**irect **O**nline **L**ine (induction machine connected direct to the grid)
DSP	**D**igital **S**ignal **P**rocessor
DUT	**D**evice **U**nder **T**est
ECM	**E**lectronically **C**ommutated **M**otor
EEI	**E**nergy **E**fficiency **I**ndex
EMF	Electro**m**otive **F**orce
FE	**F**inite **E**lement (analysis)
FIR	**F**inite **I**mpulse **R**esponse Filter
FOC	**F**ield **O**riented **C**ontrol
FPGA	**F**ield-**P**rogrammable **G**ate **A**rray
HVAC	**H**eating, **V**entilation, and **A**ir **C**onditioning
IC	**I**ntegrated **C**ircuit
IEA	**I**nternational **E**nergy **A**gency
IEC	**I**nternational **E**lectrotechnical **C**ommittee
IEEE	**I**nstitute of **E**lectrical and **E**lectronics **E**ngineers
ISO	**I**nternational **O**rganization for **S**tandardization
IGBT	**I**nsulated-**G**ate **B**ipolar **T**ransistor
IM	**I**nduction **M**achine
IPM	**I**nterior **P**ermanent **M**agnet
IIR	**I**nfinite **I**mpulse **R**esponse Filter
LabVIEW	**Lab**oratory **V**irtual **I**nstrument **E**ngineering **W**orkbench (programming language and development environment for test and measurement).

LMC	**L**oss **M**odel **C**ontrol
LPF	**L**ow **P**ass **F**ilter
LSPM	**L**ine **S**tart **P**ermanent **M**agnet Machine
MATLAB	**Mat**rix **Lab**oratory (programming language and environment for mathematical analysis).
LUT	**L**ook**u**p **T**able
MEPS	**M**andatory **E**nergy **P**erformance **S**tandards
MMF	**M**agneto**m**otive **F**orce
MOSFET	**M**etal-**O**xide-**S**emiconductor **F**ield-**E**ffect **T**ransistor
MTPA	**M**aximum **T**orque **P**er **A**mpere
NI	**N**ational **I**nstruments
PDS	**P**ower **D**rive **S**ystem
PID	**P**roportional **I**ntegral **D**erivative controller
PM	**P**ermanent **M**agnet
PMSM	**P**ermanent **M**agnet **S**ynchronous **M**achine
PWM	**P**ulse **W**idth **M**odulation
PV	**P**hoto**v**oltaic
QH	Flow-Head (pump curve)
QP	Flow-Power (pump curve)
RMSE	**R**oot **M**ean **S**quared **E**rror
ROM	**R**ead **O**nly **M**emory
RTD	**R**esistance **T**emperature **D**etector
SC	**S**earch **C**ontrol
SPM	**S**urface-mounted **P**ermanent **M**agnet
SSE	**S**um of **S**quares Due to **E**rror
THD	**T**otal **H**armonic **D**istortion
TI	**T**exas **I**nstruments
TCO	**T**otal **C**ost of **O**wnership
VSD	**V**ariable **S**peed **D**rive
ZCP	**Z**ero **C**rossing **P**oint

List of Symbols

A	cross sectional area	m^2
D	pipe diameter	m
e	back-EMF	V
f	frequency	Hz
g	acceleration of gravity	$m\,s^{-2}$
H	liquid head	m
I	current	A
i	instantaneous current	A
i_d	instantaneous d-axis current	A
i_q	instantaneous q-axis current	A
J	rotational moment of inertia	$kg\,m^2$
K_e	back-EMF constant	$V/rad\,s^{-1}$
L	inductance	H
L	pipe length	m
n	mechanical speed	rpm
P	power	W ($J\,s^{-1}$)
p	liquid pressure (gauge pressure)	Pa ($J\,m^{-3}$)
Q	flow rate	$m^3\,h^{-1}$
R	Resistance	Ω
Re	Reynolds number	(dimensionless)
t	time	s
T	torque	N m
U	liquid mean axial velocity	$m\,s^{-1}$
V	voltage	V
v	instantaneous voltage	V
v_d	instantaneous d-axis voltage	V
v_q	instantaneous q-axis voltage	V
z	elevation head, height above reference plane	m
α	rotational acceleration	$rad\,s^{-2}$
η	efficiency	%
θ_r	rotor angle	$rad\,s^{-1}$ or $^\circ$

λ	pipe friction loss coefficient	(dimensionless)
μ	dynamic viscosity	Pa s ($\mathrm{kg\,m^{-1}\,s^{-1}}$)
ρ	density	$\mathrm{kg\,m^{-3}}$
Φ	magnetic flux	Wb
ψ	magnetic flux linkage	Wb (V·s)
ω	angular frequency	$\mathrm{rad\,s^{-1}}$

Chapter 1

Introduction

Electric motors consume 44 % to 46 % of the world's electric energy [1]. With the increase in electricity prices and need to reduce carbon emissions, their has been wide spread focus on increasing the efficiency of motor systems. The International Electrotechnical Committee (IEC) has worked to revise and harmonise the international standards for motor efficiency [2]. Mandatory Energy Performance Standards (MEPS) have been introduced in a wide range of countries [1] [2], requiring motors to meet a subset of the energy efficiency classes outlined by the IEC. Countries with MEPS now represent 70 % of global electricity usage [2].

MEPS typically cover the broader motor system, including end load/ application. Pump applications represent 19 % of global electric motor energy consumption [1], and mandatory efficiency standards for pumps have been introduced. Circulator pumps for building heating/cooling when sold in Europe are required to meet a defined Energy Efficiency Index (EEI) [1]. More recently in Australia, the Council of Australian Governments (COAG) agreed to introduce MEPS for swimming pool pumps by 2020 [3]. A low level of MEPS was estimated to remove 37 % of the least efficient pool pumps in the market [4].

1.1 Improving Efficiency in Motor Systems

A motor system consists of all the components required to control the flow of electrical power from a power source and deliver it as mechanical power to a load. A direct-online (DOL) grid connected induction motor connected to a load (e.g. a pump, fan or compressor) is one of the simplest types of motor systems, with fixed speed operation and limited "on-off" control of the motor or throttling of the load (e.g. valve control in a pump application). More advanced motor systems include an variable speed drive (VSD) between the electrical power source and the motor, allowing both the motor and ultimately the mechanical load to operate at variable speed and power. Simpler VSDs for induction machines may

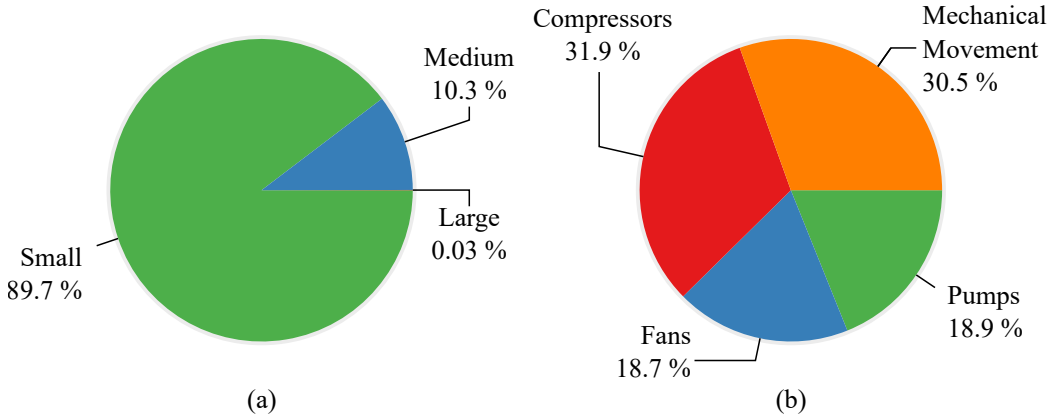

FIGURE 1.1: Breakdown of global motor usage by size and application, from [1]. Motors with power < 0.75 kW are considered small, motors with power ≥ 0.75 kW but ≤ 375 kW are considered medium sized, and motors with power > 375 kW are considered large.

use open-loop control with Volt-per-Hertz scaling. More complex VSDs use feedback sensors to provide closed loop control of torque, speed, and the end process/application.

The introduction of MEPS and newer efficiency standards are driving improvements in motor efficiency, encouraging the use of VSDs and newer motor technologies like synchronous reluctance and permanent magnet synchronous machines (PMSMs) [5], [6]. Compared to induction machines, PMSMs offer higher power density and better efficiency as a result of the excitation (rotor field) being provided by the permanent magnets instead of current in the rotor [7].

Although improving motor efficiency is important, it is only one part of the larger motor system. The overall system efficiency is dependent on the efficiency of each component and on the control strategy [8]. Traditionally, motor efficiency standards and testing considered only direct online machines operating at fixed speed. More recently, standards have evolved to consider motor efficiency as part of a larger system with VSD [2], [8]. However, these standards still fall short of thoroughly describing the efficiency of a motor system over a wide range of operating conditions. System efficiency is also not easy to determine for non-integrated motor systems where components are tested in isolation.

Efficiency maps, or iso-efficiency contours, describe efficiency over a wide operating area in a manner similar to the topographical map. For a motor, the operating area is typically a 2D area covering a range of speeds and torques, and the efficiency map describes the efficiency at each and every combination of operating points. Efficiency maps can be used to design and optimise motors [9],

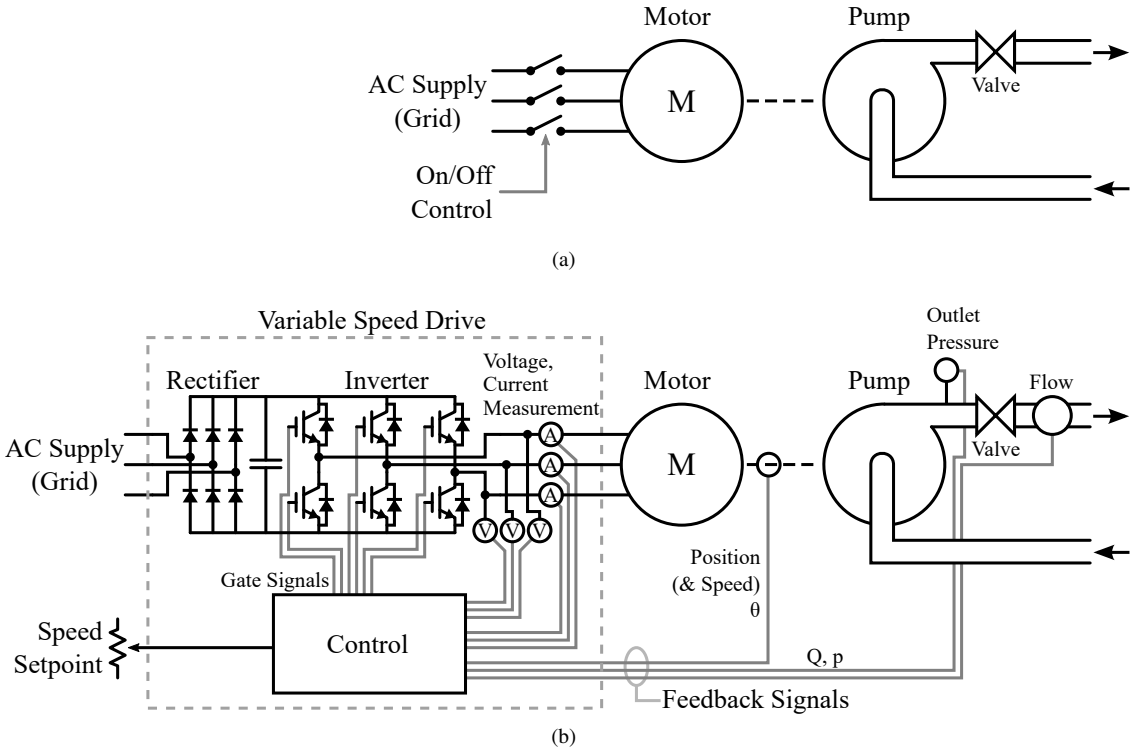

FIGURE 1.2: Components of a typical motor system, illustrated for a pump application. Simple on-off control of a direct online (grid connected) motor is shown in (a), where the system may also be controlled through inefficient mechanical throttling. A more advanced motor system with variable speed drive is shown in (b), where speed and end application feedback signals may be present to allow for feedback control to be used.

understand motor losses [10], and to analyse motor system applications [11]. Detailed efficiency maps can be obtained experimentally [12] but require a significant testing effort to obtain the necessary data [13].

The efficiency of a motor system can not only be improved at the time of design, but can also be improved during operation. The operation of a motor system is determined by the control system or control scheme used, and optimising the control scheme can have significant energy savings [14]. "On-off" control of a grid connected induction machine is one of the simplest control methods, but is limited to fixed speed operation. Throttling of the end application (e.g. varying fluid flow using a tap/valve) may also be combined with "on-off" control to allow for the system operating point to be varied. However, in the example of a fixed speed pump application, the operating point is forced to move along a fixed pump curve, and may move away from the best efficiency region [15]. Replacing "on-off" control and valve throttling with a variable speed pump can significantly reduce energy consumption of the system[15]–[17]. Similarly, large

energy savings can also be found in other fluid handling applications, including fans and compressors [16].

An effective control system requires feedback from sensors to measure and respond to the system state in order to deliver the desired output from the motor system. Typically, a VSD based motor system includes a position sensor that allows for precise position and speed control to be used. For a given application, additional sensors are required that are specific to the application's needs. In the case of a pump system, flow rate and/or pressures sensors can be used to allow a VSD to vary the pump speed to achieve precise control of flow and/or pressure. Instead of operating at an arbitrarily high speed, a variable speed pump system could reduce energy consumption by reducing the head pressure or flow rate to bring the actual pump operating point closer to the required operating point [15]. A system with better knowledge of its energy consumption could further enhance the system efficiency by better selecting the operating point to meet the demand.

Although sensors added to a motor system enable the use of more efficient control schemes, these sensors add extra cost, require more space, and reduce reliability through additional points of failure. Efficiency of a system is generally defined as the ratio between power output and power input, but the efficiency can also be considered as the ratio between the work done and total cost of ownership (including upfront costs and running costs). Complex control schemes with a plethora of sensors may reduce running costs through more efficient operation, however no benefit may be achieved if these savings do not offset the higher upfront costs. The use of *sensorless* estimation methods can avoid these additional sensor costs while retaining the benefits of feedback control systems [18].

1.2 Sensorless Estimation

Sensorless estimation in motor systems was first introduced in the mid 1980s in the form of position sensorless estimation of a brushless permanent magnet motor's rotor position using detection of the motor's back-EMF zero crossings [19]. Brushless PM motors, sometimes referred to as a brushless DC motor (BLDC), refer to a permanent magnet synchronous machine (PMSM) that is driven by trapezoidal voltages instead of traditional sinusoidal voltages. Trapezoidal control is also known as six-step commutation, because the three phase inverter applies a sequence of six combinations of DC voltage to the machine in response to the rotor position. Without knowledge of the rotor's instantaneous position, it is not

possible for the inverter's applied voltages to remain synchronised to the machine. Without the use of a position sensorless algorithm, an inverter or variable speed drive must rely on a position sensor in the form of an externally mounted incremental encoder, resolver or hall effect sensor.

Since the introduction of position sensorless estimation, a number of new and improved position sensorless methods have been introduced. These range from simpler back-EMF and zero crossing based methods suitable for only trapezoidal/BLDC control, to more complex methods using detailed mathematical models to support sinusoidal operation [20], [21]. All position sensorless methods use voltage measurements taken at the inverter terminals, and some of the more complex and capable sensorless methods also include current measurements. Simpler methods rely on just the back-EMF voltage of the motor, often measured at the inverter's terminals when one of the phases is not driven by the inverter, and determine the position with little or no knowledge of the motor's parameters. More complex methods will consider the interaction of the measured voltages and currents with a detailed model of the motor built from several known or automatically identified parameters.

The back-EMF voltage is a key quantity for any form of sensorless estimation method. The magnitude of the back-EMF voltage is speed dependent, and the phase angle is synchronised to the rotor position. At low speeds, the back-EMF voltage is also low and approaches zero as the speed approaches zero. A weak back-EMF signal is difficult to measure, and consequently almost all sensorless methods have difficulty operating at low speed. The performance of a sensorless method can be described by the operating speed range and the rotor position estimation error, where the position error ultimately determines the operating speed range of the method. When the position error becomes too large, the inverter's applied voltage ceases to be synchronised to the rotor and operation of the motor is no longer possible.

A more detailed discussion of position sensorless methods is presented in Chapter 3.

1.2.1 Speed Estimation

An inverter/variable speed drive can calculate the speed of a motor from the instantaneous rotor position (angle). Essentially this is the calculation of angular velocity using Eq. (1.1). The rotor angle can be obtained using a position sensor, with varying degrees of resolution. For example, a hall effect sensor that is commonly used for BLDC commutation only provides the rotor angle in 60° steps

per electrical cycle, whereas an incremental encoder with quadrature decoding can typically provide up to 4096 steps per mechanical cycle.

$$\omega = \frac{d\theta}{dt} \qquad (\mathrm{rad\,s^{-1}}) \tag{1.1}$$

When a position sensorless method is used, the estimated rotor position is used for the speed calculation instead of a position sensor measurement. Sensorless operation of PM motor is only possible if the rotor position is known with sufficient accuracy for the inverter's voltage output to remain synchronised to the to the rotor. Consequently, it can be expected that position sensorless methods will naturally have good estimation of the motor's speed, with the rotor position error limiting the overall operating speed range [22].

Because speed is calculated using the derivative of rotor angle position, and a derivative functions as a high pass filter with 20 dB/decade slope, the speed calculation will be sensitive to noise and fluctuations/jitter in the position estimate. To combat this sensitivity to noise and fluctuations, speed calculation methods will typically include some form of low pass filtering.

1.2.2 Torque Estimation

For PM motors, torque is proportional to current. It follows that the torque applied by a motor can be estimated using currents measured at the inverter. For a brushless DC motor (PMSM driven with six-step commutation/trapezoidal voltages), the electromagnetic (developed, or air gap) torque is described by Eq. (1.2) [7]. T is the electromagnetic torque in Nm, I is the stator current (total DC current into the inverter), and K_T is the torque constant of the machine in Nm/A.

$$T = K_T I \qquad (\mathrm{Nm}) \tag{1.2}$$

For inverters that use field oriented control (FOC), or vector control, the relationship between torque and current is more complicated. A FOC control system uses the instantaneous rotor position to transform control system quantities like voltage and current from a three phase stationary reference frame to a two phase rotating reference frame. The result is that sinusoidal voltages and currents at the motor's three phase terminals are transformed into DC voltage and current components in terms of the rotor d-axis (in phase) and q-axis (quadrature phase, 90° ahead) basis vectors. Torque is described by Eq. 1.3 [7], where p is the number of pole pairs, ψ is the peak flux linkage, L_d and L_q are the d and q-axis stator inductances, and i_d and i_q are the d and q-axis currents.

$$T = \frac{3}{2} p[\psi + (L_d - L_q) i_d] i_q \qquad \text{(Nm)} \tag{1.3}$$

Eq. 1.3 represents the more general case of a salient PM machine, where $L_d \neq L_q$ and the torque also has a d-axis current component in addition to the q-axis component. For the case of a non-salient PM machine (e.g. a surface PM machine) where $L_d \approx L_q$, the torque equation simplifies to Eq. (1.4):

$$T = \frac{3}{2} p \psi i_q \qquad \text{(Nm)} \tag{1.4}$$

Modern variable speed drives typically implement torque control by controlling the q-axis current i_q. This is often done inside a speed loop, where a control system varies the i_q current to vary the applied torque in order to maintain a speed set point. If all of the required motor parameters are known, then Eq. 1.3 can also be used to estimate the torque applied by the motor. This is the basis for many of the torque estimation methods used in industrial drives.

One of the challenges in producing a torque estimate is obtaining the necessary motor model parameters used by Eq. 1.3. Modern industrial drives now include auto-identification routines that apply a sequence of voltages and measure the response of the motor to determine the motor parameters. This enables these drives to then perform real-time torque estimation with no additional information from the user.

The torque estimation performance of two induction motors was evaluated in [23], where motors of 7.5 kW and 0.25 kW power levels where driven by Siemen's VSDs of corresponding power levels. The results showed that the error in torque estimation increased at low values of torque. The results also showed that using a position sensor or position sensorless operation did not have a significant impact on the torque estimate error. When operating at low loads (low torque), the low power drive showed significantly higher error of up to 40 % compared to the higher power drive that had up to 12 % error. The research demonstrated the difficulty in obtaining good torque estimates over the entire torque-speed operating area of the motor-drive system.

[24] measured the speed and torque estimation accuracy of a 37 kW induction motor driven by a VSD. Steady state tests at five speeds (between 400 rpm and 1550 rpm) and six torques (0 % to 100 %, in 20 % steps) were considered in addition to transient torque and speed tests. It was found that the speed estimate error was below 0.17 %, and the torque and mechanical power estimate errors were below 1.6 %. When using the flux optimisation feature on the drive (to reduce magnetising, or rotor excitation, current to improve efficiency), the torque

and power estimation error increased to 5.8 % and 4.7 % respectively.

A key issue with torque estimates based on the electromagnetic, developed, or air-gap torque described in Eq. 1.3 is that the torque estimate does not account for additional losses that reduce the torque delivered to the load [25]. This includes rotor losses, bearing losses and windage losses. Four methods of torque estimation were evaluated in [25], and in all cases voltage and current measurements from a separate power analyser (not from the drive) were used for all estimation methods. For each method, only 16 operating points were considered (a combination of four speeds and four torques). It was found that the air-gap torque method had errors as high as 7 % to 9.5 % at low torque (25 % rated torque), whereas the error could be reduced down to about 1 % to 2 % when using a sinusoidal voltage supply (no VSD) and when including all the measured motor loss components. However, when the motor was driven from an inverter's pulse width modulated (PWM) supply, the estimation method based on motor loss components had an increased error on the order of 3 % to 6 % at low torque, attributed to harmonic losses caused by the inverter's PWM output not being included in the loss modelling.

The torque estimation error can also be affected by the accuracy of the motor parameters used by the estimation model. Error propagation in a torque estimation method for an induction machine was investigated in [26]. It was found that the estimation of torque was more susceptible to errors from incorrect parameters when the machine operated at low speed. A torque error of 33 % was observed when operating at low speed and with two parameters both having an error of 10 %.

Finite element (FE) analysis can be used to provide more accurate torque estimation models, by allowing for more precise loss models and motor parameters to be found. FE analysis was used by [27] to produce a torque estimation method for an interior permanent magnet (IPM) machine. Using FE analysis, the equivalent circuit parameters were found in addition to iron and harmonic losses for the machine. FE analysis was also used by [28] for torque estimation modelling of fractional slot PM machines, with a focus on saturation and torque ripple effects.

A torque estimation method of an IPM machine was proposed in [29], where the electromagnetic torque equation in Eq. 1.3 was extended using a third order polynomial approximation for flux linkage. The flux linkage approximation captured cross coupling and saturation effects, and was valid for the maximum torque per ampere (MTPA) condition where the d and q axis currents are tied together along the MTPA curve. Measurements along the MTPA curve were used to find the model coefficients. Experimental results along the MTPA curve showed

a torque estimation error typically below 1.6 %. Experimental results only considered variable torque operation at a fixed speed of 1000 rpm. Torque estimation performance over the wider operating speed range of the machine was not considered.

1.2.3 Pump Application Estimation

The operating state of an end application or load (for example a pump or fan) can be estimated from the operating state of the motor system. Typically this is done using measurements and/or estimates of the motor's mechanical output, including speed, torque and/or mechanical power. Sensorless estimates can replace physical sensors used by feedback control systems, avoiding additional costs from these sensors and an external controller [18]. The use of sensorless estimation also unlocks the possibility of using feedback control schemes that were otherwise not possible due to cost and/or size limitations. In the case of pump and fan systems, using variable speed flow control systems instead of simpler on-off control can also improve the efficiency and reduce energy costs of the system [30].

For sensorless estimation of the end application/load to be possible, an accurate model of the application device is required. The model needs to both have a structure detailed enough to capture the behaviour of the device, and corresponding model parameters obtained from test measurements or other reliable data. For pump systems, the key quantities to be estimated are the hydraulic head pressure and the flow rate of the pump. These can be estimated by using pump curves obtained from a pump data sheet, as done in the case of the QP (flow-power curve) method [31]. The QP method uses mechanical power estimates (from estimated speed and torque) to calculate the flow rate from the pump's flow-power curve. Once flow is known, the pump's flow-head (QH) curve can be used to estimate the head pressure. However the accuracy of the QP curve in the data sheet can significantly impact the accuracy of the estimates produced by the pump model [31]. A data sheet provides only general pump performance and does not capture the unique variations of each individual pump manufactured. Pump flow rate and total head tolerances may vary from 10 % and 6 % respectively for grade 1 pumps to 18 % and 14 % respectively for grade 3 pumps, with higher tolerances again for lower power pumps (<10 kW) [32].

Better models and estimation accuracy can be obtained from direct measurements of the pump under a small number different operating conditions [18], [33].

In [33] the QP flow-power curve was measured at a constant speed at 13 different valve positions (and consequently flow rates). The QP curve was then used with an identified hydraulic system curve to provide estimates of the pump's flow rate and head from speed and mechanical power estimates provided by a VSD. Because the pump's QP curve was only known at a single speed (whereas pump's have a QP characteristic that varies with speed), affinity laws were used to scale the single speed QP curve and allow for variable speed operation of the pump estimates. Experimental results showed a flow rate estimation error ranging from 5 % at 75 % rated speed, to over 25 % error at 40 % rated speed. This error could be reduced down to under 5 % when using the identified system curve method, however this method does not support hydraulic systems/applications where the system curve may change over time. The results also did not consider the broader pump operating area from multiple pump speed and system curve combinations.

In [24], the same authors also investigated the effect of VSD based speed and torque estimation accuracy on the performance of the QP based pump estimation method. It was found that when using flux optimisation to reduce the magnetising current and flux inside the induction machine (to improve efficiency), the increased torque error would increase the QP method's flow rate error by 1.5 % to 4.1 % when the pump was operated at the best efficiency point (BEP).

A key problem with the QP curve based pump estimation approach is that it uses affinity laws that assume constant pump efficiency over the pump's operating area. However, pump efficiency does change over the operating area, and consequently limits the effective operational area of a QP based method [18]. VSD estimates can also suffer from not capturing the pump seal and bearing losses that reduce the mechanical power delivered to the pump impeller[18]. A boundary curve method was proposed by [18], with interpolation between the two boundary curves being used to estimate the pump state. Two calibration system curves were used to characterise the pump, one with a control valve fully open and one with the valve fully closed. The method captures the variable efficiency of the pump, and consequently allows for better estimates over a wider operating area. Results showed low flow rate estimation errors on the order of 0.6 % to 1 % at four speed ranges (60 %, 73 %, 87 % and 100 %) with a fixed valve position, and at four valve positions (25 %, 50 %, 75 %, 100 %) with a fixed speed. Results were only shown for a limited number of operating points. Consequently, the performance of the boundary curve method over the wider pump operating area is unknown.

One of the challenges for power based pump estimation methods is that the QP flow-power curve may feature a local maxima. This local maxima means the

QP curve is no longer monotonic (not one-to-one) and cannot be inverted to find the flow from power, limiting the estimator's operating area to the monotonic region of the QP curve [34]. A method of dynamic speed excitation was proposed by [34], where a speed step change and the resulting transient response was used to determine which side of the local maxima the pump was operating on. For pump's with non-invertible flow-power curves, this approach enables the flow rate estimator to operate over a wider operating area.

[35] implements a pressure estimation method based on the QP method (via QP and QH curves). Using the QP method the flow and total pump head is determined. Using the known pipe diameter and Bernoulli's equation, the actual pipe pressure is then calculated. The method was implemented in a programmable logic controller (PLC) connected to the VSD. The sensorless pressure estimate was used in a pressure control application to verify the operation of a physical pressure transducer and detect faults in the pressure sensor when the estimate and sensor disagree.

Pump pressure control with sensorless pressure estimation was further developed in [36], where a torque versus flow characteristic was modelled as a second order polynomial and stored in a PLC as a look up table. The approach was extended to multiple pump systems (several pumps in parallel), where the PLC based method used an additional look-up table of power consumption to select the optimal number of pumps and speed to run in order to minimise power consumption.

In addition to industrial pump applications, sensorless pump state estimation has also been developed for blood pump applications. A blood pump is a very small integrated motor drive system that contains a motor, drive and centrifugal pump in a single device. A method of flow rate and head pressure estimation for a centrifugal blood pump was proposed by [37], with a focus on miniaturisation and elimination of external sensors. Flow rate estimation for a BLDC powered pump was implemented by linearising the current versus flow curve, and head pressure estimation was implemented using a second order polynomial in terms of speed. Results plotted in [37] show flow rate estimate errors of about 3 % near maximum flow, and up to 25 % at very low flow, and pressure estimate errors of 3 % to 14 % between high and mid pressure.

Flow rate control performance of a blood pump using a fuzzy logic controller was investigated by [38]. A map of flow rates with respect to measured speed and pressure was used to fit a second order two dimensional polynomial equation. This equation was then used to estimate the flow rate from speed and differential pressure measurements. Although the control system performance was the main

focus, the flow rate estimator was noted to have an offset (error) of 0.5 L/min between 5 to 6 L/min at pressures above 250 mmHg. This offset corresponds to a relative error of 8.3 % to 10 %.

Dynamic estimates of pulsitile flow and pressure were investigated in [39]. The dynamic flow rate estimate was produced by first taking the output of a steady state flow estimator model (with second order speed and third order power terms) and feeding it through a dynamical model (equivalent of a digital filter). Another digital filter was then used to estimate the head pressure from the speed measurement and the flow rate estimate. The results plotted in [39] show a scatter of points with errors up to 15 % of flow and 20 % of the head pressure in the middle of each respective measurement range.

1.3 Research Gaps

Through the use of inverter based variable speed drives, it is possible to operate a motor over a range of speeds. Combined with a load device, the motor and drive form a motor system with the ability to operate over a wide area of different speed and load combinations. However, accurate knowledge about a motor system's operation over a wide area is not well understood in terms of the real time system state or the efficiency of the various system components.

The efficiency curves commonly used in industrial applications only consider fixed speed operation, and sometimes only consider a single load point. These curves also only consider the efficiency of the motor, ignoring other parts of the overall motor-load system. For decades motor efficiency performance and test standards have only considered direct on line (grid connected) motors operating at fixed speed and between one to six load points. More recent standards have been introduced that consider the impact of variable speed drives and inverter based losses, however these standards fall short of thoroughly describing the efficiency of a motor (and the entire motor system) over the entire speed-torque operating area of the motor. Efficiency maps have been proposed for motors, but require long and onerous testing of the motor to gather the necessary data. Existing efficiency map methods have also been limited to only the motor and drive of a system, and have not considered the end application/load device as part of an integrated motor system.

The nonlinear nature of a motor's efficiency map highlights the fact that the relationships between electrical quantities (voltage, current) and mechanical quantities (speed, torque) are also nonlinear and not ideal over broader speed-torque operating area of a motor. These relationships are often used as the basis for

many sensorless estimation methods. However, commonly used schemes like torque estimation from current do not account for the nonlinearities resulting from underlying machine loss components, and consequently their accuracy suffers when operating over a wider speed and torque area.

Sensorless state estimation in motor systems is typically focused only on a single quantity (e.g. torque) or single part of the system (e.g. pump flow and head pressure). Existing estimation schemes do not consider a broader collection of estimated motor system quantities for multiple components in the motor system. Existing systems also only consider the motor output or application output (e.g. pump), and no estimation methods have considered power flows and efficiency of an integrated motor system. Existing estimation schemes use models derived from limited data sets and simple theoretical models. These models also have performance limited to narrow operating areas, with unknown performance over the entire operating area of the motor system.

Existing estimation schemes are mostly focused on non-integrated industrial motor and drive combinations, and do not consider low cost integrated motor systems. Low power (< 0.75 kW) and low cost motors are limited in complexity, may be limited to fixed speed, and often cannot afford the space or cost of external feedback sensors. When position sensorless, variable speed operation is present in a low cost motor, it is typical via a simple sensorless method with limited operating speed range.

Low power motors account for 90 % of all electric motors, and have a mean efficiency of 30 % [1]. Due to their large volume and poor efficiency, small low cost motor systems present a significant opportunity for energy savings through efficiency gains. Efficiency improvements in small, low cost motor systems can be found through better understanding of component efficiencies, through the use of variable speed control, and through the use of sensorless feedback control schemes. By using better methods for modelling the motor system efficiency and operating state, higher performing sensorless state estimators can be implemented on low cost integrated motor system inverters. This unlocks the use of more advanced and more efficient motor systems for cost and space sensitive applications.

To address these gaps, the objective of this thesis are:

- To investigate ways to improve the operating speed range of low cost, low power permanent magnet machines and drives that use position sensorless operation.

- To develop experimental measurement techniques to better characterise the operation and efficiency of a motor-drive system over a wide operating area, including means to collect large quantities of data suitable for modelling the system.
- To better understand the performance and behaviour of an integrated motor systems comprised of an inverter, motor, load/application, sensorless feedback estimator and control system.
- To develop more general methods of motor system state estimation the can operate over a wide operating area but are also suitable for low cost, lower power drives with limited computational power.
- To validate the real time performance of a variety of sensorless motor system state estimators over a wide operating area and at different temperatures.

1.4 Original Contributions

Modern electric drives are becoming more complex and offering more benefits, however components are selected and assembled with limited consideration of the broader operating area efficiency and energy costs. This impacts the running costs for long duty cycle applications, and ultimately contributes to the total cost of ownership of a motor system. Modern drives also include methods to indirectly estimate some of the system's state variables, however the operation and performance of these methods over the broader operating area of the motor system is not well understood. A motor system includes the inverter, motor, load, feedback sensors and control system components. No study has been found that considers all of these components, both in terms of efficiencies and state estimation performance over the wide operating area of a variable speed motor system. This research specifically considers low power, low cost integrated motor systems that represent the overwhelming majority of global motor usage. The major contributions of this thesis are:

1. Brushless PM AC motors are one of the most common candidates for high efficiency motor applications. However, to broaden the utilisation of brushless PM motors requires low cost, high performance drives with position sensorless control systems that specifically offer performance at very low speed and high speed regions. This is specifically critical in variable speed systems (e.g. pump systems) that may benefit from higher efficiency as

speed is increased. To address this, an improved position sensorless method was developed for brushless motor control using flux linkage increment. The method offered wide speed operation, including very low speed operation, used a simple implementation suitable for low cost drive systems, and required only a single motor parameter derived from the back-EMF constant of the motor.

2. Although efficiency maps, or iso-efficiency contours, have been explored for motors, they have primarily been used for modelling and machine design, not for developing state estimators for motor system control. Efficiency mapping is typically focused on only the motor, rarely the drive, but not the all of the motor system components operating together. The efficiency mapping techniques and analysis used in this research consider the combined operation of the inverter, motor, load/application, feedback estimate/sensorless system and control systems. This captures interactions between system components, and evaluates the operation of each component over the load-specific operating area of an integrated, application specific motor system.

3. Efficiency map testing requires extensive data sets which have previously been achieved using manual test methods. There is a need for automated testing that can respond to the unique dynamics of the motor system, including detection of the edge of stable operation and testing at a consistent temperature. This has been achieved using an autonomous test system that can manage the real time operation and testing of a motor system with load, and can be easily reconfigured for different configurations of motors and loads.

4. Existing studies on position sensorless and motor system state estimation (torque, speed, pump head and flow) have only considered operation and performance over limited operating areas. Estimation methods have not considered the broader power flow and efficiency estimates for all components in a motor system. This research has developed and verified methods for comprehensive estimation of a motor system and load's operating state. The methods developed are not unique to the specific motor and load tested, but combined with the measurement and modelling techniques used, these methods can be utilised more broadly by other motor systems and types of loads.

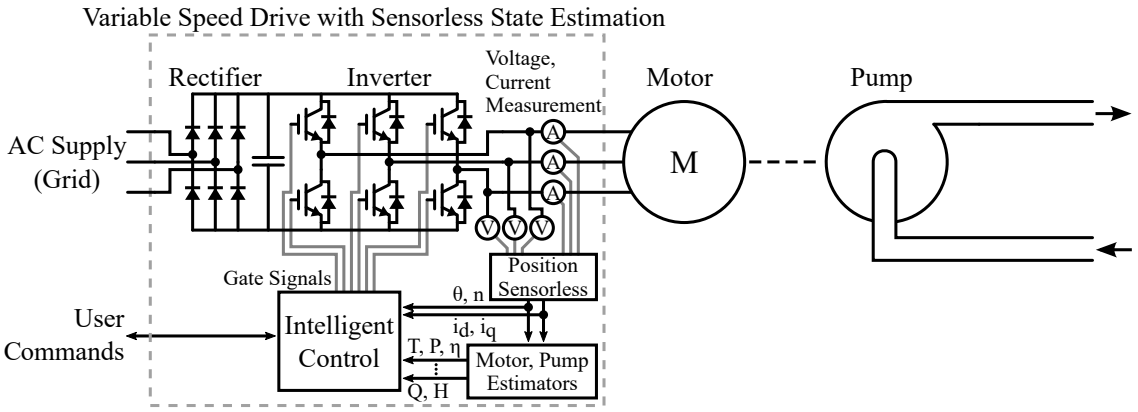

FIGURE 1.3: Proposed concept of an integrated motor system with sensorless state estimation, shown for a pump application. External feedback sensors are replaced with real time estimates of the complete motor system, including the inverter, motor and end application/load.

5. Temperature affects the losses, and hence efficiency, of the inverter, motor and load. Existing estimation methods do not consider temperature effects and do not evaluate the impact of wider temperature operation on estimator accuracy. Using temperature regulated testing, the performance of motor and load estimators was explored for different operating temperatures over the operating area of the motor system.

1.5 Thesis Outline

The outline of this thesis is as follows:

Chapter 2 provides an overview of the motor control and pump system theory used in this thesis.

Chapter 3 presents a position sensorless method for brushless DC motor control using flux linkage increment. The theory of the method is discussed in detail, and includes derivations of the flux linkage threshold for both sinusoidal and trapezoidal back-EMF machines. Experimental results are shown verifying the operation of the method, operation at low speed, dynamic operation, and the measured position error.

Chapter 4 presents a method for experimentally obtaining detailed efficiency maps using an autonomous test system. The design and operation of this system is discussed in detail, including temperature regulation and navigation of the motor system application's operating area. Experimental results include efficiency

maps for a motor and pump system, and highlight the speed and temperature regulation performance of the system.

Chapter 5 presents a general method for motor system state estimation using efficiency map test data. The data is analysed used to produce a set of estimator models that are then implemented in the firmware of a low cost inverter. Experimental test are performed to evaluate the performance of the all estimators, including temperature effects.

Chapter 6 extends the method of motor system state estimation to an integrated motor-pump system. Performance of the general motor models is evaluated when extrapolating those models to the new operating area of the pump system. New estimation models were developed to capture the effects of deep field weakening and to estimate the pump's non-linear behaviour. Experimental results are used to verify the performance of all estimator methods, including dynamic operation and temperature effects.

Chapter 7 summarises the major results and findings of this thesis, and includes a discussion of future research work.

Chapter 2

Background Theory

This chapter provides a high level summary of the background theory that underpins the research presented in this thesis. The theory presented is only brief and not aimed at providing a detailed treatment of each topic. The research in this thesis considers permanent magnet (PM) motor operation and control using inverter based drives. The research then considers the broader operation of a motor system where several components work together to control power flow and deliver energy to a load. A pump application is then considered, where the motor and pump system work together to deliver hydraulic energy (see Fig. 1.2).

2.1 Permanent Magnet Motor Operation

A permanent magnet (PM) motor is a an electrical machine that uses permanent magnets to provide the field excitation. Because no field excitation current is required, there are no excitation losses and the consequently the efficiency of the motor is higher. A PM motor is typically constructed using a polyphase (generally three phase) stator containing the armature windings, and with a rotor that has permanent magnets. Unlike brushed DC motors or excited synchronous motors, there are no brushes or slip rings, which helps to increase reliability.

PM motors are sometimes referred to as permanent magnet synchronous machines (PMSMs), brushless AC (BLAC) motors, or brushless DC motors (BLDC). These names generally refer to the same type of machine with PM rotor, however the term brushless DC may refer to either the shape of the back-EMF voltage and/or the type of control used, including shape of the voltage produced by the inverter. These motors should not be confused with permanent magnet *brushed* DC motors that have permanent magnets in the stator, wound armature on the rotor, and use a mechanical commutator to operate the motor.

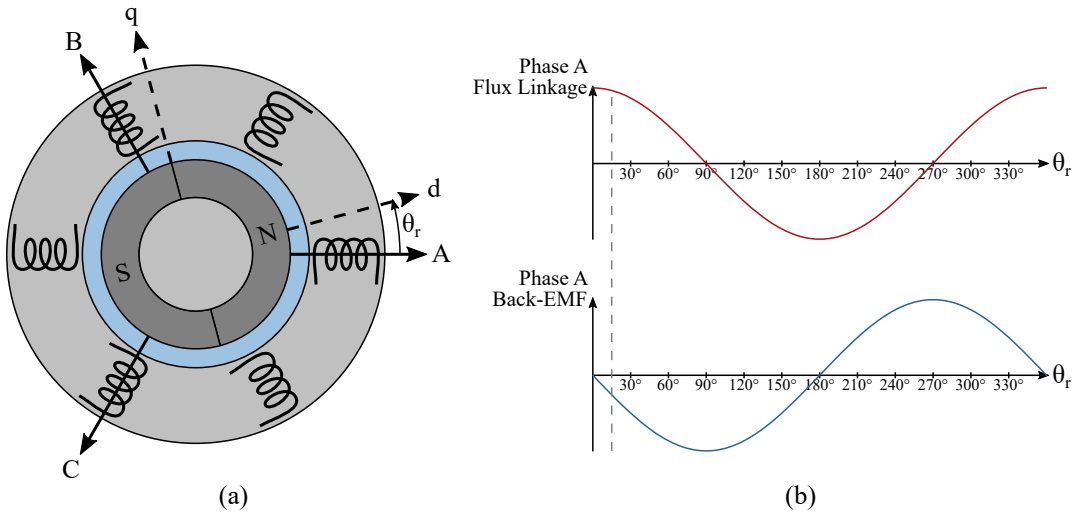

FIGURE 2.1: Simplified operation of a PM motor, where (a) the rotation of the PM rotor inside the stator causes (b) a change in flux linkage that results in a back-EMF voltage at each stator phase winding.

2.1.1 Rotating Field and Back-EMF

Figure 2.1 shows the principle of operation for a PM motor. Note that the structure shown is simplified for the purposes of illustrating the motor's operation. The PM rotor creates a magnetic circuit that flows across the air gap and through the stator windings. As the rotor moves, the field rotates and causes a change in the flux linkage. The flux linkage is the total flux linked by the stator windings, and is defined by Eq. (2.1), where Φ is the air gap flux and N is the number of coil turns.

$$\psi = N\Phi \tag{2.1}$$

As a result of Faraday's law, the change in flux linkage causes an electromotive force (EMF) at each stator phase winding. This is referred to as the back-EMF 'e' that represents the voltage seen at the windings.

$$e = \frac{d\psi}{dt} \tag{2.2}$$

Because the shape of the air gap flux and hence flux linkage is a periodic function (typically a sinusoid) in terms of rotor angle θ_r, when using the time derivative from Faraday's law the equation can be rearranged to show the back-EMF as the spatial derivative of the flux linkage multiplied by the rotor speed ω_m:

$$
\begin{aligned}
e &= \frac{d\psi(\theta_r)}{dt} \\
e &= \frac{d\psi(\theta_r)}{d\theta_r}\frac{d\theta_r}{dt} \\
e &= \frac{d\psi(\theta_r)}{d\theta_r}\omega_m
\end{aligned} \tag{2.3}
$$

For a sinusoidal flux linkage given by Eq. 2.4, the back-EMF can be described by Eq. (2.5), where the peak flux linkage ψ_p is equal to the back-EMF constant K_e. The key observation is that the back-EMF waveform is synchronised with the rotor, has the same shape as the spatial flux linkage waveform, and has a magnitude proportional to speed. This is true even for non-sinusoidal flux linkage shapes, for example trapzoidal flux linkage.

$$\psi(\theta_r) = \psi_p cos(\theta_r) \tag{2.4}$$

$$e(\theta_r) = -\psi_p \omega_m sin(\theta_r) = -K_e \omega_m sin(\theta_r) \tag{2.5}$$

Eq. (2.5) is defined for the rotor angle θ_r being the angle between the A phase axis and the rotor's d-axis. It is also common to see the back-EMF equation defined in a way that a rotor angle of zero corresponds to the the phase A back-EMF rising through the zero crossing. This convention is shown in Eq. (2.6).

$$e(\theta_r) = \psi_p \omega_m sin(\theta_r) = K_e \omega_m sin(\theta_r) \tag{2.6}$$

Note that because the back-EMF is the derivative of the flux linkage, the back-EMF appears 90° ahead of the rotor position. With respect to the rotor (rotor reference frame), the direction of the magnetic field is defined as the direct or d-axis, and the quadrature or q-axis is defined as 90° ahead. I.e. the back-EMF appears in the positive q-axis.

More generally, the rotor field can be represented as a rotating vector. This vector is described as a *space vector* because its position within the stator changes over time. Like the rotating field, the back-EMF can also be represented as a rotating space vector that leads the rotor field space vector. The voltage at each phase winding of the stator appears as the linear projection (vector projection) of the space vector onto each of the three stator phase vectors. Because the three stator phase windings are physically spaced by 120°, the three phase voltage waveforms

are consequently 120° apart.

2.1.2 Torque Production

Applying a current to a winding will produce a magnetic field. By applying a set of balanced three phase currents to the stator windings, with each current waveform 120° apart, the result is a rotating magnetic field in the middle of the stator. Providing that the rotating field and hence applied current is *synchronised* to the rotor, the stator field will interact with the rotor field and apply a rotational force (torque) to the rotor.

From the rotor's perspective (rotor reference frame), the stator field can be decomposed into two linearly independent basis vectors: a d-axis component (in phase with the field) and a q-axis component (out of phase with the field, 90° ahead). For the case of just a d-axis component being applied, the rotor field is already aligned with this stator field and no torque is produced (for simple case of a non-salient surface PM machine). Instead, the d-axis field either adds to or subtracts from the rotor field. This phenomena is typically exploited for *field weakening*, where a negative d-axis current causes a reduction in the d-axis field, reducing the flux in the machine and consequently reducing the back-EMF that is proportional to the flux. Because the d-axis component generally does not produce any torque, it follows that torque is produced from the q-axis component.

To allow for the applied three phase current to be understood in terms of the rotor's d-axis and q-axis components, it is necessary to transform the three stator currents into the rotor's rotating reference frame. This is a two step process described by the Clarke (Eq. (2.7)) and Park (Eq. (2.8)) transforms. The stator three phase currents describe the current space vector in terms of three non-orthogonal basis vectors spaced 120° apart. The Clarke transform is a linear transformation from the three phase non-orthogonal basis into a two component orthogonal basis in terms of α and β basis vectors. The $\alpha\beta$ space still represents the stator reference frame. The Park transform then uses the instantaneous rotor angle θ_r to translate the space vector into the dq rotating reference frame of the rotor. For a motor operating in steady state, the d and q-axis components are typically steady (DC) quantities.

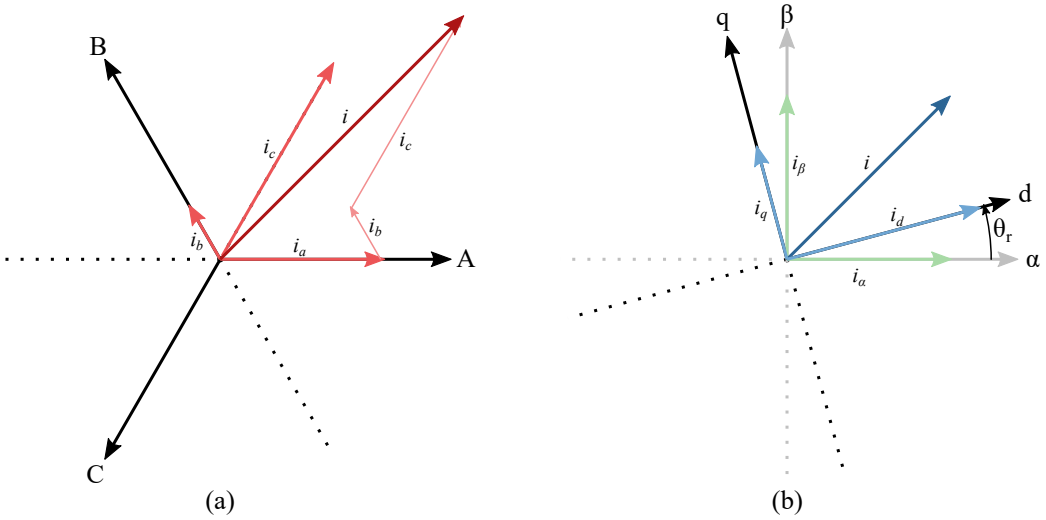

FIGURE 2.2: Space vectors in (a) the stator reference frame, and (b) in the rotor reference frame. Note that the magnitude invariant transformation is shown, where the d-q and α-β space vectors (and components) have a peak value matching the peak value of the a,b, and c phases in the stator frame. Consequently the d-q and α-β space vectors appear $\frac{2}{3}\times$ the size of the stator frame space vector, which is $\frac{3}{2}\times$ the peak phase value.

$$\begin{bmatrix} i_\alpha \\ i_\beta \end{bmatrix} = \frac{2}{3}\begin{bmatrix} 1 & -\frac{1}{2} & -\frac{1}{2} \\ 0 & \frac{\sqrt{3}}{2} & -\frac{\sqrt{3}}{2} \end{bmatrix}\begin{bmatrix} i_A \\ i_B \\ i_C \end{bmatrix} \tag{2.7}$$

$$\begin{bmatrix} i_d \\ i_q \end{bmatrix} = \begin{bmatrix} cos(\theta_r) & sin(\theta_r) \\ -sin(\theta_r) & cos(\theta_r) \end{bmatrix}\begin{bmatrix} i_\alpha \\ i_\beta \end{bmatrix} \tag{2.8}$$

For the general case of a salient PM machine, the torque is described by Eq. 2.9 [7], where p is the number of pole pairs, ψ is the peak flux linkage, L_d and L_q are the d and q-axis stator inductances, and i_d and i_q are the d and q-axis currents.

$$T = \frac{3}{2}p[\psi + (L_d - L_q)i_d]i_q \qquad \text{(Nm)} \tag{2.9}$$

Eq. 2.9 represents the more general case of a salient PM machine, where $L_d \neq L_q$ and the torque also has a d-axis current component in addition to the q-axis component. For the case of a non-salient PM machine (e.g. a surface PM machine) where $L_d \approx L_q$, the torque equation simplifies to Eq. (2.10):

$$T = \frac{3}{2}p\psi i_q \qquad \text{(Nm)} \tag{2.10}$$

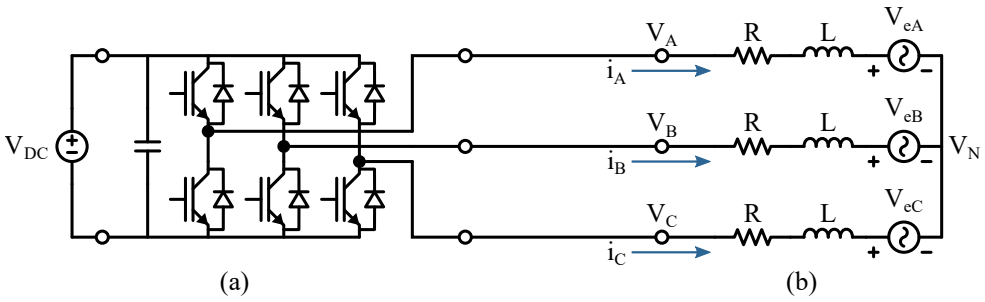

FIGURE 2.3: Equivalent circuit models for (a) a voltage source inverter and (b) a PM motor (non-salient). The inverter is shown with a DC supply, however in grid connected drives the DC supply is replaced with a rectifier or actively controlled front-end converter.

2.1.3 Motor Control

Because torque is proportional to current, it is possible to control the torque and therefore speed of motor by controlling the current. The mechanical dynamics of the motor system can be described by Eq. (2.11), where T_{net} is the net torque on the mechanical system (torque from motor minus load torque), J is the rotational moment of inertia in kgm^2, and $\frac{d^2\theta}{dt^2} = \frac{d\omega}{dt} = \alpha$ is the rotational acceleration in rad/s^2. Eq. (2.11) is essentially Newton's second law applied to rotating systems. It should be noted that for real systems Eq. (2.11) forms a second order differential equation that includes a speed dependent dampening term and a position dependent spring constant.

$$T_{net} = J\frac{d^2\theta}{dt^2} = J\frac{d\omega}{dt} \tag{2.11}$$

In order for a current to flow through the stator windings of a motor, a voltage must be applied to the stator terminals. Fig. 2.3 (b) shows the equivalent circuit for a PM motor. The corresponding voltage equations are described by Eq. (2.12) to (2.14), where for v_{AN} represents the phase A voltage from terminal to neutral, v_{eA} is the phase A back-EMF voltage, L is the stator inductance, and R is the stator winding resistance.

$$v_{AN} = v_{eA} + L\frac{di_A}{dt} + Ri_A \tag{2.12}$$

$$v_{BN} = v_{eB} + L\frac{di_B}{dt} + Ri_B \tag{2.13}$$

$$v_{CN} = v_{eC} + L\frac{di_C}{dt} + Ri_C \tag{2.14}$$

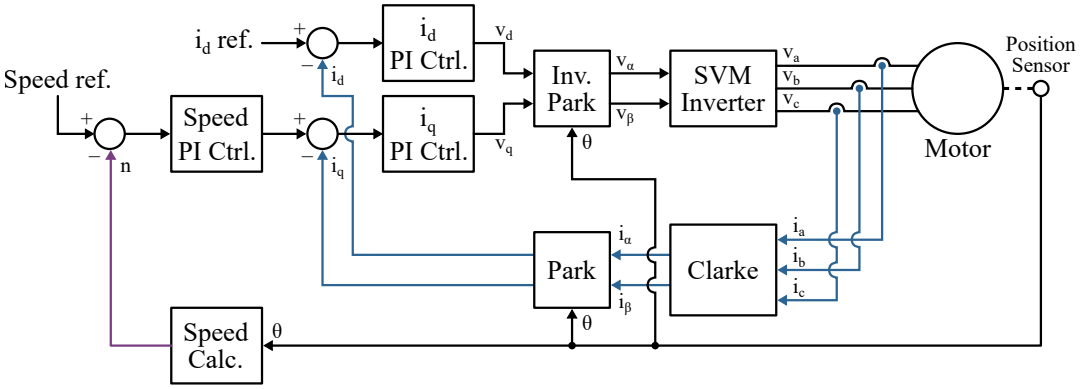

FIGURE 2.4: Control system diagram for field oriented control of a motor. Torque control is performed in the rotor reference (dq) frame by controlling the d and q-axis currents. A speed control loop is also shown, where the difference between the reference and measured speed is used to generate a torque (acceleration) command.

Note that Eq. (2.12) to (2.14) describe a non-salient surface PM motor. A salient PM motor will typically have separate d-axis and q-axis equivalent circuits. The d and q-axis voltages are shown in Eq. (2.15) and (2.16) [7], where R is the stator winding resistance, L_d and L_q are the stator d and q-axis inductances, ω is the speed and ψ is the flux linkage.

$$v_d = Ri_d + L_d\frac{di_d}{dt} - \omega L_q i_q \tag{2.15}$$

$$v_q = Ri_q + L_q\frac{di_q}{dt} + \omega L_d i_d + \omega\psi \tag{2.16}$$

Effective current control is typically achieved by a motor drive using a closed loop current controller. In such a system the current controller compares the measured current to a set point and then generates a voltage command. The result is that the controller dynamically applies the voltage necessary to achieve the desired current and hence torque in the motor. The actual magnitude of the voltage applied is generally not important, providing the required voltage is within the limits of the inverter such that the current controller can reach the required set point.

In a variable speed drive that uses vector control, or field oriented control (FOC), the current control is performed in the dq rotor reference frame. This is achieved using two independent current controllers; one for the d-axis and one for the q-axis. Currents are measured at the motor terminals and then transformed into d and q-axis components using the Clarke and Park transforms described by Eq. (2.7) and (2.8). The current controllers are typically implemented

using proportional-integral-derivative controllers (PID, or PI when the derivative term is not used).

The current controllers produce a d and q-axis voltage command respectively, representing the voltage space vector that should be applied to the motor by the drive. This voltage is transformed into a stator space vector by the inverse Park and Clarke transforms, shown in Eq. (2.17) and (2.18). In a modern drive, a voltage source inverter is used to produce the three phase voltage that is applied to the motor terminals. Although an inverse Clarke transform could be used to generate three separate voltage commands, the inverse Clarke transform is typically integrated with the inverter logic to form a *space vector modulation* (SVM) inverter.

The space vector modulation scheme is shown in Fig. 2.5 (a). A three phase inverter has three outputs that can be driven either to the positive or negative DC bus voltage. There are $2^3 = 8$ combinations, where two of those produce a space vector at the origin. The remaining combinations are the six basis space vectors that span a hexagonal region. Inside this region, the inverter can approximate an arbitrary voltage space vector by using a high frequency pulse width modulation (PWM) scheme where time is spent cycling between three of the eight combinations. After filtering, the inverter's switching voltage appears as a sinusoidal voltage (smoothly rotating space vector).

$$\begin{bmatrix} v_\alpha \\ v_\beta \end{bmatrix} = \begin{bmatrix} cos(\theta_r) & -sin(\theta_r) \\ sin(\theta_r) & cos(\theta_r) \end{bmatrix} \begin{bmatrix} v_d \\ v_q \end{bmatrix} \tag{2.17}$$

$$\begin{bmatrix} v_A \\ v_B \\ v_C \end{bmatrix} = \frac{3}{2} \begin{bmatrix} \frac{2}{3} & 0 \\ -\frac{1}{3} & \frac{1}{\sqrt{3}} \\ -\frac{1}{3} & -\frac{1}{\sqrt{3}} \end{bmatrix} \begin{bmatrix} v_\alpha \\ v_\beta \end{bmatrix} \tag{2.18}$$

The key requirement for the current control scheme to work is knowledge of the rotor's instantaneous position. The rotor's position is required by the Park and inverse Park transforms to complete the rotor reference frame transformation and to essentially keep the current (and voltage) synchronised to the motor. The rotor position is usually found using an external, physical position sensor like an encoder or resolver that provides a high resolution shaft angle measurement. However, it is also possible to use a position sensorless method to provide an estimate of the rotor position using voltage and current measurements.

Torque control through current control is the essential component of a motor control scheme. It is also possible for a motor drive to perform other forms of

control including speed and position control, or control over load device quantity (for example flow control for a pump system). In the case of speed control, an additional controller is placed around the current controller. The speed controller then uses speed measurements (e.g. via a position sensor) to generate a torque command for the current controller. When position control is required, for example in a servo drive, a position control loop is place around the speed control loop and position sensor feedback is used to generate a speed command.

2.1.4 Brushless DC Motor Control

So far vector control of PM motors has been discussed, where precise and high resolution position information is required for the motor and control system to operate. In a vector or field oriented control scheme, the inverter uses all three phase outputs to produce a voltage space vector that rotates in the stator reference frame. Although high frequency pulse width modulation (PWM) switching is used, the fundamental waveform produced by the inverter will be sinusoidal (for a sinusoidal back-EMF motor).

In the case of brushless DC, or trapezoidal operation, only two of the three inverter phase outputs are active. The result is voltage being applied across only two phases of the motor, with the third phase left floating. There are six possible non-zero switching combinations, shown in Fig. 2.5 (b). This commutation scheme is known as *six-step* commutation, because the inverter sequentially steps through each state. Each state represents 60° of an electrical cycle, and the resulting waveform is trapezoidal with 120° flat tops, shown in Fig. 2.5 (c). Pulse width modulation (PWM) can be used to vary the amplitude of the waveform.

Because only two phases are driven, current only flows through two phases of the motor. This current flows from the DC bus, through one of the high side transistors, through two phases of the motor (via the motor star point), back through one of the low side transistors before returning to the DC bus. Consequently, the current flowing in any of the six sectors will be equal to the DC bus current. Because of this, it is possible to control the motor current simply by controlling the DC bus current. Even without current control, six-step commutation where trapezoidal voltage is applied to a motor with trapezoidal back-EMF will result in a steady DC current flowing through the DC link, and consequently constant torque and power in the motor. Operation is still possible for a motor with sinusoidal back-EMF, but at the expense of torque ripple.

Noting that both the back-EMF and the torque producing current are aligned with the rotor's q-axis, torque can be applied simply by keeping the motor current

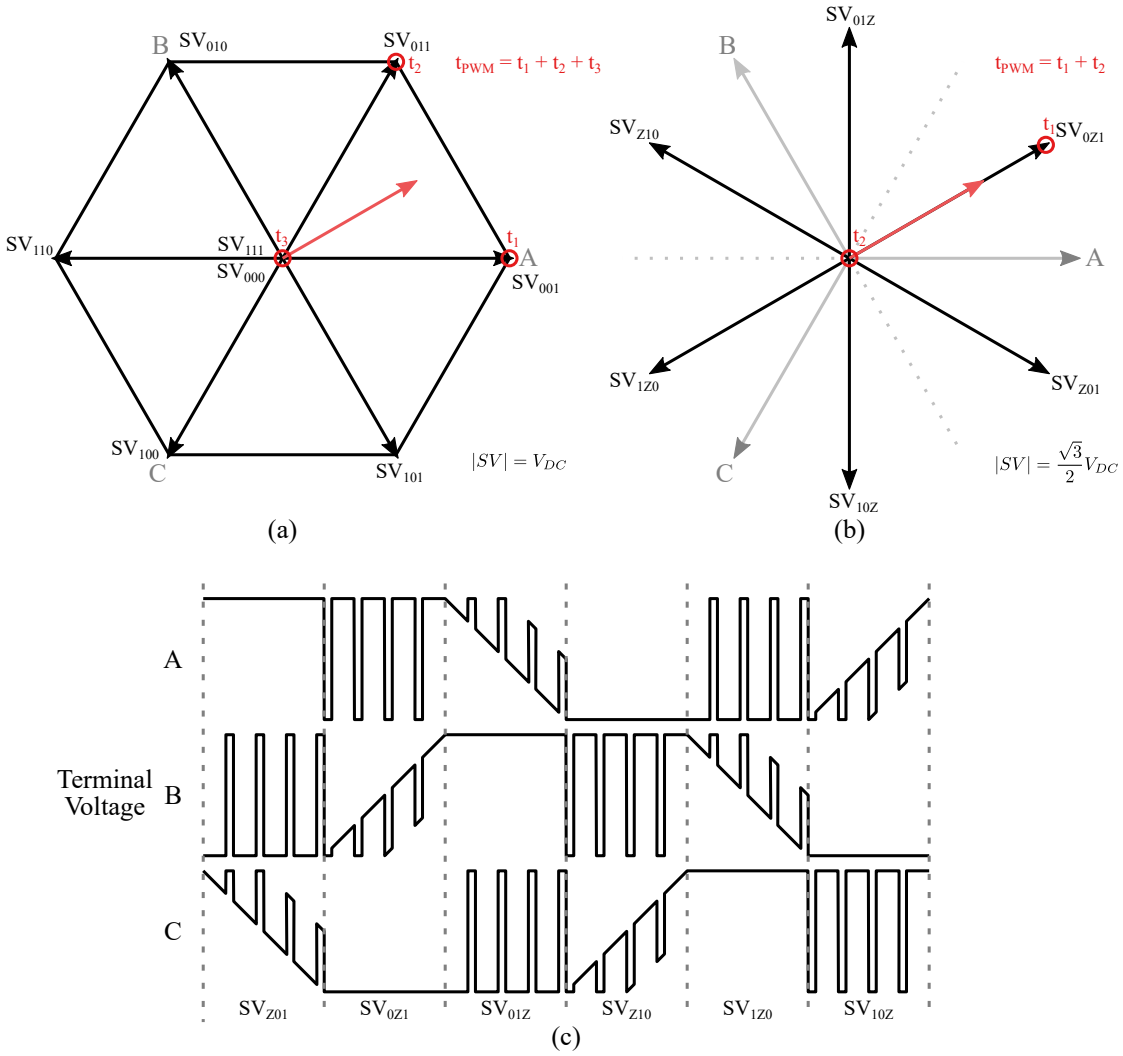

FIGURE 2.5: Inverter space vectors for (a) a three phase space vector modulation (SVM) inverter where all phases are active and generate an arbitrary space vector, and (b) a brushless DC (BLDC) modulation scheme where only two phases are active and space vectors can only be produced with six angles. Both are produced by the same design of inverter, however the SVM modulation scheme produces a smoothly rotating space vector, whereas the BLDC scheme steps through six angles to produce the trapezoidal waveform shown in (c). The subscripts shown for each space vector refer to the logical state of the inverter's C, B, and A phases, and 'Z' refers to the inverter phase not being driven (left high impedance or floating).

in phase with the back-EMF. Because the current flowing through the inverter is determined by the inverter's selected sector (of the six possible sectors), it follows that the inverter commutation (stepping between sectors) needs to be aligned to the back-EMF and hence the rotor. This is generally done using a position sensor, however considering only six angles 60° apart are required, much simpler position sensors can be used. Hall effect sensors are a common method of low

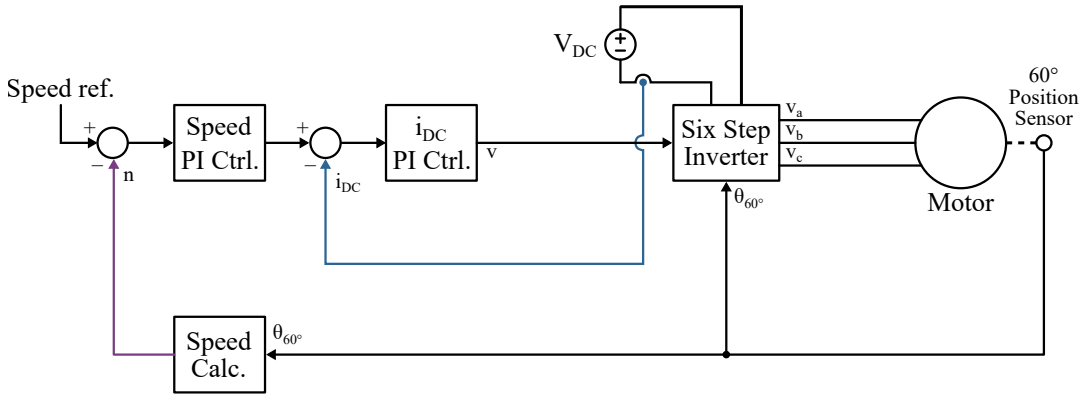

FIGURE 2.6: Control system diagram for brushless DC (six-step) control of a motor. A simple position sensor indicates which 60° sector the rotor is in. The position is then used to select the 60° sector used by the inverter and to ultimately commutate the motor. Torque control is shown where the DC bus current is controlled by varying voltage amplitude of each of the six sectors. A speed control loop is also shown, where the difference between the reference and measured speed is used to generate a torque (acceleration) command.

cost position sensing that only indicate which 60° sector the rotor is in. For very simple BLDC drives without PWM, it is possible to have the hall effect sensors directly control the inverter transistor switching through simple logic (no microcontroller used). In this way, the hall effect sensor and inverter switching function in a similar way to the brush commutator of a DC motor, hence BLDC motors are sometimes referred to as *electronically commutated motors* (ECM).

The control system of the BLDC motor is shown in Fig. 2.6. In comparison to a field oriented control system shown in Fig. 2.4, the BLDC control system is much simpler. There are no Park or Clarke transforms required, and consequently no complicated mathematical operations needed (i.e. fixed point or floating point sine and cosine calculations). There is also only one current controller required instead of two. Hence BLDC control can be realised in simpler, lower cost motor systems. Note that torque and speed control is still possible. Torque control can be performed by controlling the DC bus current, which essentially controls the q-axis current of the motor providing the inverter six-step commutation is synchronised to the motor back-EMF.

2.2 Pump System Theory

Pumps are devices that take in mechanical energy and convert it to energy in a fluid that can be used to move the fluid. There is a very large number of pump types and design variations, however they can mostly be broken into two categories: positive displacement pumps that force a volume of fluid into the pump discharge, or rotodynamic pumps that use a rotating impeller to add kinetic energy to the fluid that is then converted to pressure before exiting the pump. To understand the relationships between input power, output pressure and flow, the following sections provide a simple introduction to pumps and hydraulic systems.

2.2.1 Flow of Liquids

The flow of an incompressible liquid can be described by Bernoulli's equation, which describes the conservation of energy in terms of the liquid's potential energy, static pressure and kinetic energy. Eq. (2.19) describes Bernoulli's equation in terms of pressure, which represents the energy per cubic meter. ρ is the liquid density in $\mathrm{kg\,m^{-3}}$, g is the acceleration of gravity in $\mathrm{m\,s^{-2}}$, z is the height of the liquid above a reference plane in m, p is the gauge pressure in Pa, and U is the mean axial velocity in $\mathrm{m\,s^{-1}}$. U is defined by Eq. (2.20) where Q is the flow rate in $\mathrm{m^3\,s^{-1}}$ and A is the pipe cross sectional area in $\mathrm{m^2}$.

$$p_{Total} = \overbrace{\rho g z}^{\substack{\text{Elevation}\\ \text{Pressure}}} + \overbrace{p}^{\substack{\text{Static}\\ \text{Pressure}}} + \overbrace{\frac{1}{2}\rho U^2}^{\substack{\text{Velocity}\\ \text{Pressure}}} \qquad \left(\mathrm{Pa} = \frac{\mathrm{J}}{\mathrm{m^3}}\right) \tag{2.19}$$

$$U = \frac{Q}{A} \qquad (\mathrm{m/s}) \tag{2.20}$$

In Eq. (2.19), the total energy of the liquid is broken into three components. The first term is the elevation pressure, which represents the potential energy in the liquid when it is a height z above the reference plane. The static pressure (force per area, potential to do work) comes from the force of the column of liquid above the section of liquid at height z. The static pressure is also known as the gauge pressure, describing the relative pressure difference between the liquid and atmospheric pressure. The kinetic energy comes from the liquid's velocity.

Because the equation describes the conservation of energy of the liquid (i.e. that the total energy is constant), any change in one of the terms must be compensated for by a change in another term such that the sum of all three components

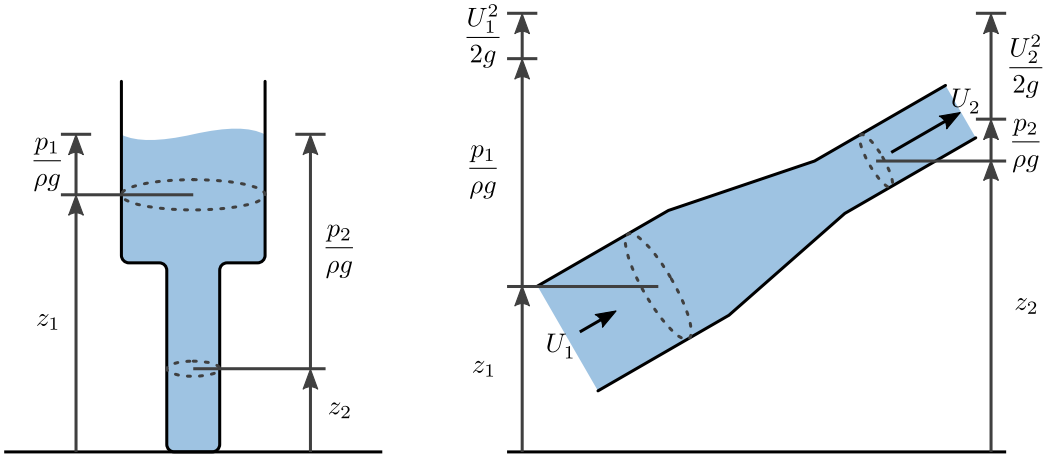

(a) (b)

FIGURE 2.7: Illustration of Bernoulli's principle for liquids in lossless conditions. (a) In a vertical column with no flow, the total head is the same for the liquid at two different cross sections. (b) For a liquid flowing through a pipe of varying elevation and size, the constant volume flow rate through a reduced cross sectional area causes an increased mean velocity and higher velocity head. However the increased velocity head and elevation head results in a lower static pressure head such that the total head remains the same.

remains the same. For example, a vertical column of liquid has the same energy throughout, even though the static pressure is higher at bottom (where potential energy is low) and the potential energy is higher at the top (where static pressure is low). For a liquid flowing from a large diameter pipe to a smaller diameter pipe, both pipes have the same flow rate (volume per time) meaning the pipe with smaller cross sectional area has an increased velocity (more kinetic energy), resulting in a lower pressure (less potential energy) but overall the same energy in the liquid.

$$H = \overbrace{z}^{\text{Elevation Head}} + \overbrace{\frac{p}{\rho g}}^{\text{Pressure Head}} + \overbrace{\frac{U^2}{2g}}^{\text{Velocity Head}} \quad \text{(m)} \tag{2.21}$$

It is common for Bernoulli's equation to be rearranged in terms of the head, representing the energy in a column of liquid of a given height. This version is shown in Eq. (2.21). This form allows for the energy of a hydraulic system to be viewed graphically. Fig. 2.7 describes the previous examples in terms of head and graphically shows the relationship between the three components for a lossless system.

2.2.2 Pipe Losses

Because Bernoulli's equation describes conservation of energy, it can only describe the lossless flow of liquid through a piping system. In real systems there are pipe friction losses that result in a loss of energy (to heat) as the liquid flows through the system. This loss can be described in terms of a loss of static pressure or loss of head. The friction head loss H_J is found from Eq. (2.22) [40], where λ is the pipe friction loss coefficient (dimensionless), L is the length of pipe (in meters), and D is the pipe diameter (in meters).

$$H_J = \lambda \frac{L}{D} \frac{U^2}{2g} \qquad \text{(m)} \tag{2.22}$$

The pipe friction loss coefficient λ is not constant but changes with the velocity of the liquid. λ is also dependent on the roughness of the pipe and the viscosity of the liquid. Viscosity describes the ability of a liquid to flow, but more specifically represents the strength of internal shear forces in a liquid that occur when there is a velocity gradient across the layers of the liquid (in a pipe there is no velocity at the boundary, but the layer at the centre has the most velocity). The flow of viscous liquids can be described by the Reynolds number which represents the ratio between inertial and viscous forces, defined in Eq. (2.23).

$$Re = \frac{\rho U D}{\mu} \tag{2.23}$$

λ can be found from the Colebrook–White equation [40], [41] shown in Eq. (2.24), where k is the equivalent uniform roughness of the pipe surface (in metres) and Re is the Reynolds number, defined by Eq. (2.23).

$$\frac{1}{\sqrt{\lambda}} = -2log_{10}\left[\frac{2.51}{Re\sqrt{\lambda}} + \frac{k}{3.7D}\right] \tag{2.24}$$

Because Eq. (2.24) is not in an explicit form, it cannot be easily solved. λ can be found through an iterative solution or can be found graphically from the Moody diagram [42], where the solutions to the Colebrook–White equation have been plotted against the Reynolds number for various values of pipe roughness.

$$H_J = \zeta \frac{U^2}{2g} \qquad \text{(m)} \tag{2.25}$$

Losses from pipe fittings (bends, branches, nozzles and changes in pipe diameter) can also be described in a similar way to pipe friction losses. Eq. (2.25) [40] describes the head loss from fittings, where ζ is the fitting friction loss coefficient (dimensionless), g is the acceleration of gravity in $\mathrm{m\,s^{-2}}$, and U is the mean axial

velocity in $\mathrm{m\,s^{-1}}$. The key observation from Eq. (2.22) and (2.25) is that in both cases the head losses are proportional to the square of the liquid's mean velocity.

2.2.3 Rotodynamic Pumps

Rotodynamic pumps use a rotating impeller to add kinetic energy to a liquid. Liquid enters through the centre of the impeller, then is guided and accelerated by impeller vanes before exiting into the volute casing. The design of the pump then causes the velocity of the liquid to reduce before exiting the pump, resulting in an increase in static pressure.

The energy a pump adds to a liquid is commonly described by the differential head ΔH, or more commonly just as H. The differential head is also known as the *pump total head*. Because the energy in the liquid can be described in terms of elevation head, static pressure head and velocity head (from Bernoulli's equation), the differential head can be described as the difference between all of these respective quantities as shown in Eq. (2.26).

$$\begin{aligned} \Delta H &= H_2 - H_1 \\ \Delta H &= z_2 - z_1 + \frac{p_2 - p_1}{\rho g} + \frac{U_2^2 - U_1^2}{2g} \quad \text{(m)} \end{aligned} \tag{2.26}$$

The hydraulic power delivered by the pump is described by Eq. (2.27), where the differential head ΔH is multiplied by the mass flow rate ρQ and the acceleration of gravity g.

$$P_h = \rho Q g \Delta H \qquad \text{(W)} \tag{2.27}$$

Efficiency can then be found from the ratio of hydraulic power P_h to mechanical input power P_2:

$$\eta = \frac{P_h}{P_2} \tag{2.28}$$

For a pump operating at a constant speed, the relationship between pump differential head and flow rate can be described by a QH curve. The ideal QH curve is linear where head decreases with increased flow, however due to hydraulic losses in the pump that are lowest in middle of the flow range, the resulting QH curve is not linear but instead resembles the shape shown in Fig. 2.8 (b) [43]. The internal design and underlying loss mechanisms of a pump are beyond the scope of this discussion, however the pump can be suitably described by the QH curve

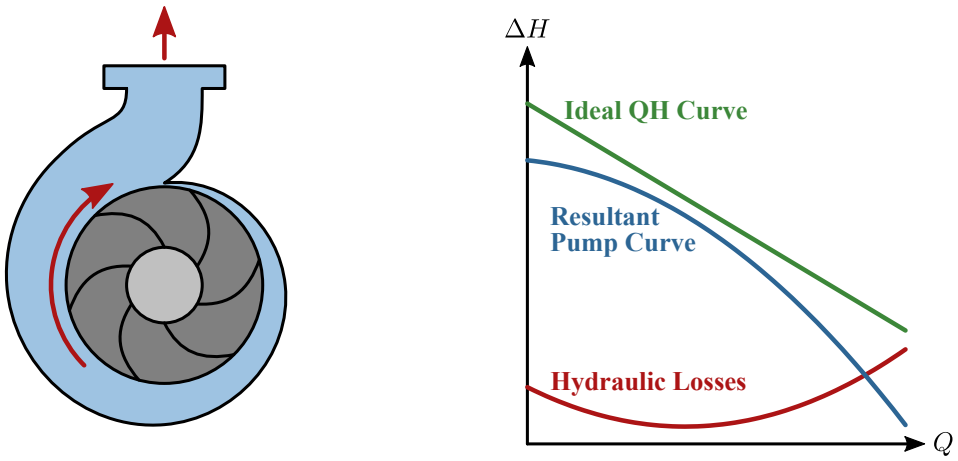

FIGURE 2.8: An example of a rotodynamic pump. (a) Liquid flows from the centre of the rotating impeller into the volute and toward the discharge outlet. (b) The head versus flow curve redrawn from [43] shows the pump curve resulting from a combination of an ideal QH curve the hydraulic losses inside the pump.

and pump efficiency along the QH curve (or efficiency over the broader QH operating area). Along the QH curve will be a point commonly referred to as the best efficiency point (BEP) where the pump operates at its highest efficiency.

By operating the pump at variable speeds, it is possible to change the pump's QH curve. This allows the pump to operate over a larger area than that of a single speed QH curve. The pump's flow Q, head H and power P can be calculated for different speeds by using the *affinity laws* shown in Eq. (2.29) to (2.31). The affinity laws essentially describe a pump as having $Q \propto n$, $H \propto n^2$, and $P \propto n^3$.

$$\frac{Q_1}{Q_2} = \frac{n_1}{n_2} \tag{2.29}$$

$$\frac{H_1}{H_2} = \left(\frac{n_1}{n_2}\right)^2 \tag{2.30}$$

$$\frac{P_1}{P_2} = \left(\frac{n_1}{n_2}\right)^3 \tag{2.31}$$

The affinity laws are approximations and only work with the assumptions that the two pump operating conditions being compared are for pumps with similar design and operation (true for the same pump operating at different speeds), and that the efficiency is constant. In reality the efficiency of a pump is not constant along the QH curve or for different QH curves.

2.2.4 Hydraulic Systems

The combination of a pump with a piping system forms a hydraulic system that operates at an equilibrium between the energy supplied by the pump and the losses of the piping system. The equilibrium point is described by the intersection of the pump's QH curve with the system curve. At the flow rate corresponding to this equilibrium point, the differential head supplied by the pump is equal to the head losses in the system.

The system curve can be described in terms of a static and dynamic component. The static component represents the energy required to lift the liquid from one elevation to another. The dynamic component represents the velocity dependent head losses of the system. Recall that Eq. (2.22) and (2.25) both described the pipe and fitting losses respectively as being proportional to the square of the liquid's mean velocity. Hence for an overall system, these losses can be described as being proportional to the square of the flow rate.

$$\begin{aligned} H_{sys} &= H_{static} + H_{dynamic} \\ H_{sys} &= H_{static} + cQ^2 \quad (\mathrm{m}) \end{aligned} \tag{2.32}$$

The pipe friction loss coefficient λ and fitting friction coefficient ζ are typically constant for large values of Reynolds Numbers [44]. Consequently, a piping system can generally be described by Eq. (2.32) as having a quadratic relationship between head and flow, where c is a constant.

For some applications the system curve may change over time. Changes may be caused by changes in the static head of the system, wear in pipes and components, changes in the temperature or the liquid properties. The system curve may also be changed by a control valve that is designed to control the flow rate of the system by introducing head losses. The result is a change in the overall shape of the system curve that shifts the operating point (intersection of the pump QH curve and system curve). By using a combination of variable pump speed and a control valve to obtain a variable system curve, it is possible to operate the system over a wide range of operating points in the QH plane. An example of variable operating areas is shown in Fig. 2.9 (d).

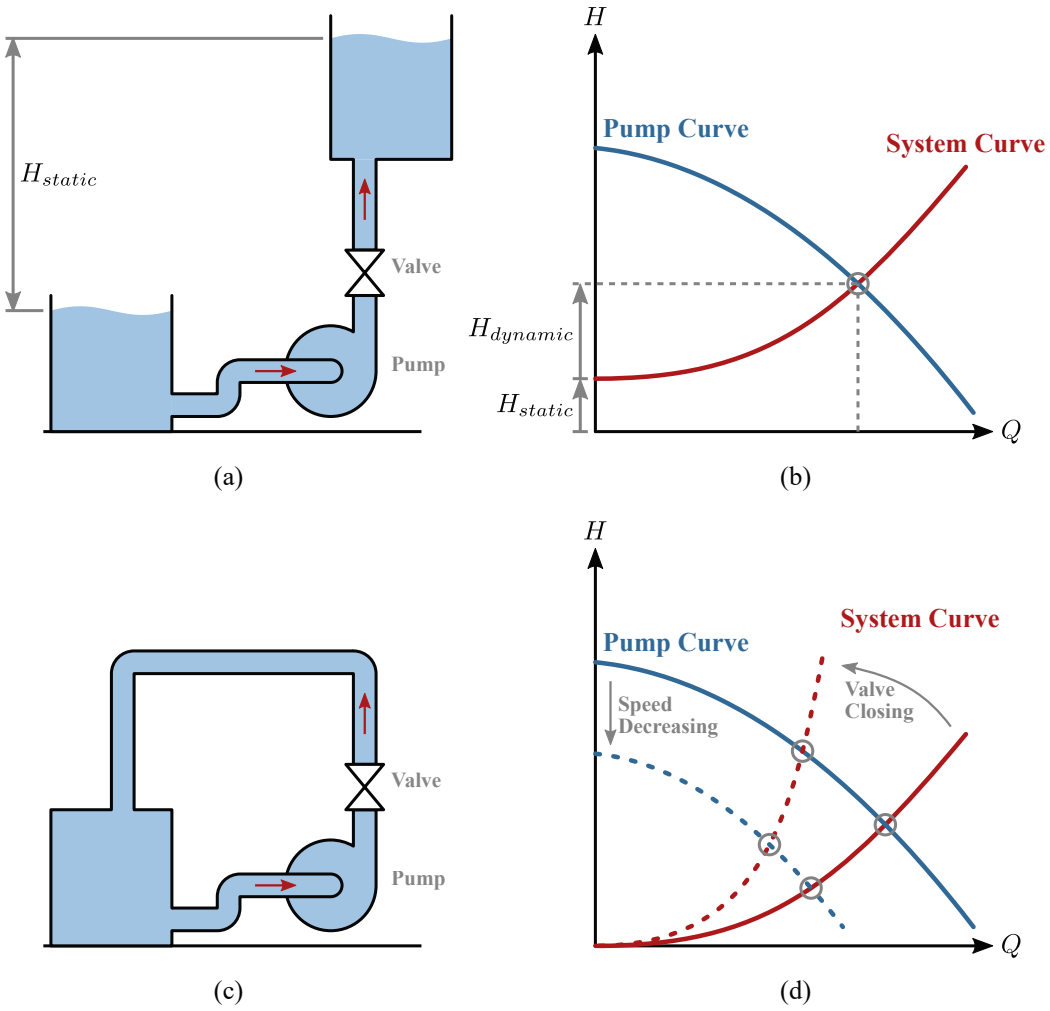

FIGURE 2.9: Example hydraulic systems and curves. (a) An open loop system with static head. (b) The QH curves for a pump system with static head, where the operating point of the system can be found from the intersection of pump curve with the system curve. (c) A closed loop system with no static head. (d) A variable speed and variable valve pump system, where multiple operating points are possible as a result of the intersection of multiple pump and system curves.

2.3 Power Conversion Operating Areas

A motor or pump can be more generally described as power conversion devices, where the flow of energy is controlled from one form of energy to another. A power conversion system may be comprised of several component devices that are each responsible for one type of energy conversion. Fig. 2.10 (a) shows an example of a variable speed pump system, where power flows through a variable speed drive, motor, pump and valve before being delivered to a hydraulic system. Each component in the system has an efficiency less than unity, meaning that the power delivered by each subsequent component gets progressively smaller as demonstrated in Fig. 2.10 (b). The overall system efficiency η_{System} can be found from the product of each component efficiency.

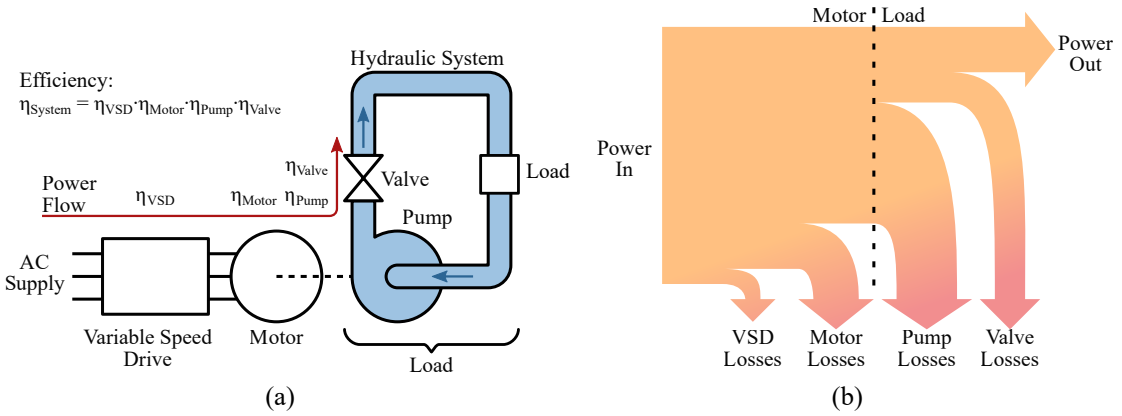

FIGURE 2.10: Power flow and losses for a motor system with end application/load. The example of a variable speed pump system is shown, with (a) the system components and (b) the losses from each component that progressively reduce the power delivered by the system.

Power flow can generally be represented as the product of two device state quantities. For electrical systems, this is the product of voltage and current. For rotating mechanical systems, it is the product of torque and angular velocity. For fluid systems, including fans and pumps, it is the product of head pressure and mass flow rate. A power conversion system must have at least one combination of the two device state quantities in order for it to operate. Most devices can typically operate over a larger range of operating points as a result of the ability to vary one or both of the device state quantities. If both quantities can be varied, then the range of operating points forms a two dimensional operating area that describes all possible operating states of the system.

Fig. 2.11 shows some common examples of power conversion devices that can be described in terms of their two dimensional operating areas. This list of

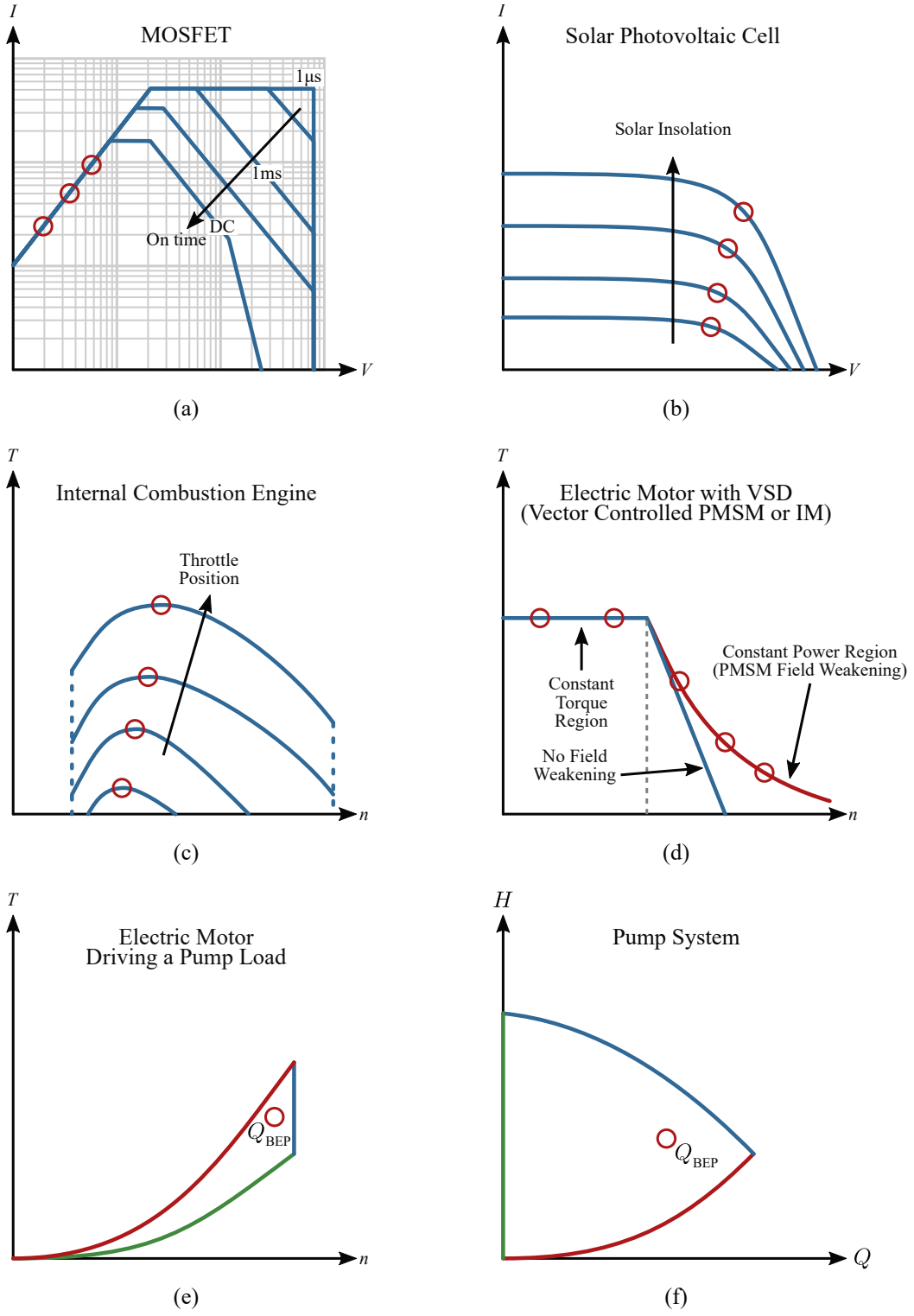

FIGURE 2.11: Operating areas for a variety of power conversion devices including: (a) a MOSFET, (b) a solar PV Cell, (c) an internal combustion engine, (d) an electric motor, (e) an electric motor driving a pump load, and (f) a pump system. Ideal operating points are shown using the ○ symbol. Q_{BEP} is the pump's best efficiency point.

examples is not exhaustive, and almost any power device can be described this way. Although the areas are expressed as being two dimensional in terms of the two key quantities that determine the device power, it is possible for several other device state quantities to affect the efficiency and operating area of the device (e.g. temperature). Fig. 2.11 (a) shows a MOSFET's safe operating area, where the device can operate over a larger area of voltage and current combinations if the pulse length is kept shorter (a result of internal thermal limitations). Fig. 2.11 (b) shows the voltage-current operating area of a solar PV cell, where the operating point is determined by the voltage-current curve (determined by solar insolation) and the load impedance on the cell. Fig. 2.11 (c) shows the torque-speed curve of an internal combustion engine that describes the operating area as being beneath the maximum torque curve.

Fig. 2.11 (d) shows the operating area of an electrical machine (permanent magnet synchronous machine or induction machine) with VSD. Operation can be broken down into a constant torque (constant current) region and a constant power region. In the case of a PMSM without field weakening, there is no constant power region with the machine torque (and current) being limited beyond a certain speed.

Fig. 2.11 (e) and (f) show the motor and pump operating areas respectively for a pump system driven by an electric motor. Fig. 2.11 (f) shows the pump system's operating area, being bound by the pump curve (shown in blue), the hydraulic system curve (shown in red), and the H-axis (shown in green) that represents the closed valve (zero flow) operation of the pump. Fig. 2.11 (e) uses the same colours to show how the pump system's operating area then determines the motor's operating area. In contrast to Fig. 2.11 (d), Fig. 2.11 (e) presents a very different operating area shape. Hence for a motor system operating with a load device (in this example, a pump), it is essential to consider the entire combination of system components and resulting system-specific operating area when designing and analysing the system.

In general, any power conversion device's operating state can be described in terms of a two dimensional operating area. In addition to the two variables that describe the operating area (the product of which is proportional to power), there are additional quantities that represent a device's state (e.g. temperature, input power, flux, losses, etc.). Each quantity may vary over the device's operating area, and consequently can be represented as a three dimensional surface. Efficiency is a key quantity of interest and can be represented as a three dimensional surface. For ease of visualisation, this three dimensional data can be represented through the use of iso-efficiency contours, or efficiency maps. Three dimensional surfaces

and contour maps can also effectively represent the non-linear relationship between each device quantity and the operating area, hence they're an effective tool for describing the non-linear losses and efficiency of a device.

Recall in Fig. 2.10 (b) that each component in a system of power devices represents a portion of the losses in the overall system. Fig. 2.10 (b) represents the power flow and loss breakdown for only a single operating point of the system. To effectively understand, model and optimise an integrated motor system, it is necessary to understand the complete power flow and loss breakdown at every possible operating point. This can be achieved using efficiency maps for each component device. Because the component devices interact with each other and have operating areas and losses unique to the combination of components, it is essential to capture power flows and efficiency maps from each component when operating as a complete system.

Before a motor system can be analysed over a wide, two dimensional operating area, the motor system must be capable of operating over such an area. The operating area capability is determined primarily by the combination of motor and drive. Brushless PM motors that can offer high efficiency operation require a drive synchronised to the motor using knowledge of the rotor's instantaneous position. To broaden the utilisation of brushless PM motors requires a low cost, high performance drive. Low cost can be achieved through position sensorless schemes, however high performance wide speed range (including low speed) operation typically increases the complexity and cost of the drive. A solid foundation for an integrated motor system would ideally be achieved through a low cost, low complexity position sensorless drive system that enabled high performance operation of a motor over a wide operating area.

Chapter 3

Wide Speed Range Sensorless Operation of Brushless Permanent Magnet Motor Using Flux Linkage Increment

Statement of Authorship

Title of Paper	Wide Speed Range Sensorless Operation of Brushless Permanent Magnet Motor Using Flux Linkage Increment.
Publication Status	Published
Publication Details	G. Haines and N. Ertugrul, "Wide Speed Range Sensorless Operation of Brushless Permanent-Magnet Motor Using Flux Linkage Increment," *Transactions on Industrial Electronics*, vol. 63, no. 7, pp. 4052–4060, Jul. 2016.

Principle Author

Author Name	Gabriel Haines
Contribution	Designed inverter hardware and software, performed all testing and analysis, wrote manuscript and acted as corresponding author.
Overall Percentage	85 %
Signature	**Date** 6/11/19

Co-Author Contributions

By signing the Statement of Authorship, each author certifies that: i. the candidate's stated contribution to the publication is accurate (as detailed above); ii. permission is granted for the candidate in include the publication in the thesis; and iii. the sum of all co-author contributions is equal to 100 % less the candidate's stated contribution.

Author Name	Nesimi Ertugrul
Contribution	Supervised development of work, guided testing and analysis, helped to review and edit the manuscript.
Signature	**Date** 6/11/19

Abstract

Conventional back-EMF and flux linkage based indirect rotor position detection methods have limitations, specifically poor position accuracy and inability to operate at low as well as at high speed. However, practical motor drives require precise operation over a wide speed range, which widens the application areas while increasing reliability compared to direct position sensor based drives. The method proposed and demonstrated in this paper uses only terminal voltage measurements to estimate the flux linkage increment in six separate sectors of an electrical cycle. This is used to determine the rotor position while avoiding the accumulated position error that is a characteristic of flux linkage based techniques. The paper also addresses the common problems associated with the practical implementations, such as low pass filter delay, integrator offset error and noise sensitivity at low speed. The theoretical explanation of the method has been given in detail and analytical solutions for the flux linkage threshold of both sinusoidal and trapezoidal permanent magnet machines is provided, avoiding trial and error tuning commonly utilised in the literature. The paper provides a range of experimental data to verify both the operational robustness and position accuracy of the method.

3.1 Introduction

Brushless permanent magnet machines offer high efficiency, high power density and low maintenance. However, they require the use of an electronic drive to synchronise the current waveforms to the rotor position. Typically this is achieved through use of external position sensors mounted to the motor shaft. Position sensors not only increases the cost of the system, but also expose the system to external noise and an additional point of failure.

To reduce costs and increase reliability, a number of position sensorless methods have been developed to estimate the rotor position. Methods range from simpler back-EMF and zero crossing detection methods, through to complex mathematical model based or state observer based methods [20], [21]. The complex methods typically measure both voltages and currents, then apply detailed knowledge of the machine parameters to provide an estimate of the rotor position. These methods have been developed for BLDC/trapezoidal operation [45], [46], but can also realise sensorless operation for sinusoidally controlled machines [47], [48]. Back-EMF sensing methods are simpler, generally require only phase voltage measurements, require minimal knowledge of machine parameters, do not

require a complex DSP, and consequently have seen widespread used. Methods include zero crossing point detection [19], [49]–[52], phase locked loop [53], and back-EMF integration (flux linkage increment) [54], [55]. Although simpler and more cost effective, these methods may lack the position sensing accuracy and dynamic performance of the more complex methods.

This paper presents a novel measurement and back-EMF reconstruction technique to address existing problems of limited speed range, poor low speed operation, and rotor position error found in back-EMF sensing methods. A Pulse Width Modulation (PWM) synchronised measurement strategy combined with auto-calibration is used to solve the problems of low pass filter delay and integrator offset error in back-EMF integration (flux linkage increment) methods of sensorless operation. A low cost, microcontroller based approach is considered, with experimental results highlighting the improvements of the proposed method over existing back-EMF sensing methods.

Section 3.2 reviews the existing back-EMF sensing methods. Section 3.3 describes the proposed method of sensorless operation. Section 3.4 outlines how the proposed method was implemented. Section 3.5 presents the experimental results using a commercially available brushless DC motor.

3.2 Back-EMF Sensing Methods

Back-EMF sensing methods are generally limited to brushless DC motors (trapezoidal control), where only two phases are driven and one phase is left floating. It is well known that the back-EMF can be measured from the floating phase once the current in that phase has been extinguished. Because brushless DC drive operation involves applying a sequence of six voltage states (sectors), the drive is only concerned with knowing the commutation point (rotor position) between each 60 electrical degree voltage state/sector.

3.2.1 Zero Crossing Detection of Back-EMF Voltage

Zero Crossing Point (ZCP) detection is the simplest method, and consequently has seen widespread use. The back-EMF voltage is measured from the floating phase and compared against a defined threshold corresponding to the back-EMF zero crossing [19]. A speed dependent time delay is then used to determine the commutation point after the zero-crossing, either by a low pass filter [19] or a software defined delay. Regardless of the solution used, a low pass filter is generally used to filter out the Pulse Width Modulation (PWM) carrier frequency. However,

such filters introduce a speed dependant phase shift in the zero-crossing location [56] that limits the speed range and performance of the drive.

A number of solutions to the phase delay problem have appeared in literature. Third harmonic back-EMF sensing is a variation on the zero-crossing method that is less sensitive to phase shifts [20], by extracting the third harmonic, integrating, then searching for the zero-crossing point. Phase locked loops have also been used to address the phase delay problem[53], but with reduced dynamic performance [20], [21]. A hysteresis comparator has been proposed [57] to reduce the low pass filter phase delay over the rated speed range, but the filter delay was only incrementally reduced. [58] uses a virtual neutral point and low pass filter to find the zero-crossing point, but compensates for the low pass filter delay in software. [59] uses a Bessel filter to a detect zero crossings from the zero sequence voltage to achieve a constant time delay.

Instead of using a low pass filter to remove the PWM carrier frequency from the back-EMF voltage, the zero-crossing may be detected only when the PWM is in the on or off state [49]. Such an approach was described in [50] where two zero-crossing conditions where established based on the PWM state, although only one condition was used. [51] uses a similar approach where the comparator reference is changed depending on the PWM state, allowing the use of all possible duty cycle values. [52] focusses on the effect of different commutation schemes on zero-crossing point detection, but does not contribute anything more other than a summary of previously stated conditions. The application note in [60] describes back-EMF measurements using analogue to digital converters that are synchronised to the middle of the PWM cycle, with zero-crossing detection being performed in the digital signal processor. [60] fails to offer a solution for the entire duty cycle range.

To further improve the precision of the zero-crossing detection when using micro-controller based analogue to digital converters synchronised to the PWM state, a method of interpolation was developed in [49]. Rather than detect a single zero-crossing once per PWM cycle, two points are measured either side of the zero-crossing point and the zero-crossing is interpolated. [56] proposes a similar method of symmetric threshold tracking, where the two points are a considerable time apart (zero-crossing still centred between them). Compared to conventional zero-crossing operation where the drive searches for the zero-crossing point before waiting 30 degrees to commutate, the symmetric tracking method aims to improve the dynamic response of the system by moving the commutation decision closer to the commutation point. [61] focuses on the calculation of the threshold used for symmetric threshold tracking, and addresses dynamic performance of

the method. Despite the benefits of improved time precision of the zero-crossing point, [49] and [56] (also [50]–[52], [57], [60]) do not address the effect of noise in the back-EMF signal causing false zero-crossing detection. This issue is worse at low speed operation where the reduced amplitude of the back-EMF waveform reduces the signal to noise ratio of the measurements. Hence the difficulty of low speed operation using these methods.

3.2.2 Back-EMF Integration/Flux Linkage Increment

The back-EMF integration/flux linkage increment method searches for the zero crossing point of the back-EMF, starts integrating the back-EMF, then upon reaching a predefined threshold the integrator is reset and the machine commutated [54]. Because of the relationship

$$\psi = \int e \, dt \tag{3.1}$$

where e is the phase back-EMF and ψ is the phase flux linkage, the method of integration obtains a portion of the flux linkage, then commutates after the flux linkage has incremented by a fixed amount (hence the term "flux linkage increment"). Unlike in [47] where voltage and current measurements are integrated to obtain a flux linkage estimate, only voltage measurements are required. The benefit of voltage only measurements comes with the limitation of only 120 electrical degree, six-step commutation (trapezoidal control).

For machines with trapezoidal back-EMF, the back-EMF during the 60 degree floating sector is a straight line with amplitude proportional to speed and 60 degree sector width in time that is inversely proportional to speed. The result is an integral that is speed independent for a given change in electrical angle. However, no relationship to the machine parameters is discussed in [54], which only describes the general effect of varying integral gain and threshold to vary the current to voltage alignment. The integral gain and commutation threshold are typically set to obtain an integrated value corresponding to a 30 degree electrical angle from the zero-crossing to the commutation point, eliminating the need for any timers or delays. Tuning using machine parameters is not discussed in [54].

The same method for control of hard disk drive motors with sinusoidal back-EMF is revisited in [55]. A method acquiring the integration threshold parameter at runtime was also proposed, but not developed or tested. In addition, the origin of the back-EMF constant and relationship to machine pole number

is not discussed, despite the technique targeting multi-pole hard disk drive motors. Furthermore, [55] suggests that the method is less sensitive to errors in the zero-crossing location caused by pole jitter, but does not verify this.

Unlike zero crossing detection methods that make the commutation decision 30 electrical degrees before the commutation point, the flux linkage increment method makes the commutation decision at the point of commutation, and should offer better dynamic performance. This type of operation also has lower sensitivity to switching noise due to the low pass filter nature of the integrator, but has poor low speed operation due to the accumulation of errors at low speed where the back-EMF amplitude is weak [20], [46]. Existing methods have used a low pass filter to remove the PWM carrier frequency from the back-EMF waveform, incurring the same phase delay problems previously mentioned. Improvements to low pass filter delay have been discussed for zero crossing methods [49]–[52], [56], [60], but no solutions have been presented for flux linkage increment methods. No solutions have been found in literature for the accumulated error at low speed operation. Despite these drawbacks, the method has seen industrial use as part of an application specific control IC [54], and featured in some digital signal processor manufacturer's motor control evaluation products [62], [63].

3.3 Proposed Sensorless Method

The proposed method in this paper uses PWM synchronised terminal voltage measurements [49], [60] to remove the PWM carrier frequency from the back-EMF voltage without using a low pass filter. This removes the speed dependant phase delay, which permits wider speed operation. The PWM synchronised measurement also permits back-EMF extraction independent of the instantaneous duty cycle, similar to [51]. The novel back-EMF reconstruction technique uses careful selection of modulation pattern and synchronised measurement point location to provide a back-EMF waveform suitable for operation of the flux linkage increment method over the entire duty cycle range. Existing methods of PWM synchronised measurements do not produce a suitable back-EMF waveform, and no techniques that eliminate the low pass filter delay in the flux linkage increment method have been reported in literature. By utilising a microcontroller with integrated analogue to digital converter, offset calibration and gain balancing (between phases) are used to reduce the impact of error accumulation from integrating the low amplitude back-EMF at low speeds, improving the low speed performance and reducing position error.

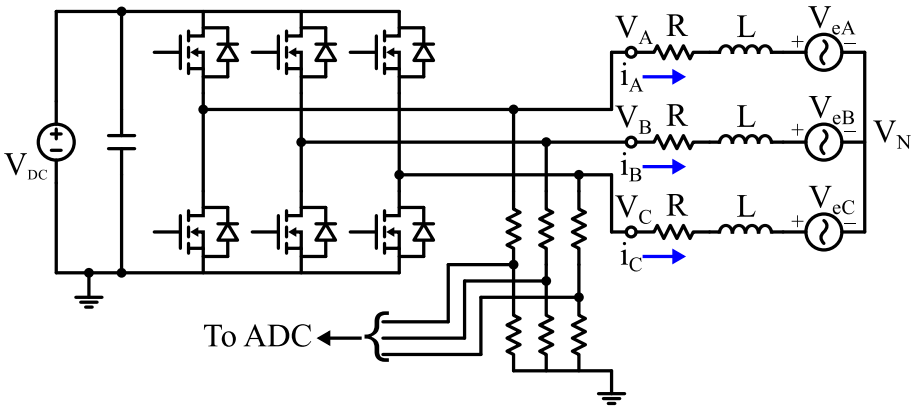

FIGURE 3.1: Inverter, brushless PM machine, and analogue to digital converter voltage divider.

3.3.1 Terminal Voltage Measurement

Figure 3.1 shows the inverter, brushless PM machine and voltage divider used for terminal voltage measurements. The measurements are made with respect to the DC link ground via a high impedance voltage divider. During each 60 degree sector, two phases are driven and the third is floating. The back-EMF voltage at the floating phase can be shown to be

$$v_{eA} = v_A - \frac{1}{3}(v_A + v_B + v_C) \tag{3.2}$$

(the result is the same for phases B and C when they are the floating phases respectively). The back-EMF waveforms may be sinusoidal or trapezoidal. This result is derived using the assumptions that the machine is balanced and three back-EMF voltages sum to zero [64], all phases have the same values for resistance and inductance, and the floating phase current is zero. Note that if $i_A \neq 0$, the free-wheeling diodes in the inverter will be conducting, pulling the terminal voltage v_A to one of the DC link rails (subject to the direction of current flow), and preventing the back-EMF from being measured. Hence zero current in the floating phase is not an assumption but a requirement for back-EMF measurement.

3.3.2 Pulse Width Modulation and Commutation Strategy

The result in equation (3.2) holds for any combination of PWM states at the two driven terminals, providing one phase is floating. For the sector of six-step commutation where a voltage is applied from phase A to B (phase C floating), there are three possible PWM states:

State 1: $v_A = v_B = 0$. The PWM is low/off,

State 2: $v_A = V_{DC}, v_B = 0$. The PWM is high/on,

State 3: $v_A = v_B = V_{DC}$. The PWM is low/off,

where V_{DC} represents the positive DC link voltage, and 0 represents the DC link ground voltage. For the first state, equation (3.2) becomes:

$$v_{eC} = \frac{2}{3}v_C \qquad (V_{ZCP} = 0) \tag{3.3}$$

the second state becomes:

$$v_{eC} = \frac{2}{3}v_C - \frac{1}{3}V_{DC} \quad (V_{ZCP} = \frac{1}{2}V_{DC}) \tag{3.4}$$

and the third state becomes:

$$v_{eC} = \frac{2}{3}v_C - \frac{2}{3}V_{DC} \quad (V_{ZCP} = V_{DC}) \tag{3.5}$$

The location of the zero-crossing point for each state is described by V_{ZCP}. The result is a choice between two possible "PWM off" states. To obtain the flux linkage increment, the back-EMF waveform for the second half of the 60 degree sector must be obtained. Free-wheeling diodes clamp any voltages above or below the DC link to the DC link rails. PWM state one only allows the positive portion of the back-EMF to be extracted. PWM state three only allows the negative portion of the back-EMF to be extracted. Hence the choice of PWM state for "PWM off" depends on the the back-EMF waveform rising or falling.

Figure 3.2 describes the required commutation sequence for all three terminal voltages. Sectors 2, 4, and 6 have a rising back-EMF and apply the PWM signal between the phase and ground to achieve state 1 when the PWM is off. Sectors 1, 3, and 5 have a falling back-EMF and apply the PWM signal between the DC link positive and the phase to achieve state 3 when the PWM is off. This allows for the second half of the back-EMF waveform to be obtained when the PWM is on or off, but limits the commutation sequence to one direction only. The reverse commutation order can be found by swapping two of the phases in Figure 3.2.

Figure 3.3 shows the rising and falling waveforms in more detail, as seen by the floating phase terminal. The slope of the back-EMF waveform compared to the number of PWM cycles has been exaggerated for increased clarity. To reduce the impact of transient noise from the PWM edges, the ADC sampling point is always moved to the larger part of the PWM cycle, and located before the next edge. This maximises the time for the transients to decay, and allows for the

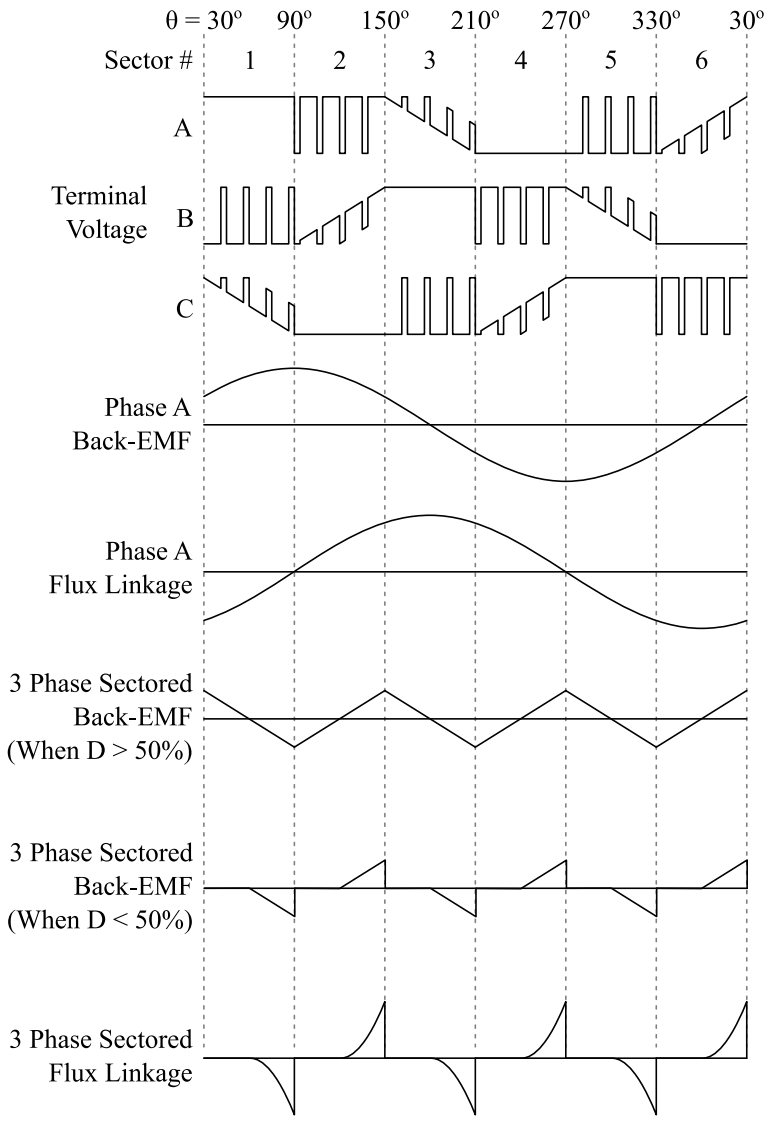

FIGURE 3.2: Ideal shapes of six-step commutation sequence, machine back-EMF, machine flux linkage, resulting sectored back-EMF and resulting sectored flux linkage waveforms referenced to one electrical cycle. D: Duty cycle

full duty cycle range to be used. The decision point is set at 50 % overall duty cycle. Figure 3.3 shows the case for a low (<50 %) overall duty cycle. Following the dashed diagonal lines for *"back-EMF (Low part of PWM cycle)"* in figure 3.3 will produce the *"3 Phase Sectored Back-EMF (D<50 %)"* waveform in Figure 3.2. When a duty cycle larger than 50 % is used, the ADC sample point is shifted to follow the dashed diagonal lines labelled *"back-EMF (High part of PWM cycle)"* in figure 3.3, producing the *"3 Phase Sectored Back-EMF (D>50 %)"* waveform in Figure 3.2.

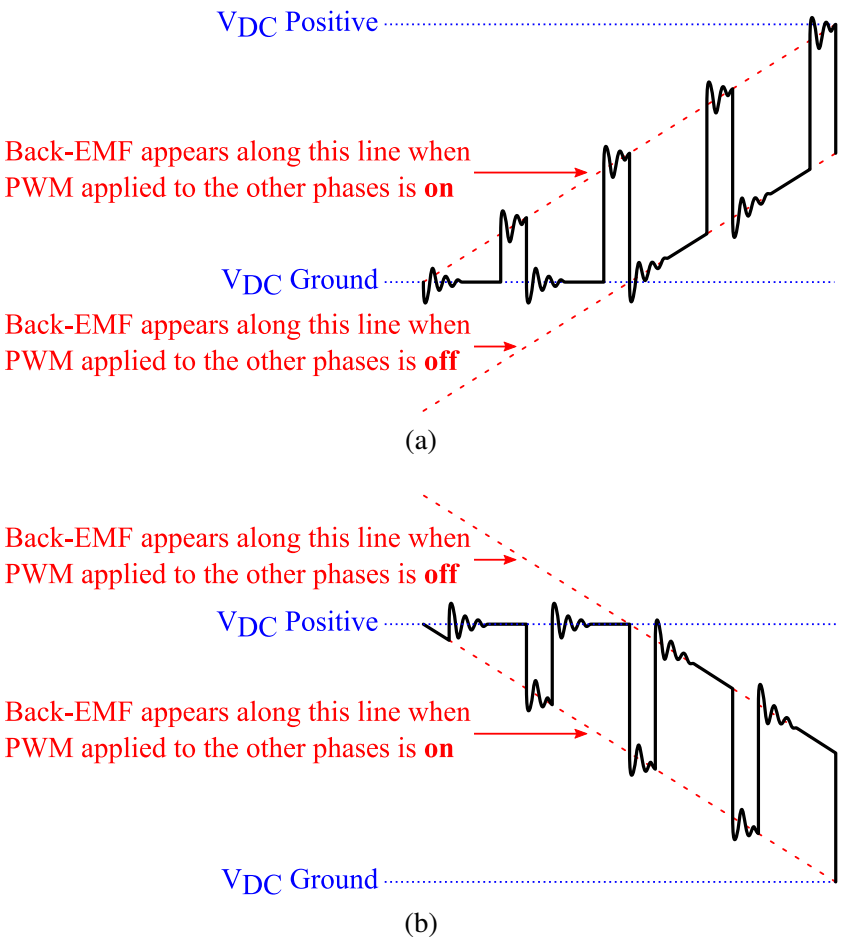

FIGURE 3.3: Instantaneous floating single phase terminal voltage waveform during (a) rising and (b) falling back-EMF sectors.

3.3.3 Back-EMF Integration/Flux Linkage Increment

Once the back-EMF waveform is extracted, it can be fed into an integrator to obtain the flux linkage increment. Figure 3.4 shows the graphical representations of this integral. Despite the different waveforms, the region of interest is approximately linear in both, hence either back-EMF shape can be used. The resulting waveform is shown at the bottom of Figure 3.2, and described as "Sectored Flux Linkage" to differentiate it from the true flux linkage waveform of the machine. For a sinusoidal machine, the back-EMF waveform in terms of rotor position θ_r can be defined as

$$e(\theta_r) = \psi_p \omega_m sin(\theta_r) = K_e \omega_m sin(\theta_r) \tag{3.6}$$

where ω_m is the mechanical angular velocity, and peak flux linkage ψ_p is equal to the per phase back-EMF constant K_e. Using the relationship between electrical

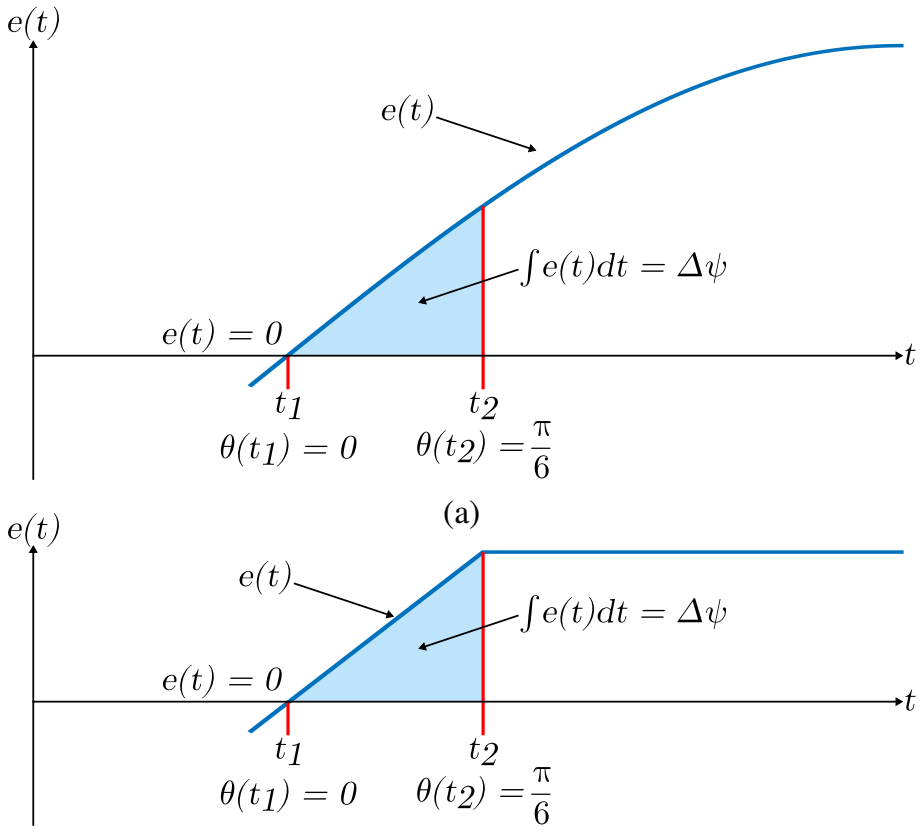

FIGURE 3.4: Back-EMF integration and change in flux linkage $\Delta\psi$ for (a) sinusoidal and (b) trapezoidal back-EMF waveforms.

angle $\theta_r(t)$ and mechanical angular velocity ω_m,

$$\frac{d\theta_r}{dt} = \frac{P}{2}\omega_m \tag{3.7}$$

where P is the number of poles, the integration from the zero crossing point time t_1 (corresponding to $\theta_r(t_1)$) to the commutation time t_2 (corresponding to $\theta_r(t_2)$) becomes:

$$\int_{t_1}^{t_2} e(t)dt = K_e\frac{2}{P}[cos(\theta_r(t_1)) - cos(\theta_r(t_2))] \tag{3.8}$$

The result in (3.8) is general for any change in angle, providing the back-EMF is measurable over the 60 degree floating sector and the initial rotor position $\theta_r(t_1)$ can be found. For commutation 30 degrees after the zero crossing point, the integral limits $\theta_r(t_1) = 0° = 0$ and $\theta_r(t_2) = 30° = \frac{\pi}{6}$ are used (see Figure 3.4). The result is equation (3.9)

$$\int_{t_1}^{t_2} e(t)dt = K_e\frac{2}{P}[1 - \frac{\sqrt{3}}{2}] \tag{3.9}$$

TABLE 3.1: Specifications for test motor, Bodine 34B3FEBL.

Parameter	Value
Poles	4
Rated Speed	2500 rpm
Rated Voltage	24 V
Power	149 W
Voltage Constant	0.0630 V/rads^{-1}

which is a time and speed independent constant, requiring only the back-EMF constant (peak flux linkage value) of the machine. The analysis is the same for trapezoidal back-EMF machines with 120 degrees flat-top, except the back-EMF is treated as a linear function (equation 3.10). The corresponding result is described by equation (3.11).

$$e(\theta_r) = \psi_p \omega_m (\frac{6}{\pi}\theta_r) = K_e \omega_m (\frac{6}{\pi}\theta_r), \quad \theta_r \in [\frac{-\pi}{6}, \frac{\pi}{6}] \tag{3.10}$$

$$\int_{t_1}^{t_2} e(t)dt = K_e \frac{\pi}{6P} \tag{3.11}$$

The time independent result in equations (3.9) and (3.11) is expected, considering the flux linkage has only spatial dependence on the rotor position.

The result in equation (3.9) is similar to that in [55], but features a pole number term to account for the back-EMF constant K_e being given as a line-neutral voltage with respect to mechanical angular velocity. The result is not limited to 30 degree commutation points, but can trigger commutation after an arbitrary change in angle (see equation (3.8)).

3.4 Implementation

The proposed method was implemented using a low cost Atmel AT32UC3C microcontroller. The microcontroller has an integrated analogue to digital converter (ADC) triggered synchronously from the pulse width modulation (PWM) module. Terminal voltages were measured according to Figure 3.1. The PWM and ADC frequency was 20 kHz. The ADC trigger point was either fixed at 6 μs before the PWM falling edge (duty cycle >50 %) or continuously shifted to be 6 μs before the rising edge (duty cycle <50 %). The 6 μs offset provides enough time to measure all terminal voltages, while maximising the settling time after the last transient edge. Providing all software tasks can complete within 25 μs (of the

50 μs PWM cycle), the sudden ADC advance or delay by 25 μs has no effect on operation of the drive.

To combat the effects of integrator offset error, all channels of the analogue to digital converter are automatically calibrated at startup. The following steps are performed:

Step 1: The internal ADC reference is checked against an external reference level.

Step 2: All inverter phases are driven to the DC link ground, then the average offset is measured.

Step 3: All inverter phases are driven to the DC link positive, and the average measured. This average is used to balance the gains of each channel.

All values were in real units using floating point representation. Back-EMF values were extracted per equation (3.2). Flux linkage was calculated by numerically integrating the back EMF:

$$\begin{aligned} \Delta\psi(k) &= \Delta T v_e + \psi(k-1), \\ \text{where } \Delta T &= \frac{1}{f_{PWM}} \end{aligned} \tag{3.12}$$

The choice of integrator gain equal to the PWM period (ADC sample period) keeps the integrated value in units of volt-seconds, and allows for changes in PWM frequency without recalculation of the required flux linkage threshold.

Zero crossing detection is achieved by resetting the integrator to zero if it is negative and the back-EMF is rising, or resetting the integrator if it is positive and the back-EMF is falling. The integrator is only started after the post commutation current recirculation has extinguished. High current operation is possible, providing current recirculation stops before the zero crossing.

The modulation sequence in Figure 3.2 was used. This sequence is generally not used by inverters with bootstrap gate drivers, but instead used with topologies that permit continuous high side output [52]. A bootstrap configuration inverter was used, but with continuous on-time regions replaced with the maximum available duty cycle of 97.7 %.

The machine is started using a commonly known open loop ramp sequence that aligns the rotor before forcibly commutating at increasing speed [20], [21].

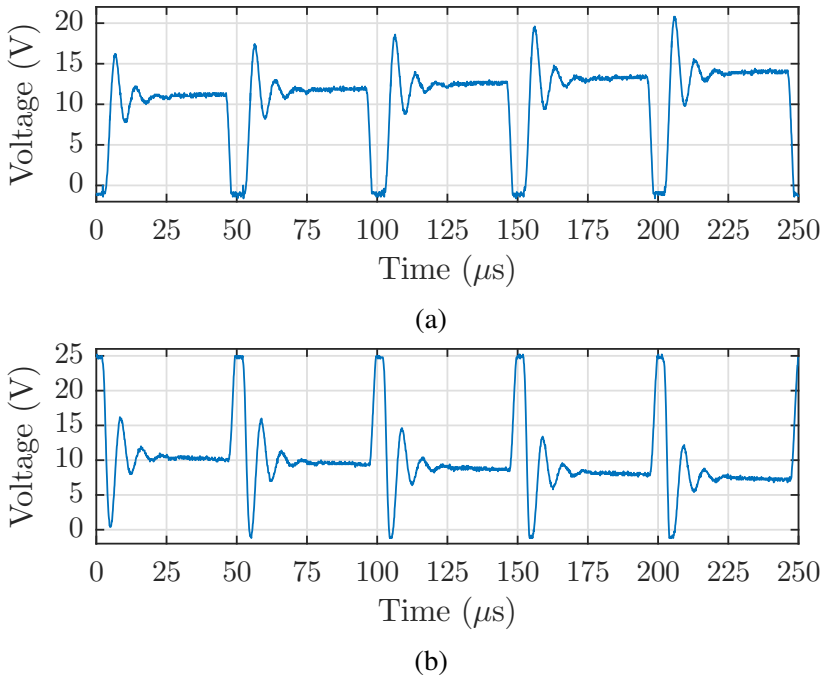

FIGURE 3.5: Enlarged view of the floating single phase terminal voltage waveform during: (a) rising and (b) falling back-EMF sectors.

3.5 Experimental Results

The proposed sensorless method was tested using a commercial brushless motor of sinusoidal back-EMF, with parameters given in Table 3.1. Note the proposed method always uses six step commutation (trapezoidal control).

3.5.1 Back-EMF Constant and Algorithm Tuning

The machine was run as a generator, and the sinusoidal back-EMF waveform measured to find the back-EMF constant:

$$\begin{aligned} K_{e,LL} &= 0.0572 \quad V/rads^{-1} \\ K_e &= \frac{K_{e,LL}}{\sqrt{3}} = 0.03302 \quad V/rads^{-1} \end{aligned} \tag{3.13}$$

where $K_{e,LL}$ is the line-to-line value measured from the open terminal machine, and K_e is the line-neutral value. Using equation (3.9), the integration threshold was calculated to be

$$V_{int} = 0.002212 \quad V \cdot s \tag{3.14}$$

3.5.2 Flux Linkage Increment Operation

Figure 3.6 shows the raw terminal voltage, terminal voltage measured by the analogue to digital converter, reconstructed back-EMF and sectored flux linkage waveforms for operation at rated speed of 2500 rpm. The waveforms in Figures 3.6a and 3.6b are for a single phase, whereas the waveforms for sectored back-EMF and sectored flux linkage in Figures 3.6c and 3.6d are derived from all three phases. Figure 3.7 shows the same set of waveforms at 1765 rpm.

Figures 3.6b and 3.7b show the recovered terminal voltage waveform as seen by the microcontroller's analogue to digital converters. Common to both is the rejection of the PWM carrier frequency with no observable phase lag compared to the raw inverter terminal voltage waveforms in Figures 3.6a and 3.7a respectively. Figure 3.5 shows and enlarged view of the PWM waveforms when the back-EMF is rising and falling (compare to Figure 3.3). The duty cycle is arbitrary and does not correspond with any other Figures. In both waveforms, the transient noise is dominant just after an edge transition and has least impact just before the next edge (where the ADC sample point is located).

The key difference between Figures 3.6 and 3.7 is the applied duty cycle. Figure 3.6 shows a 62 % duty cycle that causes the ADC sample point to shift to the high side of the PWM cycle, resulting in a back-EMF zero crossing at half of the DC link voltage. The entire back-EMF waveform for each 60 degree sector can be recovered, shown in 3.6c. Figure 3.7 shows operation with a 42 % duty cycle that causes the ADC sample point to shift to the low side of the PWM cycle, resulting in a back-EMF zero crossing at either the DC link positive (back-EMF falling) or DC link ground (back-EMF rising). Figure 3.7c highlights the dramatic change in recovered back-EMF waveform where the back-EMF is visible for only the second half of the 60 degree sector. Despite the difference in Figures 3.6c and 3.7c, the resulting sectored flux linkage waveforms in Figures 3.6d and 3.7d maintain the same shape. This result is what allows for operation of the sensorless algorithm over the entire duty cycle range.

3.5.3 Low Speed operation

Low speed operation is shown in Figures 3.8 and 3.9, highlighting the break down in sectored flux linkage waveform compared to the normal waveform shape shown in Figures 3.6d and 3.7d. Figure 3.8 shows the sectored flux linkage waveform at 42 rpm (1.4 Hz, 1.7 % rated speed), on the edge of motor stall. Compared to

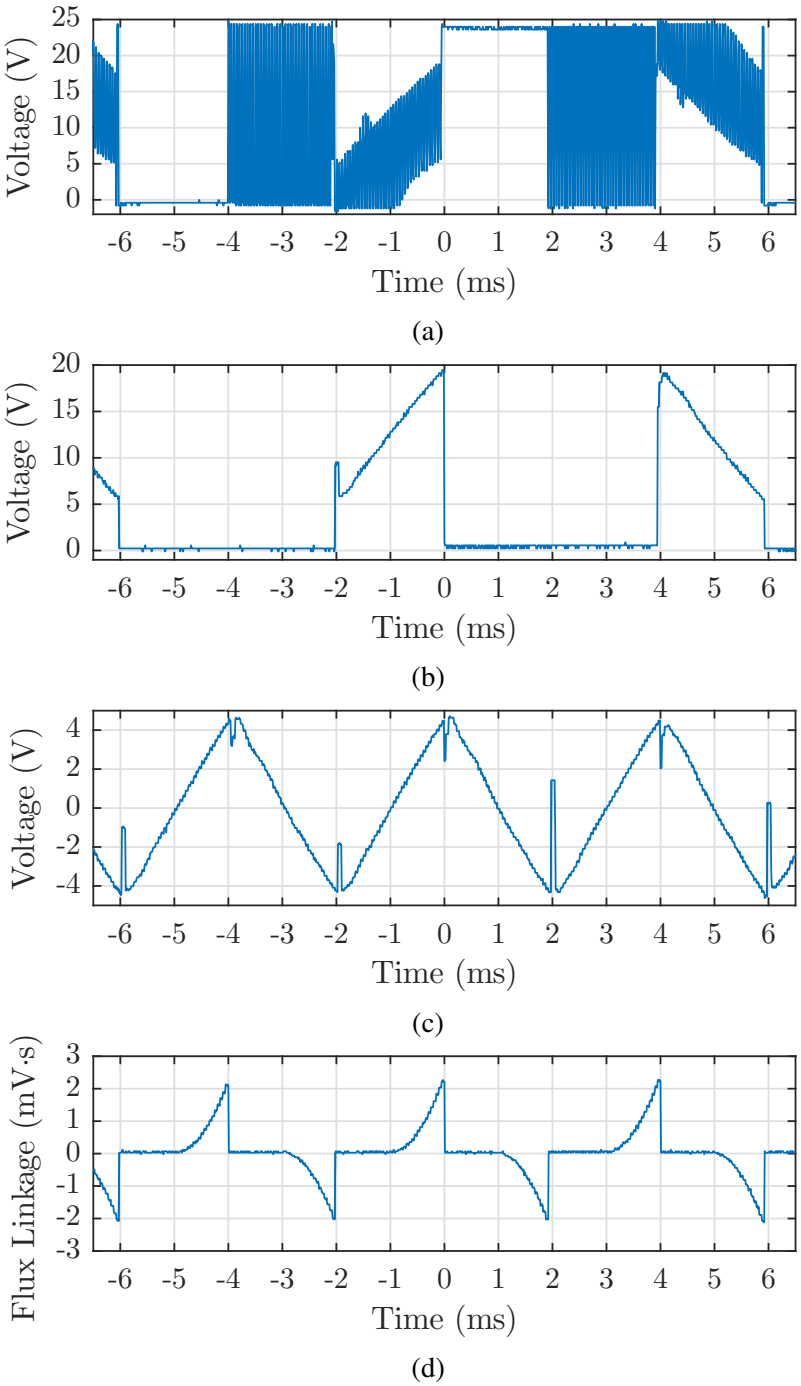

FIGURE 3.6: Measured waveforms for operation at 2500 rpm (62 % PWM duty cycle, 83.33 Hz): (a) Terminal voltage at the inverter output. (b) Terminal voltage measured by ADC. (c) Reconstructed back-EMF waveform. (d) Sectored Flux Linkage waveform.

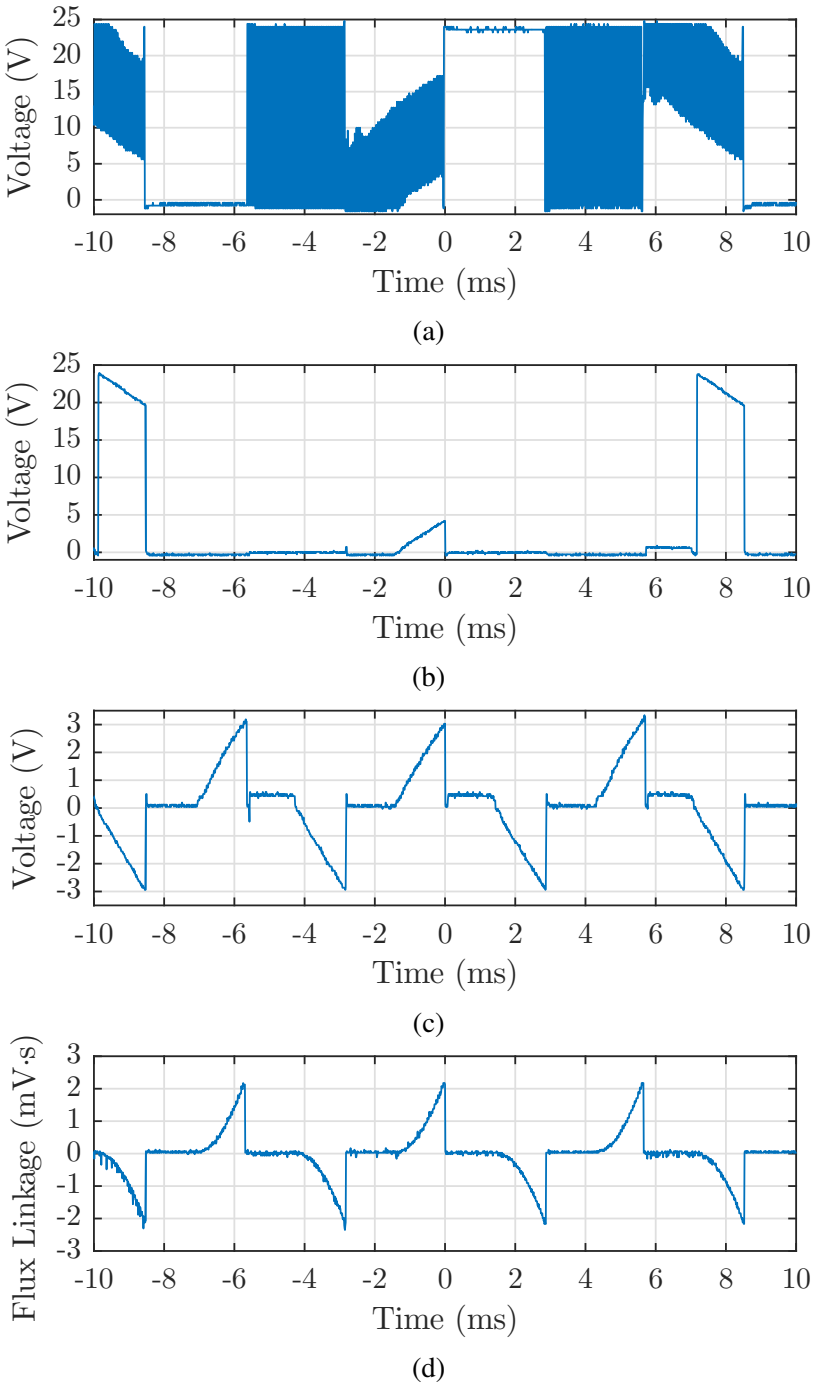

FIGURE 3.7: Measured waveforms for operation at 1765 rpm (42 % PWM duty cycle, 58.82 Hz): (a) Terminal voltage at the inverter output. (b) Terminal voltage measured by ADC. (c) Reconstructed back-EMF waveform. (d) Sectored Flux Linkage waveform.

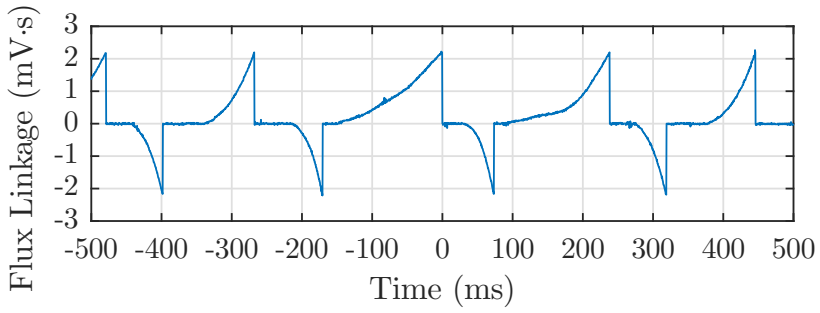

FIGURE 3.8: Low speed operation at 42.1 rpm (1.404 Hz), V_{DC} = 23.96 V

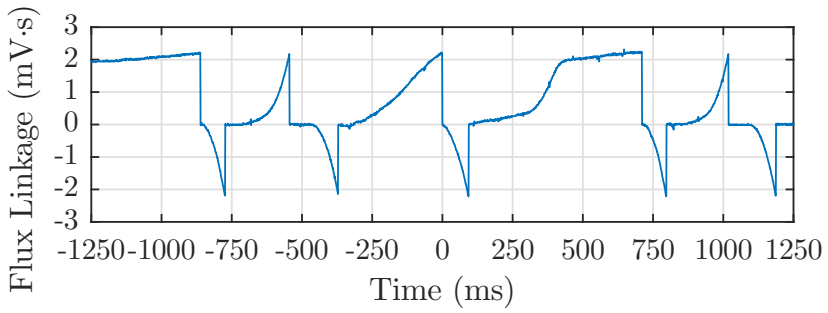

FIGURE 3.9: Low speed operation at 19.0 rpm (0.6329 Hz), V_{DC} = 5.614 V

Figures 3.6d and 3.7d, the low speed sectored flux linkage waveform shows unbalanced timing between commutation points (sectored flux linkage returning to zero), and premature start of integration from false zero crossing point detection.

The inverter mean output voltage is limited by the minimum achievable PWM duty cycle. To allow finer control at low speed operation, the DC link voltage was reduced from 23.96 V down to 5.614 V. With no other changes, the minimum speed achieved was 19 rpm (0.63 Hz, 0.76 % rated speed). Figure 3.9 shows the sectored flux linkage waveform at this speed.

Table 3.2 shows a comparison of the low speed result from this study with the experimental results from other studies. [49], [50] and [58] reported operation down to 500 rpm (16.7 Hz) with a back-EMF sensing method. [61] and [59] reported operation down to 273 rpm and 100 rpm respectively. [46], [48] and [45] presented different sensorless methods derived from a machine model, featuring complicated algorithms and large number of voltage and current measurements. [46] achieved a minimum speed of 85 rpm (1.43 Hz), and [48] achieved a minimum speed of 35 rpm (1.75 Hz). Under fixed DC link operation, the proposed method achieves a better result of 1.4 Hz (42 rpm). Reduced DC link voltage can bring the minimum speed to 19 rpm (0.63 Hz), which is closer to that of [45] where 15 rpm (0.5 Hz) was achieved.

TABLE 3.2: Comparison of the speed range reported in the literature.

Reference	Model Type	n (rpm)	f (Hz)	Poles	Position error
[49]	Back-EMF	500∼1500	16.7∼50	4	N/A
[50]	Back-EMF	500∼7500	16.7∼250	4	N/A
[58]	Back-EMF	500∼24000	16.7∼800	4	N/A
[61]	Back-EMF	273∼3810	N/A	N/A	N/A
[59]	Back-EMF	100∼3000	6.7∼200	8	N/A
[46]	Complex	>85	>1.43	2	N/A
[48]	Complex	35∼1500	1.75∼ 75	6	N/A
[45]	Complex	15∼1000	0.5∼33.3	4	3.5^o ∼1.5^o
Proposed Method	**Back-EMF**	**19∼4600**	**0.63∼153**	**4**	**9.8^o ∼2.0^o**

The minimum speed result of the proposed sensorless method is a vast improvement compared to other sensorless methods that only use terminal based back-EMF measurement. The proposed method can also produce a result better than some of the complex model based methods previously proposed, with lower complexity and less knowledge about the machine. The result can be attributed to the auto-calibration of ADC measurements limiting integrator offset error when operating with back-EMF signals as low as 30 mV (at 19 RPM).

3.5.4 Position Error

Position error of the commutation points was measured using an encoder. At each commutation point, the estimated position from the proposed sensorless method is compared to the true position, measured by the encoder. Figures 3.10 and 3.11 show the position error relative to one electrical cycle. Positive values correspond to a delay in commutation position, and negative values correspond to an advance in commutation position. Note that because of the integrator reset after each commutation, any position error is discarded by the next commutation. Hence these errors are limited to the immediate 60 degree sector, and do not accumulate. All position error tests were performed with a constant DC link voltage of 24.04 V.

At 20 kHz operation (Figure 3.10), a speed range of 40.2 rpm to 4600 rpm was observed. At 10 kHz operation (Figure 3.11), a speed range of 21.9 rpm to 4520 rpm was observed. In both cases, the highest speed was limited by the voltage supply/machine. The notable difference between each frequency of operation is the reduced low speed error with reduced switching frequency. This is a result of transient ringing from the adjacent phases becoming more dominant in the

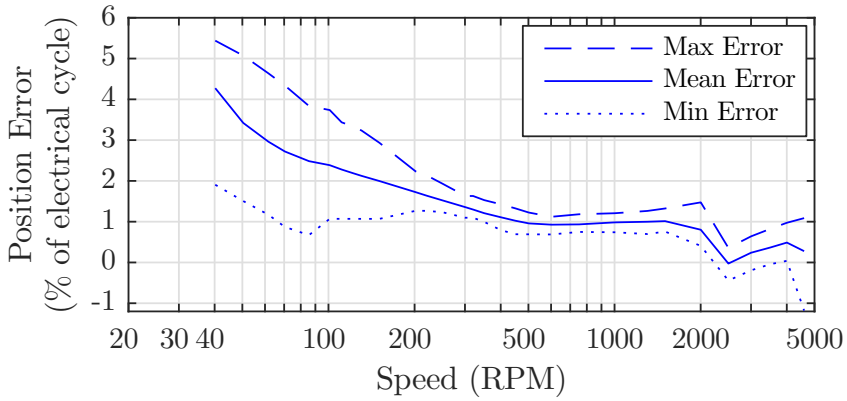

FIGURE 3.10: Position error versus speed for operation at 20 kHz PWM frequency.

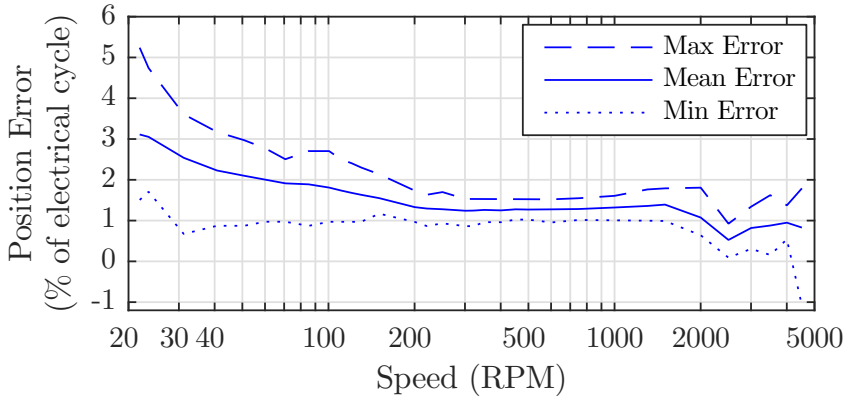

FIGURE 3.11: Position error versus speed for operation at 10 kHz PWM frequency.

floating terminal voltage waveform as the back-EMF decreases (see Figure 3.5). Reducing the switching frequency increases the time between the edge transient and the ADC sampling point, allowing the transient to decay to a lower amplitude before the floating terminal voltage is sampled. At higher speeds (>350 rpm), the reduced switching frequency increases the position error by approximately 0.2 % to 0.8 % of an electrical cycle. This may be a result of the lower sampling frequency and increased latency of commutation decisions. Position error could further be improved by using an ADC with resolution higher than the 11 bit ADC used. A variable frequency, speed dependent PWM frequency may also improve the position error.

Figure 3.12 shows the position error at rated speed and under variable load. The position error experiences little change with increasing load.

The position error result is compared to the experimental results of [45], where a complex sensorless algorithm with machine parameter dependent model achieved a worst-case commutation position error of 3.5 mechanical degrees at 20 rpm

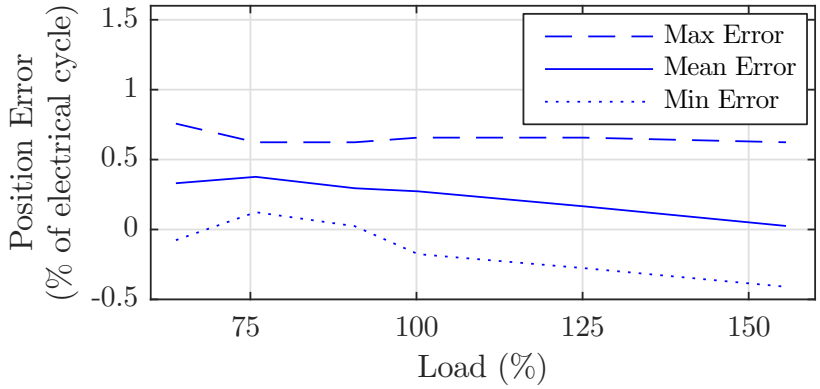

FIGURE 3.12: Position error versus load at when operated at rated speed.

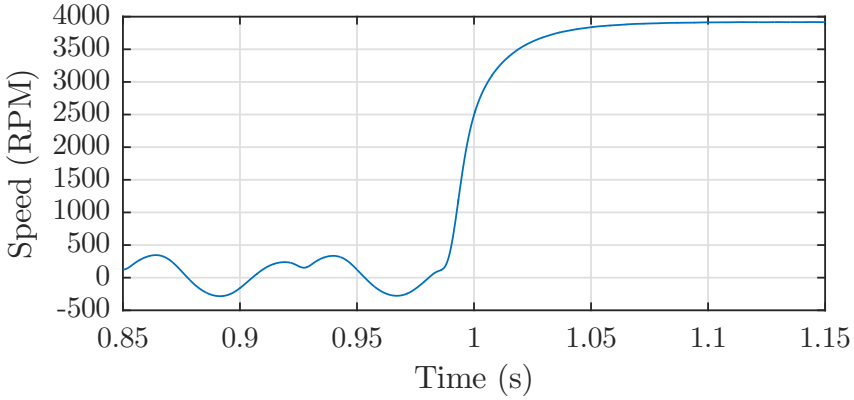

FIGURE 3.13: Speed step response, showing the transition from open loop ramp to closed loop sensorless operation.

down to 1.5 mechanical degrees at 900 rpm. The results in Figure 3.10 for nominal 20 kHz operation showed a maximum error less than 2.6 mechanical degrees between 400 rpm and 4600 rpm (between 16 % to 184 % of rated speed), and a maximum error less than 2.0 mechanical degrees between the 2500 rpm rated speed and 4600 rpm. At rated speed, the position error was less than 0.8 mechanical degrees. Although the error is generally larger than the error observed in [45], the implementation in this study is simpler and provides a wider speed range of 1.7 % to 184 % of rated speed.

3.5.5 Dynamic Performance

Figures 3.13 and 3.14 show the dynamic performance of the proposed sensorless method. The open loop ramp starts at 0.069 s, and the transition to sensorless operation occurs at 0.988 s. The machine accelerates to its steady state speed of 3911 rpm within 108 ms, reaching 90 % of the steady state speed within 32

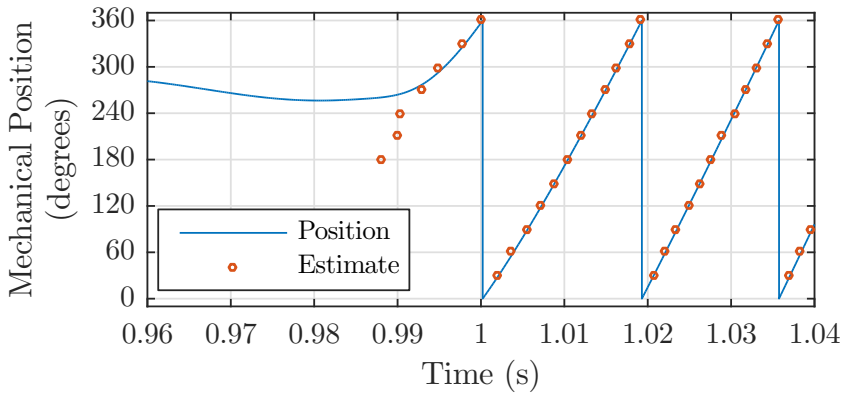

FIGURE 3.14: Speed step response, showing mechanical position and estimated position.

ms. Note that this is the maximum achievable acceleration for this machine. The position estimate starts to track the true position within one electrical cycle. The steady state speed of 3911 rpm contained a 3.5 rpm peak to peak ripple. No speed control was used. During the test, peak current reached 40 A, representing transient operation at 640 % rated power.

3.6 Conclusion

The method proposed and demonstrated in this paper uses only terminal voltage measurements to estimate the flux linkage increment in six separate sectors of an electrical cycle. This is used to determine the rotor position while avoiding the accumulated position error that is a characteristic of flux linkage based techniques. The novel measurement and back-EMF reconstruction technique synchronised terminal voltage measurements to the pulse width modulation switching state, eliminating the need for phase delay inducing low pass filters. The back-EMF waveform for each sector was recovered in a way that permitted the entire duty cycle range to be utilised. This back-EMF reconstruction technique is critical in enabling the operation of the flux linkage integrator without low pass filters, which has not been achieved in previous studies. Auto-calibration of the analogue to digital converter reduces impact of integrator offset error. The theoretical explanation of the method has been given in detail and analytical solutions for the flux linkage threshold of both sinusoidal and trapezoidal permanent magnet machines is provided, avoiding trial and error tuning commonly utilised in the literature. The technique proposed in this study improved the speed range and minimum achievable speed significantly when compared to the previous terminal voltage/back-EMF sensing methods. A minimum speed of 19 rpm (0.63 Hz,

0.76 % rated speed) was observed at low DC link voltage. An overall speed range of 42 rpm to 4600 rpm (1.4 Hz to 153 Hz) was demonstrated, corresponding to 1.7 % to 184 % of rated speed. The worst position error observed was less than 2.6 mechanical degrees above 400 rpm (16 % rated speed), and less than 2.0 mechanical degrees between 2500 rpm and 4600 rpm. The method presented in this paper addresses the limitations of previous indirect position sensor methods, specifically poor position accuracy and inability to operate at low as well as at high speed. This widens the application areas while increasing reliability compared to direct position sensor based drives.

Chapter 4

Autonomously Obtaining System Efficiency Maps from Motor Drive Systems

Statement of Authorship

Title of Paper	Autonomously Obtaining System Efficiency Maps from Motor Drive Systems
Publication Status	Published
Publication Details	G. Haines, N. Ertugrul, and W. L. Soong, "Autonomously Obtaining System Efficiency Maps from Motor Drive Systems," submitted to the *IEEE International Conference on Industrial Technology (ICIT)*, 2019.

Principle Author

Author Name	Gabriel Haines
Contribution	Designed software, performed all testing and analysis, wrote manuscript and acted as corresponding author.
Overall Percentage	85 %
Signature	**Date** 6/11/19

Co-Author Contributions

By signing the Statement of Authorship, each author certifies that: i. the candidate's stated contribution to the publication is accurate (as detailed above); ii. permission is granted for the candidate in include the publication in the thesis; and iii. the sum of all co-author contributions is equal to 100% less the candidate's stated contribution.

Author Name	Nesimi Ertugrul
Contribution	Supervised development of work, guided testing and analysis, helped to review and edit the manuscript.
Signature	**Date** 6/11/19

Author Name	Wen L. Soong
Contribution	Guided testing and analysis, helped to evaluate the manuscript.
Signature	**Date** 7/11/19

Abstract

Efficiency is one of the most important properties of an electric motor. Motor performance and testing standards have evolved to better characterise the efficiency of a motor, but are typically limited to the motor itself and describe the efficiency at a single speed. Newer standards have been developed to cover the complete motor-drive system, including variable speed drive, but exclude the efficiency of the end application. Efficiency maps can describe efficiency over the full speed-torque operating area of a motor, but significant testing effort is required. This paper describes an autonomous motor testing system that can produce efficiency maps covering the complete power drive system, including the end application device. This system level data can provide a deeper understanding of component level interactions and aid in the efficiency optimisation of combined power drive system and end application.

4.1 Introduction

Efficiency is one of the most important performance characteristics for electric motors. Minimum efficiency performance standards (MEPS) are in place in countries that represent over 70% of the global electricity usage, and paired with harmonised standards, are driving improvements in energy efficiency [2]. This has encouraged the use of variable speed drives and newer motor technologies including permanent magnet (PM) and synchronous reluctance motors [5], [6].

Traditionally, motor performance standards have targeted asynchronous induction motors, with a focus on single speed operation at a single load point or several load points. IEEE 112 [65] and IEC 60034-2-1 [66] are two key standards for determining motor performance. Although IEEE 112 is focused on induction motor (IM) testing, IEC 60034-2-1 covers other motor types including permanent magnet synchronous machines (PMSM) and DC motors. More recently a trial standard IEEE 1812 [67] was released for the testing of PM motors, and builds on previous standards IEEE 112 for induction motors and IEEE 115 [68] for synchronous machines. The test procedures for these standards are summarised in Fig. 4.1. Despite their differences, these standards are generally limited to the performance of the motor only, excluding the performance of the variable speed drive (VSD) or inverter.

IEC 60034-2-3 [69] specifically addresses the efficiency and losses from using a variable speed drive, including harmonic losses. Newer standards like IEC 61800-9-2 [70] look at the efficiencies of the individual components that make up

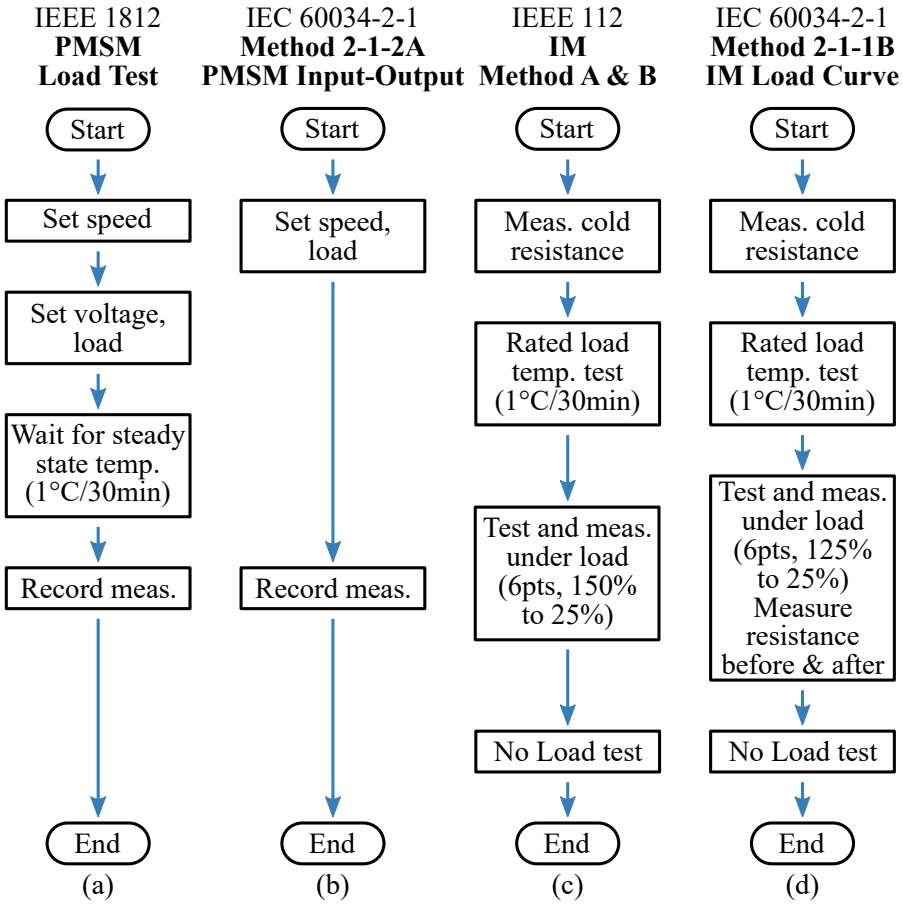

FIGURE 4.1: Summary of test procedures for (a) IEEE 1812, (b) IEC 60034-2-1 for PMSM, (c) IEEE 112, and (d) IEC 60034-2-1 for IM.

a complete power drive system (PDS), in addition to the efficiency of the complete system. Although newer test standards still determine the efficiency of the complete power drive system at one operating point, they do include a small number of additional operating points that can be used to determine the efficiency over the operating profile of the system.

Single operating point, or fixed speed efficiencies are insufficient for understanding a variable load system, and it is important for newer standards and testing to consider the efficiency and performance of the complete system [8], including the end application/load. The application of VSDs and understanding of the end application can help optimise the system and realise significant energy savings [14], [16]. However, a detailed understanding of the end application efficiencies and interaction with the power drive system efficiencies is not easy to obtain when components are tested in isolation. Further, measurement systems for combined motor and application testing may be difficult to adapt to other applications, considering the wide range and varied nature of many applications. Hence a new approach is needed to better understand integrated motor system

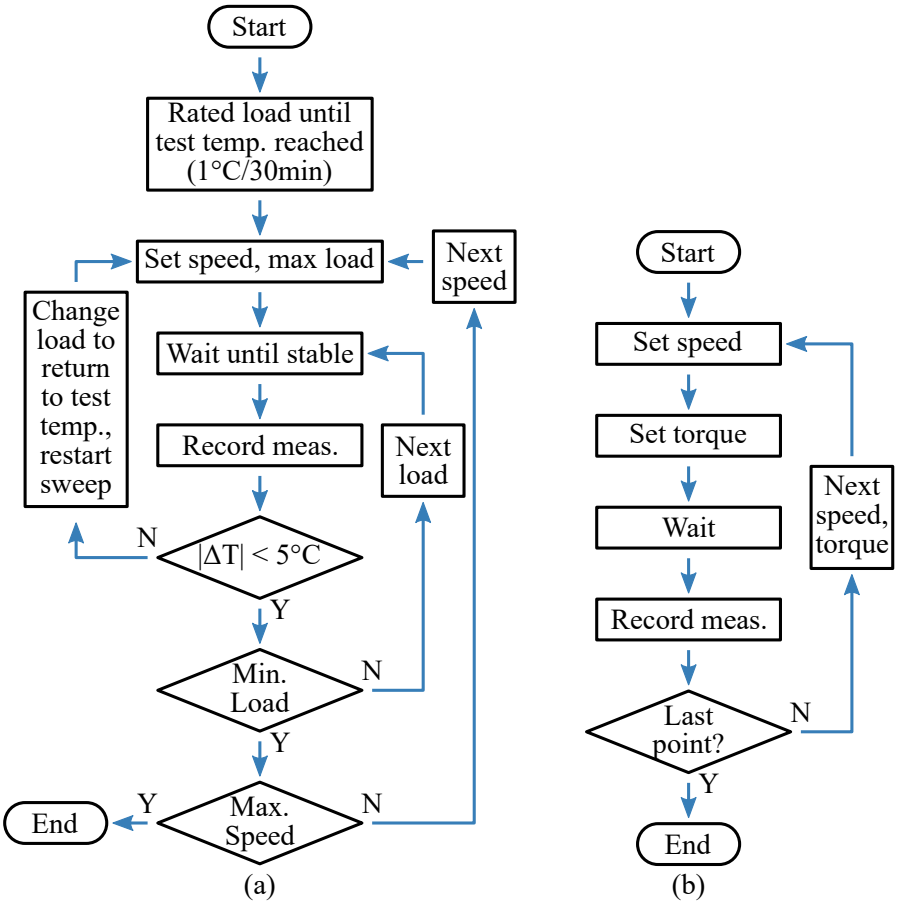

FIGURE 4.2: Summary of efficiency map measurement test procedures for (a) the manual method described by [12], and (b) the automatic method used in [71].

performance.

4.2 Efficiency Maps

Efficiency maps, or iso-efficiency contours, provide a good way to visualise and understand a motor's efficiency over the torque-speed operating area. They can aid in the selection and optimisation of a motor as part of a larger system, and for a given application. For example, efficiency maps have been used in the analysis of hybrid electric vehicles [11], [72]. They are used in the design and modelling of electric motors [9], [73], and can provide a deeper understanding of component losses over the entire operating area of a motor [10].

Experimental testing to obtain efficiencies maps was described in detail by [12], [13], [74]. [12] outlines a basic test procedure (see Fig. 4.2(a)) to obtain the iso-efficiency contours, and includes results for motor and inverter (VSD) efficiency. [13] compares the efficiency contours from different efficiency class

induction machines, and investigated the accuracy of a reduced number of measurement points. It was found that the original 40 × 40 (1600 point efficiency map) could be reduced to 16 torque values and 19 speed values (304 points) while maintaining an error of less than 0.5% compared to the 1600 point efficiency contour. [74] showed that the motor energy consumption could be predicted using the load trajectory and the measured/known iso-efficiency contour.

An automated system for measuring efficiency maps was described in [71], with results shown for a 5.3 kW internal permanent magnet machine. The system was built around a high speed data recorder and used a preset sequence (see Fig. 4.2(b)) of 20 torque values and 15 speed values (300 points). The sequence of test points progressed at a fixed rate (typically one measurement per 3 seconds), but did not adapt or respond to the state of the measured system. After the test, the data recorder's raw data file was processed offline to produce the efficiency maps.

A method of automatic synthetic load testing was described in [75], where an FPGA based motor controller applied seven constant acceleration and deceleration movements, using the motor's inertia as the load. This method can automatically test a motor within a few minutes, with the benefit of limited changes in motor temperature. However, the accuracy of the efficiency map is limited by the FPGA motor controller's uncertainty in the current, voltage and estimated rotor inertia.

Although automated test methods for collecting efficiency map data exists, they consist of simple test sequences, require offline processing, and focus only on the motor's performance. These methods do no consider the drive/inverter efficiency, the end application/load efficiency or the combined system efficiency. They also do not consider expanding or scaling the test system to meet the requirements of different combinations of motor system components and applications/loads.

4.3 Autonomous Test System

To better meet the needs of varied motor system and combined end application testing, an autonomous test system was developed. The primary goal is to obtain detailed efficiency maps from all components of a motor system, particularly when the motor system is a part of an integrated application device that includes the load. Because the types and configurations of devices under test may change, it is necessary for the test system to also be flexible and adapt to these changes.

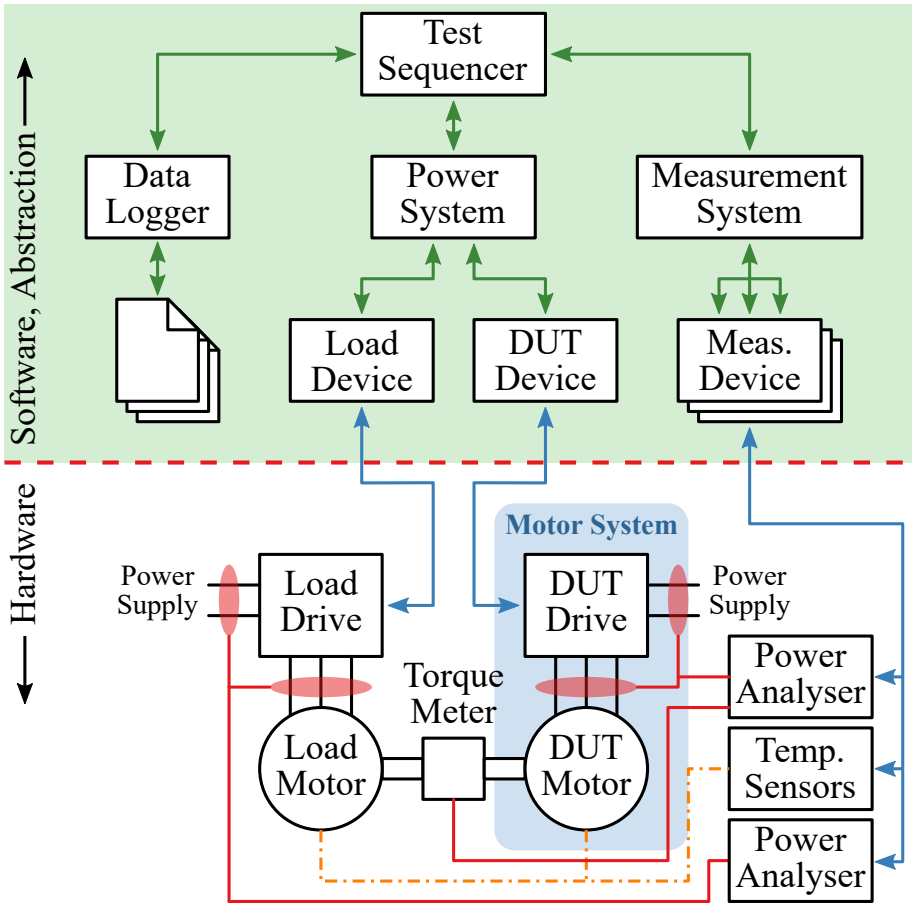

FIGURE 4.3: Software and hardware for motor system testing.

The core of the test system is the modular software, built using LabVIEW, that interfaces to and abstracts the hardware components of the test system. Every module is a plug-in that runs concurrently and communicates asynchronously with the other modules in the system. The software application is dynamically assembled at run time from a user selection of plug-in modules, specific to the needs of the test to be performed. This allows for only a portion of the software to change when the testing application changes, while reusing common and high-level test functionality. Fig. 4.3 shows a summary of the test system when applied to motor testing, and Fig. 4.4 shows the test system when applied to an integrated motor-pump device. Although testing of motor system applications is envisioned, the software could be extended to any power conversion system that can operate in a steady state. For example, testing could be extended to Solar PV panels, grid connected inverters, battery energy storage systems, hydraulic systems, fans and hybrid electric vehicle power trains.

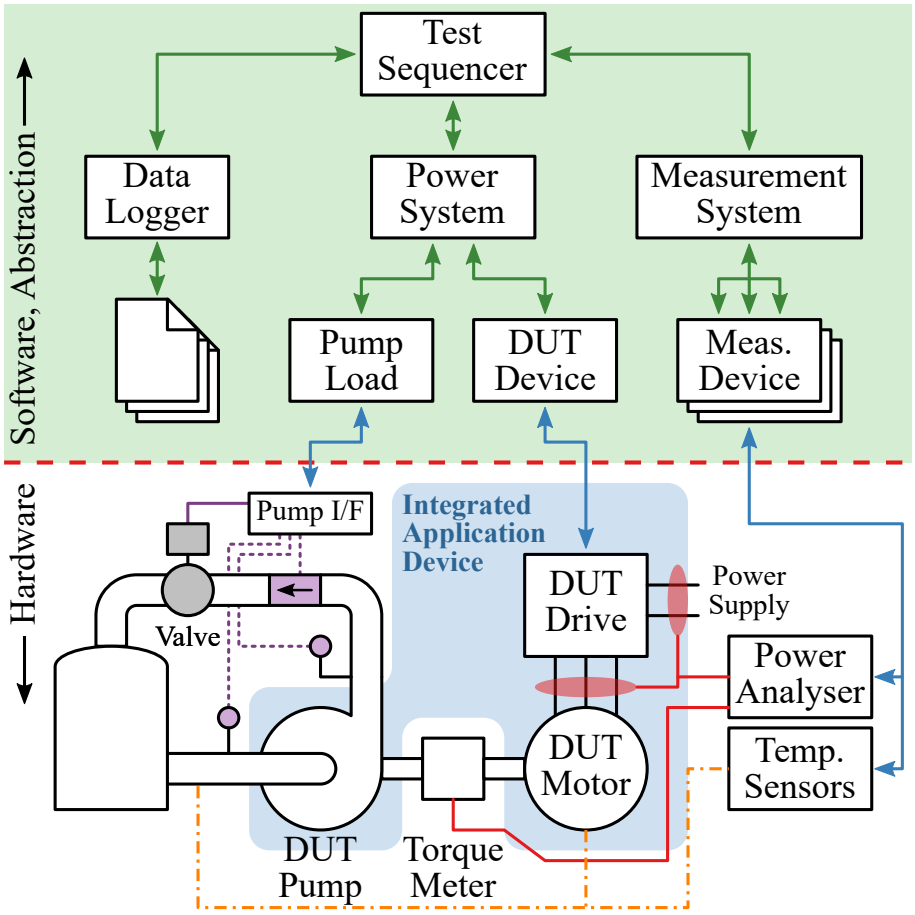

FIGURE 4.4: Software and hardware for testing an integrated pump application.

4.3.1 Autonomous Test Sequencer

The top level software module is the sequencer, and coordinates all other modules and devices in the system. The sequencer navigates a four quadrant per unit coordinate system with arbitrary units, representing the operation of the device under test. Fig. 4.5 summarises the navigation and decision making process. The sequencer may operate in manual (user controlled) or "auto" mode. In both cases, the desired coordinates in a given quadrant are broken into a smaller sequence of movements and carried out automatically. This includes limiting the movement size, resulting in small step changes that can help maintain stability of the underlying device control systems, particularly when operating at device limits.

In "auto" mode, the sequencer attempts to navigate a 2D grid of points in each quadrant, using either vertical or horizontal sweeps. After each movement, power devices respond after reaching a steady state (standard deviation is within a threshold) or if they have failed to reach the coordinate (control system saturated). This mechanism detects the edge of each quadrant's stable operating

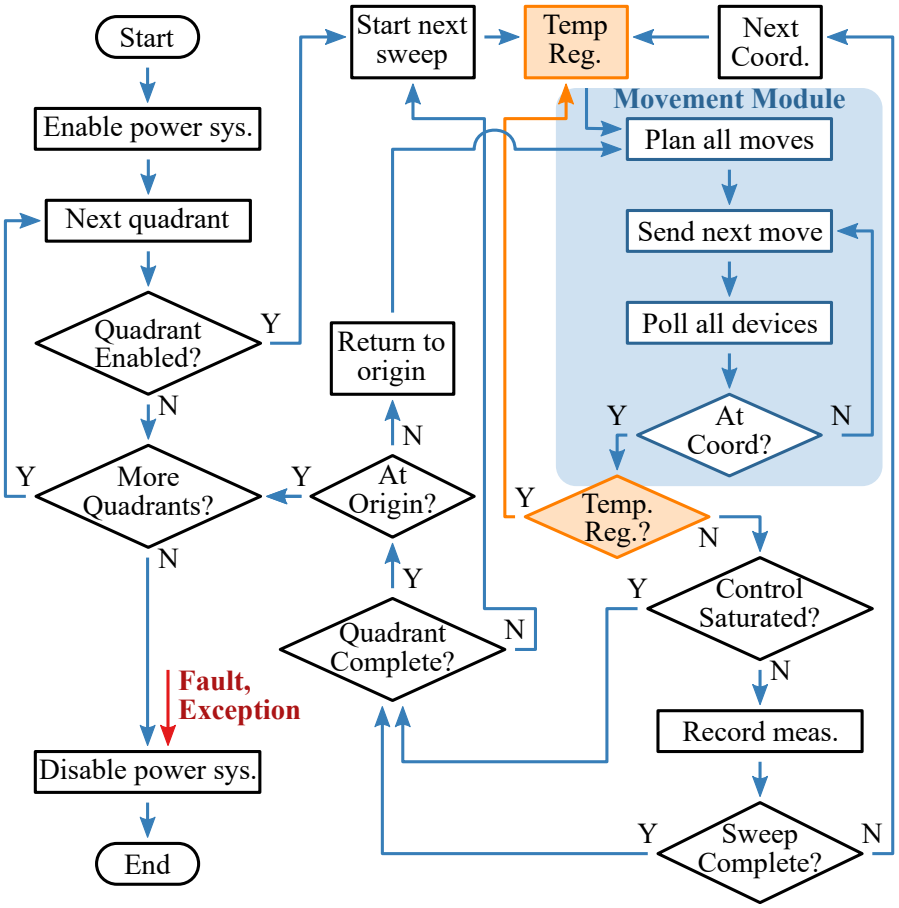

FIGURE 4.5: Simplified flowchart describing the autonomous navigation.

area. Although the shape of a motor's operating area is well known and typically controlled by a variable speed drive, other applications may not share this operating area, may not be stable over the entire area, or the area may be difficult to analytically define. Edge detection means the actual grid of test points is determined in real time in response to the system, removing unreachable or unstable operating areas, and helping to avoid control issues (e.g. integral windup when a control system is pushed past its controllable area).

The sequencer also includes a temperature regulation subsystem that performs an initial load temperature test (typically to a slope of 1°C/30min) and then maintains the load temperature. A simple hysteresis control scheme is used that interrupts testing when required to apply either a high or low power operating point to heat or cool the system respectively.

4.3.2 Power System and Devices

The power system represents an abstract four quadrant device under test, and maps this representation to the separate device under test and load devices. The individual devices are characterised by their power capability (power production and/or absorption) and their operating point capability (positive and/or negative). The combination of the two power devices results in a given quadrant capability for both devices, and determines the operating quadrants of the device under test and the sequencer. This aids in configuring the test system for devices with various limitations, and is also used to translate the sequencer's quadrant system into individual device operating point commands.

4.3.3 Measurement and Data logging Modules

The measurement system represents an arbitrary collection of measurement devices, each interfacing with a physical instrument (e.g. power analysers and temperature probes). The two power devices also behave as measurement devices, and return measurement data from the motor drives/control systems. All data is collected in a hierarchical structure of groups and channels, and sent to the data logger where it is written to file and interactively visualised. Efficiency is calculated using "Math" channels and can be viewed as the test runs. At the conclusion of the test, each 1D measurement channel is translated to a 2D grid and saved directly to a MATLAB file for further visualisation and analysis.

4.4 Test Results

Fig. 4.6 shows the efficiency maps measured using the dynamometer test configuration in Fig. 4.3. Two identical PM machines (3-phase, 0.156 V/Hz Back-EMF, rated at 13 $V_{pk\text{-}LN}$, 10 A_{pk}, 1000 rpm) were coupled to a torque meter and driven by two Texas Instruments DRV8301-69M-KIT inverters connected to a shared 51 V_{DC} supply. The inverters are a reference design for integrated motor-drive applications.

Fig. 4.7 summarises the sequencer's actual test points determined as it navigated through the first quadrant. Two sweeps are missing due to the steady state detector being too sensitive to a mechanical resonance at these speeds. Both machines were operated without field weakening, having a maximum speed vs load curve limited by the available supply voltage and motor back-EMF/flux. Both motors used position sensorless field oriented control, and testing was limited to above 200 rpm to ensure stable control at low speed. Fig. 4.8 shows the steady

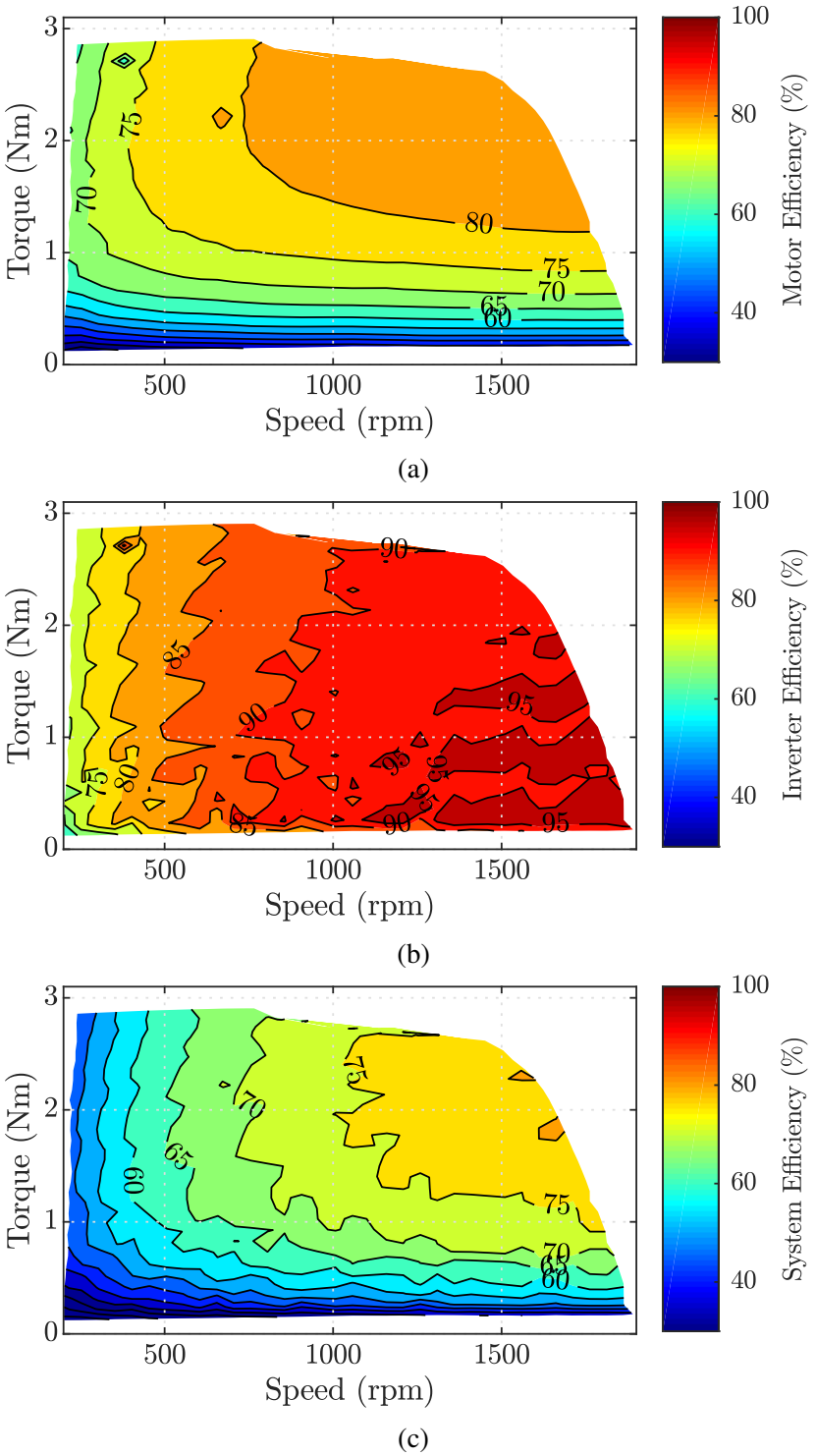

FIGURE 4.6: Motor efficiency maps in terms of torque and speed, for the (a) motor, (b) inverter, and (c) total system.

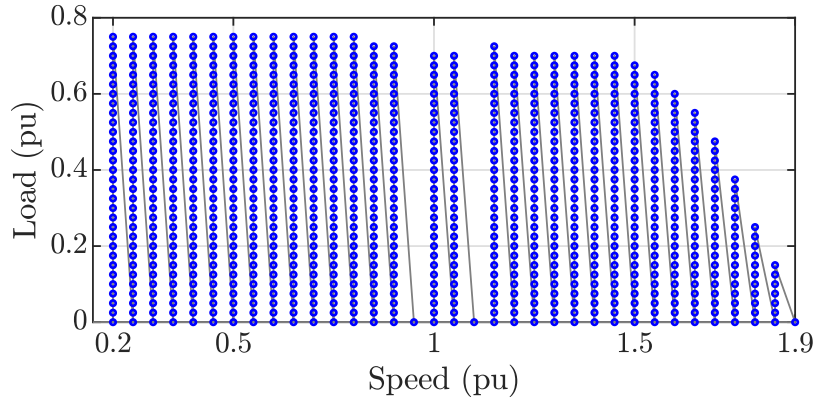

FIGURE 4.7: Actual sequencer measurement points and trajectory.

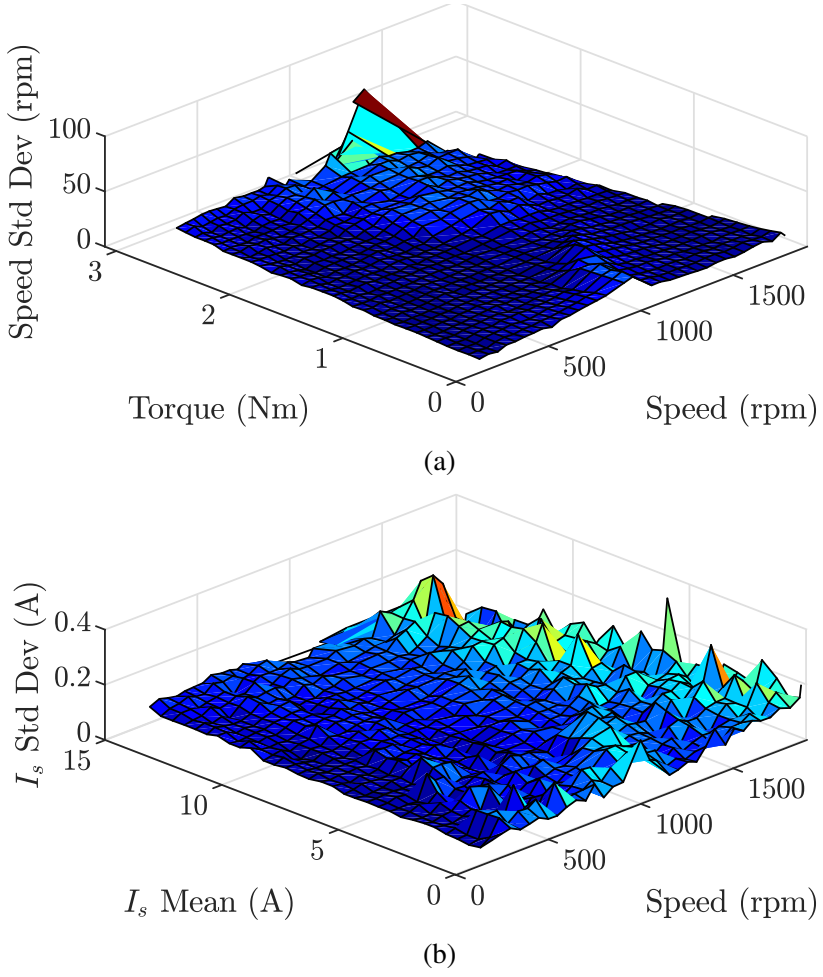

FIGURE 4.8: Steady state standard deviation for (a) the speed controlled device under test and (b) torque controlled load, used to determine the quadrant boundaries and edge of stable operation.

state detector standard deviation, using speed and current space vector feedback measurements reported by both inverters. Fig. 4.8(b) indicates less stable current control (i.e increasing oscillation) at high speeds. Fig. 4.8(a) shows less stable

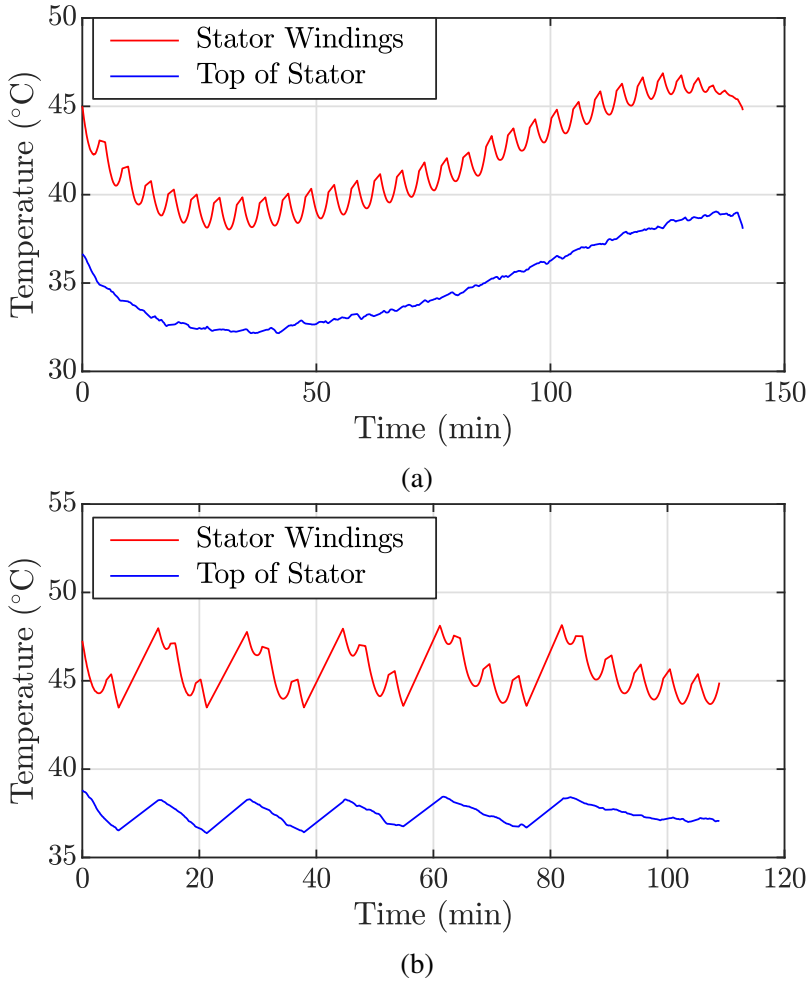

FIGURE 4.9: Temperature of the device under test with (a) no temperature regulation and (b) with temperature regulation for first half of the quadrant (to 1000 rpm).

speed control at high speed and load (higher power), but also shows the impact of a mechanical resonance at 1000 rpm with light loads. Standard deviation and mean values from both inverter control systems were used to determine the stable and achievable operating region of the combined system, with the overall test length governed by the control system responses. Of the planned 1085 points (35 speed $\times$ 31 load points), only 883 points were reached and measured by the sequencer over a period of 141 minutes.

Before testing, a rated load temperature test was performed with a load of 0.5 per unit (10 A) at 1.0 per unit speed (1000 rpm), and lasted 110 minutes. Fig. 4.9(a) shows the temperature of the 883 point efficiency map without any temperature regulation. The initial stator winding temperature was 47°C but dropped quickly during the first part of the autonomous test, falling outside the 5°C required by IEC 60034-2-1 [66] but within the 10°C range of IEEE 112 [65]. Fig. 4.9(b) shows the first half of the test but repeated with temperature regulation, resulting in a

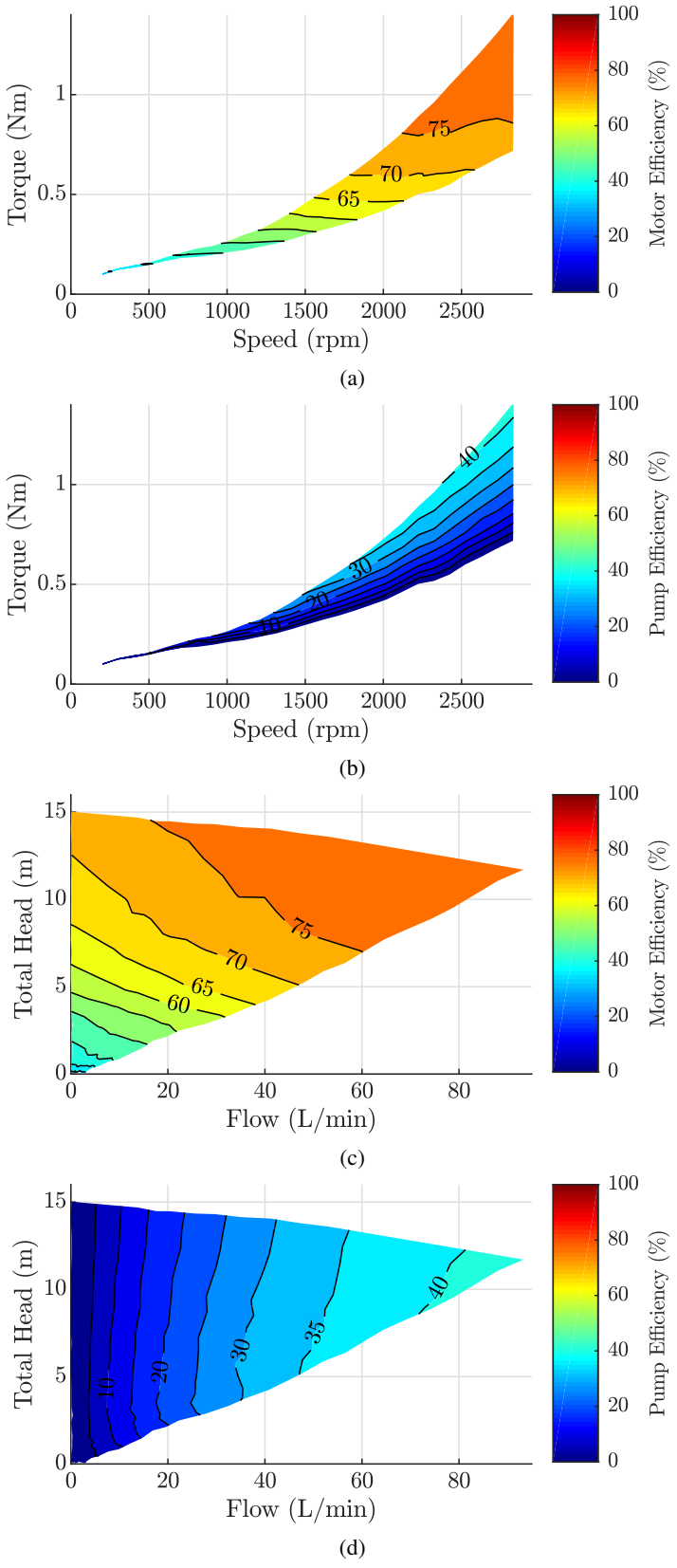

FIGURE 4.10: Combined motor and pump test showing (a) motor and (b) pump efficiency in terms of the motor operating point, and (c) motor and (d) pump efficiency in terms of the pump operating points.

longer test (489 points over 108 minutes) but more consistent temperature.

Fig. 4.10 contains motor and pump data, measured autonomously using the configuration shown in Fig. 4.4 and according to ISO 9906 grade 2 [32]. The first two plots in Fig. 4.10 show motor and pump efficiency in terms of motor quantities, whereas the second two plots show are in terms of pump quantities. Despite the test covering a broad region of the pump's operating area, only a narrow region of the motor's operating area is covered. Hence traditional "motor only" testing is useful for understanding the broader motor capabilities. End application testing, in this case with a pump, can show the optimal efficiency regions of each device in terms of the end application's operating area. This can aid the optimisation of the overall integrated device through better component matching. It also allows for energy minimisation when selecting an integrated device and/or control scheme to meet a given application. For example, Fig. 4.10(c) and (d) describe a motor and pump that are more suited to constant flow (variable pressure) applications for mid to high flow rate, or for variable flow applications at mid to high pressures. At low flow rate the pump has very low efficiency, and the motor's corresponding region below 1500 rpm and/or below 0.4 Nm contributes very little to the system efficiency. Hence in this example, selection and optimisation of the motor system should focus on the the >1500 rpm and >0.4 Nm region.

4.5 Conclusion

Efficiency of a motor system is the result of the variable speed drive, motor and load application efficiencies. Efficiency maps can characterise the efficiency of each component over the combined operating area, however comprehensive data is either unavailable or difficult to obtain.

An autonomous test system was presented that uses a modular, flexible structure to experimentally measure efficiency maps from all components of an integrated application device. The system can reduce measurement time, can carefully navigate the safe operating area of the device/application, and can be extended to other applications including solar PV, grid inverters, fans and hydraulic systems. Results were provided for both a motor only and combined motor-pump application. The data collected described component efficiencies with respect to the application and how they contribute to the total system efficiency. This data can then be applied to the optimisation of integrated motor application devices, and to better predict and minimise the energy usage of those devices.

Chapter 5

Motor System Sensorless State Estimation

5.1 Introduction

Through the use of detailed models and parameters, a position sensorless motor control system can be extended to provide general state estimation of the motor system. The motor system state includes quantities like speed, torque, power, and efficiency. Some industrial variable speed drives are capable of automatically identifying motor model parameters, and can provide torque and speed estimates using these parameters. However, these identification methods cannot fully model or understand the loss components and non-idealities of the motor. Consequently the accuracy of these estimates, particularly torque, is not ideal and can vary considerably over the operating area of the motor [23].

Existing sensorless estimation methods typically provide accurate estimates for only a narrow operating area of the motor/application. Existing methods also focus on only one component of the motor system (typically the motor output), and provide either no efficiency estimate or an estimate limited to only one component of the system.

This chapter presents a sensorless estimation method for integrated inverter-motor systems, with improved estimation accuracy over the entire operating area of the system. The estimation models were developed from comprehensive efficiency map testing of the complete inverter-motor system. Experimental efficiency map data provides a good basis for developing estimation methods because the data includes the motor operating point quantities in addition to power and efficiency measurements. Experimental results are presented for a general inverter-motor system.

Some of the content discussed in this chapter has been published in [76].

5.2 Overview of Proposed Method

The proposed method for state estimation considers a complete, integrated inverter-motor system. Estimation models are derived from data obtained experimentally from comprehensive efficiency map testing over the entire operating range of the motor. The advantage of this approach is that it captures all loss components and non-idealities in all components of the integrated motor system.

The proposed measurement, modelling and estimation approach was applied to the combination of a Texas Instruments DRV8301-69M-KIT inverter (with 51 V_{DC} supply) and a custom developed PM machine (3-phase, surface PM, 0.156 V/Hz Back-EMF, 13 $V_{pk\text{-}LN}$ @ 1000 rpm). The TI inverter is a reference design intended for integrated motor control applications, and includes a position sensorless field oriented control system.

The efficiency map and modelling data collected was used to produce the estimation models for the following parameters:

- Speed.
- Torque.
- Mechanical power out.
- AC Electrical power from the inverter to the motor.
- Motor efficiency.
- Inverter efficiency.
- System efficiency.

The following process was used to develop each estimation model:

1. Perform efficiency map testing to gather data over the operating range.
2. Using the test data, produce a model for each quantity to be estimated.
3. Enter each model's set of parameters into the inverter firmware.
4. Verify the performance of each model via additional efficiency map testing.

The estimator models are described in terms of measured current and speed estimated from the inverter's inbuilt the sensorless observer. Although speed is already present from the estimator, the testing showed the accuracy of the speed estimate varied over the broader speed-torque operating area of the motor. Hence

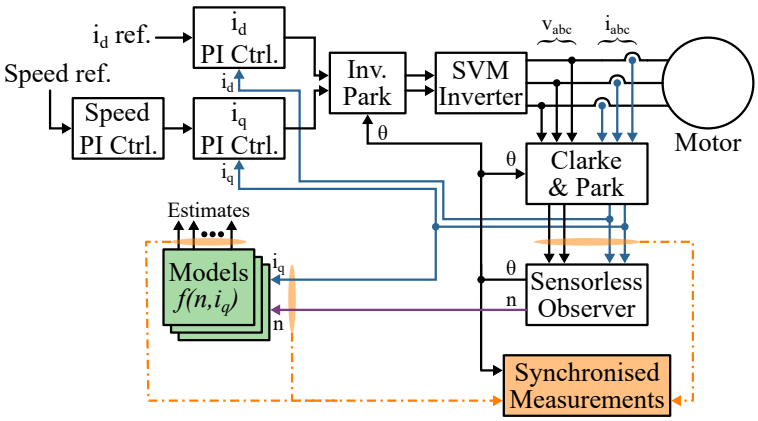

FIGURE 5.1: Control system block diagram with proposed estimation method. The proposed estimation method's components are shaded in green. The embedded measurement system is shaded in yellow.

speed was re-estimated using the original sensorless observer speed estimate and the measured current to provide a more accurate speed estimate over the motor systems operating area. Because both the original speed estimate and the current measurement are high bandwidth signals required to support dynamic motor control, the estimators also share the bandwidth and dynamics of the underlying speed estimate and current measurement.

5.2.1 Efficiency Map Testing

Efficiency maps, also known as iso-efficiency contours, provide a good way to visualise the efficiency of a motor (or other device) when operating over a two dimensional area. For a general motor application, the operating area is typically represented in terms of speed and torque. Other applications or loads connected to the motor may be represented in other operating area quantities.

To obtain a comprehensive efficiency map for a motor requires a large number of test points, on the order of 300 to 1600 individual operating points [12], [13], [74]. This scale of testing is generally time consuming and difficult when manual testing methods are used.

To obtain the efficiency map data for the entire motor system being studied, the fully automated test system described in Chapter 4 was used. This allowed for comprehensive efficiency map testing to be completed in less than half a day. Power analysers were used to measure the DC power into the inverter and AC power into the motor, a torque meter was used to measure mechanical power

out of the motor. Internal control system quantities inside the inverter were also recorded.

5.2.2 Inverter Measurements

To allow for modelling of the efficiency map data in terms of inverter control system quantities, a custom high bandwidth measurement software module and communication interface was added to the inverter's firmware (shown in Fig 5.1). These key elements differentiate the testing approach compared to standard efficiency map testing.

The measurement module was integrated with the field oriented control system and used the instantaneous control system rotor angle estimate to synchronise measurements to an integer number of mechanical cycles. Because the control system uses a fixed point numeric representation running at high speed (15 kHz), careful manipulation of numeric values was required to average a large number of samples over multiple mechanical cycles without causing a numeric overflow. The inverter's control system used a 32 bit integer fixed point representation with 24 fractional bits, having a range of -128 to 127.999 999 940, and a value of 1.0 internally represented as $2^{24} = 16777216$. For each control system value measured:

1. Individual values were first scaled down to a small enough value to avoid overflow.

2. Between 2 to 32768 values were then added to an accumulator (typically 4096).

3. Lastly, the accumulated value was scaled down to complete the averaging operation.

This process was applied point-by-point at the 15 kHz rate of the internal control system. The target number of samples used for each average was selectable during testing (typically set to 4096). Because measurements were mechanically synchronised, the measurement was ended slightly earlier on an integer number of mechanical cycles, resulting in the actual number of samples measured being lower than the target number.

Fig. 5.2 shows a set of inverter measurements taken with and without mechanical synchronisation being used. Without mechanical synchronisation (Fig. 5.2 (a), (c), (e), and (g)) the measured data does not fit into a smooth surface, instead showing considerable random noise. For the i_q signal, the source of this

noise is likely from torque ripple and periodic fluctuations in the current combined with the random start and stop times for each measurement point. This results in random bias being introduced into each averaged measurement. Mechanical synchronisation (Fig. 5.2 (b), (d), (f), and (h)) shows a considerable reduction in random noise, with the data now forming smooth continuous surfaces that can be more effectively modelled. Fig. 5.2 (b) shows the surface used for the new torque estimation model. Fig. 5.2 (f) confirms that the torque is proportional to i_q only and not i_d, which is expected for a surface PM machine.

5.2.3 Modelling and Estimation

The inverter's original speed estimate n and torque producing q-axis current measurement i_q were used as the two base variables for the estimation model. The inverter's fixed point control system represented these quantities in units of krpm (1.0 pu = 1000 rpm) and full-scale current (1.0 pu = 41.25 A). The combination of n and i_q form a 2D operating area for the motor system as seen by the inverter's control system. Each quantity to be estimated combined with the n and i_q 2D space forms a surface in a 3D space.

$$f(n, i_q) = p_{00} + p_{10}n + p_{01}i_q + p_{20}n^2 + p_{11}ni_q + p_{02}i_q^2 + p_{30}n^3 + p_{21}n^2i_q + p_{12}ni_q^2 + p_{03}i_q^3 \quad (5.1)$$

MATLAB's `cftool` was used to fit each quantity to be estimated to a polynomial surface of the form shown in Eq. (5.1). This approach is similar to the efficiency map loss modelling approach discussed in [10]. The orders of the speed and q-axis current terms were independently varied from one to three, resulting in nine possible models. The best fit was selected based on the lowest sum of squares due to error (SSE) and residual mean squared error (RMSE), where SSE represents the total deviation between the data points and the surface and RMSE is the fit standard error [77].

The polynomial orders were also carefully selected to minimise the size of coefficients to avoid numeric overflow. The inverter's native fixed point per unit values of speed n and q-axis current i_q had a typical upper limit of < 3.0 and < 1.0 respectively. Because these per unit values are typically close to or less than 1.0, the dynamic range of their higher order intermediate terms in the polynomial model are generally limited. This helps to avoid numeric overflow in intermediate terms, but care was still needed to ensure the corresponding coefficients had

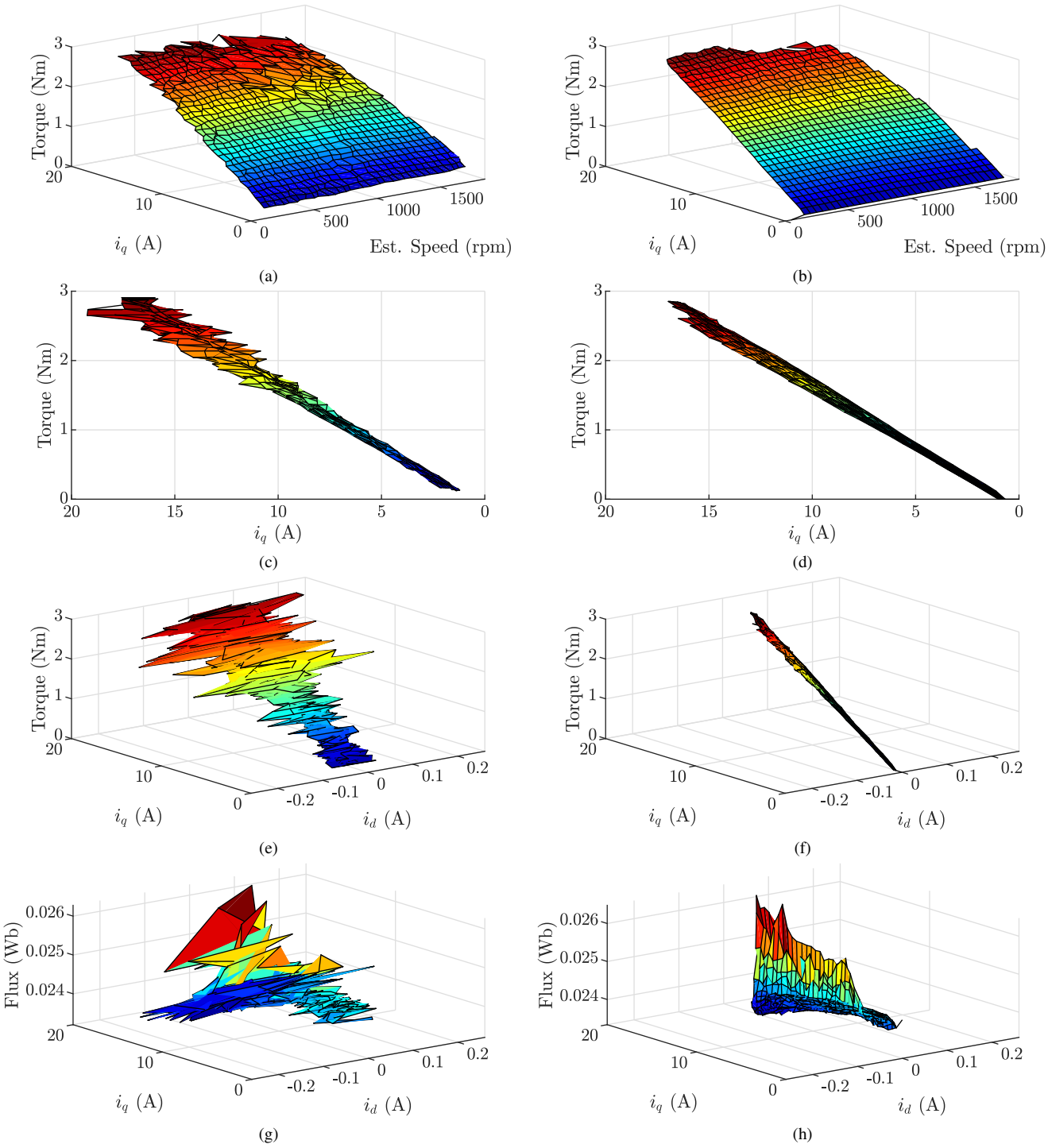

FIGURE 5.2: Inverter measurements (a), (c), (e), and (g) without mechanical synchronisation, and (b), (d), (f), and (h) with mechanical synchronisation. (a) and (b) Torque vs i_q and est. speed surfaces. (c) and (d) The same torque surfaces viewed in the Torque-i_q plane. (e) and (f) Torque vs i_d and i_q surfaces. (f) and (g) Estimated flux vs i_d and i_q surfaces.

values small enough to prevent overflow.

The shape of the efficiency surfaces was poorly modelled by polynomials of the form shown in Eq. (5.1), but could be modelled as a rational polynomial function with numerator and denominator of the form given in Eq. (5.1). In practice, this was achieved by dividing the corresponding output and input power estimates to produce each efficiency estimate. Division is typically a slow and resource intensive operation for a real time embedded system, often implemented using a slow software emulation in lieu of dedicated hardware in the processor. The Texas Instruments DSP used was a low cost device with no hardware integer division support, but instead provided a look up table based fixed point division approximation method. This provided a faster division routine that enabled efficiency estimates to be calculated in real time at a fast update rate (typically $2 \sim 5$ kHz) at the small expense of some numeric precision.

The resulting implementation is shown in Fig. 5.1. In contrast with analytical methods described in literature (e.g. [25]–[29]), the proposed method uses an experimental and empirical modelling approach. This method is comparatively simpler because it does not rely on finite element (FE) modelling, loss modelling or other detailed characterisation of the motor system. The method also captures all the component interactions, non-idealities and losses through the testing of the integrated system. Analytical or simulation based approaches require models of the system (of varying complexity) that may include assumptions or simplifications. There is no single tool that can provide a detailed simulation of the operation and interaction between the control software, power electronic hardware, electromagnetic models and mechanical models of the motor. Instead such simulations are typically run independently on a per component basis, that typically excludes detailed modelling of interactions between each component.

5.3 Test Considerations

The data used for modelling was collected through autonomous efficiency map testing, using the system described in Chapter 4. The hardware portion of the test system is shown in Fig. 5.3, and a screenshot of the autonomous test software is shown in Fig. 5.4.

5.3.1 Power Measurements

Power measurements were collected using two Newtons 4th Law (N4L) precision power analysers (PPA5530). For each motor and inverter, one power analyser was used to measure both AC power between the motor and inverter, and DC

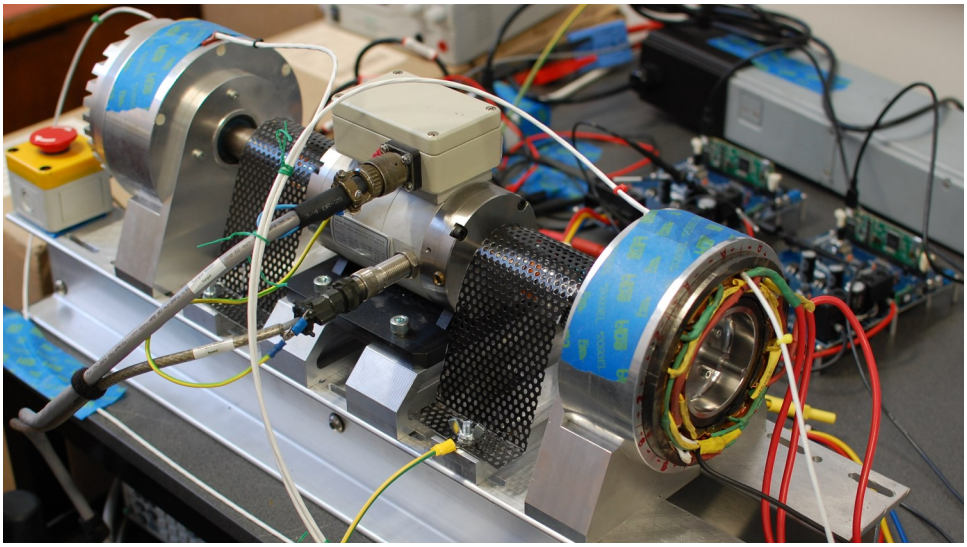

FIGURE 5.3: Dynamometer test system hardware. The rightmost machine is the device under test, the leftmost machine is an identical machine used as the load. Both machines are coupled to a torque meter in the middle. Both machines are driven by identical inverters (shown in the background).

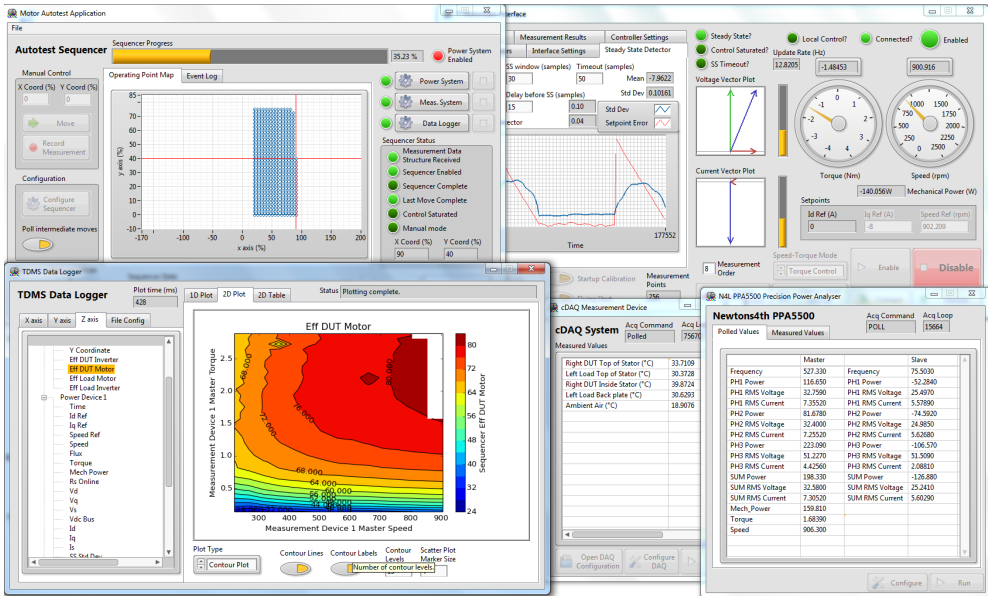

FIGURE 5.4: Autonomous test software graphical user interface.

power between the inverter and DC supply/bus. AC power was measured using two channels of the power analyser configured in a three wire two watt-meter method, and DC power was measured by an independent third channel.

Both power analysers were run as a synchronised master and slave. The master power analyser used a frequency reference set to the speed reported by the torque meter. This allowed for the power measurements to by synchronised to an integer number of mechanical cycles. Because the machines tested had 5 pole

pairs (electrical frequency 5 times higher than mechanical frequency) the resulting fundamental measurements and THD measurements were incorrect. These measurements were not required and had no impact on the other data used for modelling.

Both power analysers were remotely configured and controlled by the test software, via an Ethernet connection. This allowed for fully automated control and collection of large volumes of measurement data.

5.3.2 Torque Measurements

Torque was measured using a Himmelstein MCRT 79001V(2-2)NFZ non-contact analogue torque meter. Both the pulsed speed and analogue torque (1 Hz filtered) signals were connected to and measured by the master PPA5530 power analyser. This allowed for mechanical synchronisation of electrical measurements taken by the power analyser. The power analyser's Ethernet communication interface was also used to collect the torque and speed measurement data in addition to electrical power measurement data.

Before testing, the dynamic torque offset was measured by decoupling the load machine and running the test machine and torque meter at a series of speeds. Ideally, there should be only a small offset that remains constant as speed changes. Fig. 5.5 shows three different torque offset measurements: *Day 1 Cold* represents the torque offset before testing when all components were cold, *Day 1 Hot* shows the torque offset after testing when all components were hot, and *Day 2 Cold* shows the before testing torque offset measured two weeks later.

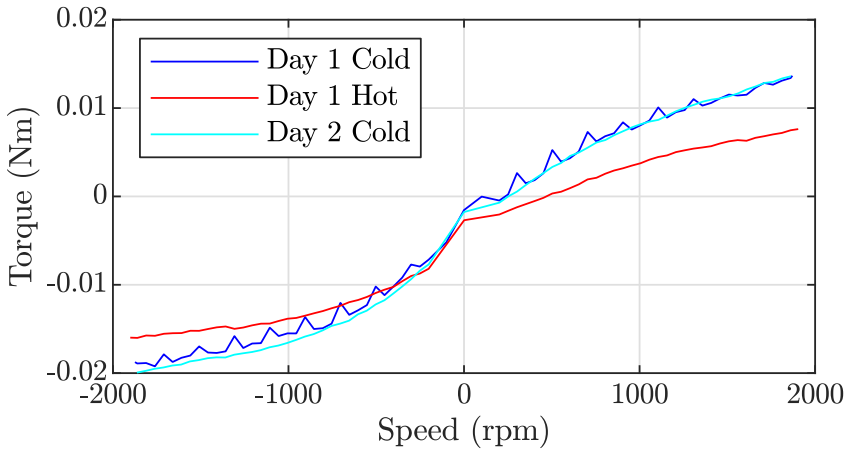

FIGURE 5.5: Torque meter dynamic offset.

The torque offset was consistent in shape with only minor changes in magnitude over temperature. For a speed of 1800 rpm, the torque offset was below

0.014 Nm, representing an error of 2.6 W. The torque meter full scale range was 4.52 Nm with a stated combined error of ±0.15 %, or ±0.0068 Nm. Fig. 5.5 shows that the measured offset itself represented an error of 0.3 % (of full scale) at 1800 rpm, however the offset variation between the cold and hot temperatures was within the combined error of the torque meter.

The torque offset curve was used to correct the torque measurements in the efficiency map tests. This was done by interpolating the torque offset based on measured speed by using a 4^{th} polynomial curve fitted to the first quadrant (positive speed, positive torque region).

5.3.3 Steady State Temperature Detection

Temperature was measured by a set of platinum 100 Ω resistance temperature detector (RTD) sensors connected to a National Instruments CompactDAQ system with NI 9216 RTD module. The following temperatures were measured and recorded:

- DUT machine top of stator external temperature.
- DUT machine winding internal temperature.
- Load machine top of stator external temperature.
- Load machine winding internal temperature.
- Ambient air temperature.

The DUT internal winding temperature was used to regulate the testing temperature, as described in Section 4.3.1 of Chapter 4. The first stage of the temperature controlled test was the detection of the steady state temperature. The autonomous test software performed this function by monitoring the machine temperature at rated load and continuously fitting the temperature data to an exponential curve of the form shown in Eq. (5.2) to determine the instantaneous temperature slope. The curve fitting used a least squares fit with exponentially weighted data to give more weight to the newest measurements.

$$T(t) = a \cdot e^{bt} + c \tag{5.2}$$

Temperature was sampled approximately once per second, and a moving window of temperature data was used for the curve fit. A minimum of 120 points (approximately 2 minutes of data) was required before curve fitting started, and the moving window was limited to a maximum of 60 minutes of data. The b term

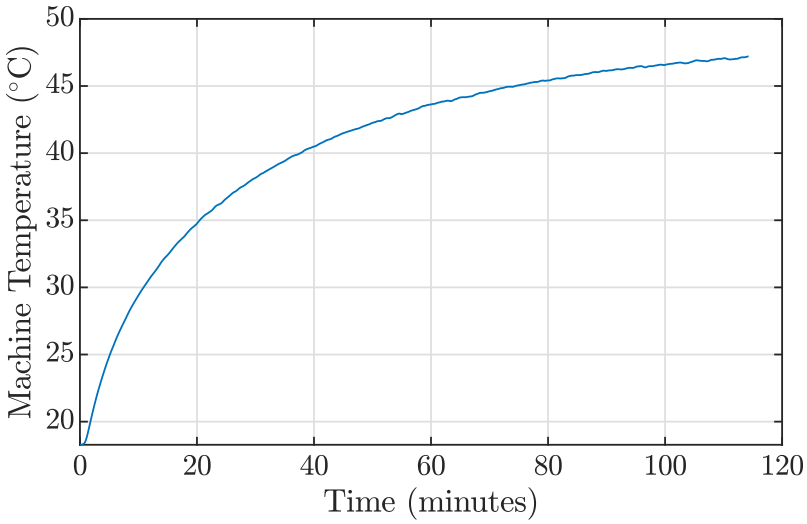

FIGURE 5.6: Machine temperature during the steady state temperature detection test, measured at the stator windings.

in Eq. (5.2) was limited to negative values to ensure curve fitting resulted in a convergent function. The c term was also limited to positive values to guide the curve fitting to a more physically realistic function.

$$\frac{dT(t)}{dt} = ab \cdot e^{bt} \tag{5.3}$$

The instantaneous slope was calculated from the fitted coefficients and Eq. (5.3). Poor curve fits from a small number of samples sometimes produced a constant function with a slope of zero. Such a slope would always be within the desired slope threshold, causing the steady state detection to end prematurely with a grossly incorrect steady state temperature measurement. An effective solution was to only consider slopes with a magnitude greater than 0.01°C/30min but less than the target slope threshold. Once the target temperature slope was reached, the exponential equation was then used to extrapolate the long term steady state temperature (at $t = \infty$). This is simply found from the constant term c in Eq. (5.2).

The temperature of the motor being tested is considered to be at a steady state once the rate of change has dropped to 1°C/30min (per IEEE Std. 112 [65], IEC 60034-2-1 [66] and IEEE Std. 1812 [67]). For the machines and test frame being used, the 1°C/30min steady state condition was typically reached in just under 2 hours. Because the temperature data is being continuously fitted to a curve, it is possible to predict the steady state temperature well before the 1°C/30min steady state condition is reached, reducing the time of this test.

Fig. 5.6 shows the internal stator winding temperature during the steady state

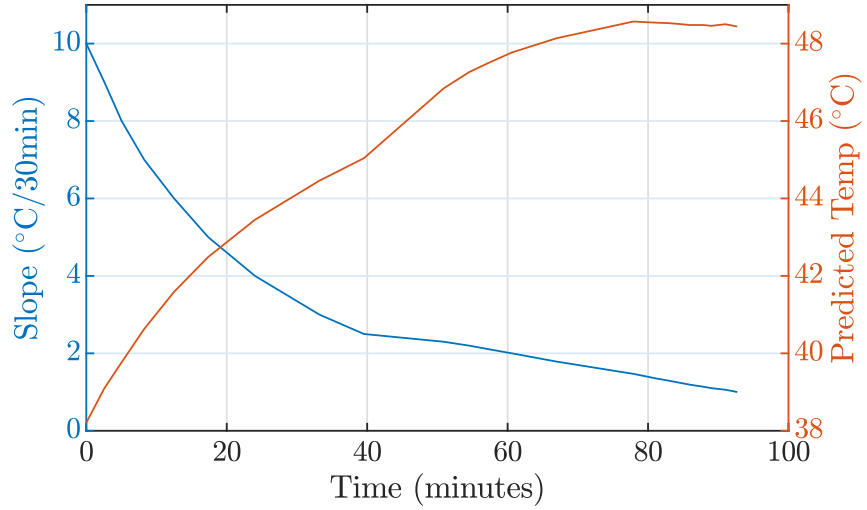

FIGURE 5.7: Steady state temperature detection slope and predicted temperature versus time.

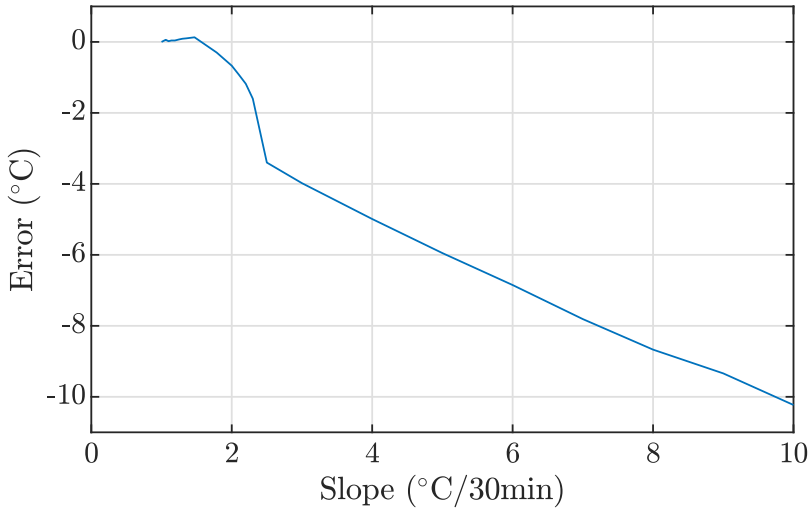

FIGURE 5.8: Steady state temperature detection error versus slope.

temperature detection test. Fig. 5.7 shows the instantaneous slope and the predicted steady state temperature over the last 1.5 hours of the test. At the end of the test (at 1°C/30min slope) the steady state temperature was taken from the last value of the predicted temperature curve. Fig. 5.8 shows the relationship between the slope of the temperature curve and the error in predicted temperature, where the error is expressed as the difference between the predicted temperature and the steady state temperature. There is an approximately linear relationship between slope and error for slopes down to 2.5°C. For slopes lower than this value, the error relationship is no longer linear. This may be an artefact of the continuous curve fitting system and exponential weighting that gives the strongest weight

to the newest data. The curve fitting may also be influenced by the thermal response of the physical system (made mostly from aluminium with large surface area, moderate thermal mass and good thermal conductivity).

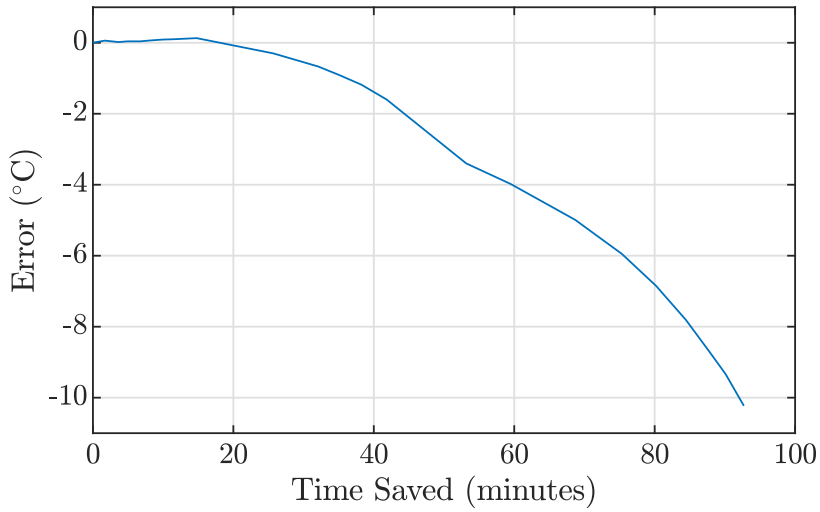

FIGURE 5.9: Steady state temperature detection error versus time saved.

In Fig. 5.9 the temperature data has been rearranged to show the error between the predicted temperature and the steady state temperature as a function of time before the end of the test. In this way, Fig. 5.9 shows the testing time that could be saved at the expense of accuracy in the steady temperature. For the test data shown in Fig. 5.7 and 5.9, using a slope threshold of 1.5°C/30min would save 15 minutes but introduce a 0.13°C error. Using a slope threshold of 1.8°C/30min would save 25 minutes but introduce a 0.30°C error. These results confirm the IEEE and IEC standard's choice of 1.0°C/30min slope as a suitable indicator of thermal equilibrium.

TABLE 5.1: Steady state temperature test results from four tests over two days. All tests finished once the machine under test reached the 1.0°C/30min threshold.

Test	**Steady State Temperature** (°C)	**Ambient Temperature** (°C)	**Temperature Rise** (°C)
Test 1 (Day 1)	48.44	19.06	29.38
Test 2 (Day 1)	47.61	19.21	28.40
Test 3 (Day 2)	51.25	22.80	28.45
Test 4 (Day 2)	51.53	23.07	28.46

For comparison, the steady state temperature test was repeated several times over two days, with data shown in Table 5.1. *Test 1* is the same test shown in

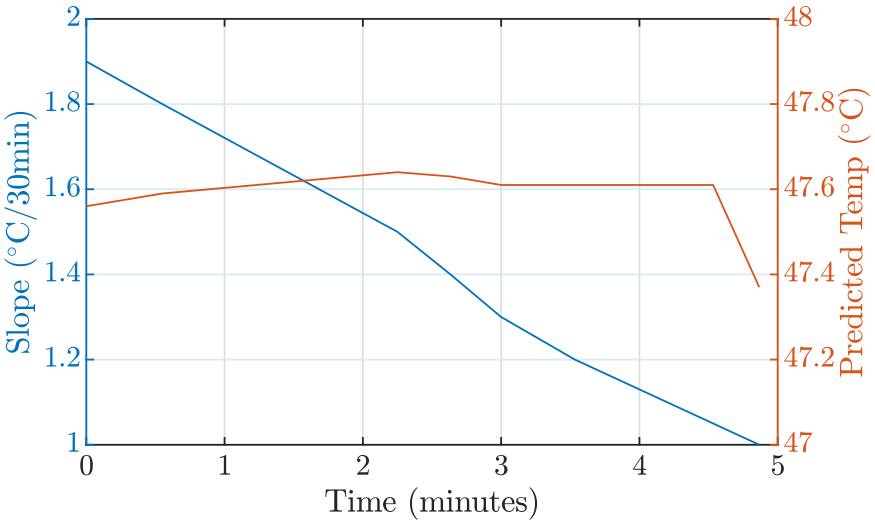

FIGURE 5.10: Steady state temperature detection slope and predicted temperature versus time when the machine was preheated for an extended period of time. Only the end of test is shown, where the temperature slope has dropped below 2°C/30min.

Fig. 5.7, 5.8, and 5.9. The other three tests where similar, but preheated the dynamometer system before the test by running the system for an extended period of time at a much higher load. This caused the system to warm up faster and allowed for heat to soak into the system before the test.

Fig. 5.7 shows the data for *Test 2*, where the preheating of the machine allowed for the steady state temperature test to be completed in 15 minutes. *Test 3* started with a cold machine that was preheated above 48°C, after which the steady state temperature test ran for just under 50 minutes. After *Test 3*, the dynamometer was left to run for two hours then *Test 4* was performed immediately after, completing the steady state temperature test in approximately 10 minutes.

When adjusting for the ambient temperature, all tests showed a similar temperature rise above ambient when run at rated load. *Test 1* is the only test run without preheating, and showed an approximate 1°C difference to the other three tests. *Tests 1 to 3* were consistent to within 0.06°C, and all involved initial preheating. *Test 3* was for a cold machine with initial preheating of approximately 40 minutes before the 50 minute steady state temperature test. This represented a mild time saving of about 25 minutes compared to *Test 1* (also performed on a cold machine). This time saving combined with better steady state consistency suggests that the better approach to steady state temperature detection is found through high power preheating followed by the continuous curve fitting detection method used in the autonomous test software.

5.4 Estimator Modelling

The inverter and motor were tested in a back-to-back dynamometer configuration, shown in Fig. 5.3. The machine under test was operated in the first quadrant (as a motor), and the identical dynamo/load machine operated as a generator to absorb mechanical power and return it to the DC bus. Both inverters were connected to the same DC bus, resulting in energy circulating around the system.

The dynamometer was controlled by the autonomous test software, and was navigated through the first quadrant to collect efficiency map data at 933 operating points, as shown in Fig. 5.11 (a). 899 of these operating points were measured under load in one test. The top and right edges of the operating area were limited by a combination of the maximum load current, maximum inverter voltage and back-EMF of the machines. The top and right edges of the operating area were found dynamically at run time. The remaining 34 points were taken from a torque offset test, where the dynamo/load machine was uncoupled. The inclusion of the torque offset test data was done to capture operation of the motor system with zero mechanical load (i.e. capturing DC power consumption and total motor loss over a range of speeds).

The inverter's original speed estimate n and torque producing q-axis current measurement i_q were used as the two base variables for all modelling. The speed estimate n was produced by the Texas Instruments inverter's proprietary position sensorless observer using auto-identified motor parameters. Speed and current input variables were represented in fixed point quantities with full scale values (1.0) of 1000 rpm and 41.25 A respectively.

Because the inverter's internal control system used fixed point full scale values, the estimator quantities also needed to be expressed in fixed point per unit quantities. This was done by setting a full scale power of 1.0 pu = 20 W, giving a maximum range of 127.99999994 pu = 2559.99999880 W that was well above the maximum power of the inverter and motor system. Because the maximum torque of the motor system was below 5 Nm, torque was not converted to a per unit value but instead left in units of Nm.

Modelling of the estimator equations was performed using MATLAB's `cftool`. Each quantity to be modelled was converted to its per unit quantity, then a polynomial surface was fitted using the speed estimate n and torque producing q-axis current measurement i_q as the independent variables. The selected best fit for each model is shown below in Table 5.2. Table 5.3 summarises the goodness of fit for each model, in terms of the sum of squares due to error (SSE) and residual mean squared error (RMSE).

TABLE 5.2: Estimator model coefficients for general motor system operation.

Estimated Quantity	Polynomial coefficient for each term.									
	p_{00}	$p_{10}n$	$p_{01}i_q$	$p_{20}n^2$	$p_{11}ni_q$	$p_{02}i_q^2$	$p_{30}n^3$	$p_{21}n^2i_q$	$p_{12}ni_q^2$	$p_{03}i_q^3$
Speed	0	0.9947	0.09222	0.008245	-0.06839	0	0	0	0	0
Torque	0	-0.2301	6.558	0.088	0.9754	4.701	0	-0.5204	-1.208	-7.909
DC Power	0.3	0.4939	7.601	0	34.7	13.38	0	0	0	0
AC Power	0	0.503	5.047	0	35.17	6.152	0	0	0	0
Mech. Power	0	-0.5366	2.073	-0.1758	36.09	0	0	0	0	0

TABLE 5.3: Motor system model's goodness of fit.

Estimated Quantity	SSE	R^2	RMSE
Speed	0.00098349	0.99999	0.0010289
Torque	0.016074	0.99997	0.0041686
DC Power	0.87139	0.99997	0.030643
AC Power	0.78812	0.99997	0.029126
Mech. Power	0.60294	0.99997	0.025476

Fig. 5.11 (b) through (f) shows the fitted surfaces for each model described in Table 5.2. Each plot shows the individual measurement data points being used to fit each polynomial surface.

The **speed** estimator model (Fig. 5.11 (b)) provides a small load dependent correction to the inverter's inbuilt speed estimator. Because accurate rotor position estimation is required to continuously commutate the PM synchronous machine, it follows that an inverter should naturally have good frequency and hence speed estimation. The Texas Instruments speed estimator is a proprietary black box system, and the method used for speed estimation is unclear. Testing showed that physically reducing the machine back-EMF by misaligning the permanent magnet rotor and stator by a small amount caused the speed estimator to produce a lower value, but still allowed the sensorless motor control to operate. This would suggest that the black-box speed estimator does not rely solely on estimated rotor position. Although the original speed estimate was good (see Fig. 5.15 (a) and (b)), it could be further improved by the proposed estimator model.

The **Torque** estimator model (Fig. 5.11 (c)) primarily maps q-axis current i_q to torque applied by the motor to a load. Because a surface PM machine was used, it is expected that torque will have strong i_q dependence. Table 5.2 shows that the largest coefficients are p_{01} (i_q term), p_{02} (i_q^2 term), and p_{03} (i_q^3 term). However, these are not the only terms present. Because the measured torque already includes all machine losses (e.g. bearing losses, windage, rotor losses, harmonic losses), the proposed model naturally captures these. Hence additional terms in the estimator model are expected to capture these loss components.

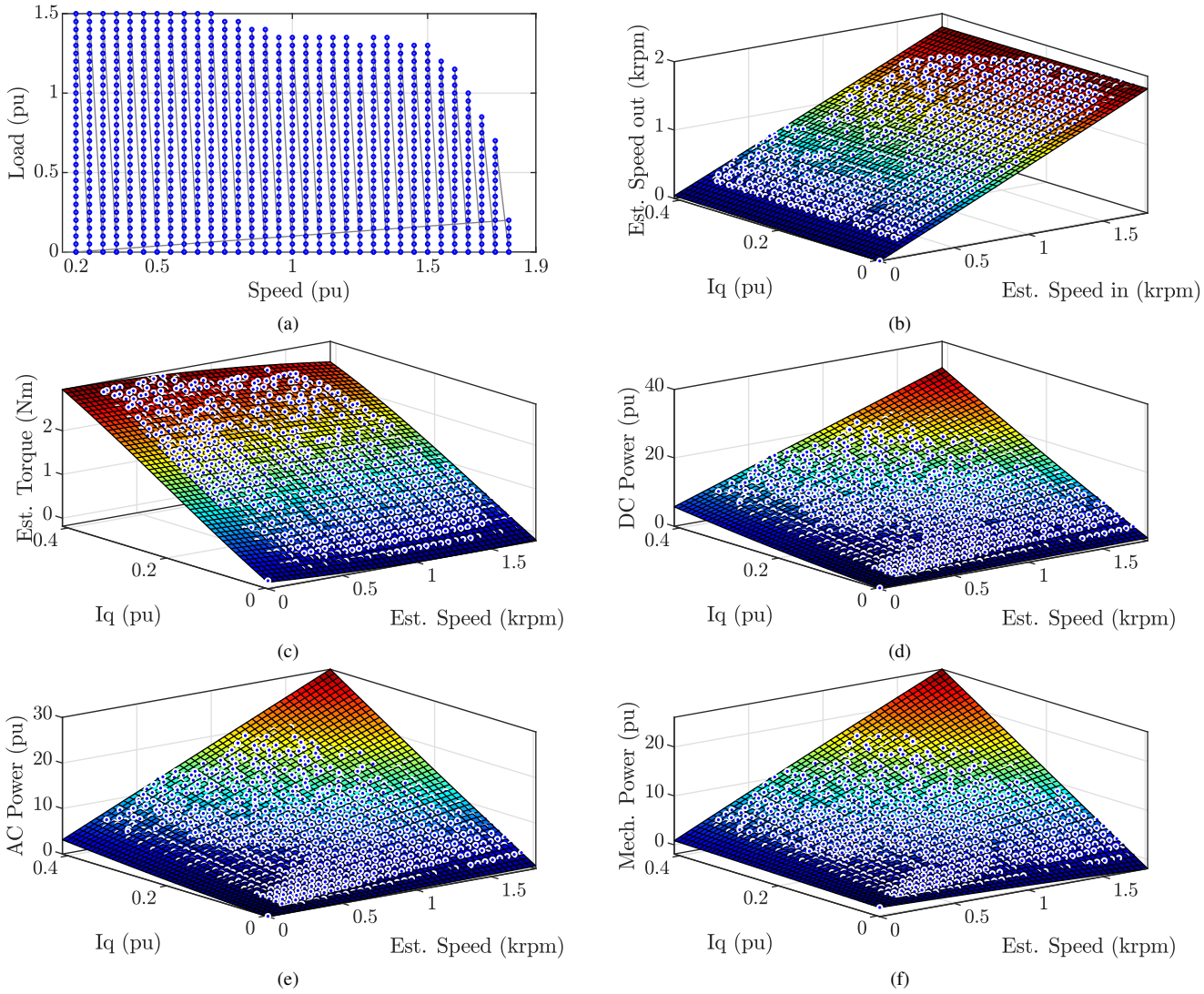

FIGURE 5.11: Motor modelling plots. (a) Is the test point trajectory for motor system modelling, covering 993 operating points. Modelled surfaces are shown for (b) speed, (c) torque, (d) DC power into the inverter, (e) AC power out of the inverter and into the motor, and (f) mechanical power out of the motor.

The **Power** estimator models (Fig. 5.11 (d), (e) and (f)) all share a similar shape, where power is highest at the highest values of speed n and q-axis current i_q. In all three power models, the dominant term was the p_{11} (ni_q) term that represents the product of speed and torque (i.e. mechanical power). The mechanical power model also had a small i_q component and negative n and n^2 components that may account for some mechanical losses. Comparatively, the AC and DC power estimators have a smaller ni_q term but larger i_q and i_q^2 terms. These terms may help capture additional power applied to but lost inside the motor (e.g. stator copper losses that are proportional to i_q^2). The AC and DC power models also have a similar structure, consistent with the high efficiency of the inverter.

5.5 Verification of Estimator Models

To verify the performance of the estimator models, the coefficients were programmed into the inverter firmware. Estimates were produced using Eq. (5.1) calculated at a rate of approximately 4 kHz, with the high bandwidth (unfiltered) speed estimate n and current measurement i_q values being used. The estimator outputs were then measured using the integrated high bandwidth synchronised measurement software module (15 kHz, typically just under 4096 points per average). The resulting inverter control scheme is shown in Fig. 5.1.

To investigate the impact of temperature on the accuracy of the estimators, two tests were performed. The first was a *cold* test that did not use any temperature regulation, and started with a machine at ambient temperature. The second test was a *hot* test that preheated the machine to a steady state temperature, and used temperature regulation to keep the machine at a consistent temperature similar to the original modelling temperature. Fig 5.12 shows the temperature used during the modelling test. Fig. 5.13 shows the temperature during the cold and hot verification tests.

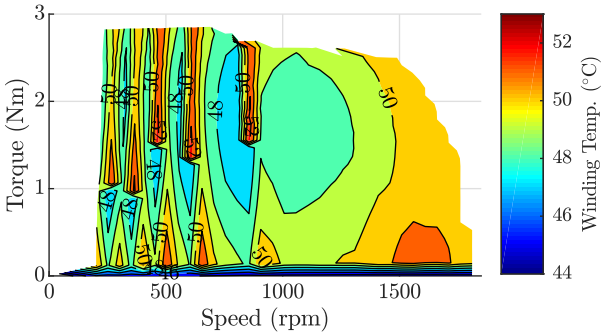

FIGURE 5.12: Motor modelling test temperature. The test temperature variations in the first half of the operating area are caused by the intermittent temperature regulation (heating) required to keep the machine at a temperature close to the steady state load temperature when operating below rated power.

The test points used during the verification tests are shown in Fig. 5.14. The cold test covered 228 points and the hot test covered 224 points. Both tests were configured to navigate the same grid of operating points. The difference of four points is a result of the real time operating area edge detection. The dynamic edge detection worked consistently to find almost the same top and right edges in both tests.

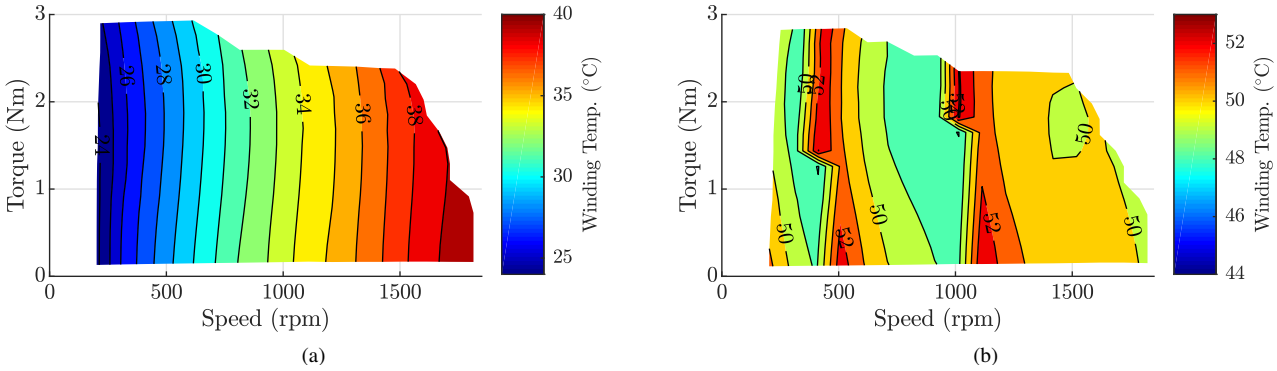

FIGURE 5.13: Motor verification test temperatures for (a) the unregulated (cold) temperature test, and (b) the regulated (hot) temperature test.

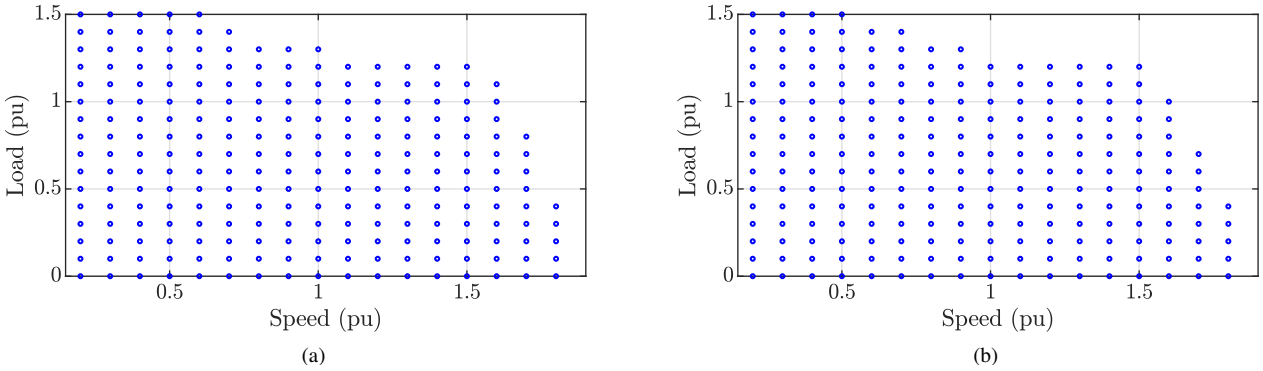

FIGURE 5.14: Motor verification test points for (a) the unregulated (cold) temperature test, and (b) the regulated (hot) temperature test.

5.5.1 Speed Estimator

The error in the inverter's original and proprietary speed estimator is shown in Fig. 5.15 (a) and (b). Colder temperatures showed better performance, with errors typically below 0.75 % for the mid to high speed, low load (bottom right) portion of the operating area. The hot test (temperature controlled) showed an increase in error of approximately 0.5 % for the same region. The top left region (low speed high load) showed speed errors above 2 %. Low speed operation is typically the most difficult region for a position sensorless control scheme to operate, often resulting in higher position errors. Because speed is derived from the position observer, it follows that position error would affect the speed estimate.

The size of the >2 % error region in the top left corner increased in size with increased temperature. This shows that the proprietary speed estimator, part of the motor parameter based position sensorless observer, is sensitive to temperature changes in the motor. These changes may cause a change in the true motor parameters compared to the originally identified parameters used by the inverter. Because the original speed estimate n is used as an input variable to all other

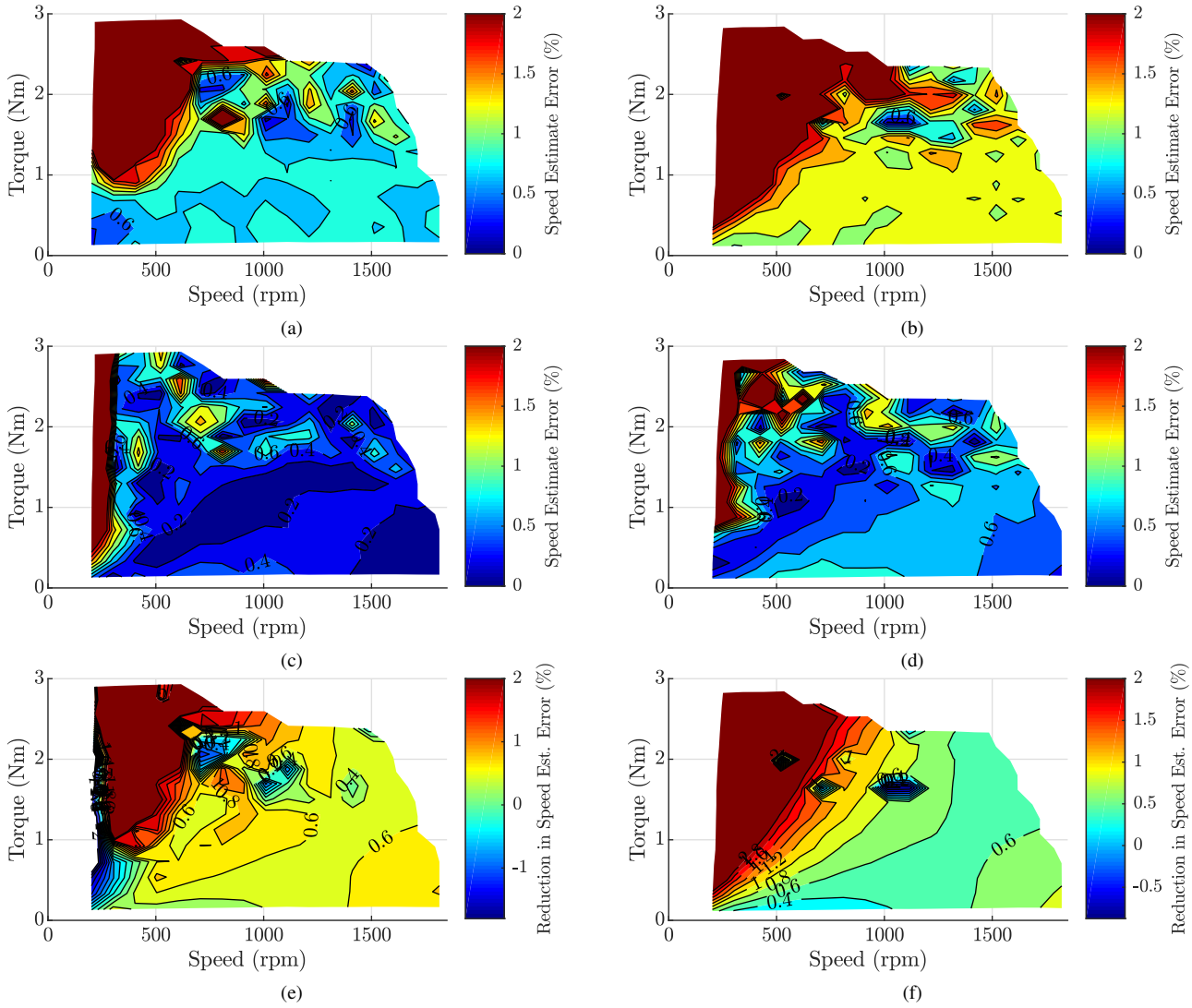

FIGURE 5.15: Motor speed estimator errors from (a), (c), (e) the unregulated (cold) temperature test, and (b), (d), (f) the regulated (hot) temperature test. The original speed estimator method using auto-identified parameters is shown in (a) and (b). The proposed method is shown in (c) and (d). The reduction in estimator error between the proposed and original methods is shown in (e) and (f).

models, an increase in speed error would affect the accuracy of all other models.

Fig. 5.15 (c) and (d) show the proposed speed estimator performance, demonstrating a much lower error over a larger part of the operating area. Although the hotter test shows a small increase in the error, in both tests the majority of the error is lower than 0.6 %. The higher error (> 2 %) region in the top left of the operating area is also smaller in the proposed method, helped by the model including load depended terms. The relative improvement between the original and proposed speed estimators is shown in Fig. 5.15 (e) and (g).

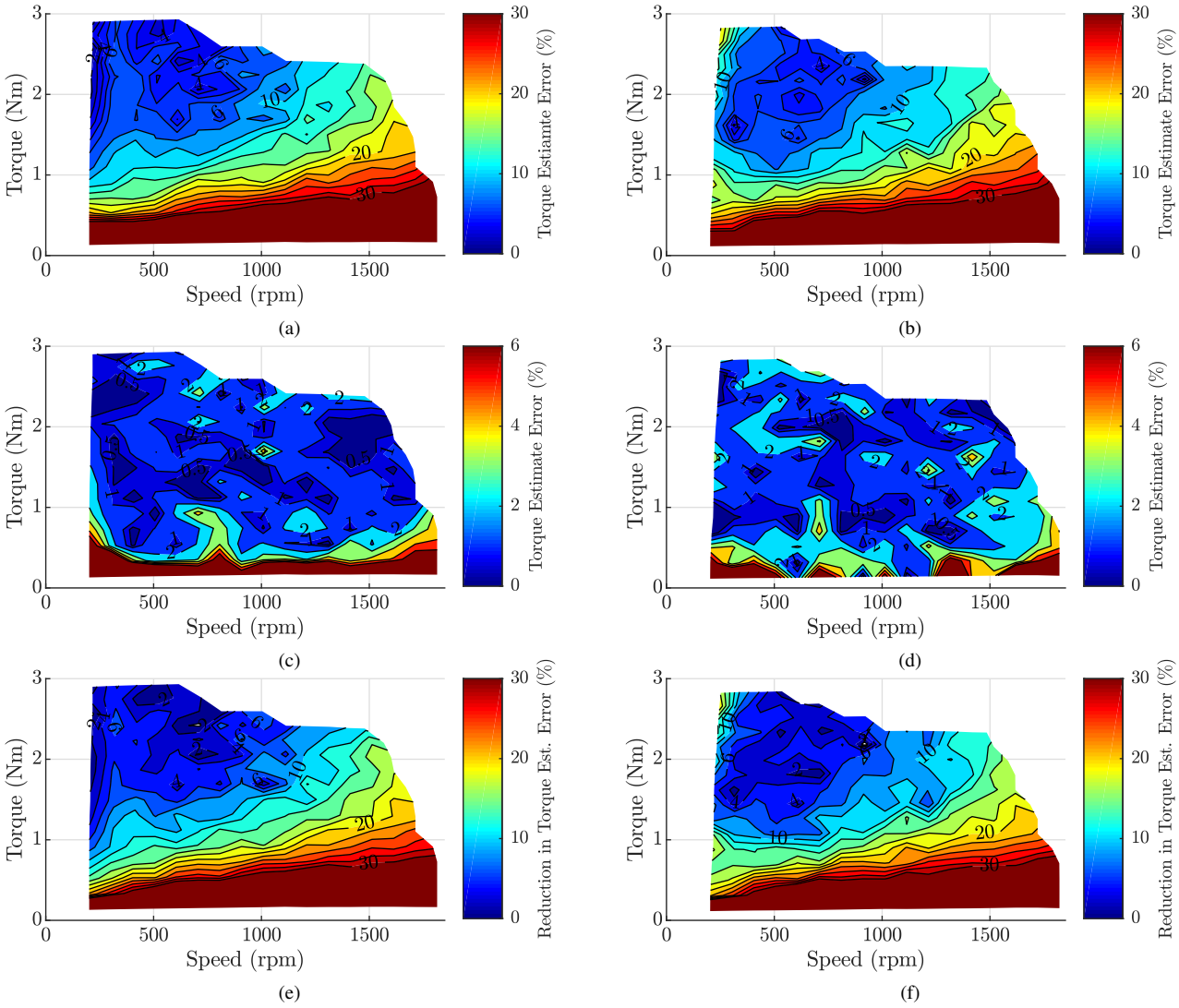

FIGURE 5.16: Motor torque estimator errors from (a), (c), (e) the unregulated (cold) temperature test, and (b), (d), (f) the regulated (hot) temperature test. The original air-gap torque estimator method using auto-identified parameters is shown in (a) and (b). The proposed method is shown in (c) and (d). The reduction in estimator error between the proposed and original methods is shown in (e) and (f).

5.5.2 Torque Estimator

The error in the inverter's original air-gap torque estimation is shown in Fig. 5.16 (a) and (b). The original method is based on the electromagnetic (developed, or airgap) torque shown in Eq. (2.9). Because a surface PM machine was used, the machine was not salient and had equal L_d and L_q values. The result is that the torque estimate becomes a product of just the q-axis current i_q and the peak flux linkage ψ, shown in Eq. (2.10). Although the flux linkage is often assumed to be constant, the original torque estimate instead used a real time estimate of flux linkage that was produced by the proprietary position sensorless observer.

The measured torque error in Fig. 5.16 (a) and (b) shows the majority of the operating area had an error above 10 %, with light loads having an error beyond 30 %. The large error is likely caused by errors in the original motor parameter estimation (being limited by the accuracy of the voltage and current measurement interfaces) and by a lack of detailed loss information for the motor. As the load approaches zero, the current also approaches zero where it is more easily affected by noise and limitations of the 12 bit ADC (range optimised for high current), which also contributes to the poor estimation error. Both cold and hot tests show a consistent shape, however there is a slight increase in error along the left edge of the region (low speed, high torque). This increase in error in the top left region may be related to the performance of the position sensorless observer, considering an increase in the observer's speed estimate error was also noticed in this same region.

Fig. 5.16 (c) and (d) show the performance of the proposed torque estimator. Unlike the original inbuilt torque estimator, the new estimator does not use a real time flux estimate. Instead, variations in flux are captured inside the model, along with motor loss components. Both cold and hot tests showed low errors of between 1 % and 2 % over most of the operating range. The low torque region (bottom edge) of the operating area showed an increase in relative error as torque dropped, with the hot test showing slightly better low torque performance. Compared to the original torque estimator, the new proposed estimator had an improvement of between 2 % to over 30 %, as shown in Fig. 5.16 (e) and (f).

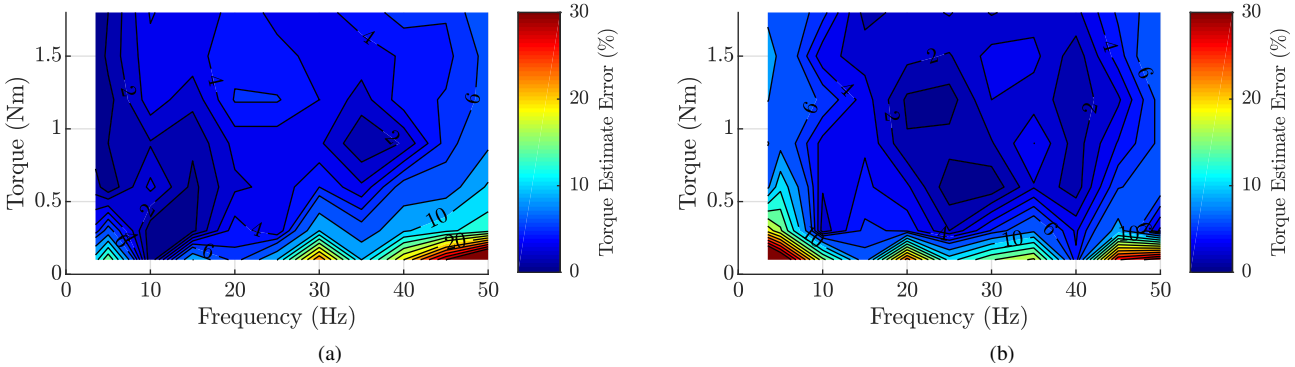

FIGURE 5.17: Comparison torque estimation error from [23] for a 250 W induction machine powered by Siemens G120 variable speed drive, using (a) position sensor and (b) position sensorless vector control. Note: the error shown is **after** compensating for windage and mechanical losses that were separately measured and not known by the variable speed drive.

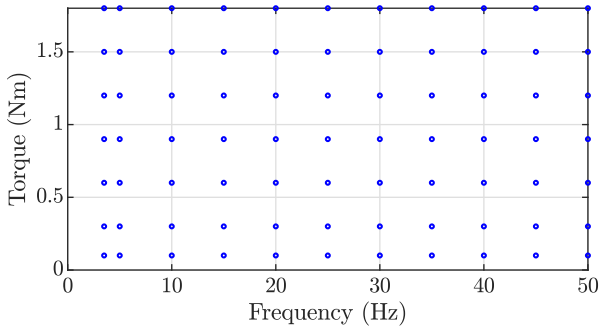

FIGURE 5.18: Measurement points used by [23] to determine the torque error of the 250 W induction machine powered by Siemens G120 variable speed drive. 77 points were used in total.

For comparison, the torque error measurements from [23] are shown in Fig. 5.17, for a Siemens G120 variable speed drive with 250 W induction machine. The machine used in [23] was similar in power rating to the machine tested in this chapter. The respective performance of the position sensor and position sensorless vector control was measured at 77 operating points (see Fig. 5.18).

The variable speed drive used auto-identified motor parameters for its torque estimate. The estimate was then compensated for windage and mechanical losses using a separate no-load test. The error between the resulting estimate and the true torque is shown in Fig. 5.17. With compensation for mechanical loss components versus speed, the results in Fig. 5.17 showed an error in the range of 2 % to 6 % over most of the operating area. This shows performance much better than the original Texas Instruments inverter's torque estimator. However, the performance is not as good as the proposed torque estimator shown in Fig. 5.16 (c) and (d), where load and speed dependent losses are included in the torque estimate.

5.5.3 Power and Efficiency Estimates

The performance of the power estimators is shown in Fig. 5.19, for DC, AC, and mechanical power. All of the estimators have errors below 2 % for most of the operating area. Interestingly, all of the estimators had significant increases in error along the left edge of the region (low speed) during the cold test, but showed much better performance during the hot test. Because the same error is present in the DC, AC, and mechanical power estimates, the cause can be attributed to a change in motor efficiency causing the actual power flow through the system to change. The true motor efficiency is shown in Fig. 5.21, and confirms the change in motor efficiency at low temperatures. This change in efficiency would result in the measured i_q current being different from the nominal value in that part of

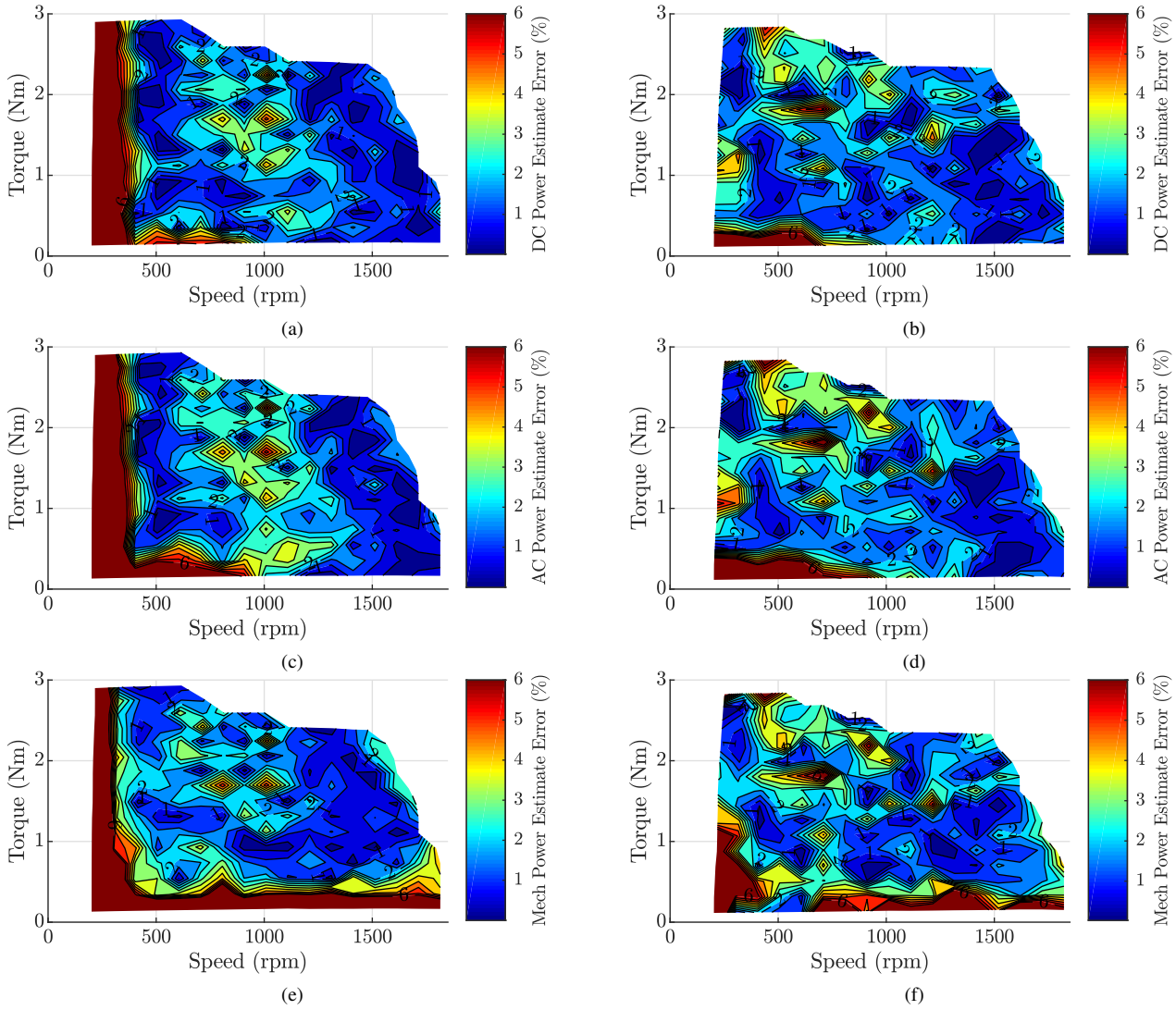

FIGURE 5.19: Motor power estimator errors from (a), (c), (e) the unregulated (cold) temperature test, and (b), (d), (f) the regulated (hot) temperature test. The inverter DC input power estimator error is shown in (a) and (b). The inverter AC power output estimator error is shown in (c) and (d). The mechanical power estimator error is shown in (e) and (f).

the operating range, and consequently causing the estimator models to predict incorrect values.

Fig. 5.20 shows the performance of the efficiency estimators, where the efficiency is calculated in real time from the estimated power flow and by using a fixed point division approximation. Error is shown as the difference between the estimated and true efficiency. The inverter efficiency estimate in Fig. 5.20 (a) and (b) has an error below 1 % over most of the operating range, with very little change between the cold and hot tests. This also suggests that the change in motor efficiency does not have much impact on the inverter efficiency estimate,

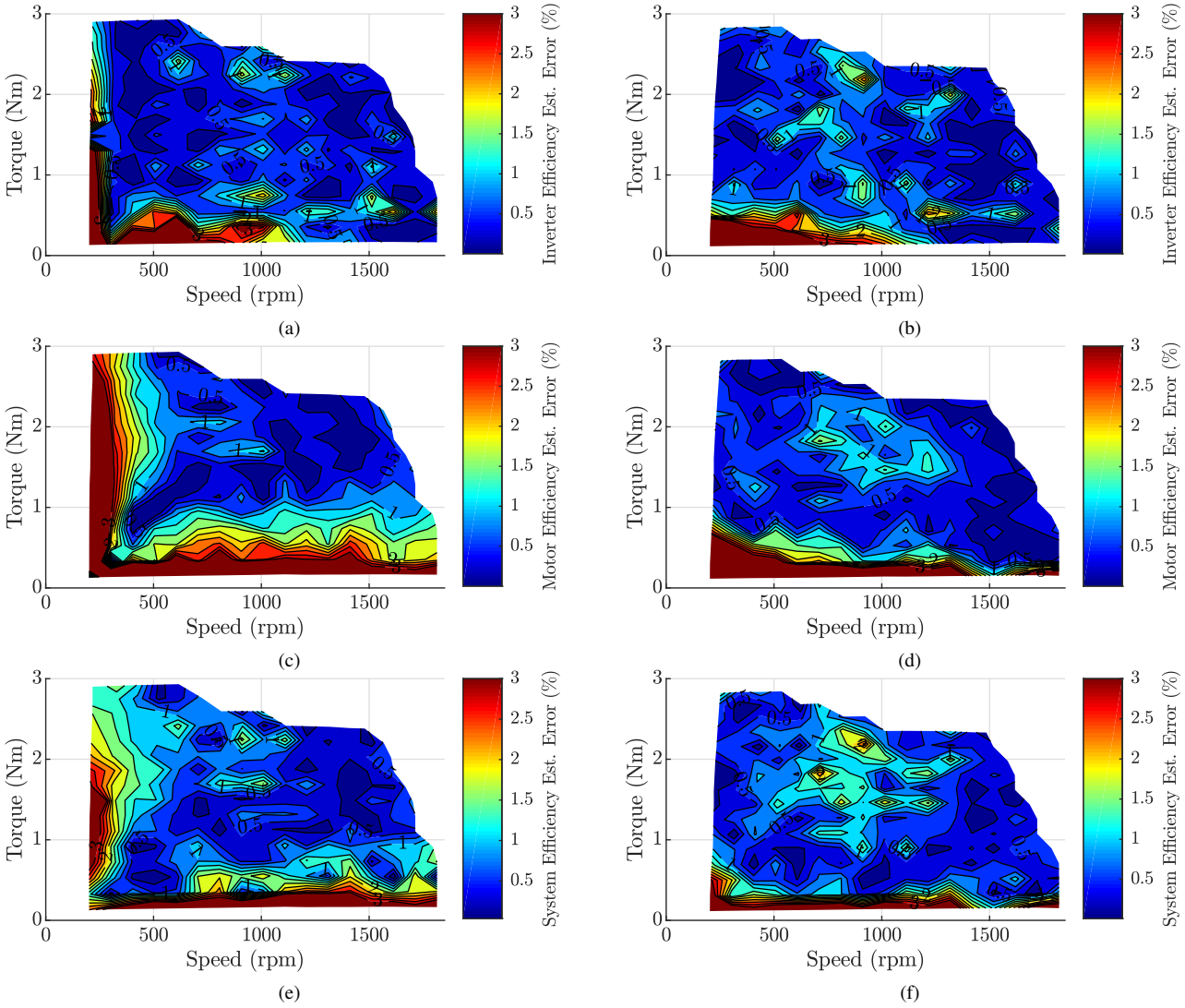

FIGURE 5.20: Motor efficiency estimator errors from (a), (c), (e) the unregulated (cold) temperature test, and (b), (d), (f) the regulated (hot) temperature test. The inverter efficiency estimator error is shown in (a) and (b). The motor efficiency estimator error is shown in (c) and (d). The system efficiency estimator error is shown in (e) and (f).

even though the AC and DC power estimates were separately affected.

The motor efficiency error in Fig. 5.20 (c) and (d) shows a more significant variation between the cold and hot tests. For the hot test, the motor efficiency estimate error is typically 1 % or lower. For the cold test, the error increases along the left and bottom edges, but remains below 1 % for the rest of the operating area. Comparing with the Fig. 5.21, the actual motor efficiency is noticeably higher along the left edge of the cold test. This highlights the temperature sensitivity of motor efficiency, particularly at the edges of the operating area.

Fig. 5.20 (e) and (f) shows the error in estimated system efficiency. System

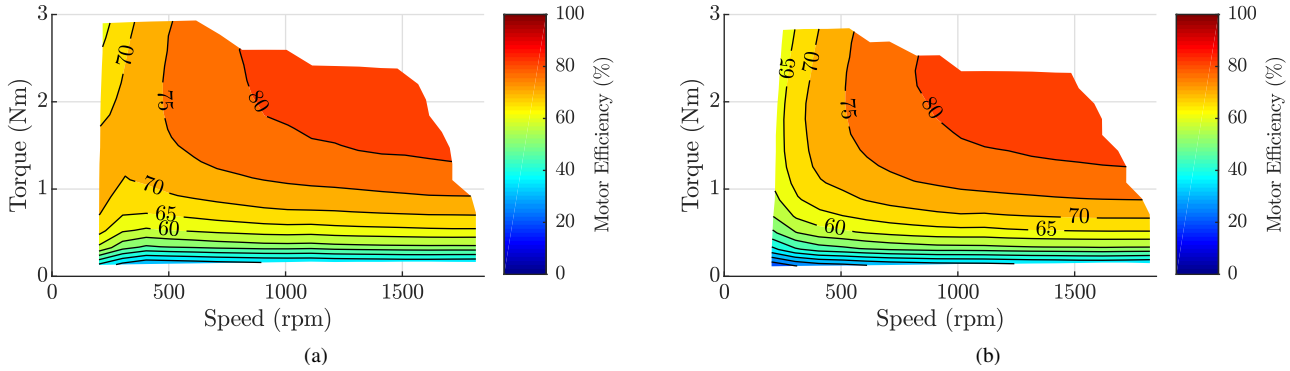

FIGURE 5.21: Motor efficiency for (a) the unregulated (cold) temperature test, and (b) the regulated (hot) temperature test.

efficiency is calculated as a ratio between the estimated mechanical power and DC power. Because of this approach, the error of the separate inverter and motor efficiency estimates don't add, but tend to cancel slightly as evidenced by the lower error compared to the motor efficiency estimate alone.

5.6 Conclusion

This chapter has introduced a new method for general state estimation of an integrated motor system over a wide operating area. The proposed method leverages automated efficiency map testing to produce comprehensive models that intrinsically capture loss components and component interactions. Despite capturing this information in a deeper level compared to the conventional motor models used for position sensorless control, the proposed method is computationally efficient and can be deployed on low cost motor drives with limited processing power. Once the efficiency map testing is complete, the modelling and analysis is relatively simple. This approach is well suited to integrated motor systems where the manufacturer models the entire system, uploads the estimator model parameters, before selling the motor system as a complete preconfigured product.

Experimental results were presented for a low power surface PM machine with a low cost inverter designed for integrated motor system applications. The speed and torque estimates had a typical error of less than 0.6 % and 2 % respectively over the vast majority of the operating range. Both of these estimator models improved upon the original methods provided by the inverter, with the new torque estimator model reducing error by up to 30 % for lower torque regions of the operating area. Power and efficiency estimates had errors on the order of 1 % to 2 % over most of the operating area, with errors increasing to 2 % to 6 % along the load speed and low torque boundaries. Motor temperature was

found to affect the motor efficiency and influence the error in the estimator models. Despite this influence, all estimator models offered consistent performance with only mild increases in error in small parts of the operating area. The experimental results demonstrated the performance and suitability of the approach, particularly for low cost integrated motor system applications.

Chapter 6

Pump System Sensorless State Estimation

6.1 Introduction

This chapter extends the sensorless estimation method introduced in Chapter 5 to provide state estimation of the end application/load of an integrated motor system, with the goal of providing a high estimation accuracy over the entire operating area of the system. A pump system was chosen as the landmark application of the method because such a system includes all components of a typical motor drive system, can be manufactured as an integrated system, and has wide spread usage. Additionally, pump applications are well suited to position sensorless motor control because they do not operate at low speeds or require position control, both of which are difficult for position sensorless control.

The sensorless estimation models presented in this chapter were developed from comprehensive efficiency map testing of the complete inverter-motor-pump system. Experimental efficiency map data provides a good basis for developing estimation methods because the data includes the pump and motor operating point quantities in addition to power and efficiency measurements. Experimental results are presented for an application specific inverter-motor-pump system operating in steady state and dynamic conditions.

Some of the content discussed in this chapter has been published in [76].

6.2 Proposed Method for Pump State Estimation

The proposed method for pump state estimation considers a complete, integrated inverter-motor-pump system. Estimation models are derived from data obtained

experimentally from comprehensive efficiency map testing over the entire operating range of the pump system. The advantage of this approach is that it captures all loss components and non-idealities in all components of the integrated motor-pump system.

The proposed measurement, modelling and estimation approach was applied using the same inverter and motor used in Chapter 5: a combination of a Texas Instruments DRV8301-69M-KIT inverter (with 51 V_{DC} supply) and a custom developed PM machine (3-phase, surface PM, 0.156 V/Hz Back-EMF, 13 $V_{pk\text{-}LN}$ @ 1000 rpm). The TI inverter is a reference design intended for integrated motor control applications, and includes a position sensorless field oriented control system. The pump used was a Davey XF171 water transfer pump (max 17 m head, max 175 L/min). Because the pump rated operating speed of 2850 rpm was beyond the maximum speed of the motor system (limited by the combination of inverter voltage and motor back-EMF), automatic field weakening was used to enable higher speed operation. The field weakening system automatically increased the magnitude of negative d-axis current to keep the applied voltage magnitude no higher than 80 % of the inverter's maximum voltage output.

In addition to the general motor system models presented in Chapter 5, the pump system efficiency map and modelling data collected was used to produce the estimation models for the following parameters:

- Flow.
- Pump total head.
- Hydraulic power out.
- Pump efficiency.
- System efficiency (updated to include the pump).
- Total volume pumped.

The following process was used to develop each estimation model:

1. Perform efficiency map testing to gather data over the operating range.
2. Using the test data, produce a model for each quantity to be estimated.
3. Enter each model's set of parameters into the inverter firmware.
4. Verify the performance of each model via additional efficiency map testing.

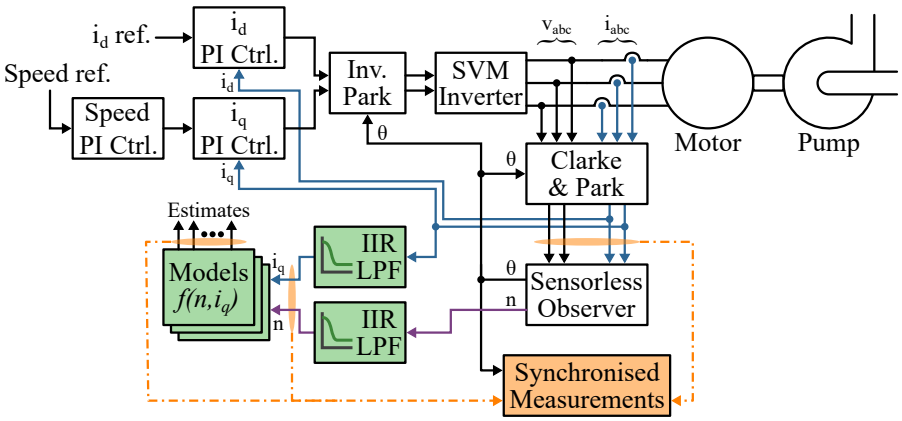

FIGURE 6.1: Control system block diagram with proposed estimation method for the pump application. The proposed estimation method's components are shaded in green. The embedded measurement system is shaded in yellow.

Because of the pump's more complex behaviour and modelling difficulty, an iterative approach of the above process was used to refine the estimator models. Modelling was performed in the same way as described in Section 5.2.3, where efficiency map data for the entire pump system was obtained using the fully automated test system described in Chapter 4. All estimator models were of the form shown in Eq. (5.1). The inverter's original speed estimate n and torque producing q-axis current measurement i_q were used as the two base variables for all estimation models, with both quantities being represented in terms of the inverter's fixed point representation used by its control system.

The resulting implementation is shown in Fig. 6.1. The key change from the general purpose motor estimation control system shown in Fig 5.1 is the inclusion of digital low pass filters on the q-axis current measurement and the original speed estimate from the sensorless observer. Of the three iterations of the pump estimator models, the first model (Section 6.4.2) did not use any low pass filtering. The second and third models (Sections 6.4.4 and 6.4.6) used low pass filters of decreasing bandwidth.

TABLE 6.1: Low pass filter specifications used for each pump model.

Model	Pass Band (Hz)	Stop Band (Hz)	Stop Band Attenuation (dB)	Pass Band Ripple (dB)
First Model	-	-	-	-
Second Model	5	50	50	0.5
Third Model	1	20	50	1

A Butterworth infinite impulse response (IIR) low pass filter was used, implemented using a direct form II biquad structure where the filter was built from

FIGURE 6.2: Pump test system. The pump is connected to a closed loop system of piping with a reservoir tank. At the top of the system is an electromagnetic flow meter followed by a computer controlled process control valve.

cascaded second order filters. Two cascaded second order filters were used, resulting in an fourth order filter. Because of the low order and minimal computations required by an IIR filter, and the use of fixed point arithmetic, two parallel filters were able to operate at the control system's sample rate of 15 kHz. The filter specifications for each pump estimator model are listed in Table 6.1.

6.3 Test Considerations

The data used for modelling was collected through autonomous efficiency map testing, using the system described in Chapter 4. The hardware portion of the test system is shown in Fig. 6.2 and 6.3, and a screenshot of the autonomous test software is shown in Fig. 6.4.

In addition to electrical power, torque, speed and temperature measurements, the pump system required measurement of flow rate, inlet pressure, outlet pressure and water temperature. These signals were used to calculate the pump flow rate, total head and hydraulic power in accordance with ISO 9906 [32].

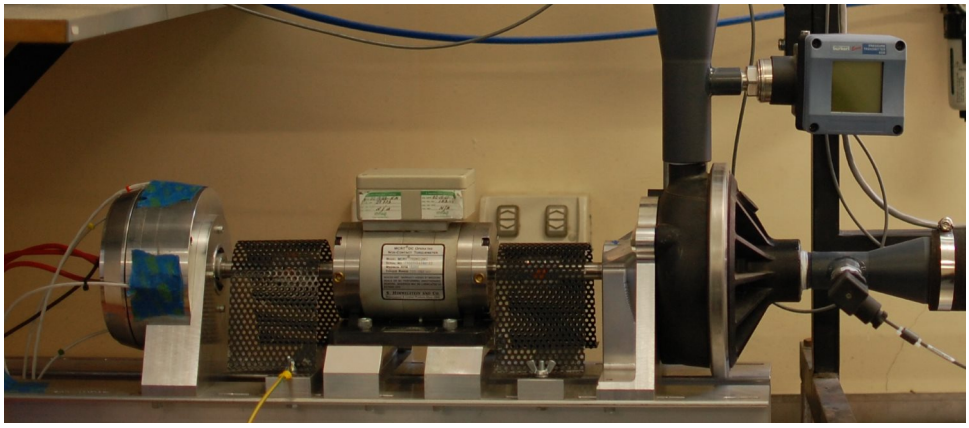

FIGURE 6.3: Pump test system hardware. The motor base frame was the same as used for the general motor testing shown in Fig. 5.3, but with the dynamo/load machine removed and replaced with a pump device. The motor is connected to the pump through a torque meter. Pump inlet and outlet pressure sensors are shown to the right and just above the pump respectively.

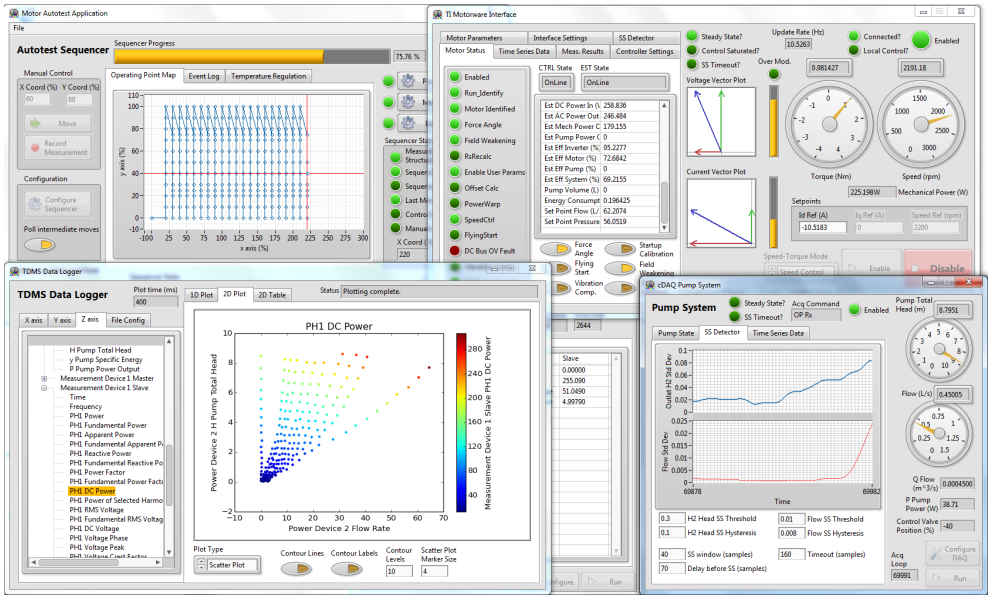

FIGURE 6.4: Autonomous test software graphical user interface, configured for pump system testing.

6.3.1 Flow Rate Measurements

Flow rate measurements were performed using a Bürkert SE 56 Electromagnetic flow meter with an ISOIL MS 1000 sensor, capable of measuring up to 1100 litres per minute for a 50 mm pipe size. The SE 56 flow meter included a low pass integrating filter with time constant on the order of 1 second. The flow rate output was sent as a 0 to 20 mA signal that was measured by a National Instruments CompactDAQ system with NI 9203 $\pm$20 mA input module.

The SE 56 flow meter was configured with an output full scale range just over

100 L/min to maximise the amplitude of the current output. Even though a current signal was used (that should have better noise immunity compared to a voltage signal), there was significant noise present in the measured signal that resulted in noticeable measurement fluctuations. To combat this noise, a digital low pass filter was applied to the signal in the form of a Bessel IIR filter with 0.1 Hz pass band, 1 Hz stop band and 90 dB stop band attenuation. A Bessel filter was chosen because of it's maximally linear phase response in order to preserve the waveform shape of the measured signals.

As a consequence of the digital IIR filter in addition to the flow meters in-built filter, there was a significant delay between motor speed or valve position changes and the new flow rate being observed. This required the autonomous test software use a seven second delay after coordinate/operating point changes before trying to detect the next steady state condition. Without this delay in the flow rate steady state detector, the test software would falsely detect a steady state condition before the underlying physical test system had time to respond to the change. The end result was a longer time between each test point compared to the general motor testing of the previous chapter, increasing the overall testing time for a given number of test points.

6.3.2 Pressure Measurements

Pressure was measured at the pump inlet and outlet at a distance of 1.6 and 2.7 times the pipe diameter respectively from each pump orifice, with measurements made at pipes with the same diameter as the pump inlet and outlet. According to ISO 9906, the nominal distance for pressure measurements is 2 diameters from the pump inlet and outlet. A single pressure tapping is used for both, consistent with grade 2 and grade 3 testing defined in ISO 9906. Both pressure tappings are horizontal, placing the pressure sensor elements at the same height as the measurement plane and avoiding the need to compensate for the precise height of the pressure sensing element above or below the measurement plane of the tapping. At the outlet, the pressure tapping was located perpendicular to the plane of the impeller, as recommended by ISO 9906.

The inlet pressure was measured by a Bürkert 8323 pressure transmitter with a measurement range of -1 bar to +1 bar (-100 kPa to +100 kPa). This corresponds to a maximum head level of 10.23 m above the pump inlet (for water at 20°C). Because the inlet pressure sensor measures a gauge pressure (the relative pressure between the fluid and the atmosphere), the minimum measurement corresponds to 1 bar (100 kPa) below atmospheric pressure (101.325 kPa). This allows

the pump inlet absolute pressure to be measured down to about 1 kPa. Due to Bernoulli's principle, increasing the flow rate causes the pressure to drop as potential energy is transferred into kinetic energy. Hence the requirement for a pressure sensor at the inlet that can measure negative gauge pressure.

The outlet pressure was measured by a Bürkert 8326 pressure transmitter with a measurement range of 0 bar to +16 bar (0 kPa to +1600 kPa). This corresponds to a maximum head level of 163.6 m above the pump inlet (for water at 20°C).

Both pressure sensors sent a 4 to 20 mA signal that was measured by a National Instruments CompactDAQ system with NI 9203 ±20 mA input module. Like the flow rate signal, both pressure signals had significant noise present in the measured signal that resulted in noticeable measurement fluctuations. To combat this noise, digital low pass filters were applied to these signals, using the same filter design as used for the flow rate signal (Bessel IIR filter with 0.1 Hz pass band, 1 Hz stop band and 90 dB stop band attenuation).

6.3.3 Flow Control Valve

After the flow meter and before the reservoir tank was a flow control valve, used to increase the pressure drop of the system to vary the overall system curve. The control valve consists of a Bürkert 2301 pneumatically actuated globe valve controlled by a Bürkert 8694 positioner. The globe valve has a moving parabolic plug and static seat, and offers good flow control compared to other valve types.

The valve used had a seat (orifice) size of 50 mm, and flow coefficient of 37 $m^3h^{-1}bar^{-1/2}$ when fully open. The flow coefficient of a valve is defined in Eq. (6.1) [44], and describes the flow rate for a pressure drop of 1 bar across the valve (when $\Delta p = 1$ bar, Q in units of m^3/h, ρ in units of kg/m^3). For a given pressure drop, the flow rate can be found by rearranging Eq. (6.1) to produce Eq. (6.2).

$$K_v = \frac{Q}{\sqrt{\Delta p \frac{\rho_{H_2O}}{\rho}}} = Q\sqrt{\frac{1}{\Delta p}\frac{\rho}{\rho_{H_2O}}} \qquad \left(\frac{m^3/h}{bar^{1/2}}\right) \tag{6.1}$$

$$Q = K_v\sqrt{\Delta p \frac{\rho_{H_2O}}{\rho}} \qquad \left(m^3/h\right) \tag{6.2}$$

The value of K_v varies with the valve stroke, however this variation has a non-linear characteristic. The 8694 positioner uses a PID control system to control the valve stroke, and includes a characteristic transformation control block that compensates for the underlying non-linear valve characteristic. The positioner was configured to present the valve as having a linear characteristic, where equal

changes in set point correspond to the equal changes in the flow coefficient K_v. The end result for a given pressure drop across the valve is a linear change in flow rate.

The 8694 positioner is controlled using a 4 to 20 mA setpoint, sent by a National Instruments CompactDAQ system with NI 9265 0 to 20 mA output module. This allows for the valve and the effective system curve to be computer controlled and automatically varied throughout the pump test.

6.3.4 ISO 9906 Calculations

The ISO 9906 standard outlines the necessary measurements and calculations required to measure the pump hydraulic power and pump efficiency. Hydraulic power is found from flow rate and pump total head. The total head is found from the difference between outlet and inlet head plus the friction head losses between the pump and the pressure sensor locations. To accurately calculate these values, the local acceleration of gravity, density of water and dynamic viscosity of water are required. Unless otherwise stated, the below definitions are taken from the ISO 9906 standard [32].

The local gravity was obtained from the Australian Fundamental Gravity Network [78]. The measurement from the nearby Mawson building was used, providing a value of 9797108.54 μms^{-2}, corresponding to $g = 9.79710854$ ms^{-2}.

The density and dynamic viscosity of water are temperature dependent. The water temperature was measured using a platinum 100 Ω resistance temperature detector (RTD) probe located in the pipe connected to the pump inlet. The water temperature probe was then connected to a National Instruments CompactDAQ system with NI 9216 RTD module.

To calculate density and dynamic viscosity, tabulated data was obtained from [79] and fitted to curves to allow for the density and dynamic viscosity to be calculated in real time using the instantaneous water temperature. Density was modelled as a 5$^{\text{th}}$ order polynomial, shown in Eq. (6.3), using 460 data points between 0.1°C and 99.974°C. The R^2 was 0.9999999895 and the RMSE was 8.4270×10^{-4}. Dynamic viscosity was modelled as rational function of two 3$^{\text{rd}}$ order polynomials, shown in Eq. (6.4), using 12 data points between 0.01°C and 99.606°C. The R^2 was 0.9999999996 and the RMSE was 0.01344. Curves for both quantities are shown in Fig. 6.5.

$$\rho = 1.427 \times 10^{-9} T^5 - 4.739 \times 10^{-7} T^4 + 7.031 \times 10^{-5} T^3 - 0.008495 T^2 + 0.06304 T + 999.9 \qquad \left(\mathrm{kg/m^3}\right) \quad (6.3)$$

$$\mu = \frac{75.18 T^3 - 2703 T^2 + 8.343 \times 10^6 T + 1.798 \times 10^8}{T^3 + 185.7 T^2 + 8151 T + 1.004 \times 10^5} \qquad (\mu\mathrm{Pa \cdot s}) \quad (6.4)$$

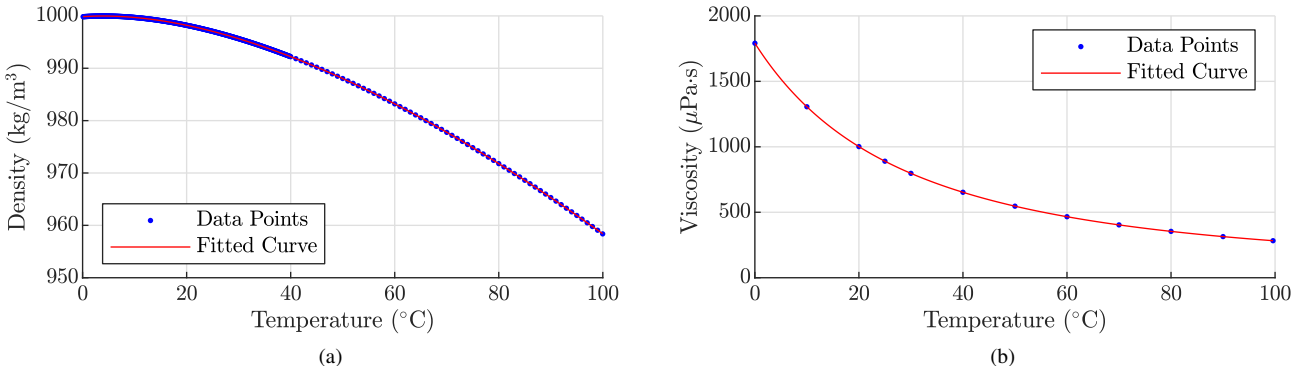

FIGURE 6.5: Water density and dynamic viscosity versus temperature, obtained from [79].

$$H_x = \overbrace{z_x}^{\text{Elevation Head}} + \overbrace{\frac{p_x}{\rho g}}^{\text{Pressure Head}} + \overbrace{\frac{U_x^2}{2g}}^{\text{Velocity Head}} \qquad (\mathrm{m}) \quad (6.5)$$

The total head in a given section of the system is found using Eq. (6.5), which is based on Bernoulli's equation for incompressible flow. The x subscripts refer to quantities at either the inlet ($x = 1$) or outlet ($x = 2$). z is the height of the centre of the cross section above the reference plane where the head is being calculated. z is the elevation head in meters, representing the component of head from the height of liquid above the reference plane. p is the gauge pressure in Pascals at the centre of the cross section, and is used to calculate the pressure head component. U is the mean axial velocity in m/s, and is used to calculate the velocity head component $U^2/2g$. The mean axial velocity U is calculated from Eq. (6.6) where Q is the volume flow rate in $\mathrm{m^3/s}$ and A is the pipe cross sectional area in $\mathrm{m^2}$.

$$U = \frac{Q}{A} \qquad (\mathrm{m/s}) \quad (6.6)$$

Eq. (6.5) reflects conservation of energy in a section of pipe: as the velocity of the water increases (increasing kinetic energy, increasing velocity head) the

pressure drops (decreasing potential energy, decreasing pressure head), however the total head stays the same. Head reflects the total energy in the liquid. Note that a pump adds energy to the liquid, hence a pump causes an increase in the head between the inlet and the outlet.

Pump total head H is found from the difference between the outlet head H_2 and inlet head H_1, corresponding to the outlet section S_2 and inlet section S_1 (i.e. at the pump fittings). Because measurements directly at the pump fittings are typically not practical, measurements are instead made some distance before and after the pump fittings, at sections $S_{1'}$ and $S_{2'}$. This produces head measurements $H_{1'}$ and $H_{2'}$. Pipe friction between the measurement sections and pump fittings causes friction head losses H_{J1} (between $S_{1'}$ and S_1) and H_{J2} (between S_2 and $S_{2'}$). The pump total head H can be found from the difference between the measured outlet and inlet head when the taking the pipe friction head losses into account, as shown in Eq. (6.7).

$$H = H_{2'} - H_{1'} + H_{J1} + H_{J2}$$
$$H = z_{2'} - z_{1'} + z_{M2'} + z_{M1'} + \frac{p_{M2'} - p_{M1'}}{\rho g} + \frac{U_{2'}^2 - U_{1'}^2}{2g} + H_{J1} + H_{J2} \quad \text{(m)} \tag{6.7}$$

$z_{1'}$ is the height of the inlet measurement section $S_{1'}$, and $z_{M1'}$ is the height of the inlet pressure gauge above $z_{1'}$. $z_{2'}$ is the height of the outlet measurement section $S_{2'}$, and $z_{M2'}$ is the height of the outlet pressure gauge above $z_{2'}$. All heights are in meters. The relationship between these heights is shown in Fig. 6.6. $p_{M1'}$ is the gauge pressure measured at $S_{1'}$, and $p_{M2'}$ is the gauge pressure measured at $S_{2'}$, both in Pascals. $U_{1'}$ is the mean velocity at $S_{1'}$ and $U_{2'}$ is the mean velocity at $S_{2'}$, both calculated from the flow rate measurement Q using Eq. (6.6), and assuming no liquid leaves the system between the inlet, outlet, and flow rate measuring sections.

The friction head loss H_J is found from Eq. (6.8), where λ is the pipe friction loss coefficient (dimensionless), L is the length of pipe (in meters), and D is the pipe diameter (in meters). The friction head loss correction is only applied when the sum of both inlet and outlet friction losses ($H_{J1} + H_{J2}$) is greater than 0.2 % of the total pump head H for ISO 9906 Grade 1, or is greater than 0.5 % of the total pump head H for ISO 9906 Grade 2 and 3.

$$H_J = \lambda \frac{L}{D} \frac{U^2}{2g} \quad \text{(m)} \tag{6.8}$$

The pipe friction loss coefficient λ is not constant but changes with the velocity

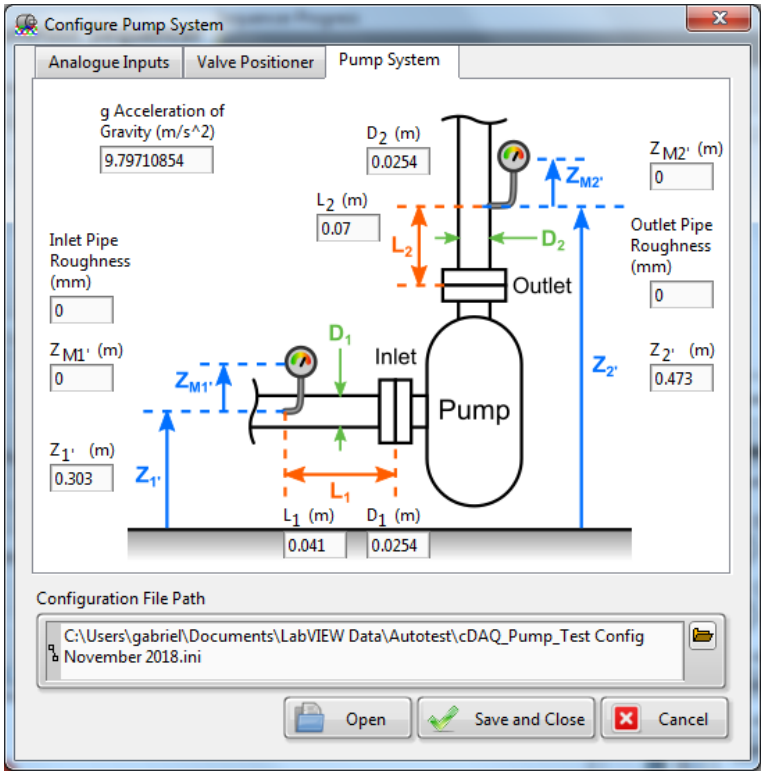

FIGURE 6.6: Autonomous test software pump configuration dialogue window, showing all fixed values required in addition to the measured flow, pressure and temperature in order to perform ISO 9906 analysis.

of the liquid. λ is found from the Colebrook–White equation [40], [41] shown in Eq. (6.9), where k is the equivalent uniform roughness of the pipe surface (in metres) and Re is the Reynolds number, defined by Eq. (6.10).

$$\frac{1}{\sqrt{\lambda}} = -2log_{10}\left[\frac{2.51}{Re\sqrt{\lambda}} + \frac{k}{3.7D}\right] \tag{6.9}$$

$$Re = \frac{\rho UD}{\mu} \tag{6.10}$$

Because Eq. (6.9) is not in an explicit form, it cannot be easily solved. λ can be found graphically from the Moody diagram [42], where the solutions to the Colebrook–White equation have been plotted against the Reynolds number for various values of pipe roughness. Such a solution is not suitable for a software based implementation. Instead, Serghide's Solution [80] was used to solve for λ, where a limited set of iterations (shown in Eq. (6.11)) are performed to produce a good approximation to the values produced by the Colebrook–White equation. Serghide's Solution was more suitable for the continuous and real time calculations performed by the autonomous test software.

$$
\begin{aligned}
A &= -2log_{10}\left[\frac{12}{Re}+\frac{k}{3.7D}\right] \\
B &= -2log_{10}\left[\frac{2.51A}{Re}+\frac{k}{3.7D}\right] \\
C &= -2log_{10}\left[\frac{2.51B}{Re}+\frac{k}{3.7D}\right] \\
\lambda &= \left(A-\frac{(B-A)^2}{C-2B+A}\right)^{-2}
\end{aligned} \tag{6.11}
$$

Once the pump total head H has been found, the hydraulic power P_h can be found using Eq. (6.12):

$$P_h = \rho Q g H \qquad \text{(W)} \tag{6.12}$$

The pump efficiency can then be calculated using equation Eq. (6.13), where P_2 is the pump power input.

$$\eta = \frac{P_h}{P_2} \tag{6.13}$$

Eq. (6.3), (6.4), (6.6), (6.7), (6.8), (6.10), (6.11), (6.12) and (6.13) were implemented in the pump measurement software module of the autonomous test system described in Chapter 4. This software module combined these equations with the pressure, flow and temperature measurements to provide a real time continuous measurement of all the pump system quantities, including power and efficiency. Combined with torque, speed and electrical power measurements, it was possible to measure the total system efficiency (also known as "wire to water" efficiency).

6.4 Estimator Model Development and Verification

Because of the pump's more complex behaviour and modelling difficulty, an iterative approach was used to develop and refine the estimator models.

6.4.1 Extrapolation of General Motor Estimators to a Pump Application

Initial testing of the pump system included the evaluation of the general motor state estimation models developed in Chapter 5. The key differences for the

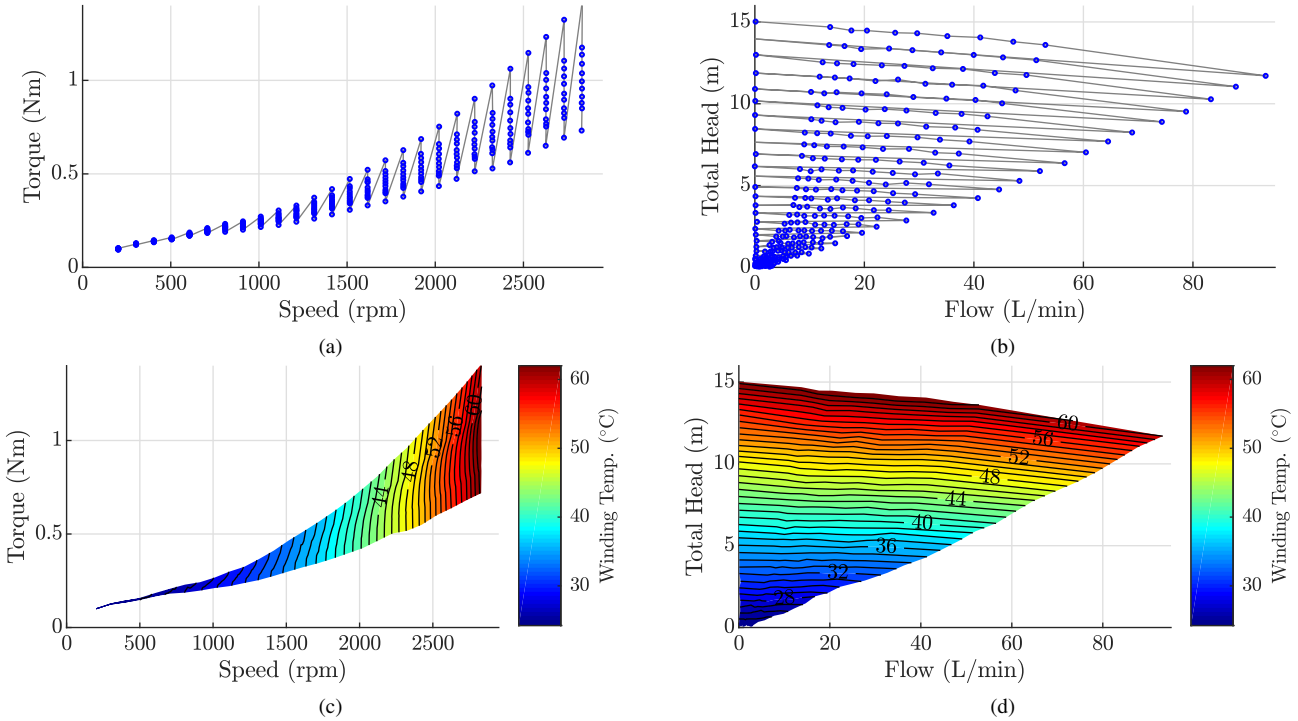

FIGURE 6.7: Pump system test points and motor winding temperature for the first modelling test, shown in terms of (a), (c) motor quantities, and (b), (d) pump quantities.

pump application were the different torque-speed operating area of the pump system and the use of field weakening to extend the speed range of the motor to reach the rated speed of the pump.

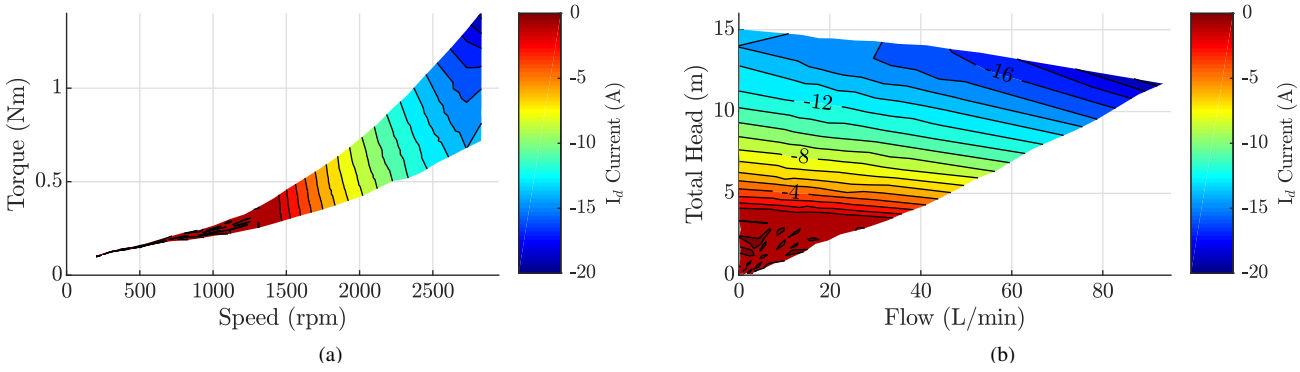

FIGURE 6.8: Pump system d-axis current for the first modelling test, shown in terms of (a) motor quantities and (b) pump quantities.

Fig. 6.7 (a) shows the test points over the motor's torque-speed operating area. The corresponding pump operating area is shown in Fig. 6.7 (b), where the left edge at zero flow corresponds to the lower torque edge of the motor's torque-speed area and the rightmost high flow rate edge corresponds to the higher torque

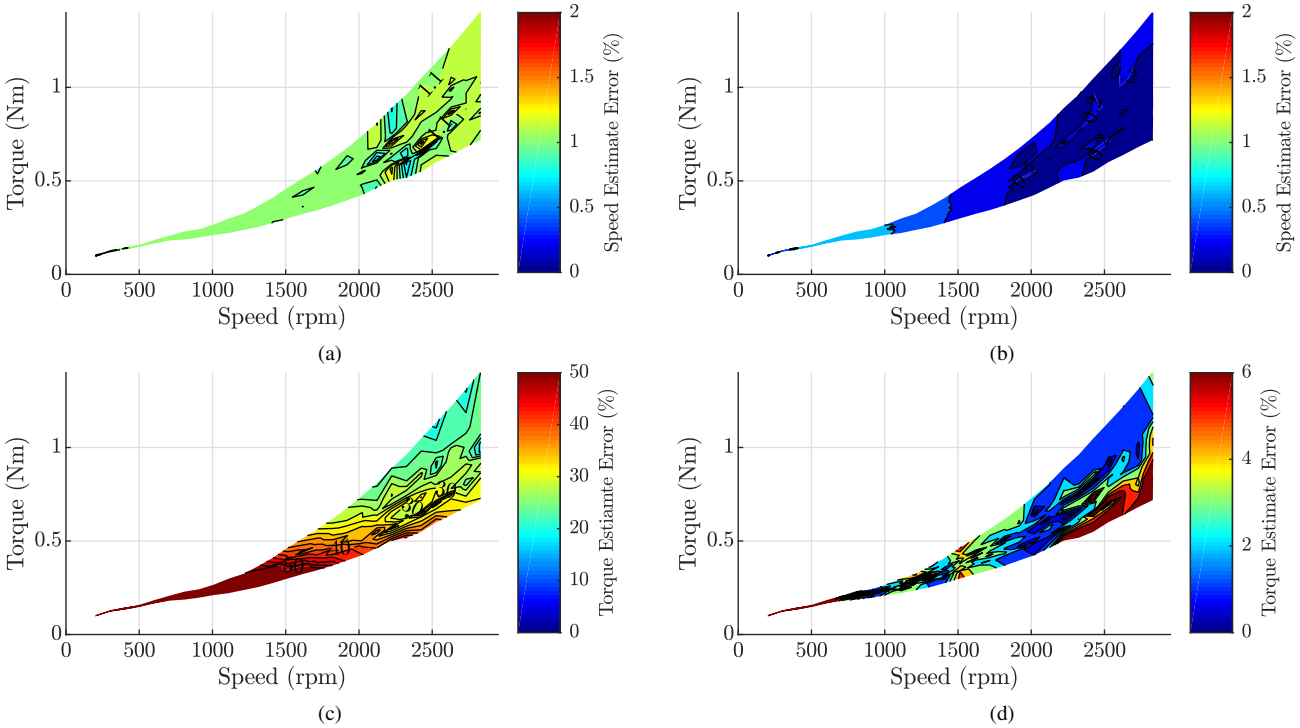

FIGURE 6.9: Motor system speed and torque estimator errors when used for a pump load and extrapolated beyond their originally modelling data. (a) is the original inverter speed estimator's error, (b) is the new speed estimator's error, (c) is the original inverter torque estimator's error, and (d) is the new torque estimator's error.

edge of the motor's torque-speed area. Note for this test the control valve's "cut-off" (sealing) function was enabled, where set point commands within 2 % of the set point limits caused the valve to lock open or lock closed. The result was a large gap between the linear range of the valve and the valve's fully open position, as seen in Fig. 6.7 (b).

The autonomous test system was configured to measure at 11 valve positions (100 % to 0 % of valved open, in 10 % steps), over 27 speeds (200 rpm to 2800 rpm, in 100 rpm steps), resulting in 297 test points. Because of the longer delay and settling time of the pump pressure and flow measurements (partly from the Bessel filter's group delay, partly from the pump dynamics), each test point waited 7 seconds before determining if the system was at a steady state. Because the motor and pump system could reach all points in the operating area, no control saturation detection or real time test point omission was used. The entire testing was completed in approximately 3 hours, corresponding to an average of 30 seconds per test point.

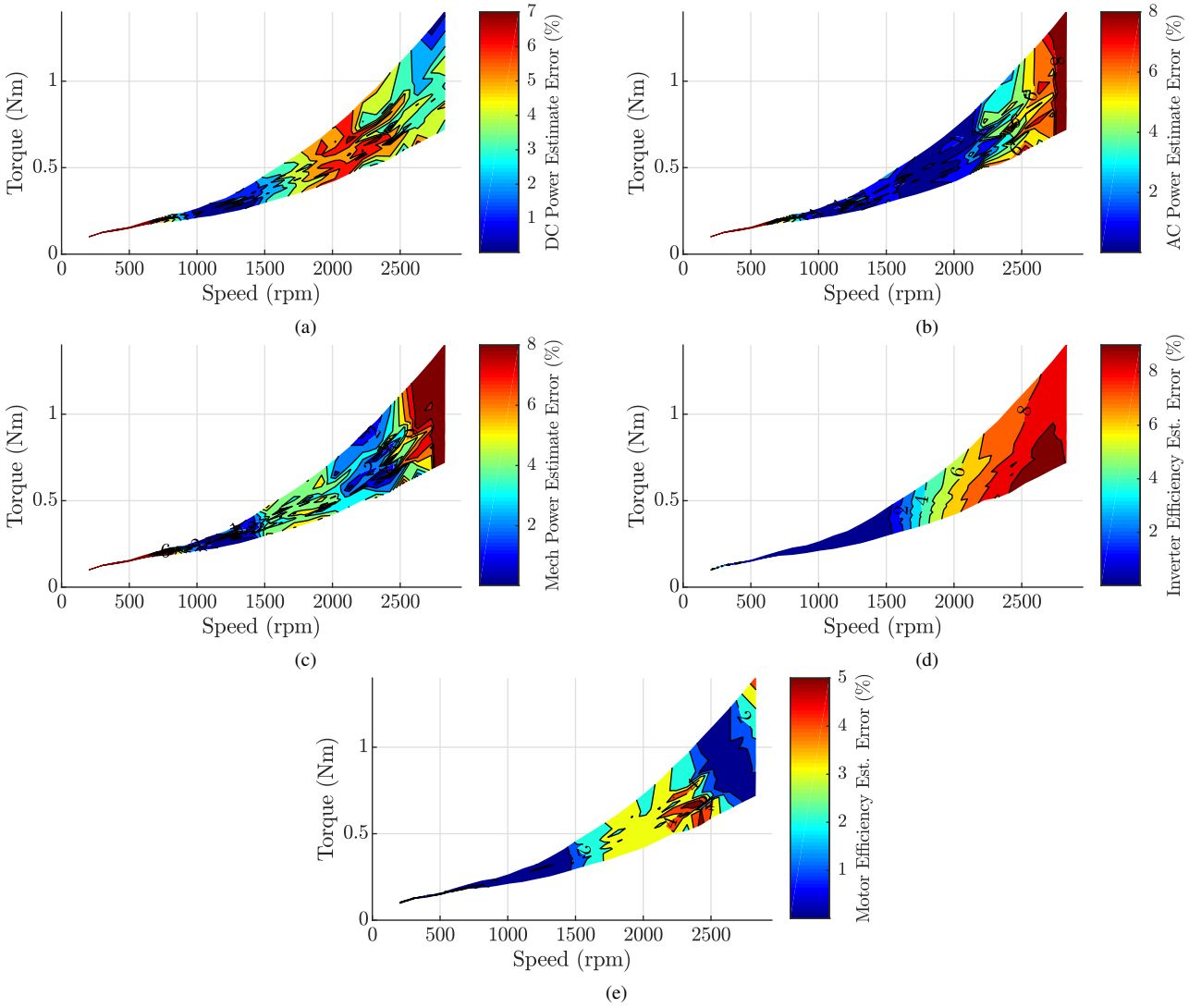

FIGURE 6.10: Motor system power and efficiency estimator errors when used for a pump load and extrapolated beyond their originally modelling data. (a) is the DC power estimator's error, (b) is the AC power estimator's error, (c) is the mechanical power estimator's error, (d) is the inverter efficiency estimator's error, and (e) is the motor efficiency estimator's error.

Fig. 6.8 shows the motor d-axis current over the motor's torque-speed operating area and the pump's flow-head operating area. The automatic field weakening starts to apply negative d-axis current from approximately 1500 rpm onward. The maximum field weakening current was approximately -18 A, approximately double the magnitude of the q-axis component.

The performance of the speed and torque estimators is shown in Fig. 6.9. The original speed estimate provided by the inverter (Fig. 6.9 (a)) had an error of approximately 1 %, whereas the proposed estimator had an error of approximately half as much (Fig. 6.9 (b)). The original inverter torque estimate (Fig. 6.9 (c))

had a large error between 20 % and 50 % over the motor's operating area. The proposed torque estimator (Fig. 6.9 (d)) performed much better, with an error between 1 % and 6% over the operating area. Beyond 1800 rpm and at higher torques the error was between 1 % and 2 %, which is a good result considering this region is outside the original modelling region used in Chapter 5.

Performance of the proposed power and efficiency estimators is shown in Fig. 6.10. The DC power estimator (Fig. 6.10 (a)) has a low error on the order of 1 % below 1500 rpm. After 1500 rpm, when field weakening begins, the error in the DC power consumption estimate increases, with a maximum value of 7 %. The AC power estimator (Fig. 6.10 (b)) and mechanical power estimator (Fig. 6.10 (c)) also show good performance up to 1500 rpm, after which the estimator error increases. Consequently, the inverter efficiency estimate (Fig. 6.10 (d)) has a low error of 1 % that increases beyond 1500 rpm, up to a peak just over 9 %. The motor efficiency estimator accuracy also suffers in a similar way, although not to the same extent.

Considering the use of field weakening increases the total current magnitude for a given amount of torque producing q-axis current, it stands to reason that an increase in current would cause increased losses in the motor (I^2R copper losses) and in the inverter (conduction and switching losses). Higher losses cause a drop in efficiency, hence for a given power output at the load, a higher input power is required. This effect would be more pronounced at the inverter, which can be seen in the inverter's efficiency estimation error shown in Fig. 6.10 (d).

6.4.2 Initial Modelling of the Pump System

The first pump estimators where modelled using the same data described in Fig. 6.7. Because a pump has a power proportional to the cube of the speed ($P \propto n^3$), there is a very large difference in the motor power and losses over the speed range, resulting in a large difference in operating temperature of the motor. In this scenario of the wide speed range variable speed pump, it is harder to define a single motor operating temperature that best reflects a real world example. Instead of regulating the motor temperature during testing, the temperature was left unregulated allowing the motor temperature to increase in response to the pump load.

The first iteration of estimator models for the pump application are shown in Table 6.2, with goodness of fit shown in Table 6.3, and surface fits shown in Fig. 6.11. Pump head was represented in units of meters, pump flow in units of litres per second, and all other quantities reusing the same per unit representations as

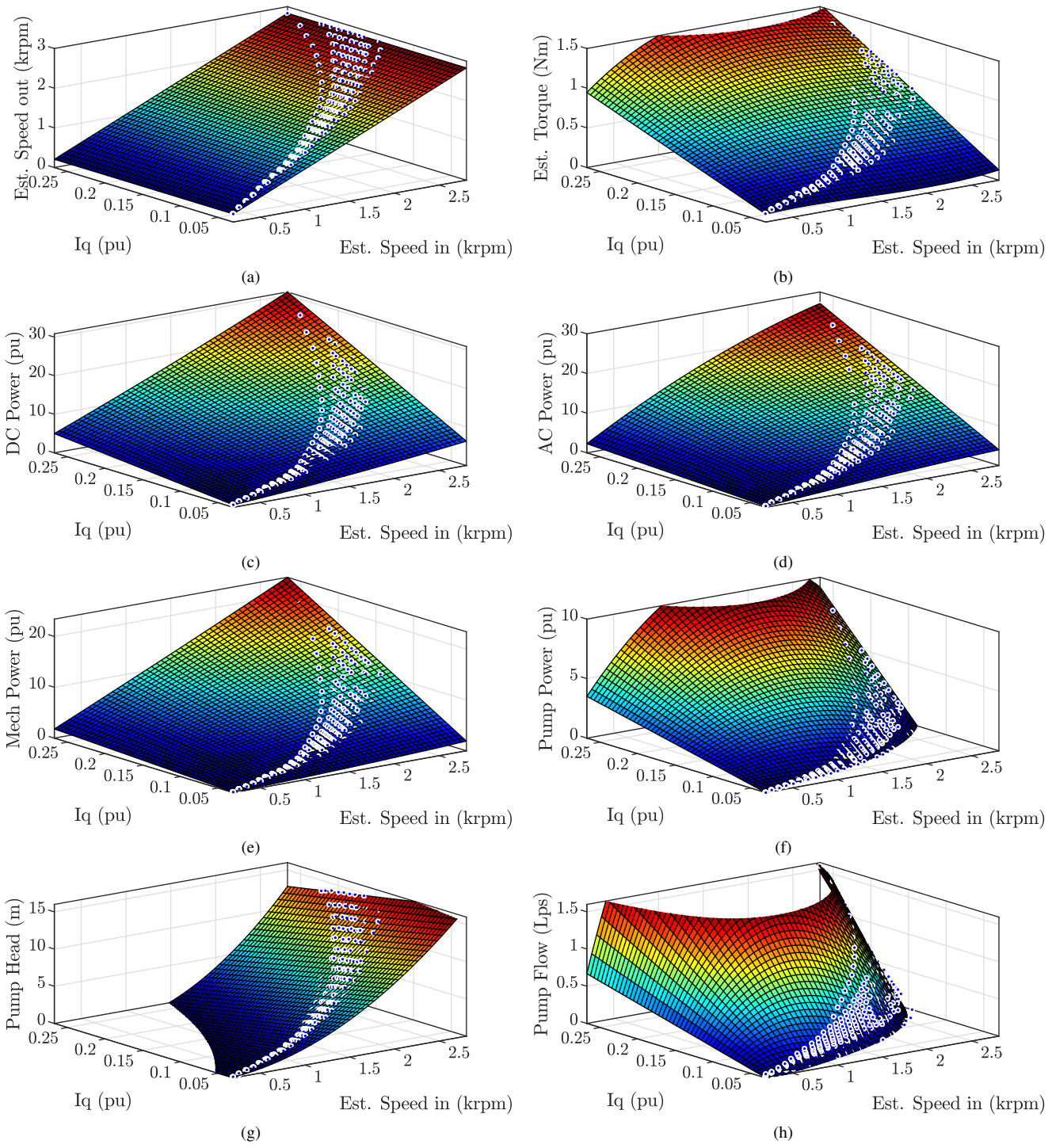

FIGURE 6.11: Modelling plots from the pump system's first modelling test. Surface fits are shown for (a) speed, (b) torque, (c) DC power, (d) AC power, (e) mechanical power, (f) pump (hydraulic) power, (g) pump head, and (h) pump flow.

Chapter 5. The models for the pump application reused the same estimator form described by Eq. (5.1) where only two basis variables were used: speed n and q-axis current i_q. The constant term p_{00} for all models was set to zero, such that a

TABLE 6.2: Model coefficients from the pump system's first estimator model.

Estimated Quantity	Polynomial coefficient for each term.									
	p_{00}	$p_{10}n$	$p_{01}i_q$	$p_{20}n^2$	$p_{11}ni_q$	$p_{02}i_q^2$	$p_{30}n^3$	$p_{21}n^2i_q$	$p_{12}ni_q^2$	$p_{03}i_q^3$
Speed	0	1.0094	0.0187	0	0	0	0	0	0	0
Torque	0	-0.0184	2.7609	-0.0803	4.2079	0	0.0289	-1.1017	0	0
DC Power	0	0.4393	11.7601	0.2534	32.6566	0	0	0	0	0
AC Power	0	0.2360	-1.4682	0.1213	50.4237	0	-0.0249	-5.4084	0	0
Mech. Power	0	-0.5884	1.3050	0	35.6481	-32.3980	0	0	0	0
Pump Power	0	-2.2329	5.4045	0.2456	48.5905	0	-0.2484	-8.9898	0	0
Pump Head	0	0.7747	-0.3234	1.9636	-21.4977	0	0.0107	5.3169	0	0
Pump Flow	0	-0.3354	-1.3897	-0.3919	22.2185	0	0.0887	-6.0659	0	0

TABLE 6.3: Goodness of fit for the pump system's first estimator model.

Estimated Quantity	SSE	R^2	RMSE
Speed	3.131×10^{-5}	0.9999	0.0003258
Torque	0.003895	0.9999	0.003659
DC Power	1.516	0.9999	0.07192
AC Power	0.6971	0.9999	0.04894
Mech. Power	0.3609	0.9999	0.0351
Pump Power	0.3839	0.9994	0.03632
Pump Head	0.5435	0.9999	0.04322
Pump Flow	0.7894	0.9645	0.05208

zero speed and current corresponded to an estimator output of zero (i.e. surfaces passing through the origin).

The results in the previous section showed increased error in the power and efficiency estimates caused by the use of field weakening and the models not able to respond to the change in d-axis current i_d (this term was not present in the estimator model). The automatic field weakening responds to the real time voltage space vector magnitude $|V_s|$, which in turn is generated by the d-axis and q-axis PI current controllers in response to real time current measurements. The voltage space vector magnitude $|V_s|$ is approximately the magnitude of the motor back-EMF, which is dependent on the rotor field and motor speed. Because the field weakening controller attempts to clamp the back-EMF magnitude and voltage space vector magnitude $|V_s|$ at a fixed level as speed increases, the rotor field must be progressively decreased using d-axis current. Hence the magnitude of d-axis current has a strong dependence on speed. Fig. 6.8 shows that although i_d is mostly speed dependent, it also changes with torque. Because torque is proportional to i_q, it is possible to capture the affects of i_d current through the existing speed n and current i_q basis variables. In this way, no additional variables are required and the effect of field weakening on the system is implicitly captured by the models.

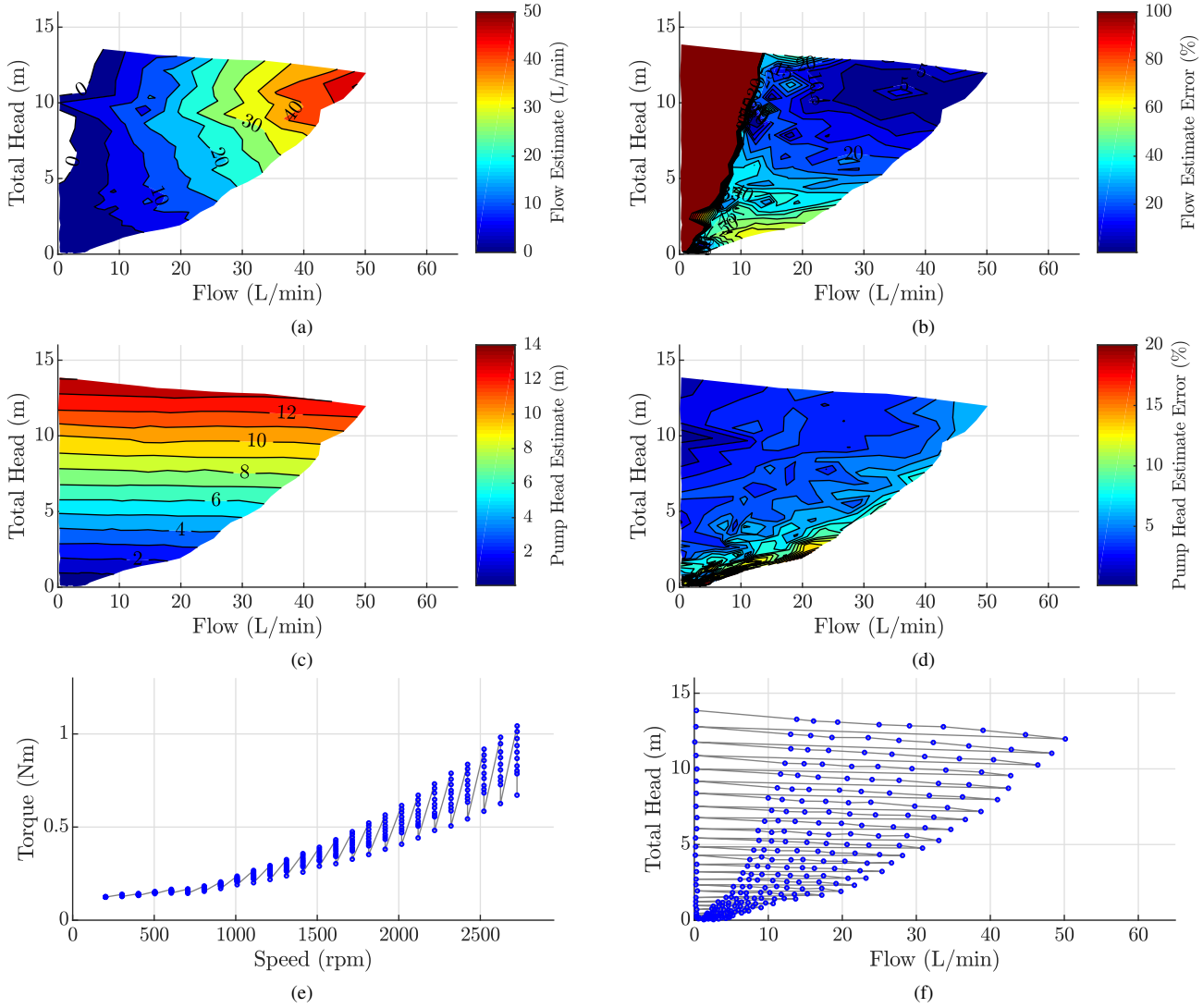

FIGURE 6.12: Verification of the first pump model. (a) is the estimated flow rate and (b) is the error in the estimated flow rate. (c) is the estimated head pressure and (d) is the error in the estimated head pressure. The operating points used for the verification test are shown in terms of motor operating quantities in (e) and pump quantities in (f).

6.4.3 Verification of Initial Pump Model

Fig. 6.12 shows the results for the head and flow rate estimators from the verification test of the first pump model. The same test points were used as shown in Fig. 6.7, except the valve's "fully open" test points have been removed from the plot. The valve's "cutoff" feature not only produced test points further from the linear region of test points in the middle of the operating area, but also produced a line of test points that did not sit well on the modelled surface used by the estimator. This is seen in Fig. 6.13, where the estimated head values sit on

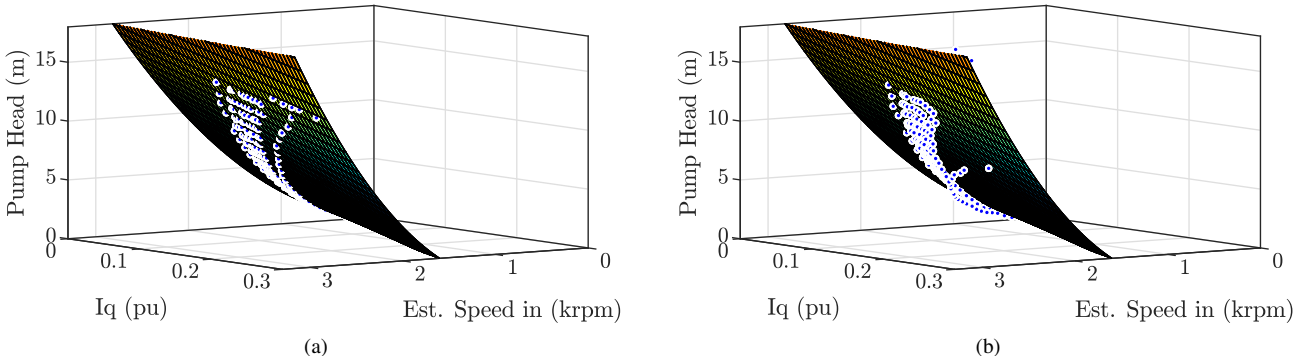

FIGURE 6.13: Measured points compared to the head pressure model's surface (from the first pump model). The head pressure estimated by the inverter at each test point is shown in (a). The measured (true) head pressure points are shown in (b). Both are compared to the same surface (estimator model).

the estimator surface in Fig. 6.13 (a) but the measured head values corresponding to the valve being fully open do not sit on the model's surface in Fig. 6.13 (b). Further non-linearity in the valve fully open position can be seen in 6.7 (b) where these points form a flat line (linear) instead of following a typical quadratic system curve ($H_{system} \propto Q^2$).

Performance of the flow estimator is shown in Fig. 6.12 (a) and (b), where the iso-flow contour lines in Fig. 6.12 (a) should ideally be vertical and aligned with the horizontal axis tick markers. The flow estimate has approximately a 5 % error at high flow rates and high head, but the error increases quickly outside this region. The low flow region (left most region) shows very high error (>100 %).

In contrast, the pump head pressure estimator shows good performance, with iso-head contour lines being mostly horizontal and aligned to the vertical axis tick markers. This is a result of the pump's strong relationship between head pressure and speed, allowing for an error typically below 5 % for most of the operating area. This strong relationship between head pressure and speed can also be seen in the pump curves for each speed (see Fig. 6.12 (f)), where each single speed sweep of test points sits on a fairly flat curve.

Note that no low pass filtering of the speed and q-axis current signals was used for this model.

6.4.4 Second Pump Model

The pump estimator performance of the first model was not ideal, particularly the the flow rate estimator. Some of the factors contributing to this were:

1. Forcing surfaces through the origin by constraining the constant term p_{00} to be zero.
2. Large fluctuations in speed and q-axis current signals, particularly during field weakening.
3. Non-linear valve operation caused by the valve's "cutoff" function.
4. Distribution of test points not well spread over the pump operating area (large clump of points at low head and flow).
5. Steep flow versus torque relationship of the pump, leading to a flow estimator with high gain on on the q-axis current term.

The second iteration of the pump model was designed to address the first and second issues (surfaces constrained through the origin, and fluctuations in the estimator input signals). The third pump model was designed to address the third and fourth issues. The fifth issue of a steep flow versus torque relationship is a property of the specific pump being used.

Fig. 6.14 highlights the difficulty in producing good pump estimator models for head and flow. Both the head (Fig. 6.14 (a)) and flow (Fig. 6.14 (b)) form steep surfaces. Fig. 6.14 (c) shows the pump head having a strong correlation with speed, making it easier to realise a head estimator with good performance. However, this results in very little change in speed between zero flow and maximum flow along a line of constant head. Consequently, the flow estimator relies heavily on the i_q current, as seen in Table 6.4 where the n, n^2 and n^3 terms are very small.

The i_q current is shown in Fig. 6.14 (f), where the iso-current lines are relatively flat compared to the flow rate, with the lines being flatter as flow rate decreases. At 12 meters of head, the i_q varies between 4.7 A and 8.1 A, corresponding to a variation between 0.114 and 0.196 per unit, with a net change of 0.082 per unit or 8.2 % of the current sensing range (where 1.0 per unit $=$ 41.25 A). At 4 meters of head, the i_q varies between 2.45 A and 3.3 A, corresponding to a variation between 0.059 and 0.080 per unit, with a net change of 0.021 per unit or 2.1 % of the current sensing range. At 2 meters of head, the i_q varies between 1.9 A and 2.3 A, corresponding to a variation between 0.046 and 0.056 per unit, with a net

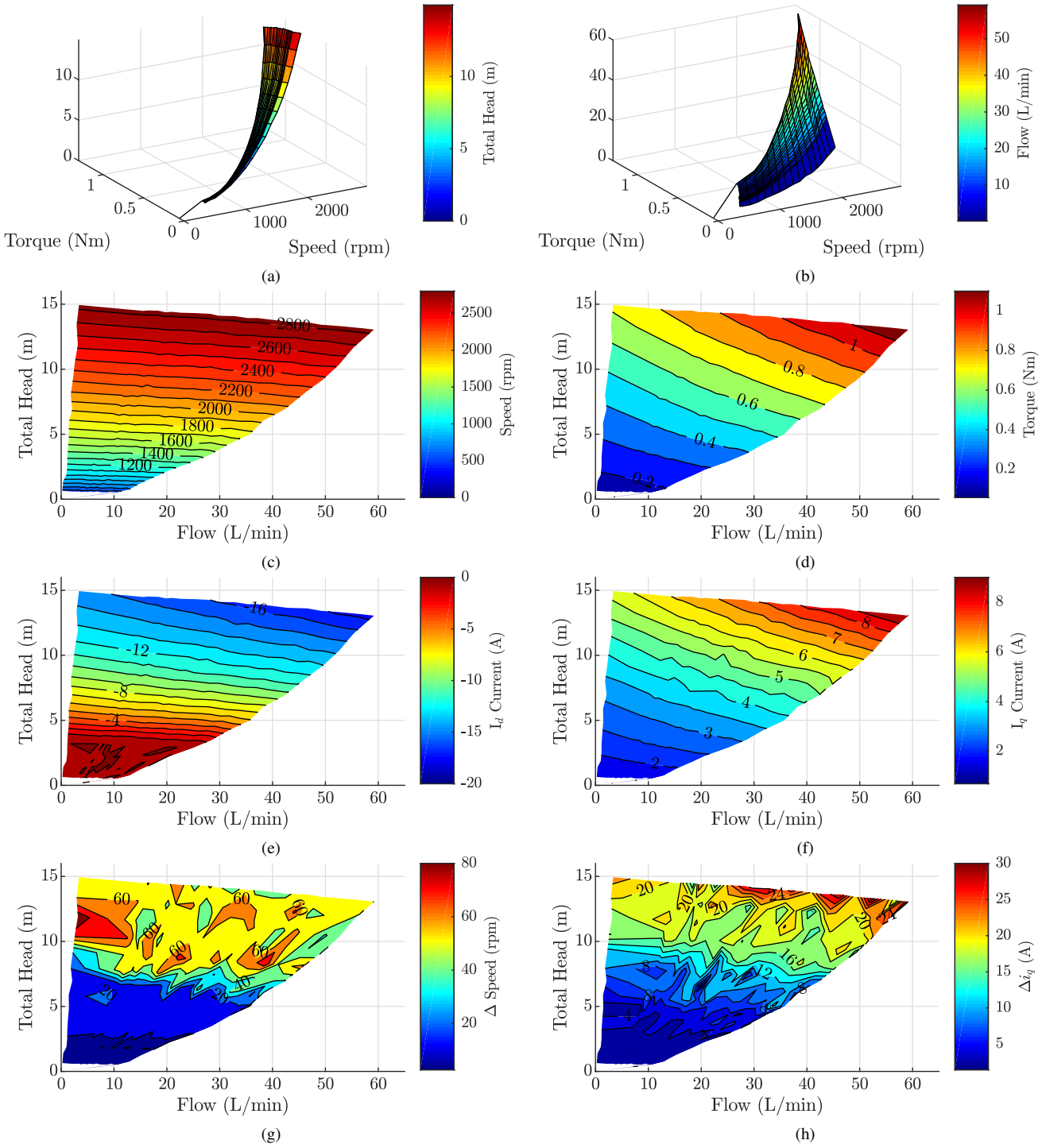

FIGURE 6.14: Relationship between pump and motor quantities, and fluctuations in measured signals. (a) is the pump head pressure and (b) is the flow rate in terms of motor speed and torque. (c) is the speed and (d) is the torque in terms of pump flow rate and head pressure. (e) is d-axis current and (f) is the q-axis current in terms of pump flow rate and head pressure. (g) is fluctuation in speed and (h) is the fluctuation in q-axis current in terms of pump flow rate and head pressure.

TABLE 6.4: Model coefficients from the pump system's second estimator model.

Estimated Quantity	Polynomial coefficient for each term.									
	p_{00}	$p_{10}n$	$p_{01}i_q$	$p_{20}n^2$	$p_{11}ni_q$	$p_{02}i_q^2$	$p_{30}n^3$	$p_{21}n^2i_q$	$p_{12}ni_q^2$	$p_{03}i_q^3$
Speed	-0.0006	1.009	0.0283	0	0	0	0	0	0	0
Torque	-0.2302	-0.0814	11.5872	0.0578	-2.2435	0	0	0	0	0
DC Power	-0.6179	0.0281	35.6519	0.4452	24.3420	0	0	0	0	0
AC Power	-1.1591	0.6027	36.8793	0.1972	19.9423	0	0	0	0	0
Mech. Power	-0.1438	-1.4452	8.1562	0.1098	50.0000	0	0.1064	-8.1788	0	0
Pump Power	0.0968	-2.2602	2.3970	0.2767	50.0000	0	-0.2619	-9.0869	0	0
Pump Head	1.2344	0.4799	-41.7517	1.8422	9.5665	0	0	0	0	0
Pump Flow	-1.1890	-0.3022	40.7778	0.0293	-10.2413	0	0	0	0	0

TABLE 6.5: Goodness of fit for the pump system's second estimator model.

Estimated Quantity	SSE	R^2	RMSE
Speed	3.016×10^{-5}	0.9999	0.0003203
Torque	0.002	0.9999	0.002617
DC Power	0.9791	0.9999	0.05791
AC Power	0.5306	0.9999	0.04263
Mech. Power	0.5214	0.9999	0.0424
Pump Power	0.3796	0.9994	0.03618
Pump Head	0.3855	0.9999	0.03633
Pump Flow	0.03442	0.9984	0.01086

change of 0.010 per unit or 1.0 % of the current sensing range. Because the change in i_q current needed to detect a change in flow rate is very small compared to the current measuring range of the inverter, it means that the flow rate estimator must amplify a very small signal and consequently will be sensitive to noise and small signal fluctuations.

Fig. 6.14 (e) shows the corresponding field weakening d-axis current over the pump operating area, where the magnitude is significantly higher than the q-axis current over the majority of the operating area. In a field oriented control system, i_q and i_d are measured using at least two or three phase current measurements that are then transformed into the rotor's rotating reference frame by Clarke and Park transforms. The Park transform also requires the instantaneous rotor angle θ_r to translate the measurements into the rotor's reference frame. For the case of the position sensorless control system used, θ_r is estimated using a sensorless observer and is not measured directly. Even though the rotor position estimate may be sufficiently accurate for the inverter to remain synchronised to the motor, noise and error in this estimate will have an impact on the i_q and i_d current measurements in addition to any existing measurement noise.

Fig. 6.14 (g) and (h) show the measured speed fluctuation and q-axis current fluctuation respectively, over the operating area of the pump. Each fluctuation

was measured as difference between the largest and smallest single value encountered during the inverter's measurement interval (see Section 5.2.2). When the system is in steady state, ideally both the motor speed and q-axis current should be constant and have no fluctuations. Fig. 6.14 (g) shows a noticeable increase in speed fluctuation in the field weakening region ($i_d < 0$), however the value is small compared to the actual speed. Fluctuations in speed can be caused by a combination of mechanical vibration/resonance, fluctuations in the load torque over each mechanical cycle, and the interaction of these phenomena with the speed PI control system. The speed controller attempts to regulate speed by generating a torque (q-axis current) set point. It follows that a speed controller attempting to manage speed fluctuations will also be generating a fluctuating torque set point that results in fluctuating q-axis current.

Fig. 6.14 (h) shows i_q having very large fluctuations of between 1.6× to 3× the steady state component. In the highest speed region where the current fluctuations are the greatest, the range of current measurements is approximately $6 \sim 7\times$ the range of q-axis current corresponding to the full scale flow rate range. The result is a wildly fluctuating instantaneous flow rate estimate. Note that because the estimator models are non-linear (see Eq. (5.1)), the principle of superposition does not hold. That is $f(x) + f(y) \neq f(x + y)$, meaning that the average estimator's output using fluctuating signals will not be the same as the estimator's output using averaged signals. Hence it is important manage these signal fluctuations before these signals are processed by the estimator models.

To address the issues of signal fluctuations and the need to extract a weak signal from noise, a pair of low pass filters were added to speed and q-axis current signals respectively, before those signals were processed by the estimator models. The second pump model used Butterworth filters each with a 5 Hz pass band. The filter's are discussed in more detail in Section 6.2.

The pump model parameters, shown in Table 6.4, were also updated to allow for constant terms and offsets. To avoid numeric overflow in the inverter's DSP, the p_{11} terms for the mechanical and pump power estimates were constrained to be no larger than 50. Table 6.5 shows an improvement in the quality of fit, particularly for flow rate where the value of R^2 increased from 0.9645 to 0.9984, and the sum of squared error (SSE) dropping from 0.7894 to 0.03442 litres per second.

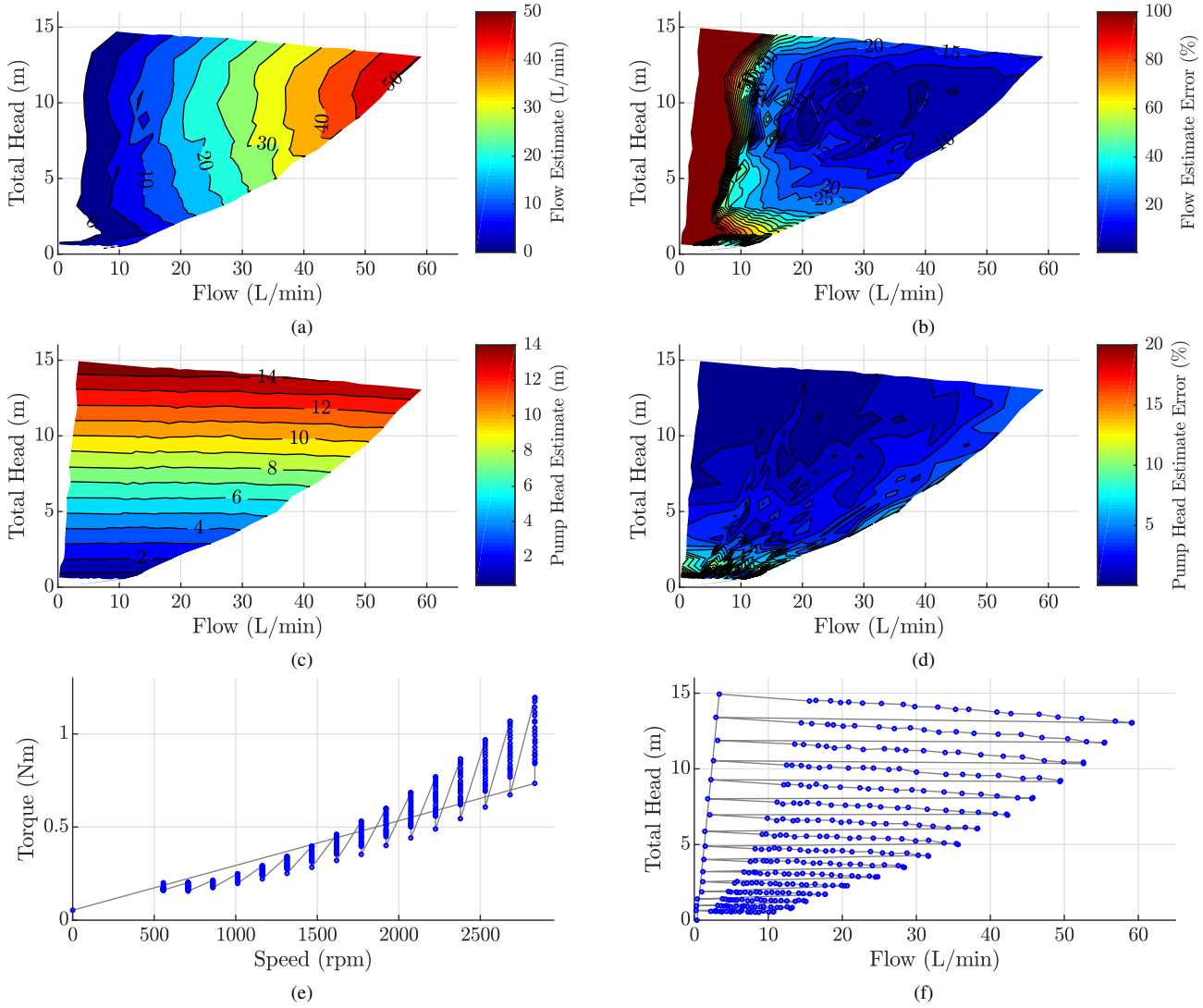

FIGURE 6.15: Verification of the second pump model. (a) is the estimated flow rate and (b) is the error in the estimated flow rate. (c) is the estimated head pressure and (d) is the error in the estimated head pressure. The operating points used for the verification test are shown in terms of motor operating quantities in (e) and pump quantities in (f).

6.4.5 Verification of Second Pump Model

The second pump model's verification test results are shown in Fig. 6.15. The flow rate estimator (Fig. 6.15 (a) and (b)) shows a good improvement over the original flow rate estimator's performance (shown in Fig. 6.12). A larger region of the flow rate estimate now has an error < 20 %. The vertical iso-flow contour lines are comparatively straighter and more closely aligned with the horizontal axis tick markers. The head estimator performance is similar to the first model, but does show a small improvement in accuracy.

It should be noted that both the first and second pump models are based on

the same data set. The improvement in estimator performance (particularly flow rate) has been achieved through the use of a narrow band low pass filter and a less constrained model (constant terms allowed). The low pass filter had a pass band of 5 Hz and transition band between 5 Hz to 50 Hz. Although this provides a significant improvement compared to no low pass filter, the transition band still allows for low frequency fluctuations to get through the filter. For example, a torque ripple or fluctuation at the fundamental mechanical frequency (a torque variation that repeats each mechanical cycle) will be between 16.7 Hz at 1000 rpm to 50 Hz at 3000 rpm. Hence in this speed range it is still reasonable to expect that some torque (and/or speed) fluctuations may get through the low pass filter.

6.4.6 Third Pump Model

For the third pump model, the low pass filter was changed to provide a more narrow pass band of only 1 Hz and a sharper transition band between 1 Hz and 20 Hz. The low pass filter was tightened to further remove signal fluctuations, but still allow for some dynamic changes to pass through the estimator. In addition to the tighter low pass filter, the main focus for this model was to address the non-linear valve operation caused by the valve's "cutoff" function (along the edge of highest flow) and the distribution of test points not being well spread over the pump operating area (large clump of points at low head and flow).

The test points used are shown in Fig. 6.15 (e) and (f). The autonomous test system was configured to measure at 21 valve positions (100 % to 0 % of valved open, in 5 % steps), over 16 speeds (550 rpm to 2800 rpm, in 150 rpm steps), resulting in 336 test points. The control valve's "cutoff" function was disabled, resulting in the high flow rate edge having a more typical quadratic system curve shape ($H_{system} \propto Q^2$). The high flow rate edge also shares the same approximate horizontal spacing, reflecting the control valve's linear operation now extending up to this edge. Note that without the "cutoff" function, the 0% valve open edge does not fully close the valve.

TABLE 6.6: Model coefficients from the pump system's third estimator model.

Estimated Quantity	Polynomial coefficient for each term.									
	p_{00}	$p_{10}n$	$p_{01}i_q$	$p_{20}n^2$	$p_{11}ni_q$	$p_{02}i_q^2$	$p_{30}n^3$	$p_{21}n^2i_q$	$p_{12}ni_q^2$	$p_{03}i_q^3$
Speed	-0.0008	1.0109	0.0227	0	0	0	0	0	0	0
Torque	-0.2131	-0.0379	10.5402	0.0340	-1.7563	0	0	0	0	0
DC Power	-0.6174	-0.3510	42.1016	0.6525	21.3363	0	0	0	0	0
AC Power	-0.9959	0.8801	27.5465	0.0616	23.7826	0	0	0	0	0
Mech. Power	0.4465	-2.0830	-0.7195	0.7499	50	0	-0.0802	-6.7935	0	0
Pump Power	0.3984	-2.2235	-6.1569	0.4981	50	0	-0.3699	-7.5035	0	0
Pump Head	1.4310	-0.1260	-39.0706	2.1758	5.8675	0	0	0	0	0
Pump Flow	-1.0170	-0.0593	33.6267	-0.0918	-7.2818	0	0	0	0	0

TABLE 6.7: Goodness of fit for the pump system's third model.

Estimated Quantity	SSE	R^2	RMSE
Speed	2.9502×10^{-5}	0.9999	2.9720×10^{-4}
Torque	0.0021	0.9999	0.0025
DC Power	0.5505	0.9999	0.0407
AC Power	0.5892	0.9999	0.0421
Mech. Power	0.3080	0.9999	0.0305
Pump Power	0.2649	0.9996	0.0283
Pump Head	0.1453	0.9999	0.0209
Pump Flow	0.0381	0.9977	0.0107

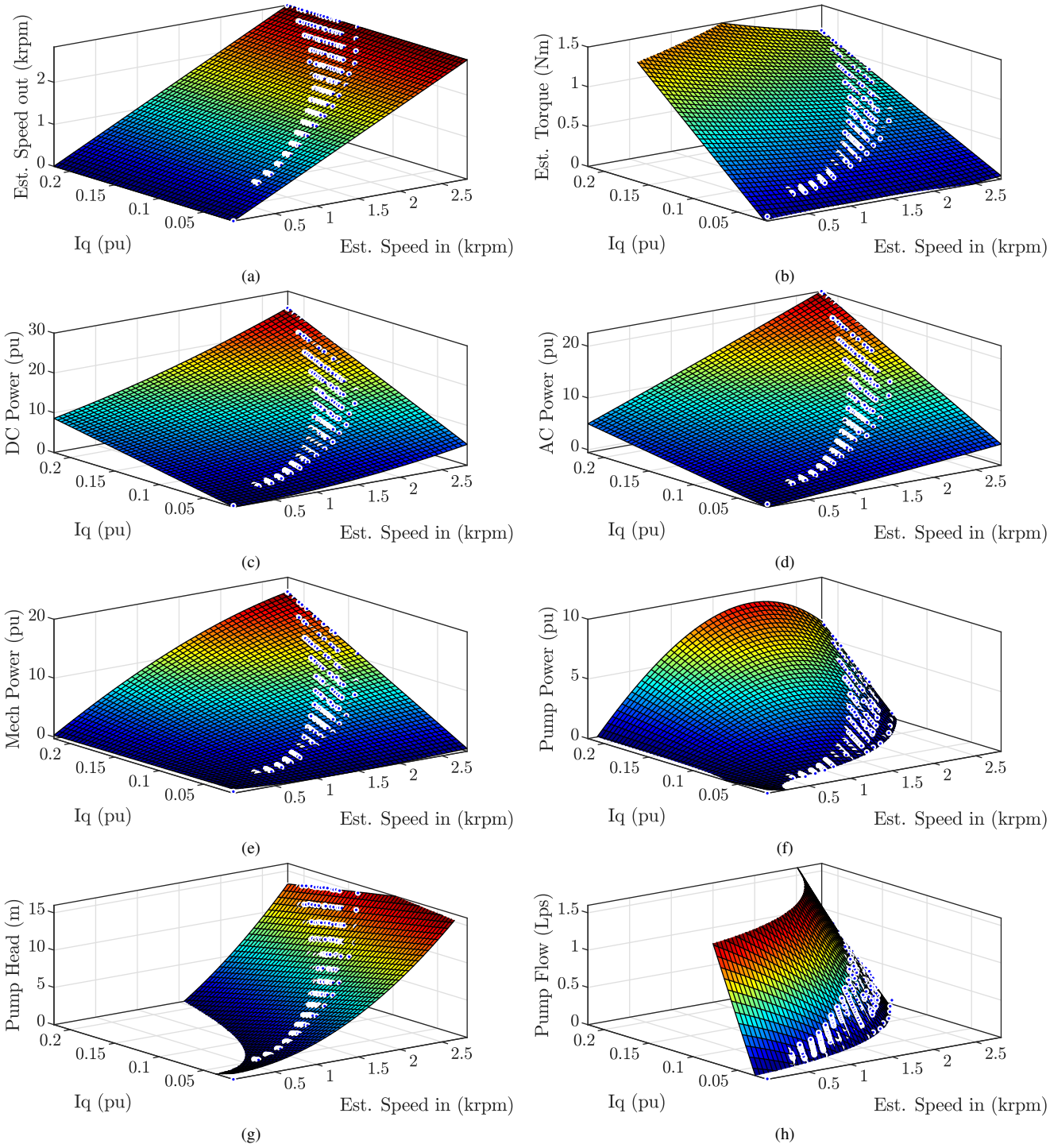

FIGURE 6.16: Modelling plots from the pump system's third modelling test. Surface fits are shown for (a) speed, (b) torque, (c) DC power, (d) AC power, (e) mechanical power, (f) pump (hydraulic) power, (g) pump head, and (h) pump flow.

The redistribution of test points reduces the speed/head resolution of the test grid and increases the flow rate resolution. That is, there are fewer speeds (pump curves) tested, but each speed (pump curve) has more test points at different

flow rates. The goal of this redistribution is to provide more points to capture the variation in flow rate, and to more evenly spread the test points over the pump's operating area. The number and location of the test points effectively changes the weighting of each region during the curve fitting process. The removal of test points from the 200 rpm to 500 rpm region and increase in test points at higher speeds and flows causes the curve fitting to more strongly weight the higher speed and flow rate regions.

6.4.7 Verification of Third Pump Model

The performance of the third pump model is compared to the first two models in Fig. 6.17 and Fig. 6.18. Fig. 6.17 (e) and (f) show a further improvement in the flow rate estimator's performance. The estimated flow rate error has dropped to < 10 % for most of the pump's operating area, with error lower than 2.5 % in smaller regions toward the centre of the operating area. Generally, the flow rate estimation error is < 15 % for speeds above 1500 rpm, and flow rates above 15 litres per minute.

The flow rate estimator still has high error at low flow rates close to zero, although the error in this region has been significantly reduced. Because the estimation error is displayed as a relative error using Eq. (6.14), as the true value approaches zero ($x \rightarrow 0$) any absolute error will cause the relative error to increase ($\delta x \rightarrow \infty$). Hence the low flow rate region is more sensitive to error's and will tend to show a higher relative error compared to other regions.

$$\delta x = \frac{\Delta x}{x} = \frac{|x_{est} - x|}{x} \tag{6.14}$$

Fig. 6.18 (e) and (f) show the head estimator's performance. The estimated head error has dropped to between 0.5 % to 1 % over almost all of the pump's operating area (speeds above 1200 rpm, any flow rate). The error increases at very low values of head ($\sim$ 1 %), but is typically below 6% at this worst case.

For comparison, the QP (flow-power) curve method described in [33] was operated at a number of speeds with fixed valve position and measured errors below 3 % at 100 % speed, with errors increasing above 15 % below 50 % speed. More generally, the region of flow rate error below 10 % was described as 61 % to 87 % of Q_{BEP} (flow rate at the pump's best efficiency point) at 70 % speed, increasing up to 29 % to 144 % of Q_{BEP} at 120 % speed. Compared to the proposed method, the QP curve method from [33] only offers accurate flow rate estimation in a narrow range of flow rates when operating away from the nominal speed of the motor and pump.

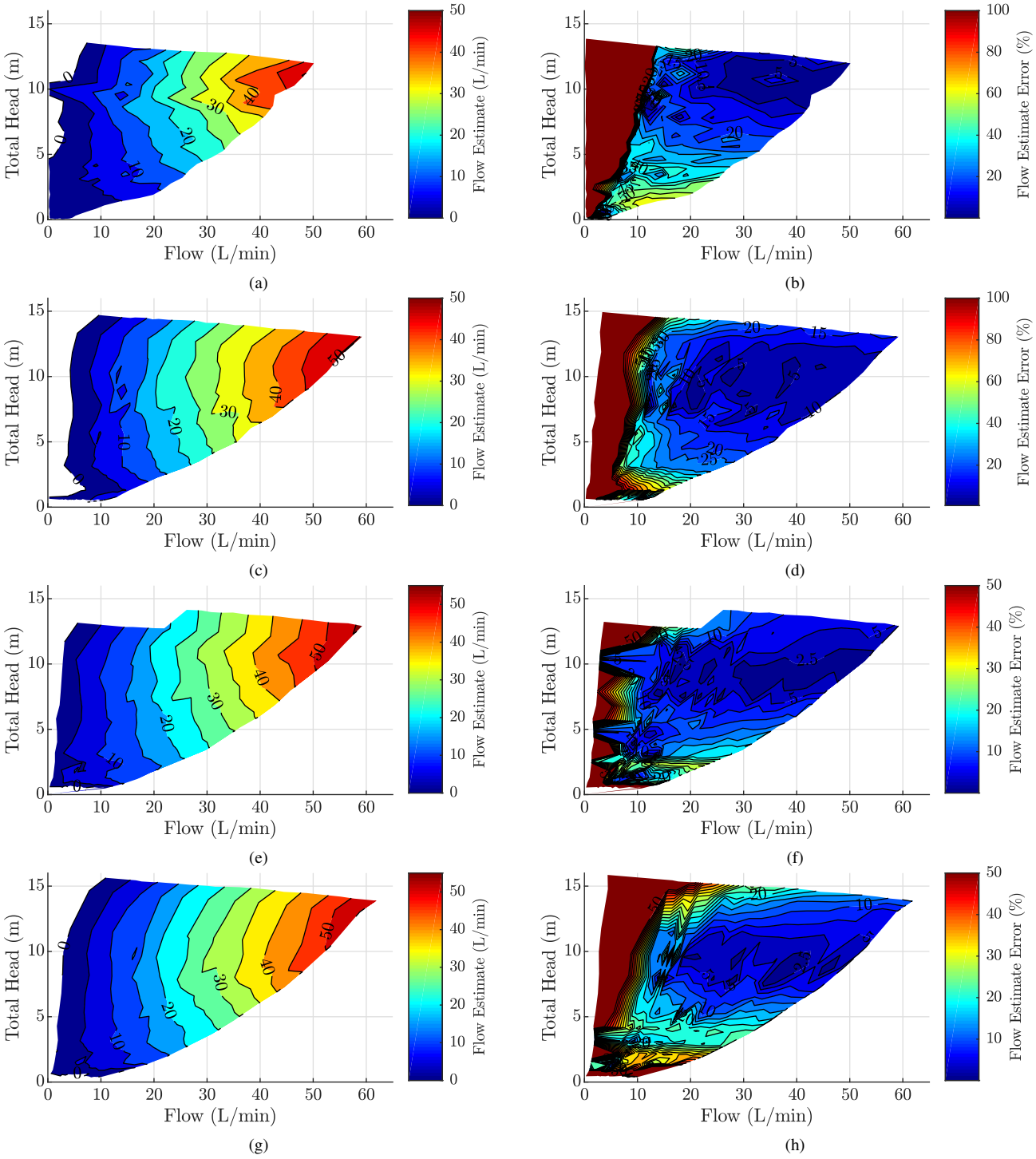

FIGURE 6.17: Flow estimator performance for all three pump models, including (a), (c), (e), (g) the flow estimate contours and (b), (d), (f), (h) flow estimator error. The first model is shown in (a) and (b), the second model is shown in (c) and (d), the third model is shown in (e) and (f), and the third model operated over a more tightly controlled motor temperature range is shown in (g) and (h).

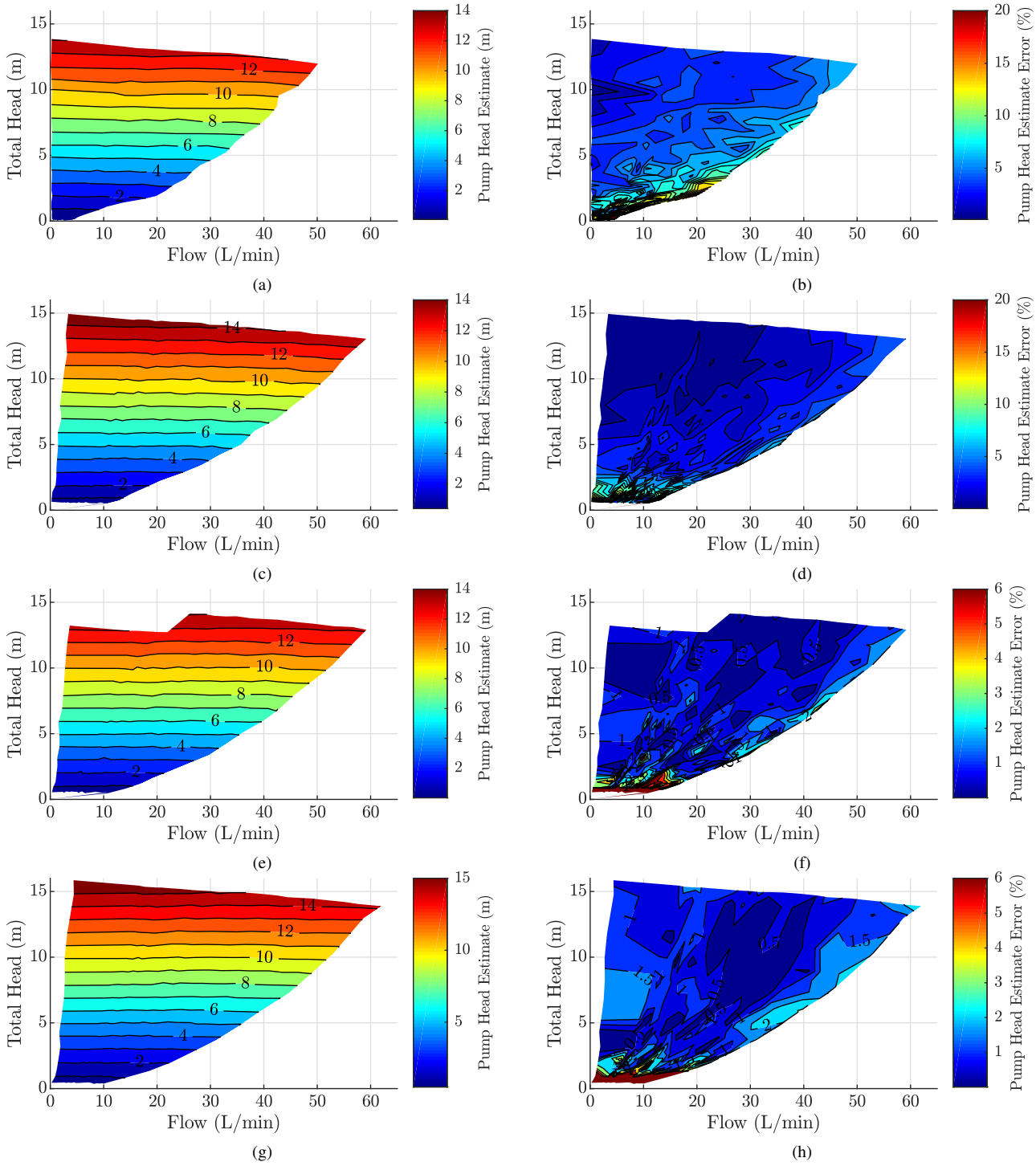

FIGURE 6.18: Head estimator performance for all three pump models, including (a), (c), (e), (g) the head estimate contours and (b), (d), (f), (h) head estimator error. The first model is shown in (a) and (b), the second model is shown in (c) and (d), the third model is shown in (e) and (f), and the third model operated over a more tightly controlled motor temperature range is shown in (g) and (h).

[33] also demonstrated low flow rate errors below 5% over a speed range of 40 % to 110 % using the hybrid process curve method. This method used the QP curve estimate to curve fit the hydraulic system curve, then used the speed estimate and affinity laws to transform the pre-measured pump QH curve and find the intersection location with the system curve (the intersecting point giving the estimate of flow and head). Although this method provided good flow rate accuracy over a wide speed range, the method is fundamentally limited to fixed system curves that do not change over time. Consequently, it does not provide a good comparison to the proposed method that provides flow and head estimates for a wide range of speeds and system curves, including changing system curves.

The boundary curve method in [18] produced low flow rate estimation errors on the order of 0.6 % to 1 % at four speed ranges (60 %, 73 %, 87 % and 100 %) with a fixed valve position, and at four valve positions (25 %, 50 %, 75 %, 100 %) with a fixed speed. [18] also measured the performance of three other methods, including the process curve method from [33], demonstrating high errors from the method under variable valve control. The boundary curve method from [18] has lower error than the proposed estimation method, however performance was only shown at a limited number of operating points. The performance of the boundary curve method over the wider pump operating area is unknown.

It should be noted that both methods discussed in [33] and [18] consider non-integrated and larger scale industrial pumps driven by induction machines with variable speed drives. In the case of [18], the pump estimation method is implemented using a PLC connected to a computer running MATLAB. Neither of these methods consider an estimation method fully implemented inside the inverter, nor do they consider the practical limitations of such an implementation.

Flow rate and head pressure estimation has also been demonstrated in blood pumps. [37] implemented flow rate estimation for a BLDC powered pump by linearising the current versus flow curve, and implemented head pressure estimation using a second order polynomial in terms of speed. [37] reported flow estimates having a mean difference of 2 % from the measured flow, with maximum error of 0.56 L/min (flow range of 0 to 10.5 L/min), and a pressure estimate with mean difference of 5.6 % from the measured values, with a maximum error of 30.7 mmHg (4.09 kPa) over a 600 mmHg range (80 kPa). Results plotted in [37] show flow rate estimate errors of about 3 % near maximum flow, and up to 25 % at very low flow, and pressure estimate errors of 3 % to 14 % between high and mid pressure. Note that the *mean difference* refers to the difference between two means taken from two different groups of data.

[38] investigated the flow rate control performance of a blood pump using a

fuzzy logic controller. The flow rate estimate was produced using a second order two dimensional polynomial that used speed and differential pressure measurements. Although the control system performance was the main focus, the flow rate estimator was noted to have an offset (error) of 0.5 L/min between 5 to 6 L/min at pressures above 250 mmHg. This offset corresponds to a relative error of 8.3 % to 10 %.

Dynamic estimates of pulsitile flow and pressure were investigated in [39]. A steady state model flow estimator of third order power and second order speed was then fed into a dynamical model (digital filter) to produce the dynamic flow rate estimate for the integrated motor-pump device. The head pressure was then estimated using another digital filter using inputs of speed and the flow estimate. For the mock loop tests, the flow rate estimate had a mean absolute error of 0.323 L/min over a range of 0 to 12 L/min. The estimated pressure had a mean absolute error of 7.682 mmHg (1.024 kPa) over a range of 40 to 180 mmHG (5.3 to 24 kPa). The results plotted in [39] show a scatter of points with errors up to 15 % of flow and 20 % of the head pressure in the middle of each respective measurement range. The mean absolute errors for both quantities reflect a typical relative error of 3 % at the full scale of the range, with that relative error increasing toward the lower end of the measuring range.

The results from blood pump studies shows that similar to slightly better flow rate estimation performance was achieved to the proposed method, but head pressure estimator performance was not as good as the proposed method. Moreover, like the industrial pump studies, the blood pump studies only demonstrate the performance of narrow operating regions, and not over the full combination of speeds and system curves. Hence it is difficult to directly compare the performance of these methods.

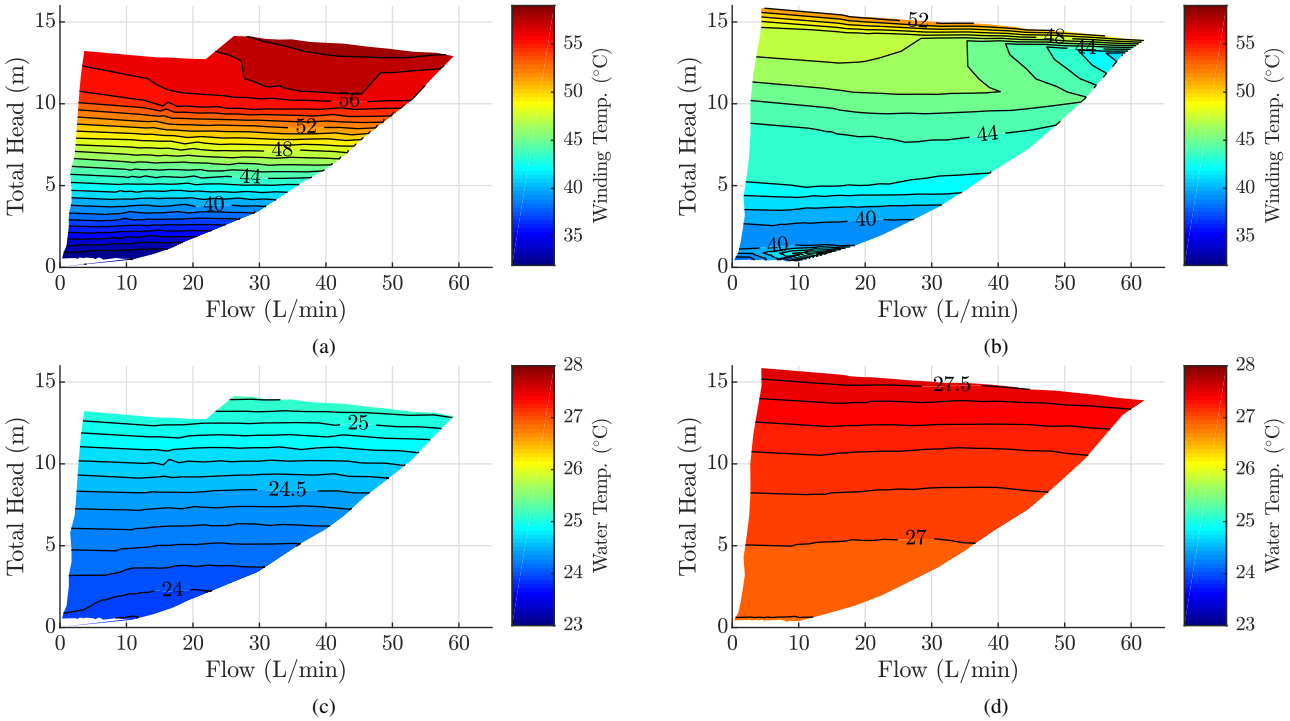

FIGURE 6.19: Motor stator winding temperatures (a), (b), and pump water temperatures (c) and (d) during testing. The original (not temperature controlled) test is shown in (a) and (c), and the temperature controlled (heated and cooled) test is shown in (b) and (d).

6.5 Temperature Effects

Because a pump has a power proportional to the cube of the speed ($P \propto n^3$), the wide operating range means there is a large difference in power and losses over the operating area. This translates to a large difference in the steady state operating temperature over the operating area. Consequently, modelling and verification tests were performed with an unregulated motor temperature, where the motor was allowed to warm up in response to the increase in power. The motor stator winding temperature and water temperature are shown in Fig. 6.19 (a) and (c) respectively.

To investigate temperature effects, the pump system was tested again with a different operating temperature. The autonomous test system was configured to regulate the temperature of the motor stator winding, by temporarily applying high speed/power or low speed/power set points during the test (in between test points). To assist in cooling the motor, a large fan was used to provide general forced air cooling for the second half of the test. The motor stator winding temperature and water temperature are shown in Fig. 6.19 (b) and (d) respectively. The result is a motor stator winding operated over a 12°C range (compared to the

original 25°C range), with the majority of the operating area having a temperature range of 7°C. Note the water temperature was also between 2.5 to 3°C higher than the previous test, however such a small change is expected to have only a mild impact on the hydraulic performance of the pump (see Fig. 6.5).

The performance of the third pump model's flow rate estimator is shown in Fig. 6.17 (e) and (f) for original operation without temperature regulation, and shown in Fig. 6.17 (g) and (h) for temperature regulation (temperature different from the modelling temperature). When operated at a different temperature, the flow rate estimator still achieves an error less than 2.5 % to 5 % in the centre of the operating area, however the error around the left (low flow), top (high head) and bottom (low head) has increased. For the majority of the operating area, the increase is between 0 % to 5 %, with this number increasing around the left (low flow) and bottom (low head) edges.

The performance of the third pump model's head estimator is shown in Fig. 6.18 (e) and (f) for original operation without temperature regulation, and shown in Fig. 6.18 (g) and (h) for temperature regulation (temperature different from the modelling temperature). The head estimation error appears to be less affected by the operating temperature of the motor. Estimation error below 0.5 % is still seen for parts of the operating area, with the majority of the operating area experiencing an error increase between 0 % and 1 %.

For both tests (original unregulated and regulated temperature test), the performance of the other estimators is shown in Figs. 6.20–6.22. The speed and torque estimator error is shown in Fig. 6.20, both for the original inverter estimator (from auto-identified motor parameters) and the proposed estimator. Both of the proposed estimators show significant improvements over the original inverter estimators. The proposed speed estimator shows a small sensitivity to temperature at the bottom of the operating area (low speed, low power). Over almost all of the operating area, the speed error is less than 2 %, with over half of the operating area having an error below 0.2 %. The proposed torque estimator shows more of a temperature sensitivity, with increases in error between 0 % to 3 % over the most of the operating area. In both cases the error is below 5 % over almost all of the operating point range, with the non temperature regulated torque error below 2 % for over half of the operating area.

The performance of the power estimators is shown in Fig. 6.21. For the original (no temperature regulation) test, the DC, AC and mechanical power estimators demonstrate an error on the order of 1 % to 2 % over the majority of the operating area, with small high error regions at low head (low speed and low power). The pump power estimator has an error on the order of 2.5 % to 10 % over most

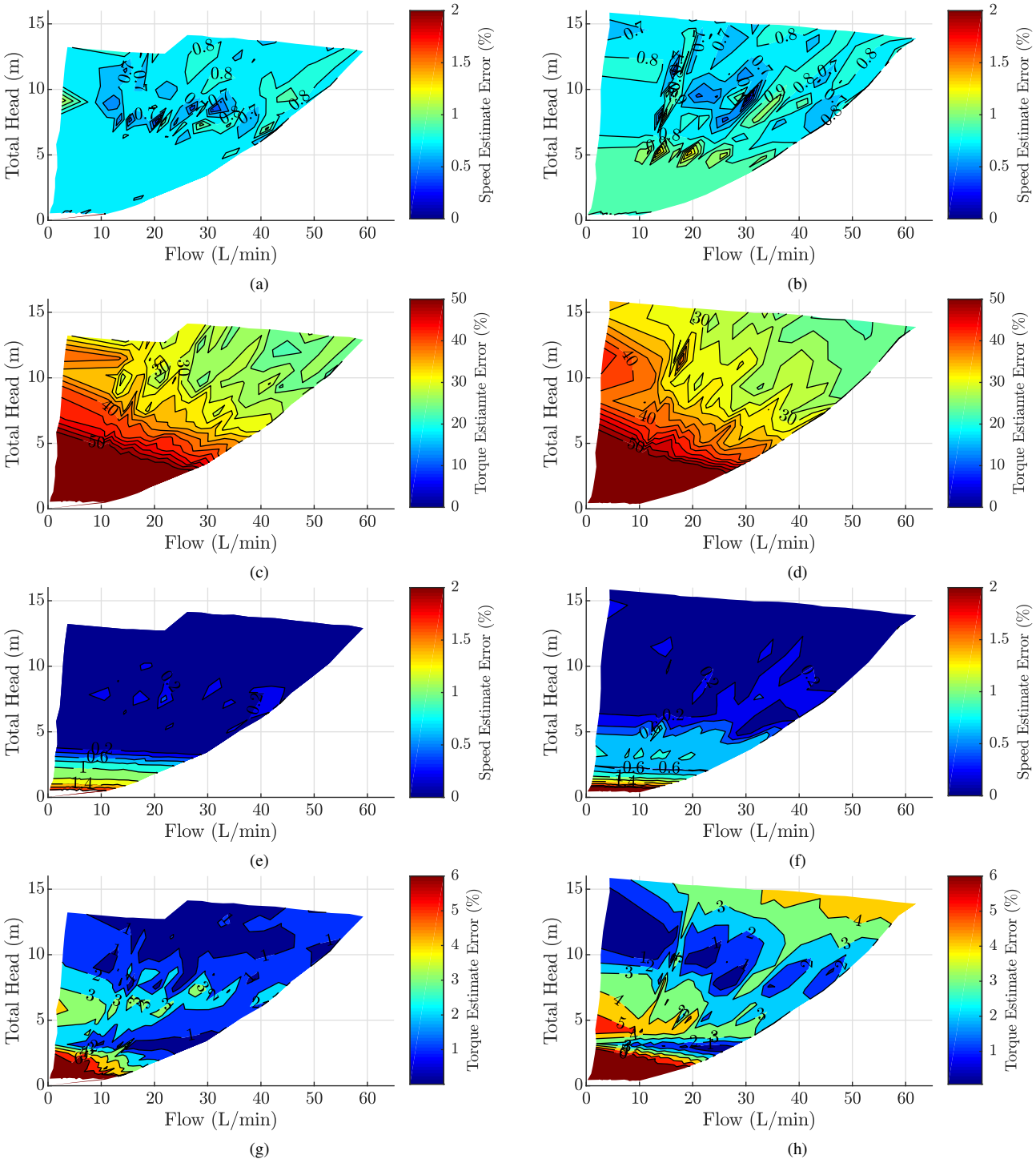

FIGURE 6.20: Torque and speed estimator errors for a pump application, for (a), (c), (e), (g) non-temperature controlled operation, and for (b), (d), (f), (h) temperature controlled (heated and cooled) operation. The original torque and speed estimator methods are shown in (a), (b), (c), (d). The proposed torque and speed estimator methods are shown in (e), (f), (g), (h).

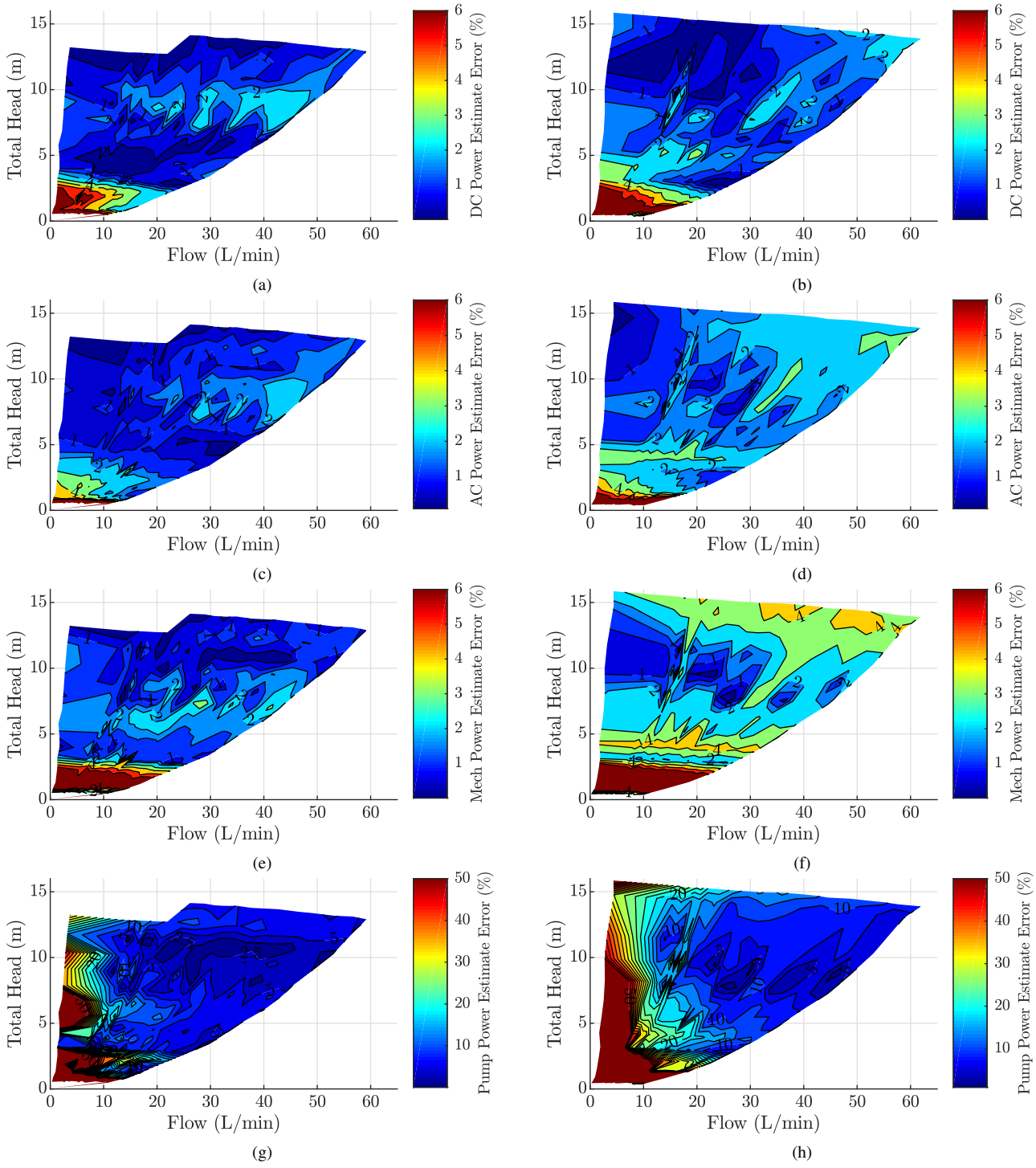

FIGURE 6.21: Power estimator errors for a pump application, for (a), (c), (e), (g) non-temperature controlled operation, and for (b), (d), (f), (h) temperature controlled (heated and cooled) operation. The inverter DC input power estimator error is shown in (a) and (b). The inverter AC power output estimator error is shown in (c) and (d). The mechanical power estimator error is shown in (e) and (f). The pump hydraulic power estimator error is shown in (g) and (h).

of the operating area, but increases toward 50 % at low flow and head. Considering pump power is proportional to the product of total head and flow rate, it follows that the difficulty in modelling and estimating flow rate also translates into a difficulty to model and estimate the hydraulic power. When operated at a different temperature (through the temperature regulation), all power estimators show an increase in error between 0 % and 3 %, except for the pump estimator that shows an increase on the order of 5 % to 20 % (or higher along the left edge of low flow).

The efficiency estimator performance is shown in Fig. 6.22. The errors are displayed as the magnitude of the absolute difference between the measured and estimated efficiency. Because the inverter calculates the efficiency from the power estimator models, it follows that errors in these estimates will affect the efficiency estimates. Inverter and motor efficiency estimates are typically within 0.5 % for most of the operating area, with a mild increase in error when operating at a different temperature. The motor efficiency estimator is more temperature sensitive at low head (low speed and power).

The pump efficiency estimator error, shown Fig. 6.22 (e) and (f), does not offer the same performance as the other estimators, however the error is typically below 2 % over most of the operating range. When operated at a different temperature, there is a noticeable increase in the error, however the pump efficiency estimate error is typically below 4 % over most of the operating range. Because the pump efficiency is the lowest compared to the other component efficiencies, it is naturally the dominant component when measuring the system efficiency. It follows that the system efficiency estimator will have performance reflecting the pump efficiency estimator. In this case, a notable increase in error when operating at different temperatures was observed. However, the system efficiency estimate error was not as high as for the pump efficiency estimate, and instead the error was below 1 % for most of the operating area, and below 2 % for most of the operating area when operating at a different temperature.

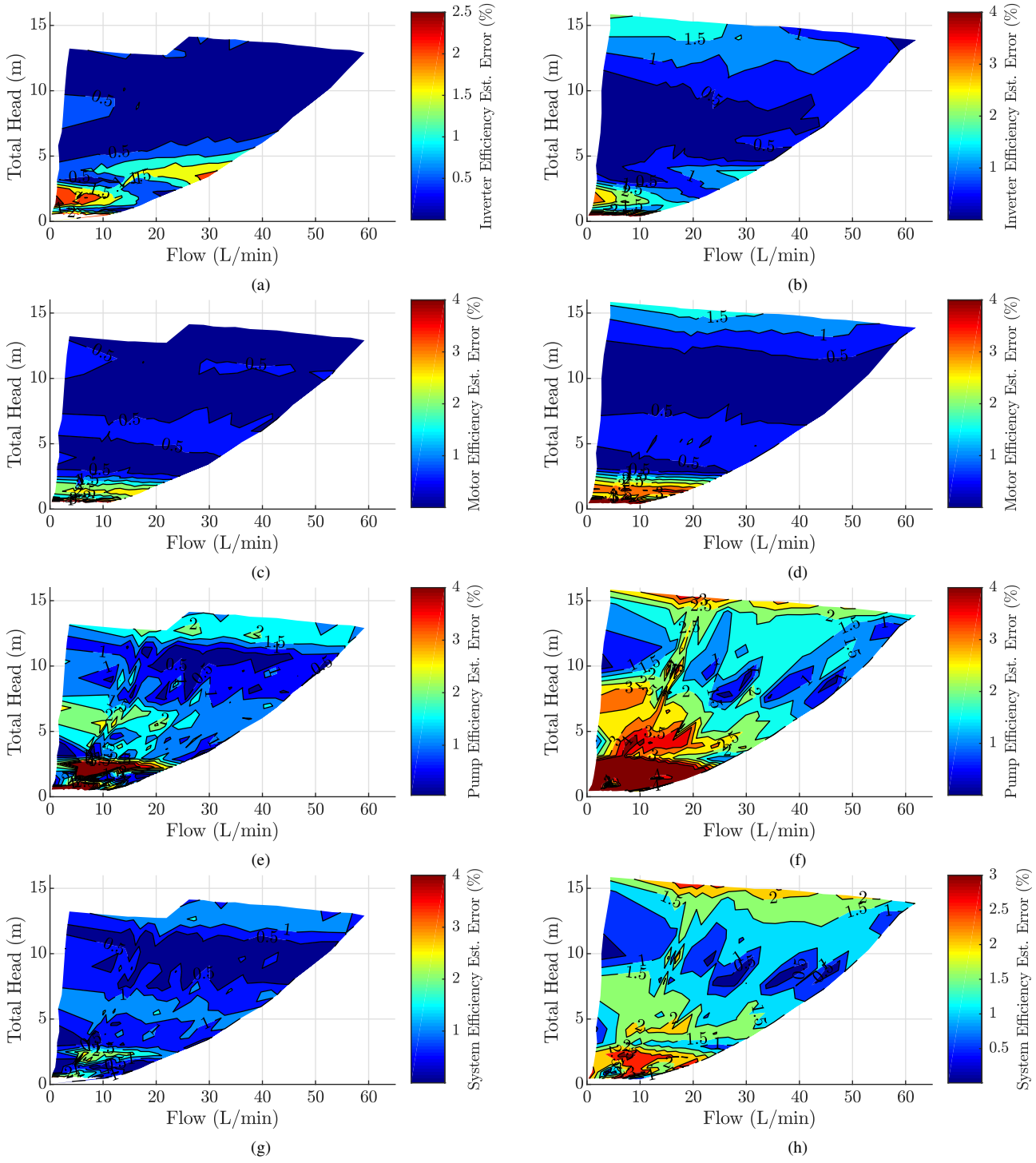

FIGURE 6.22: Efficiency estimator errors for a pump application, for (a), (c), (e), (g) non-temperature controlled operation, and for (b), (d), (f), (h) temperature controlled (heated and cooled) operation. The inverter efficiency estimator error is shown in (a) and (b). The motor efficiency estimator error is shown in (c) and (d). The pump efficiency estimator error is shown in (e) and (f). The system efficiency estimator error is shown in (g) and (h).

6.6 Dynamic Performance

The primary focus of the pump estimators was on steady state performance, and the estimators were not designed to provide accurate estimates during dynamic or transient conditions. Despite this, the dynamic performance of these estimators was investigated to better understand their behaviour under dynamic and transient conditions.

To enable transient data to be captured, the pump measurement module of the autonomous test software was reconfigured to disable the low pass filter and log data at 50 Hz. The low pass filter was previously used to remove signal noise from the 4 to 20 mA analogue signals from the pressure sensors and flow meter. This new configuration permitted high bandwidth data to be collect at the expense of more signal noise.

The inverter software remained unchanged, reusing the same control system and estimator design. The maximum acceleration limit (a run time configuration setting) was increased from 200 rpm/s to 600 rpm/s, allowing for sharper acceleration steps to be produced. The inverter was also polled at 20 Hz (instead of 10 Hz), allowing for higher bandwidth signals to be recorded.

The first set of dynamic tests considered a series of speed steps from 100 rpm to a target speed then back to 100 rpm. Fig. 6.23 shows a series of speed step responses with the control valve open, allowing for maximum flow. A key observation from Fig. 6.23 (c) is the overshoot in the flow rate estimator during acceleration and deceleration respectively. The cause of this overshoot can be attributed to additional torque (load) being present during acceleration, as needed to satisfy Newton's second law for rotational systems. The increase in torque causes an increase in q-axis current, however the flow rate estimator cannot distinguish between torque from the pump and torque required to accelerate the rotational inertia of the system. Likewise, the negative overshoot represents a sudden drop in torque and q-axis current during deceleration.

Fig. 6.24 shows a series of step responses, but with the control valve almost closed. The same overshoot can be seen in Fig. 6.24 (c). In the middle of each step (when the motor has reached the set point speed and has returned to steady state), the flow rate estimate returns to a value very close to zero. However, at lower speed the estimated flow error is much larger, and in this case produces a negative flow rate estimate.

Unlike the flow rate estimate, the dynamic head pressure estimate in Fig. 6.23 (b) and Fig. 6.24 (b) shows very little overshoot. In both figures, the estimated head pressure tracks the measured head pressure quite well, with no observable

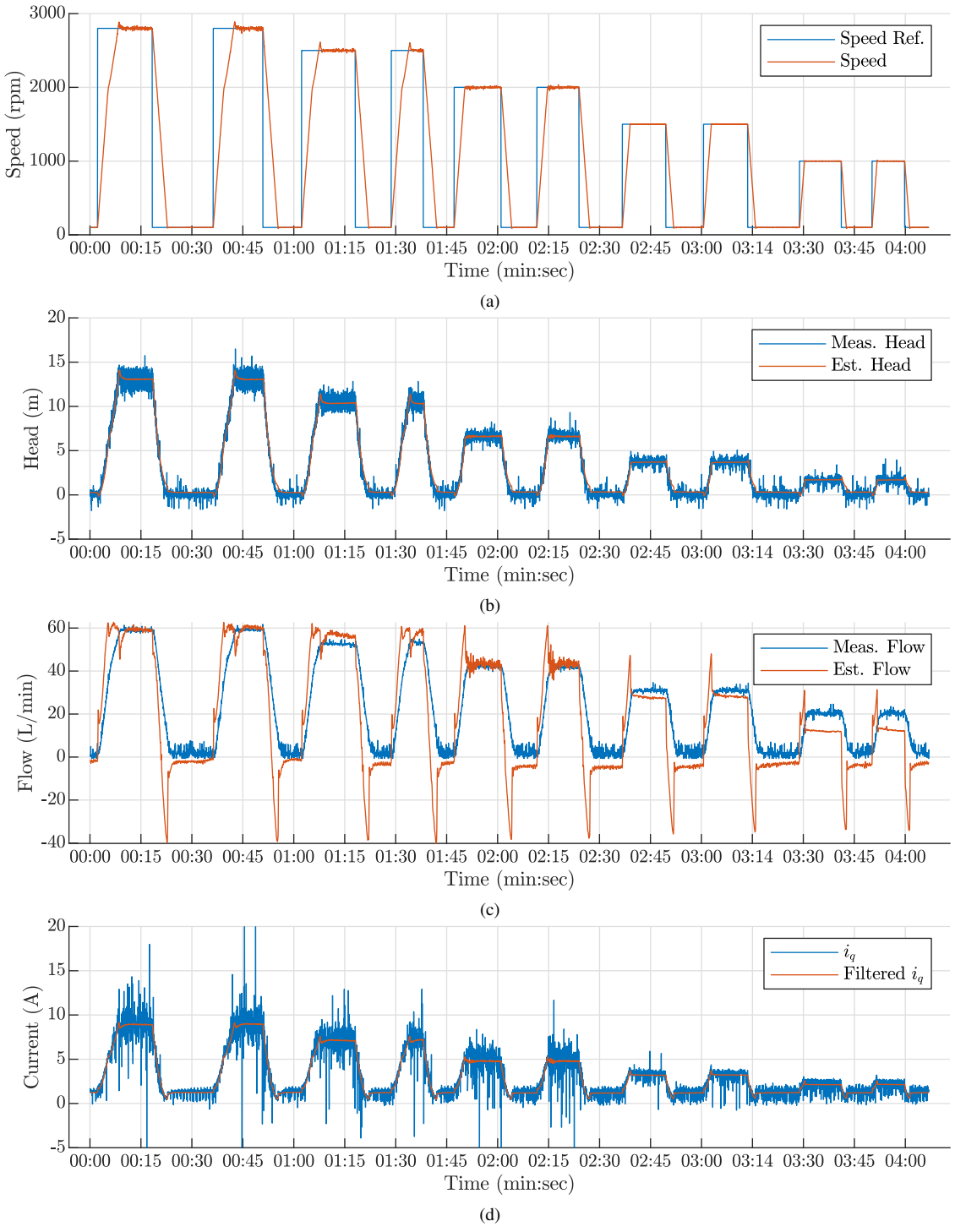

FIGURE 6.23: Dynamic step responses of the pump estimator model with valve open. The speed (a) is stepped between 100 rpm and 2800 rpm, 2500 rpm, 2000 rpm, 1500 rpm and 1000 rpm. Note the acceleration is limited to 600 rpm/s. The measured and estimated pump head is shown in (b). The measured and estimated flow is shown in (c). The inverter q-axis current and low pass filtered q-axis current are shown in (d).

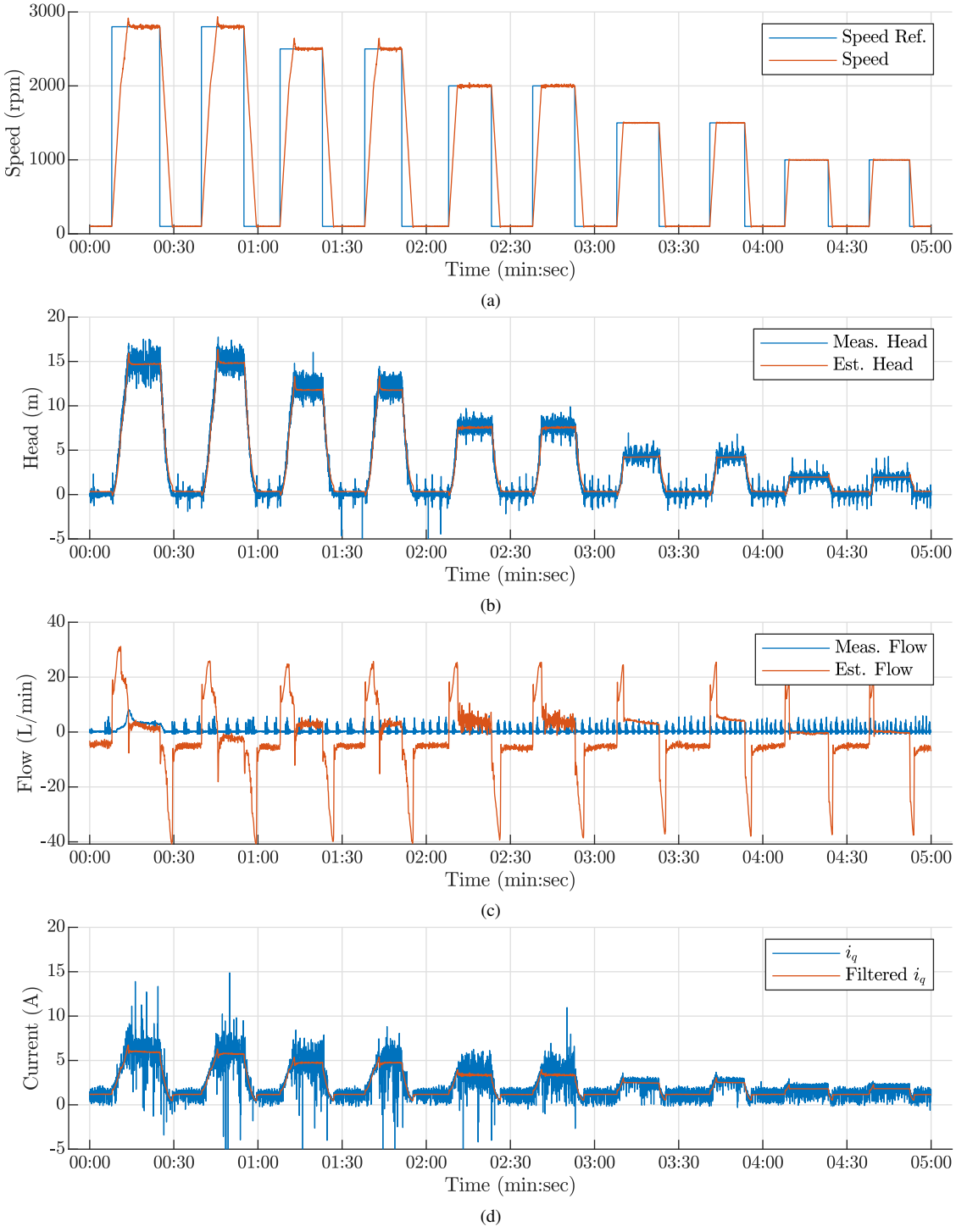

FIGURE 6.24: Dynamic step responses of the pump estimator model with valve closed. The speed (a) is stepped between 100 rpm and 2800 rpm, 2500 rpm, 2000 rpm, 1500 rpm and 1000 rpm. Note the acceleration is limited to 600 rpm/s. The measured and estimated pump head is shown in (b). The measured and estimated flow is shown in (c). The inverter q-axis current and low pass filtered q-axis current are shown in (d).

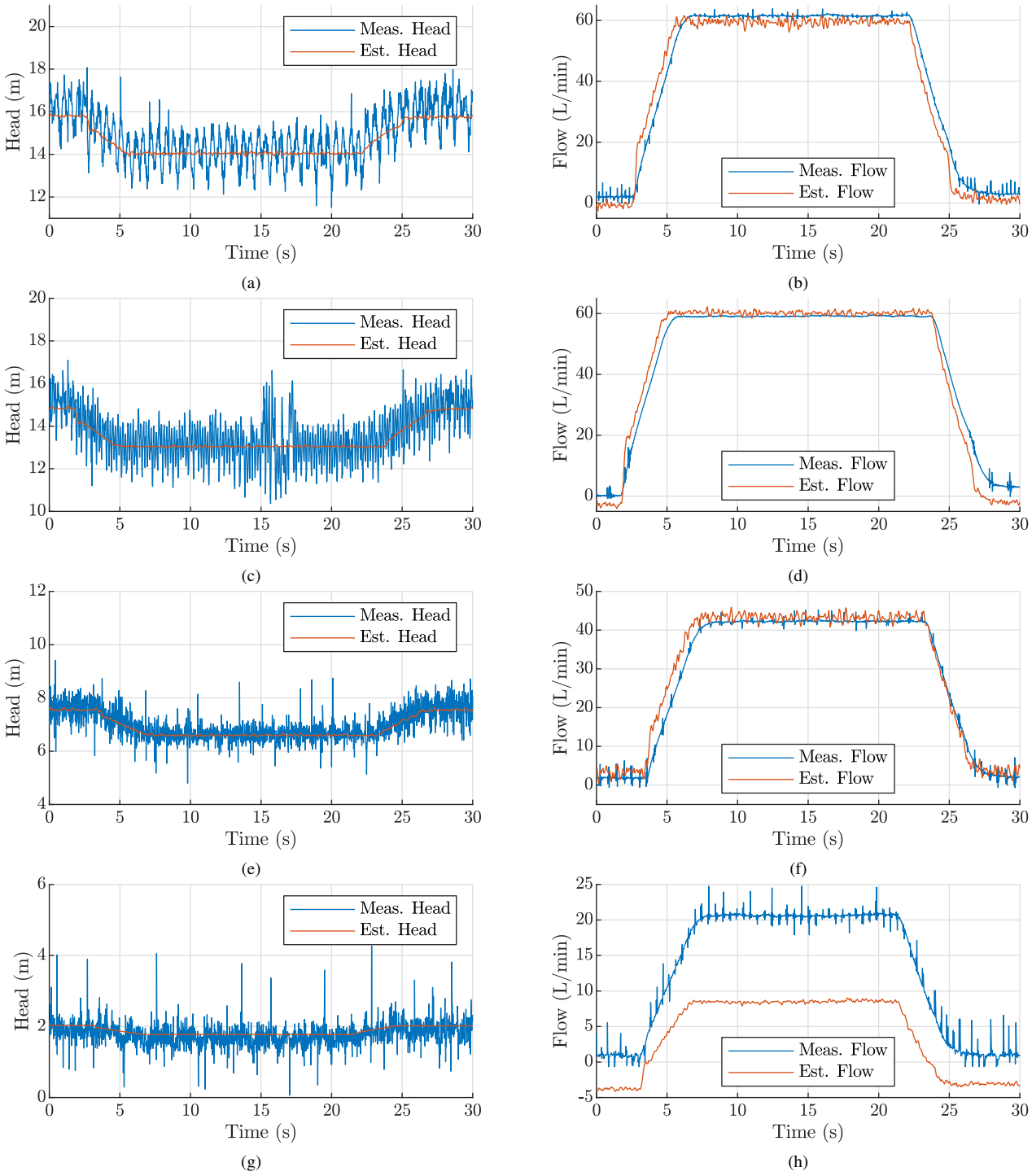

FIGURE 6.25: Dynamic responses of the pump estimator model to valve step changes. In all plots, the motor is operated at constant speed and the valve is stepped fully open then fully closed. The measured and estimated pump head is shown in (a), (c), (e), and (g). The measured and estimated flow is shown in (b), (d), (f), and (h). The pump is operated at speeds of 2900 rpm (a), (b), 2800 rpm (c), (d), 2000 rpm (e), (f), and 1000 rpm (g), (h).

phase delay. In contrast, the flow estimates both show rise and falls starting just before the measured flow rate rises and falls. Even though filtering of the analogue signals was disabled, the electromagnetic flow meter still includes a small amount of low pass filtering as part of its internal signal processing. Hence the measured flow rate will include a small delay.

Fig. 6.23 (d) and Fig. 6.24 (d) show the measured q-axis current from the inverter, before and after low pass filtering. Before filtering, the i_q signal shows a very large noise component with significant fluctuations. The problems caused by these large fluctuations was discussed in Section 6.4.4. After filtering, the signal was smoother and suitable for use by the estimators.

The second set of dynamic tests considered a series of valve steps applied to the pump system operating at different speeds. Each valve step (valve open then closed) represents a sudden change in the underlying hydraulic system curve, and also simulates a typical pump use case where a down stream flow control valve (e.g. a tap or a valve in a HVAC system) is used to provide local flow control to a small branch of the hydraulic system. Four step responses are shown in Fig. 6.25, each at a different pump operating speed.

The first three step responses (Fig. 6.25 (a)–(f)) show very good tracking of both instantaneous head and flow measurements. The head measurements contain significant noise in the analogue sensor signals, likely coupled from the nearby high frequency inverter output wiring. Despite this noise, the inverter's head estimate shows good agreement with the underlying trend in the measured data, where the estimate line sits in the middle of the noisy measured signal. The measured flow rate signal was less affected by noise, and shows good agreement in with the estimated flow rate signal, both in transient and steady state conditions. This is in contrast to the speed step changes, where the flow rate estimator could not accurately track the flow during changes. Again, the flow rate estimate has a slightly faster response compared to the measured flow rate, resulting from the small delay caused by the flow meter's inbuilt filtering and signal processing.

The last step response (Fig. 6.25 (g) and (h)) shows the head and flow estimator performance when the pump system is operated at 1000 rpm, located close to the bottom of the pump's head-flow operating area. At such a low speed, the head estimate shows a small misalignment with the measured head, but otherwise tracks the changes in the pump's total head. The flow rate shows significantly worse performance. The estimated flow rate with valve (almost) closed had an offset of -5 L/min compared to the measured flow, with this offset changing to approximately -12 L/min when the valve is open. Considering the shape of the flow rate step is the same as the measured flow rate, the poor performance

of the dynamic estimate can be attributed to the general performance of steady state flow estimator model at low speeds. Improving the steady state flow rate estimate at low speeds would naturally improve the dynamic flow rate estimate for fixed speed operating conditions.

6.7 Volume Estimate

In addition to head and flow rate estimates, an estimator for the total volume of liquid pumped was also included in the inverter. Considering that flow rate is the change in volume over time ($Q = \frac{dV}{dt}$), the volume can be estimated by integrating the estimated flow rate over time. Inside the inverter, discrete numerical integration was performed using the Euler method via Eq. (6.15). $V_{est}(k)$ is the volume estimate of the k^{th} sample, $V_{est}(k-1)$ is the volume estimate of the last sample, $Q_{est}(k)$ is the flow rate estimate of the k^{th} sample, and ΔT is the time step between integration.

$$V_{est}(k) = V_{est}(k-1) + \Delta T \cdot Q_{est}(k) \tag{6.15}$$

Because the inverter's DSP used a fixed point number system with limited dynamic range, careful attention was required when choosing scaling factors to avoid numeric overflow. For the Davey XF171 pump, the maximum flow rate of 175 L/min, or 2.917 L/s, was used as the upper limit. The volume upper limit was set such that it would be reached if the pump operated at the maximum flow rate for one day. At 175 L/min, this corresponds to an upper limit of 252000 L. The fixed point volume estimate scaling was set to 2000 litres per unit, such that the maximum fixed point value of 127.99999994 would correspond to 255999.999880 L. Conversion back to units of kL requires multiplying the per unit volume by 2. Exceeding the maximum per unit value would cause the volume to wrap to -128 per unit (-256 kL), hence the software implementation of the integration needs to also handle numeric overflows and correctly wrap the overflow back to zero.

To allow for the flow rate estimate to be correctly integrated, the flow rate must be converted from litres per second to per unit volume per second. This is done by multiplying the flow rate estimate by 1/2000 (0.0005) per unit per litre, noting that the inverter's DSP can perform fixed point multiplication very quickly compared to division. Also note that the value of 0.0005 cannot be exactly represented in the fixed point numeric system, and is instead represented as $8389/2^{24} = 0.000500023365$. This scaling factor only uses 14 bits out of the 32

bit range of a fixed point value, and multiplying by a 1.0 per unit value (i.e. 1 L/s flow represented with 24 bits of precision) reduces the flow rate to only 14 bits of precision before integration (approximate loss of 10 bits of precision). Lower flow rates are more affected by this phenomena. For example, a flow rate of 0.01 L/s uses only 18 bits of precision, but after conversion to per unit volume per second the flow rate only uses 7 bits of precision.

To complete the integration, the interval between each integration step ΔT must be chosen. Generally, Euler integration has lower error when using smaller time steps (lower ΔT), however smaller time steps reduce the size of each flow rate value added to the accumulated volume, further reducing numeric precision and leading to increased integration error. A compromise was made be setting $\Delta T = 1$ s, such that the scaled flow rate experienced no further loss in precision, and the integration was still frequent enough to capture changes in the flow rate.

The performance of the volume estimate was measured over two tests. In both cases, the measured volume was calculated from the flow rate measurements using cumulative trapezoidal integration. Fig. 6.26 shows the performance of the volume estimator during the verification test for the third pump model (see Section 6.4.7). The volume estimate agrees with the measured estimate at the start of the test, but slowly drifts over time as seen in Fig. 6.26 (b). Considering numeric integration accumulates even the smallest errors, some drift is expected. Fig. 6.26 (c) shows that the difference between the volume estimator and measured volume increased the most (larger slope) at the start and end of the test. At about $^3/_4$ through the testing, the slope of Fig. 6.26 (c) becomes flat, indicating the two volume estimates are increasing at the same rate as a result of much lower flow rate estimator error in this region.

TABLE 6.8: Pump volume measurements at the end of Fig. 6.26.

Measured Volume (L):	3030.2644
Estimated Volume (L):	2744.2094
Difference (L):	286.055
Relative Difference (%):	9.4399

TABLE 6.9: Pump volume measurements at the end of Fig. 6.27.

Measured Volume (L):	725.1225
Estimated Volume (L):	633.3182
Difference (L):	91.8043
Relative Difference (%):	12.6605

Table 6.8 provides a summary of the volume estimator at the end of Fig. 6.26. When measured over the entire operating area with approximately equal time spent at each operating point, the resulting volume estimate error was 9.44 %.

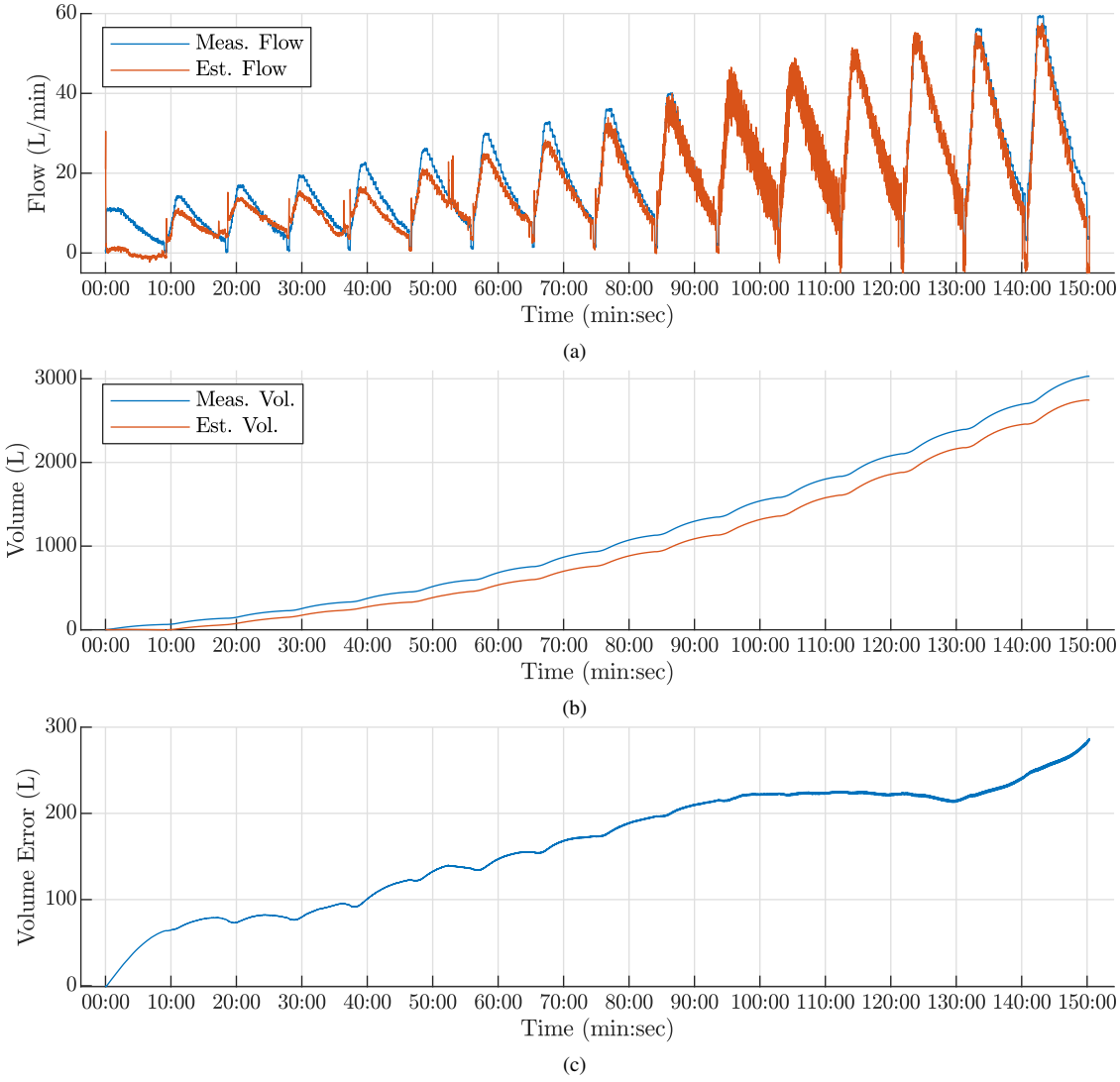

FIGURE 6.26: Pump volume estimator performance during the third pump model verification test. The measured and estimated flow is shown in (a). The measured and estimated volume is shown in (b). The error between the estimated and measured flow rates is shown in (c).

Fig. 6.27 shows the performance of the volume estimator during all of the dynamic tests discussed in Section 6.6. As seen in Figs. 6.23 and 6.24, step changes in speed caused significant flow rate estimation error. Consequently, it is expected that these dynamic changes will result in larger errors in the volume estimate. Fig. 6.27 (c) shows that this is indeed the case, where the volume error increases more (larger slope) during the speed step tests in the first half of Fig. 6.27. During the second half of Fig. 6.27 (c), the slope in the volume error is much lower as a result of lower flow rate errors for these tests (see Fig. 6.25).

Table 6.9 provides a summary of the volume estimator at the end of Fig. 6.27. Under dynamic conditions the volume estimate increased to 12.7 %. Although

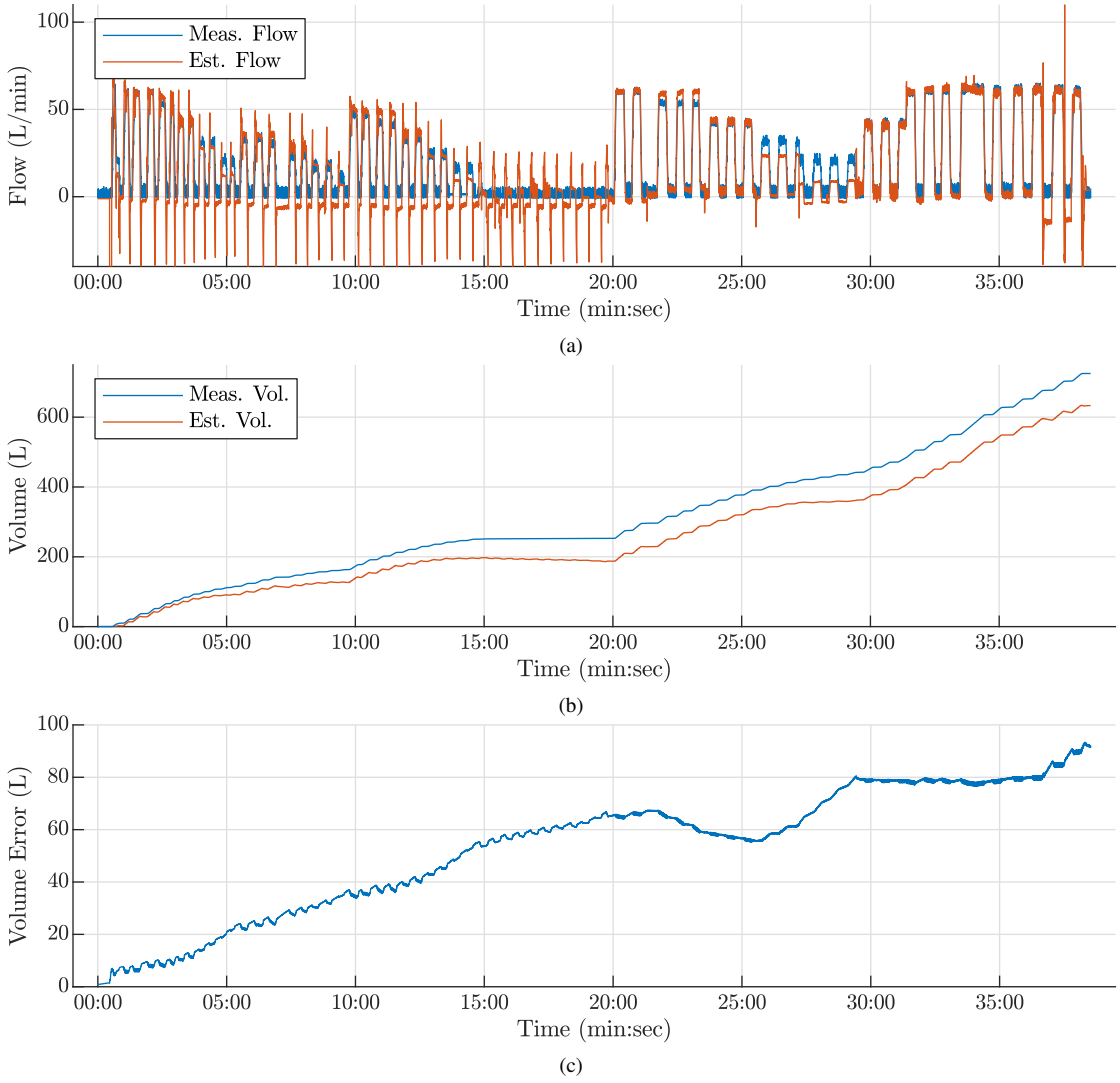

FIGURE 6.27: Pump volume estimator performance corresponding to the dynamic tests in Fig. 6.23–6.25. The measured and estimated flow is shown in (a). The measured and estimated volume is shown in (b). The error between the estimated and measured flow rates is shown in (c).

these volume errors may appear high, they are quite suitable for applications that require control over a pumped volume, but do not require precise control over the exact volume pumped. Considering both volume estimates were lower than the measured volumes, these estimate errors would not have an adverse affect on a pump application where a fixed volume of liquid needed to be pumped in a given time. For example, the filtering of water in a swimming pool or supplying water to an irrigation system. In these examples, the volume estimator allows the integrated pump system to respond to changes in the hydraulic system (e.g. filter partially blocked, taps/valves in different positions) while still delivering the required volume of water.

6.8 Conclusion

This chapter extends upon the sensorless estimation method introduced in Chapter 5 to provide state estimation of the end application/load of an integrated motor system. A pump system was chosen as the landmark application of the method because such a system includes all components of a typical motor drive system, can be manufactured as an integrated system, and has wide spread usage. Pump applications can also utilise a wide operating area, work well with position sensorless motor control, and can benefit from the elimination of external sensors in feedback control schemes.

The proposed method leverages automated efficiency map testing to produce comprehensive models that intrinsically capture loss components and component interactions. A pump load is non-linear and particularly difficult to characterise, however the method used was sufficiently detailed to capture these more complex relationships yet was computationally efficient enough to allow for real time processing on low cost motor drives with limited processing. Even though the pump models were more complex compared to general motor models, the testing effort and analysis was no more difficult than for the general motor case.

Experimental results were presented for a small centrifugal water transfer pump, powered by a low power surface PM machine with low cost inverter designed for integrated motor system applications. The pump model was iterated three times, with the key improvements in estimator performance being linked to the use of a narrow band low pass filter to remove signal fluctuations, a more even distribution of test points over the pump operating area, and the use of only the linear operation of the test system's control valve. Flow rate was particularly challenging to estimate, being highly sensitive to measurement error and noise in the q-axis current signal. Use of field weakening is also believed to contribute to the large fluctuations in the q-axis current. The flow rate estimator's error was below 10 % for most of the pump's operating area, with regions showing error below 2.5 %. The pump total head estimator performed much better, with error between 0.5 % and 1 % over most of the operating area.

Estimators for speed, torque, electrical power and mechanical power all provided similar performance to the general motor application, with errors typically lower than 1 % to 2 % over most of the operating area. The original estimators from Chapter 5 were tested with the pump application, but showed increased error when operating outside the original modelling range and when operating with field weakening. Remodelling these estimators to account for field weakening and the new pump operating area significantly improved their performance.

Motor temperature was also found to affect the performance of all estimators to a small degree (0 % to 3 % increase in error), except the flow rate estimator and pump hydraulic power estimator that show more significant increases in error.

Although not designed for dynamic performance, the pump head and flow estimators were tested under a series of transient conditions. It was found that speed step changes caused significant flow estimator overshoot attributed to the estimator not accounting for the additional torque present during acceleration. When operating at a constant speed, it was found that step changes in the valve position (step changes in the hydraulic system curve) could be accurately tracked during the transient.

The estimator for the total volume of liquid pumped had an error of 9.44 % when operated over the entire pump operating area, with that error increasing to 12.7 % during the dynamic tests. In both cases, the estimated volume was lower than the measured volume. The performance of the volume estimator was deemed suitable for pump control applications that need to pump an approximate volume of liquid in a given time while also responding to changes in the system curve (e.g. from filter blockage or changing tap/valve positions).

The experimental results demonstrated that the the performance and suitability of the estimation approach, particularly for low cost integrated motor-pump system applications. The simple implementation and wide operating area allow for this estimation method to replace physical sensors in feedback control systems, and also unlocks the possibility of using feedback control schemes that were otherwise not possible due to cost and/or size limitations. The inclusion of pumped volume and power consumption estimators also enable the operation of a pump system in more flexible and energy efficient ways.

Chapter 7

Conclusion

This thesis focuses on methods to better understand an integrated motor system's operation over a wide operating area, in terms of the real time system state and the efficiency of each system component. Low cost and low power motors represent the largest portion of all motors in the world, however their efficiency is poor. Through a better understanding of the efficiency and operating behaviour of all components, in addition to the application of more efficient feedback control systems, it is possible to improve efficiency and reduce consumption costs for small motor systems. This research has considered techniques for providing sensorless estimates for a large number of motor system real time quantities, with a key focus on these estimates providing good accuracy over a wide operating area but also being simple enough to be implemented in low cost drives.

Using inverter based variable speed drives, a motor can operate over a range of speeds. Combined with a load device, the motor, drive and load form a system that can operate over a wide area of different speed and load combinations. Using voltage and current measurements from the inverter paired with models of the system, it is possible to produce a set of sensorless estimates for various parts of the motor system. Sensorless estimates can replace physical sensors in feedback control systems, increasing reliability and reducing both the size and cost of the motor system. Motor control depends on the quality of feedback signals, hence it is important for sensorless estimates to perform well over the system's operating area.

Position sensorless operation is one of the first and most known forms of motor sensorless estimation. Operation of a permanent magnet (PM) machine requires accurate rotor position information to allow the inverter to apply the correct voltage waveforms that remain synchronised to the machine. The rotor position can be obtained through a sensorless estimate instead of external position sensors, however the quality and error in this estimate limits the operating range of the motor system. Better operating speed range can be achieved through more

detailed models, however these require additional effort to identify all necessary parameters and require a higher performance digital signal processor (DSP). As part of this research, an improved method of position sensorless control for brushless DC motors was developed, enabling wider speed operation compared to methods of similar complexity. The method used was simple enough to be implemented on low-cost motor drive systems. Experimental results were used to verify the operation and performance of the method.

Motor efficiency is one of the key characteristics used when designing and optimising a motor system. Traditional standards have only considered fixed speed efficiency at a small number of load points. Newer efficiency standards consider all the components of a motor system, but still only provide a limited description of efficiency over a motor system's operating area. Efficiency maps provide a good way to describe and visualise the efficiency of a motor, but the required data is difficult and time consuming to collect. To allow for comprehensive efficiency map data to be collected experimentally, a method of autonomous testing was developed. The method was realised as a flexible hardware and software based test system that could be adapted to a range of motor system applications. The experimental test system obtained large volumes of temperature controlled efficiency data, and made it possible to measure and characterise a motor system in greater detail over its operating area.

Using inverter based voltage and current measurements, it is possible to produce estimates of a motor's mechanical output in terms of speed and torque. The performance of these estimates varies over the operating area, and the performance of existing methods is not well understood over the broader operating area of a motor system. Existing torque estimator performance is typically limited by a lack of understanding of the motor's detailed loss components, with this information being difficult to obtain accurately over the motor's entire operating area. By utilising large sets of experimental efficiency data, a new method for general motor state sensorless estimation was developed. Estimator models were developed for speed, torque, DC power, AC power, mechanical power, inverter efficiency, motor efficiency and system efficiency. The estimators were simple enough to be implemented in the firmware of a low-cost inverter, and experimental measurements were used to verify the performance over the operating area of the motor system.

In addition to motor quantities, it is possible to produce sensorless estimation of an end application's quantities. For this research, a pump system was chosen as the landmark application of the sensorless method because such a system includes all components of a typical motor drive system, can be manufactured as an

integrated system, and has wide spread usage. The sensorless method used for motor quantities was extended to a small, low power pump system. The same modelling approach was used, and demonstrated its ability to model the non-linear relationship between motor and pump quantities. Estimator models were developed for pump head pressure, flow, hydraulic power, efficiency and total volume pumped. The performance of the estimators over the system's operating area was experimentally verified, with temperature changes and dynamic performance also being considered. This confirmed the proposed sensorless method's ability to provide comprehensive estimates for multiple components in an integrated motor system, and the method's ability to work with non-linear loads over a wide operating area.

7.1 Key Findings

A method of position sensorless control was introduced, using only terminal voltage measurements to estimate the flux linkage increment in six separate sectors of an electrical cycle. The method was applicable to permanent magnet (PM) machines using brushless DC or trapezoidal operation, where the machine back-EMF was measured from one of the non-driven phase terminals. Key findings include:

- By using terminal voltage measurements synchronised to the pulse width modulation (PWM) waveform produced by the inverter, it was possible to remove the PWM waveform from the terminal voltages measurements without the use of a low pass filter. This allowed for the machine back-EMF to be obtained without any speed (and frequency) dependent phase delays that are present in conventional low pass filter based back-EMF sensorless methods. This allows for effective measurement at any speed over the speed range of the machine.

- In addition to PWM synchronised measurements, careful selection of the modulation pattern and synchronised measurement location (phase relative to the PWM waveform) allowed for a suitable back-EMF waveform to be extracted over the entire PWM duty cycle range. This allows for the inverter to utilise the full PWM range and hence full output voltage range, allowing for wider speed operation (noting that speed is proportional to voltage for a PM machine).

- The method was implemented on a low cost microcontroller with integrated analogue to digital converter (ADC). The use of automatic offset calibration

and gain balancing between phases was able to reduce the impact of error accumulation when integrating low amplitude back-EMF voltages at low speed operation. This improved the low speed performance and reduced the position error, allowing for the method to operate at a much lower speed compared to other back-EMF based methods.

- The method only required one machine parameter (the time independent flux linkage constant). The derivation of this parameter for both trapezoidal and sinusoidal multi-pole machines was shown, and in both cases the constant can be derived from the machine back-EMF constant. This parameter is easily measurable from a PM machine, and does not require any comprehensive testing or analysis to obtain.

- It was found that reducing the PWM frequency increased the settling time between each transient switching event and the ADC sampling point, reducing noise and consequently position error, and ultimately allowing for operation at lower speeds. Reduction of the DC bus voltage also had a similar effect and allowed for lower speed operation.

To better understand the performance of an integrated motor system over a large operating area, a method of autonomous testing was developed. The flexible hardware and software-based test system was adaptable to different motor system applications and collected large volumes of temperature-controlled efficiency data, allowing for a motor system to be characterised in greater detail over its operating area. Key findings include:

- Using a modular hardware and software system, it was possible to measure detailed efficiency maps from both a motor system and pump system, with both systems having different operating area shapes.

- The steady state detector was able to respond to the dynamics of each system, regulating the speed of testing to be as fast as the system dynamics allowed. A simple steady state detection scheme using the standard deviation of a sliding window was sufficient to detect the system steady state.

- For the case of motor system operated along the edge of its torque-speed curve, the steady state detector was able to dynamically find the edge of the motor system's operating area, and adjust the sequence of test points in real time. A simple comparison of the set point and mean feedback signal at steady state was sufficient to detect the operating area edges, and configurable steady state timeouts were also able to detect the onset of control system instability (oscillations starting and a failure to reach steady state).

- The autonomous test sequencer design allowed for the lengthy steady state temperature detection test to be automated, and allowed for the automatic regulation of the motor stator winding temperature to within the $\pm 5^{\circ}$C range required by international motor efficiency testing standards. It was found that the real time predictive model used by the steady state temperature detector could also reduce the detection test time by 25 minutes at the cost of a 0.30°C error.

Using large sets of experimental data, a new method for general motor state sensorless estimation was developed. The estimators were implemented in the firmware of a low-cost inverter, and the performance over the operating area of the motor system was experimentally verified. Later, the method was then extended to a pump system, demonstrating the method's ability to model the non-linear relationship between motor and pump quantities.

- Estimator models were developed for speed, torque, DC power, AC power, mechanical power, inverter efficiency, motor efficiency and system efficiency. All models shared the same third order two dimensional surface polynomial equation, but with coefficients individually set. This provided a good trade-off between the complexity required to capture the motor system state over the full operating area and the simplicity required for implementation in a real time, low cost inverter control system.

- Detailed efficiency map testing was able to provide the large data set required for the modelling approach used. Efficiency measurements naturally capture the power flow and operating points of the system, and the use of autonomous testing allows for this data set to be gathered in a timely manner.

- In addition to external measurements, measurements from inside the inverter's control system were required to complete the modelling of the sensorless estimators. This was achieved through a measurement software module embedded in the inverter's firmware that provide high bandwidth averaging at the current control system's frequency of 15 kHz. Mechanical synchronisation and averaging over an integer number of mechanical revolutions was required to remove noise caused by torque ripple, mechanical oscillations and control system oscillations.

- The speed and torque estimates typically achieved errors of 0.6 % and 2 % respectively over the operating area of the motor system. The torque estimator showed a vast improvement compared to the conventional air-gap

torque estimation method using auto-identified parameters, where an error over 30 % was seen when operating at lower values of torque.

- Power and efficiency estimates achieved errors on the order of 1 to 2 % over most of the operating area.
- The performance of all the estimators was found to be temperature dependent, with mild increases in estimator error around the axis edges of the operating area. One of the contributing factors was the change in motor efficiency at different operating temperatures. At low speeds (and powers), a cold motor was found to have slightly better efficiency compared to a hot motor, reflecting a change in loss components that ultimately impact the sensorless estimates.
- To demonstrate the performance of the estimation method for a motor system with nonlinear load, the method was extended to a pump system. Additional estimator models were developed for pump head pressure, flow, hydraulic power, efficiency and total volume pumped.
- Automatic field weakening was used to operate the motor beyond the limits of the inverter voltage supply, allowing for the pump to operate up to its rated speed. This resulted in the d-axis current varying over the operating area, however these variations could be captured implicitly in the estimator models in terms of speed and q-axis current.
- Estimation of flow rate was found to rely more heavily on current measurements. At low speeds, the entire flow rate range corresponded to a change in current of only 1 % of the full scale inverter current range. At high speeds, the entire flow rate range corresponded to a change in current of 8 % of the full scale inverter current range. Fluctuations in the real time q-axis current were found to be up to 7$\times$ the current range corresponding to the full scale flow rate range, meaning the flow rate current component was buried in noise and difficult to use. The introduction of a high sample rate (15 kHz) but very narrow bandwidth (1 Hz) low pass filter was able to address these issues, resulting in a flow rate error below 10 % for most of the pump's operating area, with error below 2.5 % in the middle of the operating area.
- The pump head estimator performed well with an error typically between 0.5 % and 1 %, partly attributed to the strong speed versus head relationship of the pump tested.

- When operating in the pump system, the original speed, torque, power and efficiency estimators (that were modelled on the original motor system) operated beyond their original operating areas (extrapolated estimates), resulting in increased error compared to that of the original motor system. Remodelling these specifically for the pump application returned the performance of these estimators to that of the original motor system's estimators.

- Similar to the motor system estimators, the pump estimators were also found to be sensitive to temperature, where the error around the operating area edges would increase when the temperature was different to that of the modelling temperature.

- In addition to temperature, the accuracy of all sensorless estimators depends on the accuracy of the q-axis current measurement, which in turn depends on the accuracy of the position sensorless rotor angle estimate. Consequently, the performance of motor and end application state estimation cannot be determined in isolation, but must include the full set of sensorless estimators operating in an integrated motor system.

- The pump estimators were only modelled for steady state, but it was found that they could provide good dynamic estimation of the pump system when the speed was constant. That is, sudden changes in the hydraulic system could be accurately captured in terms of flow and head estimates. However, the estimators produced incorrect estimates during dynamic speed changes, attributed to the models not capturing the additional torque required as the mechanical inertia in the system accelerates.

- Estimation of the volume of liquid pumped had an error of 9.4 % over the entire system operating area, using the simple method of Euler integration. When the system was operated with a large number of dynamic changes, the error increased to just under 13 % as a result of the large dynamic estimation error during speed changes.

7.2 Recommendations and Future Work

The performance of the motor system state estimators could be further improved by compensating for temperature changes in the motor. The Texas Instruments inverter used for testing includes the ability to estimate stator resistance using

small variations in d-axis current. Combined with calculations for stator temperature from copper winding resistance described in IEEE Std 112 [65], real time stator resistance could be used to provide dynamic temperature estimates. These temperature estimates could then be included in all other motor estimates. This would allow for wide speed operation of these estimators not just over speed and torque combinations, but also over widely varying ambient temperature and motor temperature conditions.

Moreover, the estimators could also be extended to cover the general condition of a non-zero d-axis current. Although field weakening operation was demonstrated, the d-axis current changes were implicitly captured in the estimators as a speed dependent quantity. By explicitly accounting for the influence of d-axis current, motor state estimators would be able to operate with arbitrary d-axis current. This would allow for the use of real-time optimisation schemes that make use varying d-axis current, for example induction motors with flux optimisation.

The pump state estimator had difficulty producing a low error flow rate estimate as a result of the large fluctuations in q-axis current and the small current sensing range that corresponded to changes in flow rate. Moreover, for the case of the pump system tested, this showed that the quality of the flow rate estimate was impacted by the selection and matching of system components. Improved flow rate estimation could be achieved by carefully designing and selecting the inverter and motor to provide more stable current control with a current sensing range more closely matched to the characteristic of the pump. More broadly, future studies could consider how best to design and match a range of specific integrated motor systems and applications to optimise motor state estimation performance.

The proposed method of motor state estimation included the estimation of the power into the inverter, and in the case of the pump system also included the estimation of total volume pumped. These estimates could be used in an integrated motor system that provides demand side management as part of a larger nano-grid or micro-grid system. Demand side management involves the load device (in this case an integrated motor/pump system) dynamically responding to requests to reduce power consumption in response to changing grid (or micro-grid) power supply-demand balance. In the case of a pump system with volume estimate, the inverter control systems could be extended to achieve a total pumped volume while optimising system efficiency and satisfying the power consumption commands of a nano-grid or micro-grid system.

A pump system was chosen as the landmark application of the motor state

estimation method because such a system includes all components of a typical motor drive system, can be manufactured as an integrated system, and has wide spread usage. However, the proposed estimation methods are not limited to pump systems, but could be applied to other motor system applications including fans, compressors and vehicles. In the future, these applications will likely be implemented as fully integrated motor systems with components carefully designed to maximise system efficiency. The research presented in this thesis is beneficial to a variety of integrated motor systems and can help expand the knowledge of how these systems operate and perform over a wide range of operating conditions. In particular, the proposed sensorless methods can be used to further develop integrated motor systems into smart devices that provide extensive performance history, condition monitoring and advanced control for a variety of applications.

Bibliography

[1] P. Waide and C. U. Brunner, *Energy-Efficiency Policy Opportunities for Electric Motor-Driven Systems, Working Paper*, English, Working Paper, 2011. [Online]. Available: https://webstore.iea.org/energy-efficiency-policy-opportunities-for-electric-motor-driven-systems (visited on Jul. 11, 2014).

[2] A. de Almeida, F. Ferreira, and A. Quintino Duarte, "Technical and Economical Considerations on Super High-Efficiency Three-Phase Motors", *IEEE Trans. Ind. Appl.*, vol. 50, no. 2, pp. 1274–1285, Mar. 2014, ISSN: 0093-9994. DOI: 10.1109/TIA.2013.2272548.

[3] *Swimming Pool Pumps*, en, Dec. 2018. [Online]. Available: http://www.energyrating.gov.au/products/swimming-pool-pumps (visited on Feb. 8, 2019).

[4] Commonwealth of Australia (Department of the Environment and Energy), "Decision Regulation Impact Statement: Swimming pool pumps", en, Tech. Rep., Dec. 2018, p. 87. [Online]. Available: http://www.energyrating.gov.au/document/decision-ris-swimming-pool-pumps.

[5] A. de Almeida, F. Ferreira, and G. Baoming, "Beyond Induction Motors - Technology Trends to Move Up Efficiency", *IEEE Trans. Ind. Appl.*, vol. 50, no. 3, pp. 2103–2114, May 2014, ISSN: 0093-9994. DOI: 10.1109/TIA.2013.2288425.

[6] V. Dmitrievskii, V. Prakht, V. Kazakbaev, S. Oshurbekov, and I. Sokolov, "Developing ultra premium efficiency (IE5 class) magnet-free synchronous reluctance motor", in *2016 6th Int. Electric Drives Production Conf. (EDPC)*, Nov. 2016, pp. 2–7. DOI: 10.1109/EDPC.2016.7851306.

[7] J. Gieras, *Permanent Magnet Motor Technology: Design and Applications, Third Edition*, en, ser. Electrical and Computer Engineering. CRC Press, 2010, vol. 20096073, ISBN: 978-1-4398-5901-8.

[8] F. J. T. E. Ferreira and A. T. de Almeida, "Overview on energy saving opportunities in electric motor driven systems - Part 1: System efficiency improvement", in *2016 IEEE/IAS 52nd Industrial and Commercial Power Systems Tech. Conf. (I CPS)*, May 2016, pp. 1–8. DOI: 10.1109/ICPS.2016.7490219.

[9] C. Tang, W. L. Soong, G. S. Liew, and N. Ertugrul, "Modelling of surface PM machine using soft magnetic composites and a bonded magnet ring", in *2012 XXth Int. Conf. on Electrical Machines*, Sep. 2012, pp. 364–371. DOI: 10.1109/ICElMach.2012.6349892.

[10] A. Mahmoudi, W. L. Soong, G. Pellegrino, and E. Armando, "Loss Function Modeling of Efficiency Maps of Electrical Machines", *IEEE Trans. Ind. Appl.*, vol. 53, no. 5, pp. 4221–4231, Sep. 2017, ISSN: 0093-9994. DOI: 10.1109/TIA.2017.2695443.

[11] S. Williamson, S. Lukic, and A. Emadi, "Comprehensive drive train efficiency analysis of hybrid electric and fuel cell vehicles based on motor-controller efficiency modeling", *IEEE Trans. Power Electron.*, vol. 21, no. 3, pp. 730–740, May 2006, ISSN: 0885-8993. DOI: 10.1109/TPEL.2006.872388.

[12] W. Deprez, J. Lemmens, D. Vanhooydonck, W. Symens, K. Stockman, S. Dereyne, and J. Driesen, "Iso efficiency contours as a concept to characterize variable speed drive efficiency", in *2010 XIX Int. Conf. on Electrical Machines (ICEM)*, Sep. 2010, pp. 1–6. DOI: 10.1109/ICELMACH.2010.5607991.

[13] K. Stockman, S. Dereyne, D. Vanhooydonck, W. Symens, J. Lemmens, and W. Deprez, "Iso efficiency contour measurement results for variable speed drives", in *2010 XIX Int. Conf. on Electrical Machines (ICEM)*, Sep. 2010, pp. 1–6. DOI: 10.1109/ICELMACH.2010.5608035.

[14] F. J. T. E. Ferreira and A. T. de Almeida, "Overview on energy saving opportunities in electric motor driven systems - Part 2: Regeneration and output power reduction", in *2016 IEEE/IAS 52nd Industrial and Commercial Power Systems Tech. Conf. (I CPS)*, May 2016, pp. 1–8. DOI: 10.1109/ICPS.2016.7490220.

[15] A. Marchi, A. R. Simpson, and N. Ertugrul, "Assessing variable speed pump efficiency in water distribution systems", en, *Drink. Water Eng. Sci.*, vol. 5, no. 1, pp. 15–21, Jul. 2012, ISSN: 1996-9465. DOI: 10.5194/dwes-5-15-2012.

[16] A. de Almeida, F. Ferreira, and D. Both, "Technical and economical considerations in the application of variable-speed drives with electric motor systems", *IEEE Trans. Ind. Appl.*, vol. 41, no. 1, pp. 188–199, Jan. 2005, ISSN: 0093-9994. DOI: 10.1109/TIA.2004.841022.

[17] T. Ahonen, J. Tamminen, J. Ahola, J. Viholainen, N. Aranto, and J. Kestilä, "Estimation of pump operational state with model-based methods", *Energy Conversion and Management*, vol. 51, no. 6, pp. 1319–1325, Jun. 2010, ISSN: 0196-8904. DOI: 10.1016/j.enconman.2010.01.009.

[18] S. Leonow and M. Mönnigmann, "Soft sensor based dynamic flow rate estimation in low speed radial pumps", in *2013 European Control Conference (ECC)*, Jul. 2013, pp. 778–783. DOI: 10.23919/ECC.2013.6669438.

[19] K. Iizuka, H. Uzuhashi, M. Kano, T. Endo, and K. Mohri, "Microcomputer Control for Sensorless Brushless Motor", *IEEE Trans. Ind. Appl.*, vol. IA-21, no. 3, pp. 595–601, May 1985, ISSN: 0093-9994. DOI: 10.1109/TIA.1985.349715.

[20] J. Johnson, M. Ehsani, and Y. Guzelgunler, "Review of sensorless methods for brushless DC", in *Conference Record of the 1999 IEEE Industry Applications Conference, 1999. Thirty-Fourth IAS Annual Meeting*, vol. 1, 1999, 143–150 vol.1. DOI: 10.1109/IAS.1999.799944.

[21] P. Acarnley and J. Watson, "Review of position-sensorless operation of brushless permanent-magnet machines", *IEEE Trans. Ind. Electron.*, vol. 53, no. 2, pp. 352–362, Apr. 2006, ISSN: 0278-0046. DOI: 10.1109/TIE.2006.870868.

[22] G. Haines and N. Ertugrul, "Wide Speed Range Sensorless Operation of Brushless Permanent-Magnet Motor Using Flux Linkage Increment", *IEEE Trans. Ind. Electron.*, vol. 63, no. 7, pp. 4052–4060, Jul. 2016, ISSN: 0278-0046. DOI: 10.1109/TIE.2016.2544250.

[23] L. Beran and M. Diblík, "Indirect torque measurement using industrial vector control frequency converter", in *2016 17th International Carpathian Control Conference (ICCC)*, May 2016, pp. 48–53. DOI: 10.1109/CarpathianCC.2016.7501065.

[24] T. Ahonen, J. Tamminen, L. Niinimäki, C. A. A. Mar, and M. Niemelä, "Estimation accuracy of a vector-controlled frequency converter used in the determination of the pump system operating state", in *2013 15th European Conference on Power Electronics and Applications (EPE)*, Sep. 2013, pp. 1–10. DOI: 10.1109/EPE.2013.6634379.

[25] L. Aamiovuori, H. Kärkkäinen, M. Niemelä, P. Lindh, and J. Pyrhönen, "Induction motor torque estimation accuracy using motor terminal variables", in *2017 IEEE International Electric Machines and Drives Conference (IEMDC)*, May 2017, pp. 1–7. DOI: 10.1109/IEMDC.2017.8002304.

[26] C. Bastiaensen, W. Deprez, W. Symens, and J. Driesen, "Parameter Sensitivity and Measurement Uncertainty Propagation in Torque-Estimation Algorithms for Induction Machines", *IEEE Trans. Instrum. Meas.*, vol. 57, no. 12, pp. 2727–2732, Dec. 2008, ISSN: 0018-9456. DOI: 10.1109/TIM.2008.926053.

[27] K. Yamazaki, "Torque and efficiency calculation of an interior permanent magnet motor considering harmonic iron losses of both the stator and rotor", *IEEE Trans. Magn.*, vol. 39, no. 3, pp. 1460–1463, May 2003, ISSN: 0018-9464. DOI: 10.1109/TMAG.2003.810515.

[28] M. Barcaro, N. Bianchi, and F. Magnussen, "Remarks on Torque Estimation Accuracy in Fractional-Slot Permanent-Magnet Motors", *IEEE Trans. Ind. Electron.*, vol. 59, no. 6, pp. 2565–2572, Jun. 2012, ISSN: 0278-0046. DOI: 10.1109/TIE.2011.2160517.

[29] F. Tinazzi and M. Zigliotto, "Torque Estimation in High-Efficency IPM Synchronous Motor Drives", *IEEE Trans. Energy Convers.*, vol. 30, no. 3, pp. 983–990, Sep. 2015, ISSN: 0885-8969. DOI: 10.1109/TEC.2015.2408214.

[30] F. J. T. E. Ferreira and A. T. de Almeida, "Reducing Energy Costs in Electric-Motor-Driven Systems: Savings Through Output Power Reduction and Energy Regeneration", *IEEE Ind. Appl. Mag.*, vol. 24, no. 1, pp. 84–97, Jan. 2018, ISSN: 1077-2618. DOI: 10.1109/MIAS.2016.2600685.

[31] T. Ahonen, J. T. Kortelainen, J. K. Tamminen, and J. Ahola, "Centrifugal pump operation monitoring with motor phase current measurement", *International Journal of Electrical Power & Energy Systems*, vol. 42, no. 1, pp. 188–195, Nov. 2012, ISSN: 0142-0615. DOI: 10.1016/j.ijepes.2012.04.013.

[32] *ISO 9906:2012 : Rotodynamic Pumps - Hydraulic Performance Acceptance Tests - Grades 1, 2 and 3*. Geneva, Switzerland: International Organization for Standardization, Apr. 2012.

[33] T. Ahonen, J. Tamminen, J. Ahola, and J. Kestila, "Frequency-Converter-Based Hybrid Estimation Method for the Centrifugal Pump Operational State", *IEEE Trans. Ind. Electron.*, vol. 59, no. 12, pp. 4803–4809, Dec. 2012, ISSN: 0278-0046. DOI: 10.1109/TIE.2011.2176692.

[34] S. Leonow and M. Monnigmann, "Operating point estimation in hydraulic turbomachines with non-invertible characteristics", in *2016 European Control Conference (ECC)*, Jun. 2016, pp. 2380–2385. DOI: 10.1109/ECC.2016.7810646.

[35] V. Vodovozov and I. Bakman, "Sensorless pressure calculation for parallel redundancy in pumping systems", in *2014 16th European Conference on Power Electronics and Applications*, Aug. 2014, pp. 1–9. DOI: 10.1109/EPE.2014.6910706.

[36] V. Vodovozov, L. Gevorkov, and Z. Raud, "Multi-motor pressure management system with minimal energy consumption", in *2016 IEEE 14th International Conference on Industrial Informatics (INDIN)*, Jul. 2016, pp. 243–247. DOI: 10.1109/INDIN.2016.7819166.

[37] A. Funakubo, S. Ahmed, I. Sakuma, and Y. Fukui, "Flow Rate and Pressure Head Estimation in a Centrifugal Blood Pump", en, *Artificial Organs*, vol. 26, no. 11, pp. 985–990, Nov. 2002, ISSN: 1525-1594. DOI: 10.1046/j.1525-1594.2002.07134.x.

[38] F. Casas, N. Ahmed, and A. Reeves, "Minimal sensor count approach to fuzzy logic rotary blood pump flow control", eng, *ASAIO J.*, vol. 53, no. 2, pp. 140–146, 2007 Mar-Apr, ISSN: 1538-943X. DOI: 10.1097/01.mat.0000250786.56697.f2.

[39] A. H. AlOmari, A. V. Savkin, D. M. Karantonis, E. Lim, and N. H. Lovell, "Non-invasive estimation of pulsatile flow and differential pressure in an implantable rotary blood pump for heart failure patients", en, *Physiol. Meas.*, vol. 30, no. 4, p. 371, Apr. 2009, ISSN: 0967-3334. DOI: 10.1088/0967-3334/30/4/003.

[40] "3 - Flow of liquids", in *Handbook of Pumps and Pumping*, B. Nesbitt, Ed., Oxford: Elsevier Science Ltd, 2006, pp. 95–124, ISBN: 978-1-85617-476-3. DOI: 10.1016/B978-185617476-3/50005-6.

[41] C. F. Colebrook and C. M. White, "Experiments with fluid friction in roughened pipes", en, *Proc. R. Soc. Lond. A*, vol. 161, no. 906, pp. 367–381, Aug. 1937, ISSN: 0080-4630, 2053-9169. DOI: 10.1098/rspa.1937.0150.

[42] L. F. Moody, "Friction factors for pipe flow", *Trans Asme*, vol. 66, pp. 671–684, 1944.

[43] "4 - Pump theory", in *Handbook of Pumps and Pumping*, B. Nesbitt, Ed., Oxford: Elsevier Science Ltd, 2006, pp. 125–153, ISBN: 978-1-85617-476-3. DOI: 10.1016/B978-185617476-3/50006-8.

[44] "5 - Pumps and piping systems", in *Handbook of Pumps and Pumping*, B. Nesbitt, Ed., Oxford: Elsevier Science Ltd, 2006, pp. 155–174, ISBN: 978-1-85617-476-3. DOI: 10.1016/B978-185617476-3/50007-X.

[45] T.-H. Kim and M. Ehsani, "Sensorless control of the BLDC motors from near-zero to high speeds", *IEEE Trans. Power Electron.*, vol. 19, no. 6, pp. 1635–1645, Nov. 2004, ISSN: 0885-8993. DOI: 10.1109/TPEL.2004.836625.

[46] B. Hu, J. Lee, S. Sathiakumar, and Y. Shrivastava, "A novel sensorless algorithm of the trapezoidal back-electromagnetic force brushless DC motors from near-zero to high speeds", *Aust. J. Electr. Electron. Eng.*, vol. 9, no. 3, pp. 263–273, 2012, ISSN: 1448-837X. DOI: 10.7158/E11-922.2012.9.3.

[47] N. Ertugrul and P. Acarnley, "A new algorithm for sensorless operation of permanent magnet motors", *IEEE Trans. Ind. Appl.*, vol. 30, no. 1, pp. 126–133, Jan. 1994, ISSN: 0093-9994. DOI: 10.1109/28.273630.

[48] N. Matsui, "Sensorless PM brushless DC motor drives", *IEEE Trans. Ind. Electron.*, vol. 43, no. 2, pp. 300–308, Apr. 1996, ISSN: 0278-0046. DOI: 10.1109/41.491354.

[49] Y. Kang, S. B. Lee, and J.-Y. Yoo, "A microcontroller embedded AD converter based low cost sensorless technique for brushless DC motor drives", in *Industry Applications Conference, 2005. Fourtieth IAS Annual Meeting. Conference Record of the 2005*, vol. 3, Oct. 2005, 2176–2181 Vol. 3. DOI: 10.1109/IAS.2005.1518748.

[50] H.-G. Yee, C.-S. Hong, J.-Y. Yoo, H.-G. Jang, Y.-D. Bae, and Y.-S. Park, "Sensorless drive for interior permanent magnet brushless DC motors", in *Electric Machines and Drives Conference Record, 1997. IEEE International*, May 1997, TD1/3.1–TD1/3.3. DOI: 10.1109/IEMDC.1997.604275.

[51] J. Shao, "An improved microcontroller-based sensorless brushless DC (BLDC) motor drive for automotive applications", in *Industry Applications Conference, 2005. Fourtieth IAS Annual Meeting. Conference Record of the 2005*, vol. 4, Oct. 2005, 2512–2517 Vol. 4. DOI: 10.1109/IAS.2005.1518813.

[52] Y.-S. Lai and Y.-K. Lin, "A Unified Approach to Zero-Crossing Point Detection of Back EMF for Brushless DC Motor Drives without Current and Hall Sensors", *IEEE Trans. Power Electron.*, vol. 26, no. 6, pp. 1704–1713, Jun. 2011, ISSN: 0885-8993. DOI: 10.1109/TPEL.2010.2081379.

[53] Y. Amano, T. Tsuji, A. Takahashi, S. Ouchi, K. Hamatsu, and M. Iijima, "A sensorless drive system for brushless DC motors using a digital phase-locked loop", en, *Elect. Eng. Jpn.*, vol. 142, no. 1, pp. 57–66, 2003, ISSN: 1520-6416. DOI: 10.1002/eej.10074.

[54] R. Becerra, T. Jahns, and M. Ehsani, "Four-quadrant sensorless brushless ECM drive", in *Applied Power Electronics Conference and Exposition, 1991. APEC '91. Conference Proceedings, 1991., Sixth Annual*, Mar. 1991, pp. 202–209. DOI: 10.1109/APEC.1991.146165.

[55] S. Lin, C. Bi, and Q. Jiang, "An effective method to obtain commutation positions in BLDC drive mode", en, *Microsyst Technol*, vol. 17, no. 3, pp. 347–350, Mar. 2011, ISSN: 0946-7076, 1432-1858. DOI: 10.1007/s00542-011-1265-3.

[56] A. Darba, F. De Belie, and J. Melkebeek, "Sensorless commutation and speed control of Brushless DC-machine drives based on the back-EMF symmetric threshold-tracking", in *Electric Machines Drives Conference (IEMDC), 2013 IEEE International*, May 2013, pp. 492–497. DOI: 10.1109/IEMDC.2013.6556141.

[57] T.-W. Chun, Q.-V. Tran, H.-H. Lee, and H.-G. Kim, "Sensorless Control of BLDC Motor Drive for an Automotive Fuel Pump Using a Hysteresis Comparator", *IEEE Trans. Power Electron.*, vol. 29, no. 3, pp. 1382–1391, Mar. 2014, ISSN: 0885-8993. DOI: 10.1109/TPEL.2013.2261554.

[58] C. Cui, G. Liu, K. Wang, and X. Song, "Sensorless Drive for High-Speed Brushless DC Motor Based on the Virtual Neutral Voltage", *IEEE Trans. Power Electron.*, vol. 30, no. 6, pp. 3275–3285, Jun. 2015, ISSN: 0885-8993. DOI: 10.1109/TPEL.2014.2337292.

[59] S. Tsotoulidis and A. Safacas, "Deployment of an Adaptable Sensorless Commutation Technique on BLDC Motor Drives Exploiting Zero Sequence Voltage", *IEEE Trans. Ind. Electron.*, vol. 62, no. 2, pp. 877–886, Feb. 2015, ISSN: 0278-0046. DOI: 10.1109/TIE.2014.2334654.

[60] Freescale Semiconductor, "AN1913 3-phase BLDC Motor Control with Sensorless Back-EMF ADC Zero Crossing Detection using 56F80x", Nov. 2005. [Online]. Available: http://cache.freescale.com/files/product/doc/AN1913.pdf (visited on Jan. 27, 2015).

[61] A. Darba, F. De Belie, and J. Melkebeek, "A Back-EMF Threshold Self-Sensing Method to Detect the Commutation Instants in BLDC Drives", *IEEE Trans. Ind. Electron.*, vol. 62, no. 10, pp. 6064–6075, Oct. 2015, ISSN: 0278-0046. DOI: 10.1109/TIE.2015.2423651.

[62] Freescale Semiconductor, "AN4597 BLDC Sensorless Algorithm Tuning", Oct. 2012. [Online]. Available: http://cache.freescale.com/files/microcontrollers/doc/app_note/AN4597.pdf (visited on Jan. 27, 2015).

[63] Texas Instruments, "SPRABN7 Application Report - InstaSPIN BLDC Lab", Nov. 2011. [Online]. Available: http://www.ti.com/tool/instaspin-bldc (visited on Jan. 27, 2015).

[64] N. Ertugrul and P. P. Acarnley, "Analytical Solution of the System Equations of the Axial Field Permanent Magnet Synchronous Motor Drive", in *ICEM International Conference on Electrical Machines*, Manchester, UK, Sep. 1992, pp. 785–789.

[65] "IEEE Standard Test Procedure for Polyphase Induction Motors and Generators", *IEEE Std 112-2004 Revis. IEEE Std 112-1996*, 0_1–79, 2004. DOI: 10.1109/IEEESTD.2004.95394.

[66] "Rotating electrical machines - Part 2-1: Standard methods for determining losses and efficiency from tests (excluding machines for traction vehicles)", *IEC 60034-2-12014*, p. 186, Jun. 2014.

[67] "IEEE Trial-Use Guide for Testing Permanent Magnet Machines", *IEEE Std 1812-2014*, pp. 1–56, Feb. 2015. DOI: 10.1109/IEEESTD.2015.7047988.

[68] "IEEE Guide for Test Procedures for Synchronous Machines Part IAcceptance and Performance Testing Part IITest Procedures and Parameter Determination for Dynamic Analysis", *IEEE Std 115-2009 Revis. IEEE Std 115-1995*, pp. 1–219, May 2010. DOI: 10.1109/IEEESTD.2010.5464495.

[69] "Rotating electrical machines - Part 2-3: Specific test methods for determining losses and efficiency of converter-fed AC induction motors", *IEC TS 60034-2-32013*, p. 44, Nov. 2013.

[70] "Adjustable speed electrical power drive systems - Part 9-2: Ecodesign for power drive systems, motor starters, power electronics and their driven applications - Energy efficiency indicators for power drive systems and motor starters", *IEC 61800-9-22017*, p. 226, Mar. 2017.

[71] R. Bojoi, E. Armando, M. Pastorelli, and K. Lang, "Efficiency and loss mapping of AC motors using advanced testing tools", in *2016 XXII Int. Conf. on Electrical Machines (ICEM)*, Sep. 2016, pp. 1043–1049. DOI: 10.1109/ICELMACH.2016.7732654.

[72] C. Depature, W. Lhomme, A. Bouscayrol, P. Sicard, and L. Boulon, "Efficiency Map of the Traction System of an Electric Vehicle from an On-Road Test Drive", in *2014 IEEE Vehicle Power and Propulsion Conf. (VPPC)*, Oct. 2014, pp. 1–6. DOI: 10.1109/VPPC.2014.7007056.

[73] E. Dlala, M. Solveson, S. Stanton, Z. Tang, M. Christini, R. Ong, and B. Peaslee, "Efficiency map simulations for an interior PM motor with experimental comparison and investigation of magnet size reduction", in *Electric Machines Drives Conf. (IEMDC), 2013*, May 2013, pp. 23–29. DOI: 10.1109/IEMDC.2013.6556124.

[74] D. Vanhooydonck, W. Symens, W. Deprez, J. Lemmens, K. Stockman, and S. Dereyne, "Calculating energy consumption of motor systems with varying load using iso efficiency contours", in *2010 XIX Int. Conf. on Electrical Machines (ICEM)*, Sep. 2010, pp. 1–6. DOI: 10.1109/ICELMACH.2010.5607992.

[75] Y. Loayza, A. Reinap, and M. Alaküla, "Performance and efficiency evaluation of FPGA controlled IPMSM under dynamic loading", in *8th IEEE Symp. on Diagnostics for Electrical Machines, Power Electronics Drives*, Sep. 2011, pp. 550–555. DOI: 10.1109/DEMPED.2011.6063677.

[76] G. Haines and N. Ertugrul, "Application Sensorless State and Efficiency Estimation for Integrated Motor Systems", in *13th IEEE Int. Conf. on Power Electronics and Drive Systems (PEDS 2019)*, Toulouse, France, Jul. 2019, pp. 1–6.

[77] MathWorks Inc., *Evaluating Goodness of Fit*, 2019. [Online]. Available: https://au.mathworks.com/help/curvefit/evaluating-goodness-of-fit.html (visited on Jan. 31, 2019).

[78] Geoscience Australia, *Australian Fundamental Gravity Network*. [Online]. Available: http://www.ga.gov.au/afgn/ (visited on Nov. 8, 2019).

[79] W. M. Haynes, *CRC Handbook of Chemistry and Physics, 95th Edition*. Oakville, UNITED KINGDOM: CRC Press LLC, 2014, ISBN: 978-1-4822-0868-9.

[80] T. K. Serghides, "Estimate friction factor accurately", *Chem. Eng.*, vol. 91, no. 5, pp. 63–64, 1984.